nanomaterials

Applications of Nanofluids

Edited by

Mikhail A. Sheremet

Printed Edition of the Special Issue Published in *Nanomaterials*

www.mdpi.com/si/nanomaterials

MDPI

Applications of Nanofluids

Applications of Nanofluids

Editor

Mikhail A. Sheremet

MDPI • Basel • Beijing • Wuhan • Barcelona • Belgrade • Manchester • Tokyo • Cluj • Tianjin

Editor
Mikhail A. Sheremet
Tomsk State University
Russia

Editorial Office
MDPI
St. Alban-Anlage 66
4052 Basel, Switzerland

This is a reprint of articles from the Special Issue published online in the open access journal *Nanomaterials* (ISSN 2079-4991) (available at: https://www.mdpi.com/journal/nanomaterials/special_issues/applications_nanofluids).

For citation purposes, cite each article independently as indicated on the article page online and as indicated below:

LastName, A.A.; LastName, B.B.; LastName, C.C. Article Title. *Journal Name* **Year**, *Volume Number*, Page Range.

ISBN 978-3-0365-2169-5 (Hbk)
ISBN 978-3-0365-2170-1 (PDF)

Contents

About the Editor

Mikhail A. Sheremet (Professor) is Head of the Laboratory on Convective Heat and Mass Transfer and Head of the Department of Theoretical Mechanics at Tomsk State University. He received a Candidate of Science in Physics and Mathematics degree from Tomsk State University (2006), and habilitation (Russia, Doctor of Science in Physics and Mathematics) (2012) from Tomsk State University. Prof. Mikhail Sheremet has published over 350 papers in peer-reviewed journals and conference proceedings, and contributed to several books. He obtained the Web of Science Award 2017 in the category of Highly Cited Researcher in Russia. His h-index is 56 (Scopus Database). He is a member of Editorial Boards of the International Journal of Numerical Methods for Heat & Fluid Flow, Journal of Magnetism and Magnetic Materials, Journal of Applied and Computational Mechanics, Nanomaterials, Coatings, and Entropy. He is a member of the Scientific Council of the International Centre for Heat and Mass Transfer.

nanomaterials

MDPI

Editorial

Applications of Nanofluids

Mikhail A. Sheremet

Laboratory on Convective Heat and Mass Transfer, Tomsk State University, 634050 Tomsk, Russia; sheremet@math.tsu.ru; Tel.: +7-3822-529740

Nanofluids as a combination of base fluid and a low concentration of nano-sized particles of metal or metal oxides are used in different fields of human activity, including engineering devices in power and chemical engineering, medicine, electronics, and others. The main reason for such huge variety of nanofluid applications is the possibility, from one side, to enhance the heat and mass transfer due to the low concentration of nano-sized particles and, from the other side, to control the transport processes that can be used, e.g., in the drag delivery systems.

This Special Issue consists of twelve articles dedicated to nanofluid properties [1], the influence of nanoparticles on properties of other materials [2–4], as well as the possibility to enhance the heat transfer in different engineering devices using nanofluids, including the cooling of heat-generating elements in electronic devices [5–8], minichannel [9] and microchannel [10] optimization, and heat exchangers [11,12]. The objective of this Special Issue is to demonstrate the recent studies on nanoparticles and nanofluid applications in material treatment and engineering device optimization, which could be very useful for various specialists in mechanical and chemical engineering, physics, and mathematics. The following paragraphs include a brief overview of these mentioned papers with some innovative ideas.

Thus, we begin with a paper on an artificial neural network application for the prediction of the physical properties of nanofluids. Sadeghzadeh et al. [1] have synthesized the TiO_2-Al_2O_3/H_2O nanofluid and experimentally measured the specific heat capacity and thermal conductivity. After taking into account the opportunities of the neural networks, the multilayer perceptron structure has been employed to develop a model for the analysis of the thermal attributes of nanofluids. A good correlation can be achieved using the neural networks. Xie et al. [2] have analyzed features of the corrosive nature of a brass surface under the influence of nanofluids. It has been found that sodium dodecyl benzene sulfonate (SDBS) as a dispersant allows the formation of a protective film on the brass surface in simulated cooling water (SCW). At the same time, the addition of nanoparticles to the SCW-SDBS system can improve or degrade the protective properties of the film on the brass surface. Thus, an addition of negatively charged TiO_2 nanoparticles does not allow the formation of an SDBS adsorption film, while in the case of positively charged Al_2O_3 nanoparticles, the properties of the protective film can be improved. García-Beltrán et al. [3] have studied opportunities of hybrid nanosystems for the improvement of the dynamic nonlinear optical effects. Thus, it has been revealed that the third-order nonlinear optical nature of metal/carbon nanosuspensions can be employed for developing dynamic nanoantennas. Zhu et al. [4] have analyzed novel opportunities to employ nanowires and nanotubes in chemical and bio-sensing engineering devices. The authors have analyzed the synthesis techniques for nanowires and nanotubes, sensing mechanisms of nanofluidic devices based on nanowires and nanotubes, and some applications.

Nanofluids are widely employed in different cooling systems for effective heat removal from electronics. Thus, Asadi et al. [5] have scrutinized the numerically convective heat transfer of copper oxide/water nanosuspension in a porous I-shaped chamber with a centered isothermal triangular block. Analysis has been performed using the Buongiorno nanofluid model with empirical correlations for effective viscosity and thermal

Citation: Sheremet, M.A. Applications of Nanofluids. *Nanomaterials* **2021**, *11*, 1716. https://doi.org/10.3390/nano11071716

Received: 10 June 2021
Accepted: 21 June 2021
Published: 29 June 2021

conductivity. It has been ascertained that the orientation of an internal hot triangular block has an essential influence on the thermal pattern and flow structures within the chamber. Moreover, an addition of nanoparticles can enhance the heat removal from the local hot element. Bondareva et al. [6] have numerically investigated an opportunity to enhance the heat removal from the local heat-generating element under the influence of a heat sink filled with a phase change material. Five different phase change materials, enhanced with alumina nanoparticles, have been studied. It has been shown that n-octadecane, RT-80, and lauric acid are more effective materials for cooling enhancement. At the same time, an addition of alumina nanoparticles can slightly reduce the heat source temperature. An interesting numerical problem on the natural convection of alumina/water nanosuspension in a square chamber with inner solid block has been solved by Pop et al. [7] using the finite difference schemes and non-primitive variables. Such an approach allows a reduction in the computational time, but one of the main difficulties for such a formulation is a definition of the stream function value at the inner block. This problem was solved in the present study by employing the single-valued pressure along this block. As a result, a value of the stream function has been defined. Using the experimentally based correlations for nanofluid viscosity and thermal conductivity, the obtained outcomes have demonstrated that the growth of nanoparticle concentration reduces the energy transference strength. Using Fluent software, Jilte et al. [8] have numerically studied the heat transfer performance of a concentric channel thermal sink with an additional slot for the liquid. Taking into account the single-phase nanofluid approach with theoretical correlations for effective viscosity and thermal conductivity, it has been revealed that a rise in the flow rate characterizes a diminution of the maximum local temperature, while an inclusion of nanoparticles can also enhance the cooling effect.

An optimal design of minichannels can improve the heat transfer performance for various engineering devices. Thus, Ahmadi et al. [9] have studied a technique for the multi-objective optimization of minichannels in the case of alumina/water nanosuspension. The surface response methodology has been employed for the present analysis. Using the single-phase nanofluid approach with temperature-dependent properties, several numerical experiments have been performed. After, using statistical approaches, an analysis of the results has been conducted, and optimized parameters have been defined. Computational analysis of copper-water nanofluid flow and heat transfer in single and multi-channel heat sink has been performed by Khan et al. [10], employing Fluent software for the single-phase nanofluid model. The analysis has shown that the multi-channel system can increase the heat transfer rate, while an addition of nanoparticles also illustrates the energy transport enhancement. Alsabery et al. [11] have computationally examined the influence of a rotated inner cylinder on convective energy transport in a wavy differentially heated chamber filled with alumina-water nanofluid. Using the Buongiorno nanofluid model with effects of Brownian diffusion and thermophoresis, the authors have shown a possible energy transference enhancement with nanoparticle concentration. At the same time, the rotation of the cylinder and the waviness of the right vertical wall can intensify the convective heat transference. Ghalambaz et al. [12] have shown that using solid nanoadditives and twisted tape inserts allows the enhancement of the thermal performance of the double-pipe heat exchanger. Using Fluent software with two-phase nanofluid model, the authors have demonstrated the average Nusselt number increment for twisted tape inserts and alumina nanoparticles.

These published papers have shown a huge diversity of nanofluid and nanoparticle applications based on detailed analyses using numerical and experimental techniques.

Funding: This work was supported by the Russian Science Foundation, Project No. 17-79-20141.

Institutional Review Board Statement: Not applicable.

Informed Consent Statement: Not applicable.

Data Availability Statement: All data can be found in this paper or in papers cited here.

Acknowledgments: I am grateful to all the authors for submitting their studies to the present Special Issue and for its successful completion. I deeply acknowledge the Nanomaterials Reviewers for enhancing the quality and impact of all submitted papers. Finally, I sincerely thank Erika Zhao and the editorial staff of Nanomaterials for their stunning support during the development and publication of this Special Issue.

Conflicts of Interest: The author declares no conflict of interest.

References

1. Sadeghzadeh, M.; Maddah, H.; Ahmadi, M.H.; Khadang, A.; Ghazvini, M.; Mosavi, A.; Nabipour, N. Prediction of Thermo-Physical Properties of TiO_2-Al_2O_3/Water Nanoparticles by Using Artificial Neural Network. *Nanomaterials* **2020**, *10*, 697. [CrossRef] [PubMed]
2. Xie, S.; Zhang, Y.; Song, Y.; Ge, F.; Huang, X.; Ge, H.; Zhao, Y. Comparison of the Corrosion Behavior of Brass in TiO_2 and Al_2O_3 Nanofluids. *Nanomaterials* **2020**, *10*, 1046. [CrossRef] [PubMed]
3. García-Beltrán, G.; Mercado-Zúñiga, C.; Torres-SanMiguel, C.R.; Trejo-Valdez, M.; Villalpando, I.; Torres-Torres, C. Navigation of Silver/Carbon Nanoantennas in Organic Fluids Explored by a Two-Wave Mixing. *Nanomaterials* **2020**, *10*, 1886. [CrossRef] [PubMed]
4. Zhu, X.-Y.; Wang, B.-R.; Gu, Y.; Zhu, H.; Chen, L.; Sun, Q.-Q. Novel Nanofluidic Cells Based on Nanowires and Nanotubes for Advanced Chemical and Bio-Sensing Applications. *Nanomaterials* **2021**, *11*, 90. [CrossRef] [PubMed]
5. Asadi, A.; Molana, M.; Ghasemiasl, R.; Armaghani, T.; Pop, M.-I.; Pour, M.S. A New Thermal Conductivity Model and Two-Phase Mixed Convection of CuO–Water Nanofluids in a Novel I-Shaped Porous Cavity Heated by Oriented Triangular Hot Block. *Nanomaterials* **2020**, *10*, 2219. [CrossRef] [PubMed]
6. Bondareva, N.S.; Gibanov, N.S.; Sheremet, M.A. Computational Study of Heat Transfer inside Different PCMs Enhanced by Al_2O_3 Nanoparticles in a Copper Heat Sink at High Heat Loads. *Nanomaterials* **2020**, *10*, 284. [CrossRef] [PubMed]
7. Pop, I.; Sheremet, M.A.; Groşan, T. Thermal Convection of Nanoliquid in a Double-Connected Chamber. *Nanomaterials* **2020**, *10*, 588. [CrossRef] [PubMed]
8. Jilte, R.; Ahmadi, M.H.; Kumar, R.; Kalamkar, V.; Mosavi, A. Cooling Performance of a Novel Circulatory Flow Concentric Multi-Channel Heat Sink with Nanofluids. *Nanomaterials* **2020**, *10*, 647. [CrossRef] [PubMed]
9. Ahmadi, A.A.; Arabbeiki, M.; Ali, H.M.; Goodarzi, M.; Safaei, M.R. Configuration and Optimization of a Minichannel Using Water–Alumina Nanofluid by Non-Dominated Sorting Genetic Algorithm and Response Surface Method. *Nanomaterials* **2020**, *10*, 901. [CrossRef] [PubMed]
10. Khan, M.Z.U.; Uddin, E.; Akbar, B.; Akram, N.; Naqvi, A.A.; Sajid, M.; Ali, Z.; Younis, M.Y.; García Márquez, F.P. Investigation of Heat Transfer and Pressure Drop in Microchannel Heat Sink Using Al_2O_3 and ZrO_2 Nanofluids. *Nanomaterials* **2020**, *10*, 1796. [CrossRef] [PubMed]
11. Alsabery, A.I.; Ghalambaz, M.; Armaghani, T.; Chamkha, A.; Hashim, I.; Pour, M.S. Role of Rotating Cylinder toward Mixed Convection inside a Wavy Heated Cavity via Two-Phase Nanofluid Concept. *Nanomaterials* **2020**, *10*, 1138. [CrossRef] [PubMed]
12. Ghalambaz, M.; Arasteh, H.; Mashayekhi, R.; Keshmiri, A.; Talebizadehsardari, P.; Yaïci, W. Investigation of Overlapped Twisted Tapes Inserted in a Double-Pipe Heat Exchanger Using Two-Phase Nanofluid. *Nanomaterials* **2020**, *10*, 1656. [CrossRef] [PubMed]

nanomaterials

MDPI

Article

Prediction of Thermo-Physical Properties of TiO_2-Al_2O_3/Water Nanoparticles by Using Artificial Neural Network

Milad Sadeghzadeh [1], Heydar Maddah [2], Mohammad Hossein Ahmadi [3,*], Amirhosein Khadang [2], Mahyar Ghazvini [4], Amirhosein Mosavi [5,6,7,8,*] and Narjes Nabipour [9,*]

1 Department of Renewable Energy and Environmental Engineering, University of Tehran, Tehran 1439957131, Iran; milad.sadeghzadeh@gmail.com
2 Department of Chemistry, Payame Noor University (PNU), Tehran P.O. Box, 19395-3697, Iran; heydar.maddah@gmail.com (H.M.); Amirhossein.khadang77@gmail.com (A.K.)
3 Faculty of Mechanical Engineering, Shahrood University of Technology, POB- Shahrood 3619995161, Iran
4 Department of Ocean and Mechanical Engineering, Florida Atlantic University, 777 Glades Road Boca Raton, FL 33431, USA; m.ghazvini@alumni.ut.ac.ir
5 Kalman Kando Faculty of Electrical Engineering, Obuda University, 1034 Budapest, Hungary
6 Institute of Structural Mechanics (ISM), Bauhaus-Universität Weimar, 99423 Weimar, Germany
7 Thuringian Institute of Sustainability and Climate Protection, 07743 Jena, Germany
8 Department of Mathematics and Informatics, J. Selye University, 94501 Komarno, Slovakia
9 Institute of Research and Development, Duy Tan University, Da Nang 550000, Viet Nam
* Correspondence: mohammadhosein.ahmadi@gmail.com or mhosein.ahmadi@shahroodut.ac.ir (M.H.A.); amir.mosavi@uni-weimar.de (A.M.); narjesnabipour@duytan.edu.vn (N.N.)

Received: 28 December 2019; Accepted: 29 March 2020; Published: 7 April 2020

Abstract: In this paper, an artificial neural network is implemented for the sake of predicting the thermal conductivity ratio of TiO_2-Al_2O_3/water nanofluid. TiO_2-Al_2O_3/water in the role of an innovative type of nanofluid was synthesized by the sol–gel method. The results indicated that 1.5 vol.% of nanofluids enhanced the thermal conductivity by up to 25%. It was shown that the heat transfer coefficient was linearly augmented with increasing nanoparticle concentration, but its variation with temperature was nonlinear. It should be noted that the increase in concentration may cause the particles to agglomerate, and then the thermal conductivity is reduced. The increase in temperature also increases the thermal conductivity, due to an increase in the Brownian motion and collision of particles. In this research, for the sake of predicting the thermal conductivity of TiO_2-Al_2O_3/water nanofluid based on volumetric concentration and temperature functions, an artificial neural network is implemented. In this way, for predicting thermal conductivity, SOM (self-organizing map) and BP-LM (Back Propagation-Levenberq-Marquardt) algorithms were used. Based on the results obtained, these algorithms can be considered as an exceptional tool for predicting thermal conductivity. Additionally, the correlation coefficient values were equal to 0.938 and 0.98 when implementing the SOM and BP-LM algorithms, respectively, which is highly acceptable.

Keywords: thermal conductivity; TiO_2-Al_2O_3/water; nanofluid; artificial neural network

1. Introduction

Recently, numerous endeavors have been made in order to enhance the performance of various applications with the help of nanotechnology [1–4]. As an illustration, it is practicable to reduce system size or enhance the thermal performance of materials [5–8]. In this way, some investigations have been implemented on the use of nanotechnology in thermal applications [9–19]. Additionally, some studies have focused on the prediction of the thermal conductivity ratio associated with various nanofluids

with the help of using experiments and artificial neural networks [20–31]. Vafaei et al. [32] predicted the thermal conductivity ratio of MgO-MWCNTs/EG hybrid nanofluids by using ANN (artificial neural network) at the temperature range of 25–50 °C. According to the results, the best performance belonged to the neural network with 12 neurons in the hidden layer. Also, an investigation has been carried out by Afrand et al. [33] to estimate the thermal conductivity of MgO/water nanofluid. Furthermore, by implementing an ANN, convective heat transfer of TiO_2/water nanofluid has been studied by Esfe et al. [34]. As indicated in the results, the regression coefficient of the model for the Nusselt number's data is 99.94%. Azizi et al. [35] employed ANN to estimate the water holdup in different layouts of oil-water two-phase flow. In another use of ANN, Azizi et al. [36] investigated the estimation of void fraction in pipes with different inclination. ANN-based methods have this potential to give high precision estimation which can be beneficial in real practice since the actual experiment is not only so expensive but also very time-consuming.

On the other hand, the sol–gel process involving hydrolysis and condensation reactions of alkali precursors is an appropriate method for the synthesis of ultra-fine metal oxide [37]. Different researchers have used the sol–gel method in different conditions. Li et al. [38] added tetra-n-butyl titanate to deionized water and hydrochloric acid or ammonia. After milling and drying the gel at different temperatures, TiO_2 nanopowder was obtained. Zhang et al. [39] used the sol–gel microemulsion method. They synthesized TiO_2 nanoparticles by hydrolysis of tetraizo titanium Prop Oxide with 80 Tween-Span in a microemulsion and then calcined it is at different temperatures. The results show that the particles are spherical. In some cases, the surfactant is used in the sol–gel process. Pavasupree et al. [40] synthesized semi-porous TiO_2 nanoparticles by adding hydrochloride clarinylamine (LAHC) as a surfactant to the precursor solution. The resulting powders were calcined for 4 h at 400 °C. In the same way, Colon et al. [41] increased the specific surface area of the particles by adding activated carbon to the solution. The XRD results showed only the presence of the anatase phase in the powders. Li et al. [37] aged the gel for 12 h at 100 °C after drying it. The results showed that aging help to remove organic compounds and influence atomic penetration and crystalline anatase. In 2014, SiO_2 nanoparticles were synthesized by Oliveira et al. They used the polypropylene matrix in their research. Their results showed that the production of inorganic nanoparticles in a polymer solution does not require solvent through the reaction in the molten phase [42]. Moreover, the influence of adding Al_2O_3 and TiO_2 nanoparticles into the drilling mud was studied by Ghasemi et al. [43]. The size of Al_2O_3 and TiO_2 nanoparticles were 20 and 60 nm, respectively, and a concentration of 0.05 wt. %. Based on the obtained results of temperature and pressure effects, the drilling mud rheological properties such as plastic viscosity are decreased by increasing the temperature, nonetheless, the pressure rise augments these properties. Additionally, the influences of pressure in low temperature outweighs in high temperatures. Also, the effective electrical conductivity of Al_2O_3 nanoparticles was experimentally measured by Ganguly et al. [44]. For examining the influences of temperature variations and volume fraction on the electrical conductivity of Al_2O_3 nanofluids, experiments have been carried out as a function of these parameters. As indicated in the results, the electrical conductivity increases significantly with augmenting volume fraction and temperature. Nonetheless, the effective conductivity's reliance on the volume fraction is much higher than the temperature. Furthermore, some investigations have been intensively carried out for increasing the nanofluids' thermal conductivity with the help of applying different kinds of nanoparticles [45,46].

The aim of this study is to investigate the thermo-physical properties of TiO_2-Al_2O_3 nanoparticles in water that can be employed as a coolant fluid with its improved thermal properties. This is accomplished by conducting experiments on various volumes of nanoparticles in water. In this study, special attention has been paid to the temperature effect on the nanofluid's thermal conductivity. The temperature's influence on the thermal conductivity of TiO_2 nanofluid has not been reported yet. Furthermore, the current investigation discloses the influence of temperature and nanoparticle concentrations on the thermal properties of hybrid nanofluids. With the help of the experimental results

obtained by this study, researchers can acquire exceptional information regarding the displacement of nanofluid and its properties, in which appropriate theoretical models can be achieved in the future.

2. Test section

Synthesis of TiO_2-Al_2O_3 Nanoparticles and Characterization

In this study, the sol–gel method was used to synthesize TiO_2-Al_2O_3 nanoparticles prepared in various percentages of Al_2O_3 (10–60). Two different solution samples were prepared for this nanofluid. In the first sample, 0.1105 mol (2 g) of $TiCl_4$ was dissolved in a solution that contains 10 mL of methyl acetate, 10 mL of ethanolamine and 100 mL of ethanol, and stirred for one hour at room temperature. Finally, a uniform suspension was produced. Then, $AlCl_3$ was added to the solution in various weights (0–100%) and the resulting solution was stirred for one hour at 80 °C. The second sample solution was made up of 30 mL of n-hexane, 20 mL of ethanol, 4 mL of methyl acetate and 5 mL of ammonium hydroxide. The second sample was added to the first sample and the solution was mixed simultaneously to obtain the hydrogel. By adding the second sample, the viscosity of the hydrogel increased. After the addition of the sample was complete, the solution was stirred at room temperature for 48 h and then kept at room temperature for 12 h. After 12 h, with the help of water, the obtained gel was washed to remove the chloride salts and then separated solids from it. The solids were washed three times with distilled water and then placed in an oven for 3 h at 900 °C. Figure 1 shows the schematic of nanocomposite synthesis.

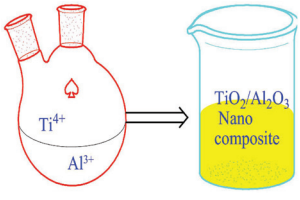

Figure 1. Schematic of nanocomposite synthesis.

The preparation of nanofluid is the first step in changing the heat transfer efficiency. The preparation of nanofluid by adding the nanoparticles to the base fluid should not be considered as a solid–liquid mixture. Because the preparation of nanofluid requires special conditions. Some of these special conditions include uniform and stable suspension, aggregation of particles and the lack of change in the nature of the base fluid. Different methods are used to achieve these specific properties. Various concentrations of nanofluids are prepared by using the equation below:

$$\varphi\ (Volume\ \text{concentration}\%) = \frac{\frac{w_{np}}{\rho_{np}}}{\frac{w_{np}}{\rho_{np}} + \frac{w_{water}}{\rho_{water}}} \quad (1)$$

where ρ_{np} and ρ_{water} represent the nanoparticles' density and water density, respectively. w is their mass [5].

Nanofluids that are prepared by the two-step method should be stable and the particle should not be sedimented in the fluid. Therefore, the nanofluid's stabilization should be considered.

In this study, a magnetic stirrer was used for nanofluid stability. The agitation intensity is crucially important for the nanoparticles' dispersion. The particles are connected to each other through bonds and the weak bonds are broken with force. However, there is a forceful propensity in nanoparticles for agglomerating because of the van der Waals force. We used the TEM analysis to evaluate the produced nanoparticles (Electro Microscopy) (PHILIPS EM 208, FEI, Hillsboro, Oregon, USA). SEM analysis was used to evaluate the morphology of synthesized nanoparticles. Figure 2 shows the SEM of pure nanoparticles and nanocomposites.

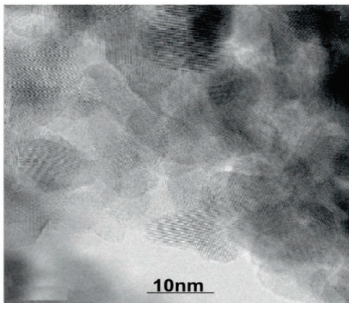

Figure 2. SEM images of nanoparticles after dispersion (20% alumina and 80% titanium).

According to the above, 20% alumina and 80% titanium were selected as samples for heat transfer analysis (the main objective of this study is to improve the properties of TiO_2). Therefore, adding more alumina will keep TiO_2 away from its main. With the help of the TCi Thermal Conductivity analyzer made by Canada's C-Therm, the thermal conductivity of the nanocomposite has been calculated experimentally. Also, the Brookfield Viscometer was used to measure the viscosity of prepared nanofluid. Based on the manufacturer and the obtained results, the proposed approach for measuring thermal conductivity brings an uncertainity of ±2% with the deviation of 4% for each measurement. The repeatability and accuracy of the viscometer used are ±0.2% and ±1% in the full-scale range (FSR) of measurements, respectively. One noteworthy approach in the field of thermal analysis is differential scanning calorimetry (DSC). This approach can be found in ASTM E1269. The ASTM E1269 is the standard defined procedure for measuring specific heat capacity through DSC approach. In this research, the improved modulated-DSC approach is used to obtain the specific heats. In modulated-DSC, a sinusoidal temperature fluctuation is employed instead of a linear ramp. This novel technique is capable to calculate the heat capacity and the heat flow of the samples, simultaneously.

3. Results and Discussion

As shown in Figure 3, the specific heat capacity of the nanocomposite varied linearly within the range 300–360 K. For temperatures of 300 K, the nanocomposite has a higher thermal capacity than its components. At this temperature, the nanocomposite's average heat capacity was 0.75 J/gK. In the range of 300–360 K, the average heat capacity was 0.78 J/gK. Since the temperature of the heat transfer analysis was mainly in this range, this number was chosen as the basis for our calculation.

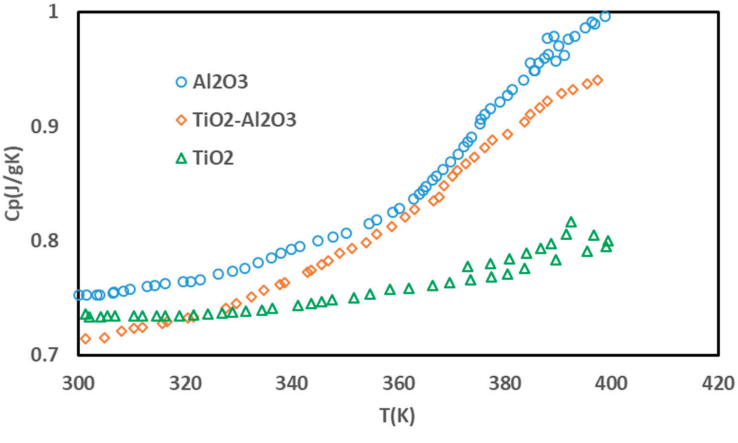

Figure 3. The results of the specific heat capacity of the nanocomposite.

Based on the results, it can be said that in the initial intervals, the thermal conductivity of the nanocomposite was within the range of its components. Because of the large number of Al_2O_3 particles in the nanocomposite, the thermal conductivity of the nanocomposite was very close to that of Al_2O_3. Based on Figure 4, the thermal conductivity coefficient was calculated to be 11.7 W/mK within the range of 300–360 K.

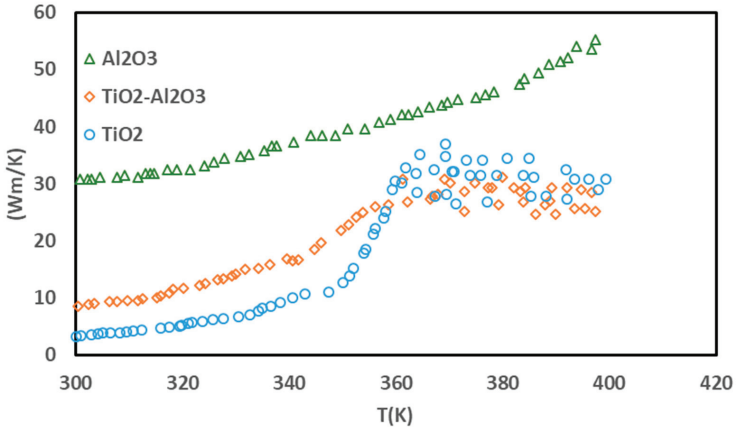

Figure 4. The results of the thermal conductivity coefficient of the nanocomposite.

The variations in the thermal conductivity of the nanofluid with respect to concentration are shown in Figure 5. According to Figure 5, with increasing nanofluid concentration, thermal conductivity also increased. It should be noted that overconcentration may be due to the agglomeration of particles and the reduction of the thermal conductivity of the nanofluid. Increasing the temperature leads to enhanced thermal conductivity. This is due to Brownian motion and an increase in the collision of the particles with each other. Since the presented equations are not based on nanocomposite in nanofluid, or the base fluid is not combined, it is not possible to match the data with this equation. Here, the experimentally measured data is fit on the basis of temperature and concentrations to be employed in heat transfer analysis.

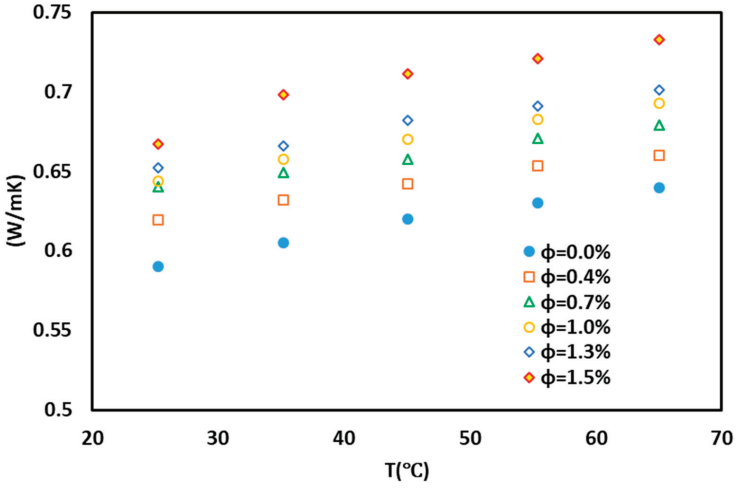

Figure 5. Variations in thermal conductivity coefficient of nanofluid with temperature and concentration of nanoparticles.

The relationships among the temperature, concentration, and thermal conductivity of the nanofluid were obtained on the basis of the experimental data. In Figures 5 and 6, the 3D contour illustrates the predicted data resulting from the experimental data. In the equations, x represents the concentration, y represents the temperature, and z is the thermal conductivity coefficient.

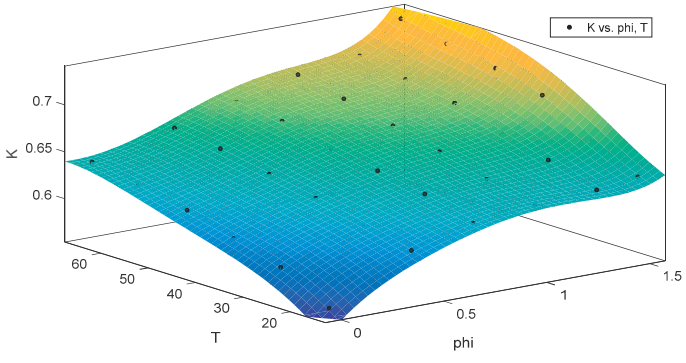

(a)

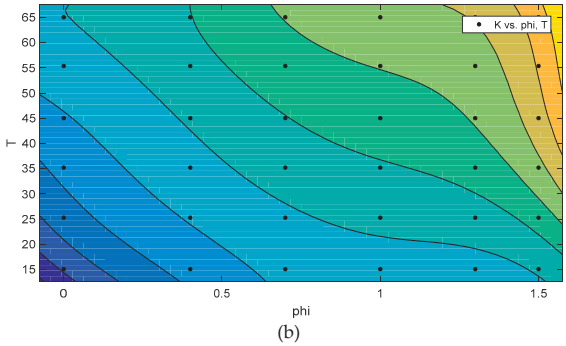

(b)

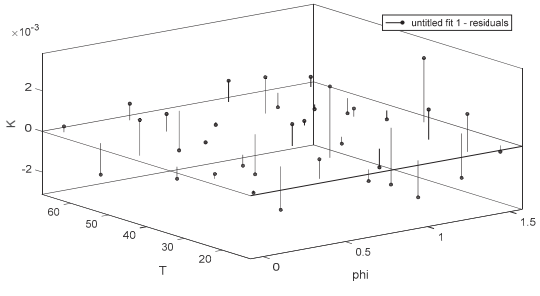

(c)

Figure 6. (**a**) Contour plots, (**b**) 3D, and (**c**) proposed model for the thermal conductivity coefficient (Temperature is in °C and phi (Volumetric Concentration (%)).

Linear model Poly55:

$$F(x, y) = p00 + p10 \times x + p01 \times y + p20 \times x^2 + p11 \times x \times y + p02 \times y^2 + p30 \times x^3 + p21 \times x^2 \times y + p12 \times x \times y^2 + p03 \times y^3 + p40 \times x^4 + p31 \times x^3 \times y + p22 \times x^2 * y^2 + p13 \times x \times y^3 + p04 \times y^4 + p50 \times x^5 + p41 \times x^4 \times y + p32 \times x^3 \times y^2 + p23 \times x^2 \times y^3 + p14 \times x \times y^4 + p05 \times y^5 \quad (2)$$

Coefficients (with 95% confidence bounds):

p10 = 3.494×10^{-1} (1.966×10^{-1}, 5.022×10^{-1})
p01 = 7.815×10^{-3} (-1.715×10^{-2}, 3.279×10^{-2})
p20 = -3.843×10^{-1} (-8.201×10^{-1}, 5.145×10^{-2})
p11 = -1.749×10^{-2} (-2.926×10^{-2}, -5.721×10^{-3})
p02 = -1.736×10^{-4} (-1.623×10^{-3}, 1.276×10^{-3})
p30 = 4.467×10^{-1} (-2.094×10^{-1}, 1.103)
p21 = 8.337×10^{-3} (-1.159×10^{-3}, 1.783×10^{-2})
p12 = 4.972×10^{-4} (7.729×10^{-5}, 9.171×10^{-4})
p03 = 1.163×10^{-6} (-3.839×10^{-5}, 4.071×10^{-5})
p40 = -3.24×10^{-1} (-7.665×10^{-1}, 1.186×10^{-1})
p31 = -4.751×10^{-3} (-1.065×10^{-2}, 1.146×10^{-3})
p22 = -4.931×10^{-5} (-2.011×10^{-4}, 1.025×10^{-4})
p13 = -7.265×10^{-6} (-1.401×10^{-5}, -5.195×10^{-7})
p04 = 1.758×10^{-8} (-4.95×10^{-7}, 5.302×10^{-7})
p50 = 8.486×10^{-2} (-2.493×10^{-2}, 1.946×10^{-1})
p41 = 2.198×10^{-3} (5.41×10^{-4}, 3.855×10^{-3})
p32 = -2.4×10^{-5} (-6.092×10^{-5}, 1.293×10^{-5})
p23 = 5.426×10^{-7} (-5.136×10^{-7}, 1.599×10^{-6})
p14 = 3.898×10^{-8} (-1.76×10^{-9}, 7.971×10^{-8})
p05 = -2.131×10^{-10} (-2.756×10^{-9}, 2.33×10^{-9})
p00 = 4.794×10^{-1} (3.199×10^{-1}, 6.388×10^{-1})

Figure 7 shows the effect of the increase of nanoparticles on the viscosity of the base fluid. As shown in Figures 7 and 8, as the nanofluid concentration increases, the viscosity increases. These solid particles in the base fluid increased the collision of particles, leading to an increase in viscosity. The equation and the corresponding graph for viscosity are presented below.

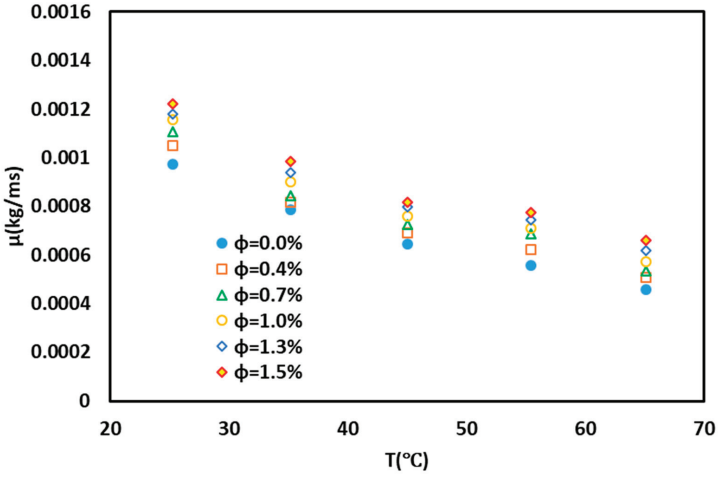

Figure 7. Viscosity variations of nanofluid with temperature and nanoparticle concentrations.

Linear model Poly55:

$$f(x, y) = p00 + p10 \times x + p01 \times y + p20 \times x^2 + p11 \times x \times y + p02 \times y^2 + p30 \times x^3 + p21 \times x^2 \times y + p12 \times x \times y^2 + p03 \times y^3 + p40 \times x^4 + p31 \times x^3 \times y + p22 \times x^2 \times y^2 + p13 \times x \times y^3 + p04 \times y^4 + p50 \times x^5 + p41 \times x^4 \times y + p32 \times x^3 \times y^2 + p23 \times x^2 \times y^3 + p14 \times x \times y^4 + p05 \times y^5 \quad (3)$$

Coefficients (with 95% confidence bounds):

p00 = 1.043×10^{-3} (1.442×10^{-4}, 1.941×10^{-3})
p10 = -1.066×10^{-4} (-9.675×10^{-4}, 7.544×10^{-4})
p01 = 4.699×10^{-5} (-9.37×10^{-5}, 1.877×10^{-4})
p20 = -5.178×10^{-4} (-2.973×10^{-3}, 1.937×10^{-3})
p11 = 4.561×10^{-5} (-2.071×10^{-5}, 1.119×10^{-4})
p02 = -3.333×10^{-6} (-1.15×10^{-5}, 4.832×10^{-6})
p30 = 4.982×10^{-4} (-3.198×10^{-3}, 4.195×10^{-3})
p21 = 2.274×10^{-5} (-3.076×10^{-5}, 7.625×10^{-5})
p12 = -2.283×10^{-6} (-4.649×10^{-6}, 8.235×10^{-8})
p03 = 6.58×10^{-8} (-1.57×10^{-7}, 2.886×10^{-7})
p40 = -2.457×10^{-4} (-2.739×10^{-3}, 2.248×10^{-3})
p31 = -1.03×10^{-5} (-4.352×10^{-5}, 2.292×10^{-5})
p22 = -3.773×10^{-7} (-1.233×10^{-6}, 4.781×10^{-7})
p13 = 4.347×10^{-8} (5.466×10^{-9}, 8.147×10^{-8})
p04 = -4.355×10^{-10} (-3.324×10^{-9}, 2.453×10^{-9})
p50 = 4.998×10^{-5} (-5.686×10^{-4}, 6.685×10^{-4})
p41 = 1.876×10^{-6} (-7.46×10^{-6}, 1.121×10^{-5})
p32 = 6.451×10^{-8} (-1.435×10^{-7}, 2.725×10^{-7})
p23 = 2.166×10^{-9} (-3.785×10^{-9}, 8.116×10^{-9})
p14 = -2.81×10^{-10} (-5.105×10^{-10}, -5.151×10^{-11})
p05 = 1.276×10^{-13} (-1.42×10^{-11}, 1.445×10^{-11})
Goodness of fit:
SSE: 2.306×10^{-9}
R-square: 0.9991
Adjusted R-square: 0.9979
RMSE: 1.24×10^{-5}

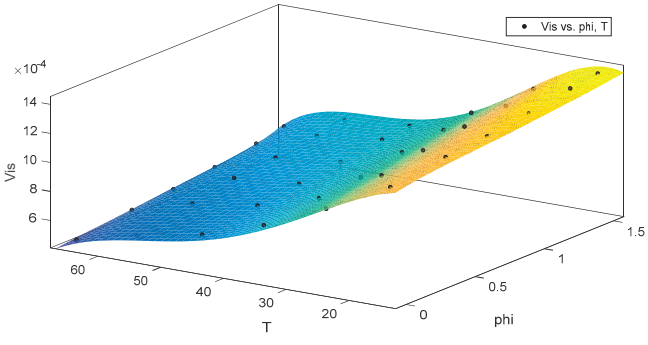

(a)

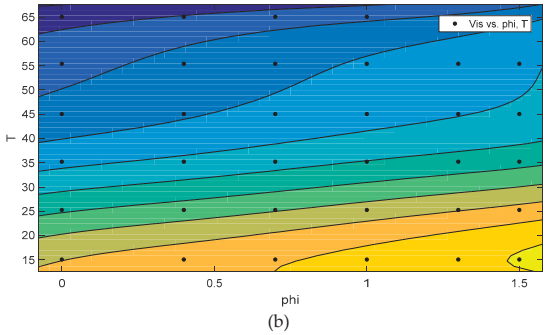

(b)

Figure 8. *Cont.*

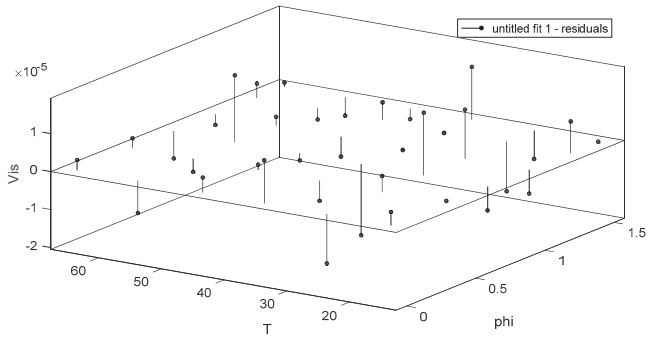

(c)

Figure 8. Contour graphs (3D) describing the model's (**a** to **c**) viscosity (Vis) distribution. (T (temperature) and phi (Volumetric Concentration (%)).

The data were obtained from the experiment that were necessary to find a favorable relation between output and input data, and these were the volumetric concentration and temperature of the fluid, respectively. Table 1 presents the range of each of these input parameters.

Table 1. Input parameters' range.

Parameter	Range
Temperature (°C)	10–70
Volumetric Concentration (%)	0.25–6

The nanofluid's thermal conductivity with respect to the base fluid is considered to be its thermal conductivity ratio, which is an appropriate measurement of nanoparticles with respect to thermal conductivity. As an illustration in SOM, competitive learning methods were developed based on particular properties of the human brain and were used for training. The arrangement of the human brain's cells in a distinct area is precise and meaningful. As an example, the sensory inputs of hearing or touch can contribute to an important geometric arrangement in distinct regions. Furthermore, processor units are located in nodes in SOM. By considering input patterns, units are arranged in a competitive learning approach. The units' position is arranged so that a useful coordinate system is created. Thus, a topographic map of the input patterns is created by the SOM in which units' position is associated with the input patterns' intrinsic characteristics. As illustrated in Figure 9, the base fluid's hexagonal arrangement leads to the prediction of the nanofluid's thermal conductivity ratio. The arrangement of the number of neurons is implemented in 9×9 shapes. The overall number associated with the neurons used is 81, with a neuron winner of 9 data. Thus, here, the neuron number 76 is the winner.

Radial basic networks are another kind of neural network. The comparison of baseline radius and post back networks indicates that the former requires a greater number of neurons, and the design of the latter requires more time. The performance of the former is exceptional under conditions in which there are very large educational vectors. Meanwhile, the input layer does not perform any processing. On the other hand, the hidden or second layer performs a significant part in converting nonlinear patterns to linear separation patterns. Finally, in order to find an approximation, a summation function with a linear output is produced by the third layer. Based on Figure 10, the correlation coefficient value was equal to 0.93875, which is auspicious.

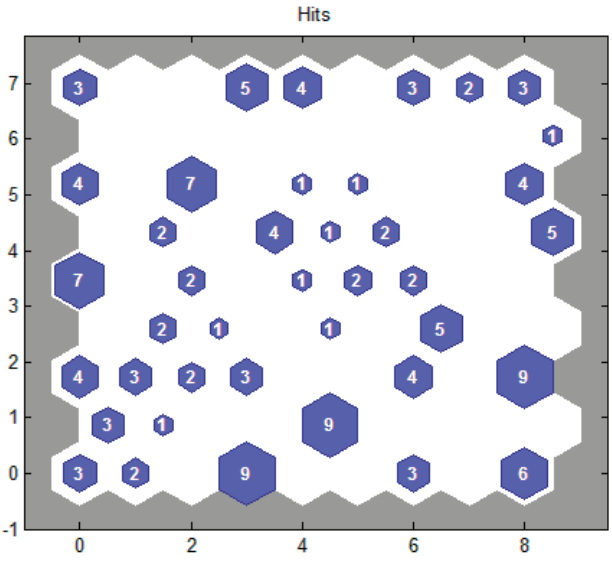

Figure 9. The structure of the neurons used and the quantity of assigned data.

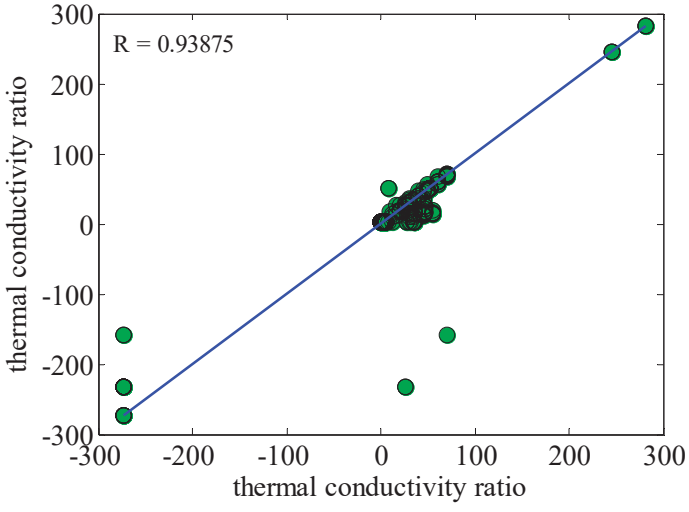

Figure 10. Correlation coefficient data based on investigating the predicted and experimental thermal conductivity ratio.

A BP-LM network training algorithm with a two-layered neural network was used for modeling. In this way, the nanoparticle size, volumetric concentration, and temperature were chosen as input data. Furthermore, the thermal conductivity ratio coefficient was employed as the target parameter. The sensitivity analysis is required for the number of neurons in the hidden layer. To achieve this purpose through application of the trial and error method, the quantity of neurons associated with the hidden layer was studied. As indicated in the Figure 10, the best performance belonged to the network with 76 neurons in the hidden layer. The reason for which numbers of neurons greater than 76 are not more attractive is that augmentation of the number of neurons increases the runtime as well as intensifying the possibility error in the model, even though exceptional outcomes are sometimes achieved by augmenting the number of neurons. According to Figure 11, the quantity of 0.98 expresses

the achieved correlation coefficient of the thermal conductivity ratio. The overall obtained data are placed within the circumference of the diameter line. The correlation coefficient can be enumerated as the most crucial predictive factor, such that better predictions can be made when this value is closer to 1. It can be clearly observed that the predicted and experimental data can be easily fitted, which is evidence of exceptionally favorable network prediction using 76 neurons.

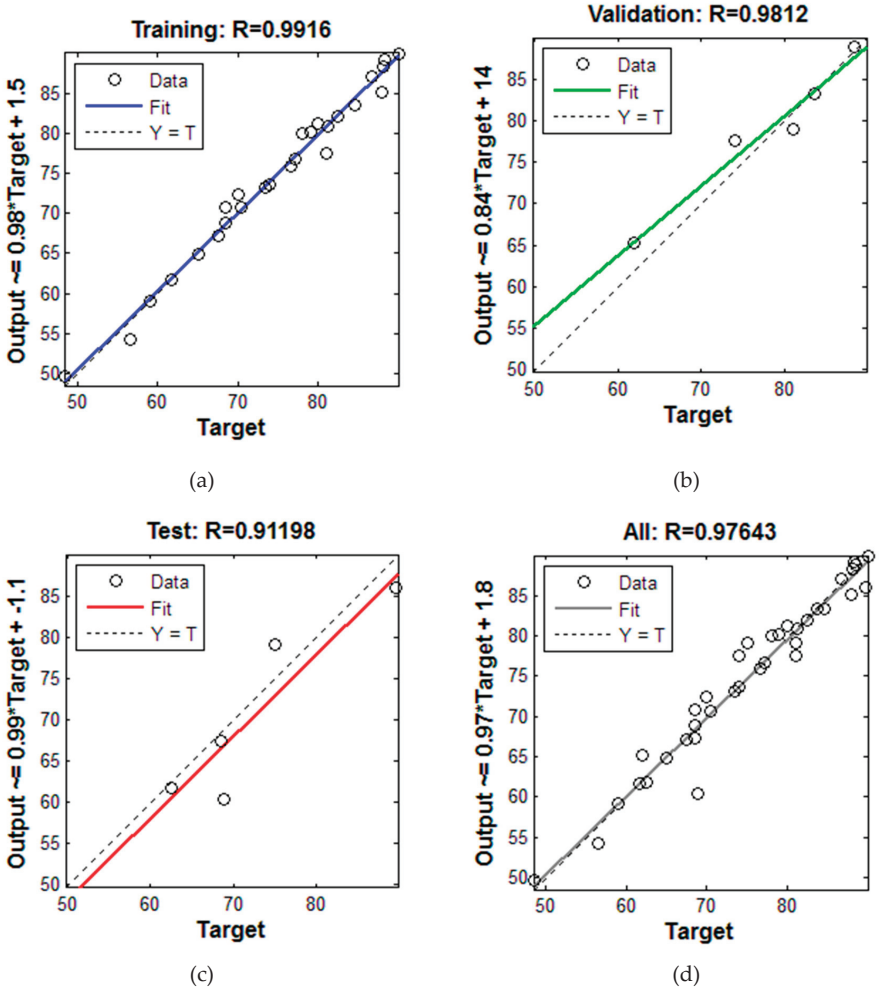

Figure 11. Results based on the correlation coefficient of thermal conductivity ratio. (**a**) Training, (**b**) Validation, (**c**) Test, (**d**) totally).

4. Conclusions

Firstly, the TiO_2-Al_2O_3 nanocomposite was synthesized. For the synthesis of nanocomposites, the sol–gel method and $TiCl_4$ and $AlCl_3$ compounds were used. The results of the analysis showed that all synthesized samples had dimensions in the nano range. After the synthesis of the nanocomposites, they were characterized by TEM. Adding alumina had a significant effect on the TiO_2 crystal size. The main reason for this is the formation of a homogeneous mixture of Ti-O-Al bonds during the sol–gel process. DSC (differential scanning calorimetry) was used to measure the specific heat capacity of the nanofluid. The nanocomposite showed a higher thermal capacity than its components at

300 K. A TC-Thermal Conductivity Analyzer (C-Therm Canada) was used to measure the thermal conductivity of the nanofluid-containing nanocomposite. The results showed that the average thermal conductivity was 11.7 W/mK. It should be noted that as the concentration of nanofluid increases, the agglomeration of particles also increases; as a result, the thermal conductivity of the nanofluid decreased. An increase in temperature also increases the thermal conductivity coefficient. Based on the experimental data, the relationships among concentration, temperature, thermal conductivity and viscosity were obtained. Finally, neural networks were used to predict the electrical properties of the nanofluid. For this purpose, a neural network with a multilayer perceptron structure was used to develop a model for estimating the thermal properties of nanofluids. In the end, the neural network was able to predict thermal properties by a correlation coefficient of 98%.

Author Contributions: Conceptualization, M.S., and H.M.; methodology, A.K.; writing—review and editing, M.G., M.H.A., A.M. and N.N.; supervision, M.H.A., A.M. and N.N.; Funding acquisition, A.M. and N.N. All authors have read and agreed to the published version of the manuscript.

Funding: This research is supported by the Hungarian State and the European Union under the EFOP-3.6.1-16-2016-00010 project and the 2017-1.3.1-VKE-2017-00025 project.

Acknowledgments: We acknowledge the support of the German Research Foundation (DFG) and the Bauhaus-Universität Weimar within the Open-Access Publishing Programme.

Conflicts of Interest: The authors declare no conflict of interest.

References

1. Ahmadi, M.H.; Ghazvini, M.; Alhuyi Nazari, M.; Ahmadi, M.A.; Pourfayaz, F.; Lorenzini, G.; Ming, T. Renewable energy harvesting with the application of nanotechnology: A review. *Int. J. Energy Res.* **2018**, *43*, 1387–1410. [CrossRef]
2. Ahmadi, M.H.; Ghazvini, M.; Baghban, A.; Hadipoor, M.; Seifaddini, P. Computing Approaches for Thermal C onductivity Estimation of CNT/Water Nanofluid. *Rev. des Compos. des Matériaux Avancés Soft* **2019**, *29*, 71–82. [CrossRef]
3. Ahmadi, M.H.; Baghban, A.; Sadeghzadeh, M.; Zamen, M.; Mosavi, A.; Shamshirband, S.; Kumar, R.; Mohammadi-Khanaposhtani, M. Evaluation of electrical efficiency of photovoltaic thermal solar collector. *Eng. Appl. Comput. Fluid Mech.* **2020**, *14*, 545–565. [CrossRef]
4. Sadeghzadeh, M.; Ahmadi, M.H.; Kahani, M.; Sakhaeinia, H.; Chaji, H.; Chen, L. Smart modeling by using artificial intelligent techniques on thermal performance of flat-plate solar collector using nanofluid. *Energy Sci. Eng.* **2019**, *7*, 1649–1658. [CrossRef]
5. Ahmadi, M.H.; Ghazvini, M.; Sadeghzadeh, M.; Alhuyi Nazari, M.; Kumar, R.; Naeimi, A.; Ming, T. Solar power technology for electricity generation: A critical review. *Energy Sci. Eng.* **2018**, *6*, 340–361. [CrossRef]
6. Shulepova, E.V.; Sheremet, M.A.; Oztop, H.F.; Abu-Hamdeh, N. Mixed convection of Al_2O_3–H_2O nanoliquid in a square chamber with complicated fin. *Int. J. Mech. Sci.* **2020**, *165*, 105192. [CrossRef]
7. Ahmadi, M.H.; Ghazvini, M.; Sadeghzadeh, M.; Alhuyi Nazari, M.; Ghalandari, M. Utilization of hybrid nanofluids in solar energy applications: A review. *Nano Struct. Nano Objects* **2019**, *20*, 100386. [CrossRef]
8. Nazari, M.A.; Ahmadi, M.H.; Sadeghzadeh, M.; Shafii, M.B.; Goodarzi, M. A review on application of nanofluid in various types of heat pipes. *J. Cent. South Univ.* **2019**, *26*, 1021–1041. [CrossRef]
9. Ahmadi, M.H.; Tatar, A.; Seifaddini, P.; Ghazvini, M.; Ghasempour, R.; Sheremet, M.A. Thermal conductivity and dynamic viscosity modeling of Fe_2O_3/water nanofluid by applying various connectionist approaches. *Numer. Heat Transf. Part A Appl.* **2018**, *74*, 1301–1322. [CrossRef]
10. Baghban, A.; Kahani, M.; Nazari, M.A.; Ahmadi, M.H.; Yan, W.-M. Sensitivity analysis and application of machine learning methods to predict the heat transfer performance of CNT/water nanofluid flows through coils. *Int. J. Heat Mass Transf.* **2019**, *128*, 825–835. [CrossRef]
11. Paluru, S.; Sudarsana Reddy, P.; Sheremet, M.A. A comparative study of Al_2O_3 and TiO_2 nanofluid flow over a wedge with non-linear thermal radiation. *Int. J. Numer. Methods Heat Fluid Flow* **2019**, *30*, 1291–1317.
12. Baghban, A.; Jalali, A.; Shafiee, M.; Ahmadi, M.H.; Chau, K.; Baghban, A.; Jalali, A.; Shafiee, M.; Ahmadi, M.H.; Chau, K.-W. Developing an ANFIS-based swarm concept model for estimating the relative viscosity of nanofluids. *Eng. Appl. Comput. Fluid Mech.* **2019**, *13*, 26–39. [CrossRef]

13. Maddah, H.; Aghayari, R.; Ahmadi, M.H.; Rahimzadeh, M.; Ghasemi, N. Prediction and modeling of MWCNT/Carbon (60/40)/SAE 10 W 40/SAE 85 W 90(50/50) nanofluid viscosity using artificial neural network (ANN) and self-organizing map (SOM). *J. Therm. Anal. Calorim.* **2018**, *134*, 2275–2286. [CrossRef]
14. Maddah, H.; Aghayari, R.; Mirzaee, M.; Ahmadi, M.H.; Sadeghzadeh, M.; Chamkha, A.J. Factorial experimental design for the thermal performance of a double pipe heat exchanger using Al_2O_3-TiO_2hybrid nanofluid. *Int. Commun. Heat Mass Transf.* **2018**, *97*, 92–102. [CrossRef]
15. Ahmadi, M.-A.; Ahmadi, M.H.; Fahim Alavi, M.; Nazemzadegan, M.R.; Ghasempour, R.; Shamshirband, S. Determination of thermal conductivity ratio of CuO/ethylene glycol nanofluid by connectionist approach. *J. Taiwan Inst. Chem. Eng.* **2018**, *91*, 383–395. [CrossRef]
16. Kahani, M.; Ahmadi, M.H.; Tatar, A.; Sadeghzadeh, M. Development of multilayer perceptron artificial neural network (MLP-ANN) and least square support vector machine (LSSVM) models to predict Nusselt number and pressure drop of TiO_2/water nanofluid flows through non-straight pathways. *Numer. Heat Transf. Part A Appl.* **2018**, *74*, 1190–1206. [CrossRef]
17. Baghban, A.; Pourfayaz, F.; Ahmadi, M.H.; Kasaeian, A.; Pourkiaei, S.M.; Lorenzini, G. Connectionist intelligent model estimates of convective heat transfer coefficient of nanofluids in circular cross-sectional channels. *J. Therm. Anal. Calorim.* **2018**, *132*, 1213–1239. [CrossRef]
18. Ahmadi, M.H.; Alhuyi Nazari, M.; Ghasempour, R.; Madah, H.; Shafii, M.B.; Ahmadi, M.A. Thermal conductivity ratio prediction of Al_2O_3/water nanofluid by applying connectionist methods. *Colloids Surfaces A Physicochem. Eng. Asp.* **2018**, *541*, 154–164. [CrossRef]
19. Nazari, M.A.; Ghasempour, R.; Ahmadi, M.H.; Heydarian, G.; Shafii, M.B. Experimental investigation of graphene oxide nanofluid on heat transfer enhancement of pulsating heat pipe. *Int. Commun. Heat Mass Transf.* **2018**, *91*, 90–94. [CrossRef]
20. Ramezanizadeh, M.; Ahmadi, M.H.; Nazari, M.A.; Sadeghzadeh, M.; Chen, L. A review on the utilized machine learning approaches for modeling the dynamic viscosity of nanofluids. *Renew. Sustain. Energy Rev.* **2019**, *114*, 109345. [CrossRef]
21. Rezaei, M.H.; Sadeghzadeh, M.; Alhuyi Nazari, M.; Ahmadi, M.H.; Astaraei, F.R. Applying GMDH artificial neural network in modeling CO_2 emissions in four nordic countries. *Int. J. Low Carbon Technol.* **2018**, *13*, 266–271. [CrossRef]
22. Ahmadi, M.H.; Sadeghzadeh, M.; Raffiee, A.H.; Chau, K. Applying GMDH neural network to estimate the thermal resistance and thermal conductivity of pulsating heat pipes. *Eng. Appl. Comput. Fluid Mech.* **2019**, *13*, 327–336. [CrossRef]
23. Ahmadi, M.H.; Baghban, A.; Sadeghzadeh, M.; Hadipoor, M.; Ghazvini, M. Evolving connectionist approaches to compute thermal conductivity of TiO_2/water nanofluid. *Phys. A Stat. Mech. Its Appl.* **2019**, *540*, 122489. [CrossRef]
24. Nasirzadehroshenin, F.; Sadeghzadeh, M.; Khadang, A.; Maddah, H.; Ahmadi, M.H.; Sakhaeinia, H.; Chen, L. Modeling of heat transfer performance of carbon nanotube nanofluid in a tube with fixed wall temperature by using ANN-GA. *Eur. Phys. J. Plus* **2020**, *135*, 217. [CrossRef]
25. Ahmadi, M.H.; Sadeghzadeh, M.; Maddah, H.; Solouk, A.; Kumar, R.; Chau, K. Precise smart model for estimating dynamic viscosity of SiO_2/ethylene glycol–water nanofluid. *Eng. Appl. Comput. Fluid Mech.* **2019**, *13*, 1095–1105. [CrossRef]
26. Hemmat Esfe, M.; Rostamian, H.; Esfandeh, S.; Afrand, M. Modeling and prediction of rheological behavior of Al_2O_3-MWCNT/5W50 hybrid nano-lubricant by artificial neural network using experimental data. *Phys. A Stat. Mech. Its Appl.* **2018**, *510*, 625–634. [CrossRef]
27. Hemmat Esfe, M.; Tatar, A.; Ahangar, M.R.H.; Rostamian, H. A comparison of performance of several artificial intelligence methods for predicting the dynamic viscosity of TiO_2/SAE 50 nano-lubricant. *Phys. E Low-dimensional Syst. Nanostructures* **2018**, *96*, 85–93. [CrossRef]
28. Hemmat Esfe, M.; Rostamian, H.; Reza Sarlak, M.; Rejvani, M.; Alirezaie, A. Rheological behavior characteristics of TiO_2-MWCNT/10w40 hybrid nano-oil affected by temperature, concentration and shear rate: An experimental study and a neural network simulating. *Phys. E Low Dimens. Syst. Nanostructures* **2017**, *94*, 231–240. [CrossRef]

29. Bahrami, M.; Akbari, M.; Bagherzadeh, S.A.; Karimipour, A.; Afrand, M.; Goodarzi, M. Develop 24 dissimilar ANNs by suitable architectures & training algorithms via sensitivity analysis to better statistical presentation: Measure MSEs between targets & ANN for Fe–CuO/Eg–Water nanofluid. *Phys. A Stat. Mech. Its Appl.* **2019**, *519*, 159–168.
30. Nafchi, P.M.; Karimipour, A.; Afrand, M. The evaluation on a new non-Newtonian hybrid mixture composed of TiO_2/ZnO/EG to present a statistical approach of power law for its rheological and thermal properties. *Phys. A Stat. Mech. Its Appl.* **2019**, *516*, 1–18. [CrossRef]
31. Mikhailenko, S.A.; Sheremet, M.; Öztop, H.; Abu-Hamdeh, N. Thermal convection in Al_2O_3-water nanoliquid rotating chamber with a local isothermal heater. *Int. J. Mech. Sci.* **2019**, *156*, 137–145. [CrossRef]
32. Vafaei, M.; Afrand, M.; Sina, N.; Kalbasi, R.; Sourani, F.; Teimouri, H. Evaluation of thermal conductivity of MgO-MWCNTs/EG hybrid nanofluids based on experimental data by selecting optimal artificial neural networks. *Phys. E Low Dimens. Syst. Nanostructures* **2017**, *85*, 90–96. [CrossRef]
33. Afrand, M.; Hemmat Esfe, M.; Abedini, E.; Teimouri, H. Predicting the effects of magnesium oxide nanoparticles and temperature on the thermal conductivity of water using artificial neural network and experimental data. *Phys. E Low Dimens. Syst. Nanostructures* **2017**, *87*, 242–247. [CrossRef]
34. Hemmat Esfe, M.; Nadooshan, A.A.; Arshi, A.; Alirezaie, A. Convective heat transfer and pressure drop of aqua based TiO_2 nanofluids at different diameters of nanoparticles: Data analysis and modeling with artificial neural network. *Phys. E Low Dimens. Syst. Nanostructures* **2018**, *97*, 155–161. [CrossRef]
35. Azizi, S.; Awad, M.M.; Ahmadloo, E. Prediction of water holdup in vertical and inclined oil–water two-phase flow using artificial neural network. *Int. J. Multiph. Flow* **2016**, *80*, 181–187. [CrossRef]
36. Azizi, S.; Ahmadloo, E.; Awad, M.M. Prediction of void fraction for gas–liquid flow in horizontal, upward and downward inclined pipes using artificial neural network. *Int. J. Multiph. Flow* **2016**, *87*, 35–44. [CrossRef]
37. Li, Y.; White, T.; Lim, S. Low-temperature synthesis and microstructural control of titania nano-particles. *J. Solid State Chem.* **2004**, *177*, 1372–1381. [CrossRef]
38. Li, B.; Wang, X.; Yan, M.; Li, L. Preparation and characterization of nano-TiO_2 powder. *Mater. Chem. Phys.* **2003**, *78*, 184–188. [CrossRef]
39. Zhang, R.; Gao, L. Preparation of nanosized titania by hydrolysis of alkoxide titanium in micelles. *Mater. Res. Bull.* **2002**, *37*, 1659–1666. [CrossRef]
40. Pavasupree, S.; Suzuki, Y.; Pivsa-Art, S.; Yoshikawa, S. Synthesis and characterization of nanoporous, nanorods, nanowires metal oxides. *Sci. Technol. Adv. Mater.* **2005**, *6*, 224–229. [CrossRef]
41. Colón, G.; Hidalgo, M.; Navío, J. A novel preparation of high surface area TiO_2 nanoparticles from alkoxide precursor and using active carbon as additive. *Catal. Today* **2002**, *76*, 91–101. [CrossRef]
42. Oliveira, M.; Machado, A.V. *Preparation of Polymer-Based Nanocomposites by Different Routes*; Portuguese Foundation of Science and Technology: Lisbon, Portugal, 2013.
43. Ghasemi, N.; Mirzaee, M.; Aghayari, R.; Maddah, H. Investigating Created Properties of Nanoparticles Based Drilling Mud. *Heat Mass Transf.* **2018**, *54*, 1381–1393. [CrossRef]
44. Ganguly, S.; Sikdar, S.; Basu, S. Experimental investigation of the effective electrical conductivity of aluminum oxide nanofluids. *Powder Technol.* **2009**, *196*, 326–330. [CrossRef]
45. Ahammed, N.; Asirvatham, L.G.; Wongwises, S. Effect of volume concentration and temperature on viscosity and surface tension of graphene–water nanofluid for heat transfer applications. *J. Therm. Anal. Calorim.* **2016**, *123*, 1399–1409. [CrossRef]
46. Toghraie, D.; Chaharsoghi, V.A.; Afrand, M. Measurement of thermal conductivity of ZnO–TiO_2/EG hybrid nanofluid. *J. Therm. Anal. Calorim.* **2016**, *125*, 527–535. [CrossRef]

nanomaterials

MDPI

Article

Comparison of the Corrosion Behavior of Brass in TiO_2 and Al_2O_3 Nanofluids

Siyu Xie, Yi Zhang, Yanfang Song, Fang Ge, Xin Huang, Honghua Ge * and Yuzeng Zhao

Shanghai Engineering Research Center of Energy-Saving in Heat Exchange Systems, Shanghai Key Laboratory of Materials Protection and Advanced Materials in Electric Power, Shanghai University of Electric Power, Shanghai 200090, China; siyuxie97@163.com (S.X.); zzzyyy1997@163.com (Y.Z.); yanfang_song16@163.com (Y.S.); ShainSQian@outlook.com (F.G.); hxqiuren@163.com (X.H.); zhaoyuzeng@shiep.edu.cn (Y.Z.)

* Correspondence: gehonghua@shiep.edu.cn; Tel./Fax: +86-21-6041-4107

Received: 4 May 2020; Accepted: 28 May 2020; Published: 29 May 2020

Abstract: The corrosion behavior of brass in TiO_2 and Al_2O_3 nanofluids using a simulated cooling water (SCW) as the base solution and sodium dodecyl benzene sulfonate (SDBS) as the dispersant was studied by electrochemical measurements and surface analysis in this paper. It was found that SDBS could be adsorbed on the brass surface to form a protective film and have a corrosion inhibition effect on brass in SCW. In the SCW-SDBS-TiO_2 nanofluid, some negatively charged TiO_2 nanoparticles were attached to the brass surface and no obvious SDBS adsorption film was found, and the SDBS in this nanofluid had almost no corrosion inhibition on brass. In the SCW-SDBS-Al_2O_3 nanofluid, the brass surface was covered by a uniformly distributed SDBS film containing some Al_2O_3 nanoparticles which were positively charged, and the corrosion inhibition of brass was significantly improved in this nanofluid. It is concluded that the adsorption of SDBS on the brass surface in nanofluids is related to the charge status of the nanoparticles, which makes brass have different corrosion resistance in various nanofluids.

Keywords: TiO_2 nanofluid; Al_2O_3 nanofluid; sodium dodecyl benzene sulfonate; brass; corrosion

1. Introduction

Nanofluids are a new type of energy-saving cooling medium, which refer to a uniformly dispersed medium formed by adding nanoparticles to a base solution. The addition of nano-sized particles can enhance the heat and mass transfer performance of the fluid [1,2]. Nanofluids have a good application prospect, such as in automobiles [3], solar energy [4] and air conditioners [5]. Replacing a traditional coolant with nanofluids in heat transfer systems can reduce energy consumption, decrease the size of the equipment and improve the working efficiency of systems [6]. However, the direct contact between the nanofluids and equipment may affect the corrosion behavior of metals. Some researchers have found that the addition of nanoparticles to the solution can promote metal corrosion [7,8]. The results of Fotowat et al. [9] indicated that alumina nanofluids had significant corrosive effects on both aluminum and copper, and the corrosion of copper was more severe. Bubbico et al. [10] found that the abrasion corrosion of the nanoparticles on the metal was not obvious, but the electrochemical corrosion on the metal surface under static conditions was relatively serious. The Brownian motion of nanoparticles in media can enhance the mass transfer process and accelerate the corrosion of metals in nanofluids [7]. However, other studies suggest that nanoparticles can inhibit metal corrosion. Nithiyanantham et al. [11] pointed out that nanoparticles can be incorporated into the oxide layer of the metal to reduce the corrosion rate of carbon steel.

In order to evenly disperse nanoparticles in the base solution, a certain amount of dispersants (surfactants) is often added to the nanofluids during the preparation [12–14]. Different dispersants not only have different influences on the stability and dispersibility of nanofluids, but also affect

the corrosion behavior of metals to some extent [15]. The piperine surfactants which were synthesized by Tantawy et al. [16] can be chemically adsorbed on the steel surface, and have a corrosion inhibition effect on C1018 steel in a 3.5% NaCl solution. Sodium dodecyl benzene sulfonate (SDBS) is a common surfactant used in nanofluids, and it also exhibits a corrosion inhibition effect on metals at appropriate concentrations [17].

As a corrosion medium, a nanofluid contains both liquid and solid phases which can impact the corrosion behavior of metals. In this paper, TiO_2 and Al_2O_3 nanoparticles with opposite charging properties were selected to prepare a TiO_2 nanofluid and Al_2O_3 nanofluid, respectively, with simulated cooling water and commonly used SDBS as the base solution and dispersant. TiO_2 and Al_2O_3 nanoparticles are both cheap and commonly used in nanofluids. In order to determine the effect of the nanoparticles' charging properties on the aggressiveness of the nanofluids, the corrosion behavior of brass in these two kinds of nanofluids was studied and compared by electrochemical and surface analysis methods in this paper.

2. Experimental

2.1. Materials

The brass used in the experiments were type ASTM B111-C44300, and the composition is shown in Table 1. Brass plates were machined into 1 × 1 cm test pieces for the electrochemical experiments. Copper wire was welded onto the back of the working surface of the test piece, and the non-working surface was sealed with epoxy resin. Before each measurement, the working surface was ground step by step with emery papers ranging from 400 to 2000 mesh and rinsed with alcohol and distilled water.

Table 1. The composition of brass (ASTM B111-C44300) (wt %).

Elements	Cu	Sn	Fe	Pb	As	Bi	P	Zn
Contents	69.9	0.90	0.10	0.05	0.04	0.002	0.01	the rest

2.2. The Experimental Medium

The base solution used for preparing the nanofluids was a simulated cooling water (SCW) which was composed of 7.5 mmol/L NaCl, 2 mmol/L $NaHCO_3$, 3.5 mmol/L Na_2SO_4, 0.25 mmol/L $MgSO_4$ and 0.5 mmol/L $CaCl_2$. The pH value of SCW was adjusted to 8.0 with 0.01 mol/L HNO_3 or 0.01 mol/L NaOH. The experimental TiO_2 and γ-Al_2O_3 nanoparticles had an average particle size of 20 nm. The nanoparticles and dispersant SDBS were all from Aladdin Industries of China.

The TiO_2 and Al_2O_3 nanofluids were prepared using sodium dodecyl benzene sulfonate (SDBS) as the dispersant [18]. First, the 500 mg/L nanoparticles and 500 mg/L SDBS were added into the prepared SCW. Then, the medium was stirred for 30 min by a magnetic agitator and further dispersed by ultrasound at a frequency of 45 kHz for 30 min, and finally a uniformly dispersed nanofluid was obtained. The zeta potential (ζ) was determined by a Melvin zeta potential analyzer (Nano—ZS90, Worcestershire, UK) to analyze the dispersion stability of the nanofluids.

The experiments were performed in the following four media: simulated cooling water (SCW), simulated cooling water with 500 mg/L SDBS (SCW-SDBS), TiO_2 nanofluid containing 500 mg/L SDBS (SCW-SDBS-TiO_2 nanofluid) and Al_2O_3 nanofluid containing 500 mg/L SDBS (SCW-SDBS-Al_2O_3 nanofluid).

2.3. Electrochemical Measurements

The electrochemical measurements were conducted in a three-electrode system by using a CHI604E electrochemical workstation. A saturated calomel electrode (SCE) was used as the reference while a platinum plate was used as the auxiliary electrode. All tests were performed in an open system at 30 ± 1 °C. Electrochemical impedance spectroscopy (EIS) measurements were run at the open

circuit potential. The test frequency range was from 100 kHz to 10 mHz, and the ac amplitude was 10 mV. The results of the EIS were fitted by the ZSimpWin software (ZSimpWin 3.60, EChem software, Michigan, MI, USA). The scanning rate for the measurement of the polarization curves was 1 mV/s. All tests were repeated more than three times for reliable results.

2.4. Characterization of the Metal Surface

The surface morphology of brass was observed by a JSM-7800 scanning electron microscope, and the composition of the brass surface was analyzed by EDS.

3. Results and Discussion

3.1. Stability Analysis of TiO_2 and Al_2O_3 Nanofluids

The stability of a nanofluid mainly depends on the charging state of the nanoparticles' surface, and the repulsive or attractive force between the nanoparticles determines the dispersion or agglomeration of nanoparticles in the medium [19]. Surfactants can achieve a stable dispersion of nanofluids by altering the charging state of the nanoparticles [20–22]. Zeta potential (ζ) is usually used to judge the stability of nanofluids. When the absolute value of the zeta potential (|ζ|) of a nanofluid is higher than 30 mV, it can be considered that the nanofluid is stably dispersed [23,24].

Table 2 shows the zeta potentials of the TiO_2 and Al_2O_3 nanofluids. The pH of the simulated cooling water for the experiment was about 8.0 and the surface of the TiO_2 nanoparticles is negatively charged at this pH [25]. The ζ value of the TiO_2 nanofluid without the surfactant was −19.8 mV. The Al_2O_3 nanoparticles are positively charged at this pH and the ζ value of the surfactant-free Al_2O_3 nanofluid was 3.28 mV. As a kind of anionic surfactant, the dissolved SDBS in the water solution can ionize and release in the form of anionic DBS^-. In the SCW-SDBS-TiO_2 nanofluid, SDBS can be adsorbed onto the TiO_2 nanoparticles by van der Waals force, which makes the ζ value of the nanofluid more negative and increases the electrostatic repulsion between the TiO_2 nanoparticles [26]. The |ζ| value of the SCW-SDBS-TiO_2 nanofluid was 46.4 mV when the SDBS concentration was 500 mg/L. In the SCW-SDBS-Al_2O_3 nanofluid, the SDBS anions can be adsorbed on the surface of the positively charged Al_2O_3 nanoparticles by electrostatic adsorption, which improved the electrostatic repulsion between the nanoparticles as well. When the SDBS concentration was 500 mg/L, the |ζ| value of the SCW-SDBS-Al_2O_3 nanofluid was 40.9 mV. SDBS can disperse TiO_2 and Al_2O_3 nanoparticles well in simulated cooling water.

Table 2. The zeta potential (ζ) (mV) of the different nanofluids.

C_{SDBS} (mg/L)	0	500
SCW-SDBS-TiO_2 nanofluid	−19.8	−46.4
SCW-SDBS-Al_2O_3 nanofluid	3.28	−40.9

3.2. EIS Analysis

The corrosion behavior of brass in different media was analyzed by EIS. Figure 1 shows the Nyquist plots of brass after five days of immersion in SCW, SCW-SDBS, the SCW-SDBS-TiO_2 nanofluid and the SCW-SDBS-Al_2O_3 nanofluid. All the Nyquist plots of brass in the four media showed capacitive arcs, indicating that the brass corrosion in these media was mainly controlled by the charge transfer process. The Nyquist plots showed depressed capacitive arcs, which was mainly attributed to the dispersion effect caused by the uneven electrode surface roughness [27,28]. The EIS was fitted by using the equivalent circuit displayed in Figure 2 with two time constants, where R_s is the solution resistance, R_f and R_{ct} are the film resistance (due to the corrosion products or SDBS film on the metal surface) and the charge transfer resistance, respectively, and Q_{dl} and Q_f represent the double-layer capacitance and the film capacitance, respectively. The fitting results are displayed in Figure 1 (the

solid line) and Table 3. For the purpose of obtaining better fitting results, the constant phase element Q was used instead of the pure capacitance when fitting [29].

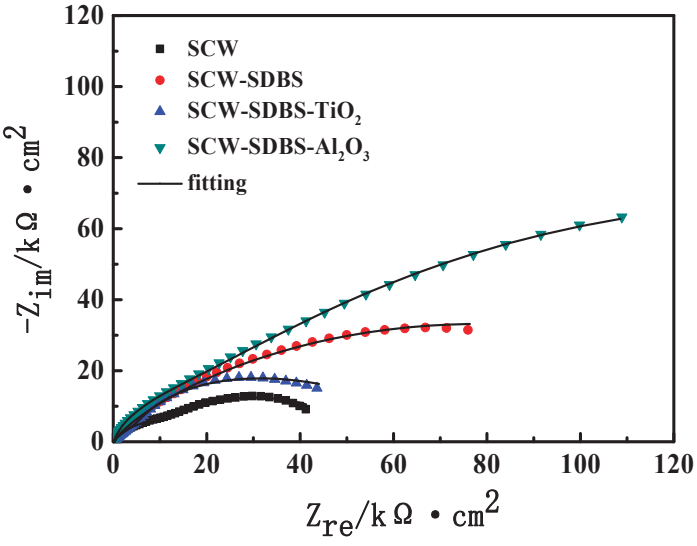

Figure 1. Nyquist plots of brass immersed in different media for 5 days.

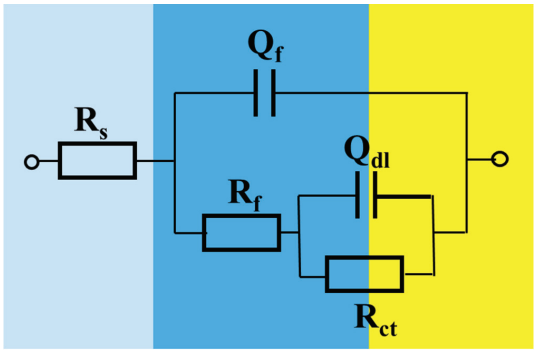

Figure 2. Equivalent circuit for fitting electrochemical impedance spectroscopy (EIS).

Table 3. Fitting results of the EIS in Figure 1.

Test Media	R_s Ω·cm^2	R_f kΩ·cm^2	Q_f Y_f(μS·s^{n}cm^{-2})	n_1	R_{ct} kΩ·cm^2	Q_{dl} Y_{dl}(μS·s^{n}cm^{-2})	n_2
SCW	162.1	10.59	28.71	0.80	44.70	53.57	0.58
SCW-SDBS	173.8	21.01	23.44	0.74	163.5	32.25	0.85
SCW-SDBS-TiO_2	131.7	13.58	26.57	0.75	62.61	48.82	0.65
SCW-SDBS-Al_2O_3	150.0	27.27	18.94	0.87	266.1	27.17	0.75

Figure 1 shows that the fitting results were consistent with the experimental data. In SCW, two arcs in the Nyquist plot can be clearly distinguished, which correspond to the film resistance (R_f) and film capacitance (Q_f), the charge transfer resistance (R_{ct}) and double-layer capacitance (Q_{dl}), respectively. The R_f and Q_f are due to the corrosion products on the brass surface. In the Nyquist plots of the other media, the two arcs cannot be clearly separated, indicating that the two time constants are

relatively close. It is shown in Table 3 that the R_{ct} values and R_f values of brass increased significantly after the addition of SDBS in SCW, which is due to the adsorption film of SDBS formed on the brass surface. The adsorption of SDBS can reduce the active sites on the brass surface and hinder the charge transfer [30]. Compared with the results in the SCW-SDBS medium, the R_{ct} and R_f values of the brass decreased significantly in the SCW-SDBS-TiO_2 nanofluid, which indicates that the existence of TiO_2 nanoparticles reduced the corrosion inhibition effect of SDBS on brass. In the SCW-SDBS-Al_2O_3 nanofluid, the R_f and R_{ct} values of the brass electrode were obviously higher than that in the SCW-SDBS medium, indicating that the Al_2O_3 nanoparticles enhanced the corrosion inhibition effect of SDBS on brass.

3.3. Potentiodynamic Polarization Analysis

The polarization curves of brass after immersing in different media for five days are displayed in Figure 3. Table 4 exhibits the corrosion potential (E_{corr}) and corrosion current density (j_{corr}) obtained through the polarization curves. The results in Table 3 show that the j_{corr} value of the brass in SCW after five days of immersion is the largest (0.388 μA·cm^{-2}), and it is the smallest (0.105 μA·cm^{-2}) in the SCW-SDBS-Al_2O_3 nanofluid. The values of the Tafel slope (b_a) were higher in both the SCW-SDBS-Al_2O_3 nanofluid and SCW-SDBS medium, indicating that the brass surfaces were well adsorbed by SDBS in these two media, which obviously suppressed the anodic dissolution of the brass electrode. The polarization current increases rapidly when the polarization potential is above 0.1 V, which corresponds to the desorption of SDBS on the brass surface. However, in the SCW-SDBS-TiO_2 nanofluid, the j_{corr} value of the brass electrode is close to that in SCW. The shape of the anodic polarization curves in these two media is also similar, indicating that the surface states of brass in these two media may be similar. Besides, the b_a value of the brass electrode decreased in the SCW-SDBS-TiO_2 nanofluid, indicating a decrease in the protection of the surface film. The change trend of b_c in the different media is consistent with b_a, except in SCW, where concentration polarization might appear during the cathodic polarization process because of the large polarization current density. In the media containing SDBS, the cathodic polarization current density of the brass electrode at the same polarization value is relatively small, which should be due to the adsorption of SDBS on the metal surface, and reduces the effective area of the cathode. In addition, compared with the results in SCW, the corrosion potential of brass is negatively shifted, especially in the SCW-SDBS-Al_2O_3 nanofluid and SCW-SDBS medium, indicating that SDBS has a stronger inhibition on the cathode reaction.

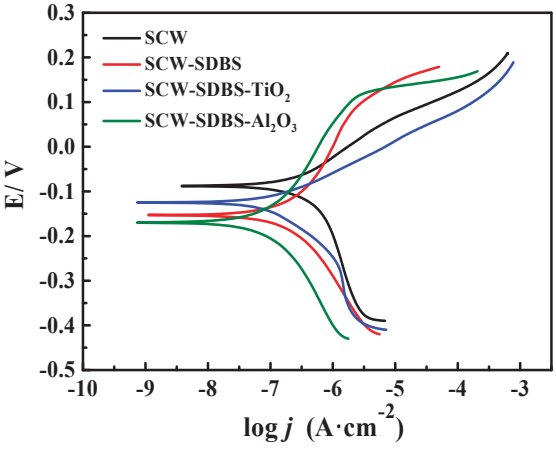

Figure 3. Potentiodynamic polarization curves of the brass electrode after immersion for 5 days in different media.

Table 4. Electrochemical parameters of brass in the four media.

Test Media	E_{corr} (mV)	b_a (mV dec^{-1})	b_c (mV dec^{-1})	j_{corr} (μA·cm^{-2})
SCW	−87	103	250	0.388
SCW-SDBS	−154	188	174	0.161
SCW-SDBS-TiO_2	−125	95	157	0.302
SCW-SDBS-Al_2O_3	−171	192	197	0.105

3.4. Corrosion Products Characterization

Figure 4 shows the results of the SEM and EDS of the brass surfaces after five days of immersion in different media. As can be seen from Figure 4(a1), the brass surface was covered with loose corrosion products after five days immersion in SCW. According to the EDS results (Figure 4(a2)), the corrosion products were mainly composed of C, O and Zn, which should be the zinc compound $Zn_5(CO_3)_2(OH)_6$ [17]. The surface morphology of brass in SCW-SDBS is shown in Figure 4(b1). It can be seen that there were many aggregates attached to the brass surface. The EDS results (Figure 4(b2)) show that these aggregates mainly contained the elements C, O, S and Zn, among which the element C accounts for 59.24%, indicating that these aggregates were mainly SDBS and mixed with a small amount of the corrosion products of zinc. Alternatively, the surface that was not covered by the aggregates mainly contained the elements Cu, O and C (Figure 4(b3)), and the ratio of Cu to O was close to 2:1, implying the existence of the corrosion product Cu_2O [31]. In the SCW-SDBS-TiO_2 nanofluid, the surface morphology of brass was different from that in the previous two media. As shown in Figure 4(c1), no obvious accumulation of corrosion products and adsorption of SDBS were found on the brass surface, only some small particles were adsorbed and distributed on the surface. The EDS results (Figure 4(c2)) show that the brass surface with no particles was mainly composed of the elements C, O, Cu and Zn, with the atomic percentages of 14.55%, 22.89%, 59.23% and 3.33%, respectively, implying the existence of the corrosion product Cu_2O. The EDS results of the particles attached to the brass surface show that the particles contained 51.06% of O and 22.80% of Ti (Figure 4(c3)), which should be the aggregate of the TiO_2 nanoparticles. This indicates that the brass surface was mainly adhered to by the TiO_2 nanoparticles in the SCW-SDBS-TiO_2 nanofluid, and no obvious adsorption of SDBS was found. For specimens in the SCW-SDBS-Al_2O_3 nanofluid, it is shown in Figure 4(d1) that there was a relatively uniform adsorption film on the brass surface after five days of immersion. The EDS results (Figure 4(d2)) show that the brass surface contained 56.65% of C, 24.57% of O and 5.38% of S, which should correspond to the SDBS adsorption film on the brass surface. In addition, 4.39% of the Al element was also detected, indicating the existence of small amounts of Al_2O_3 nanoparticles mixed with the SDBS adsorption film. Comparing Figure 4(b1) and Figure 4(d1), it can be found that the adsorption film of SDBS on the brass surface was relatively dense and uniform in the SCW-SDBS-Al_2O_3 nanofluid, making the corrosion resistance of brass in this nanofluid better than that in the SCW-SDBS medium [17].

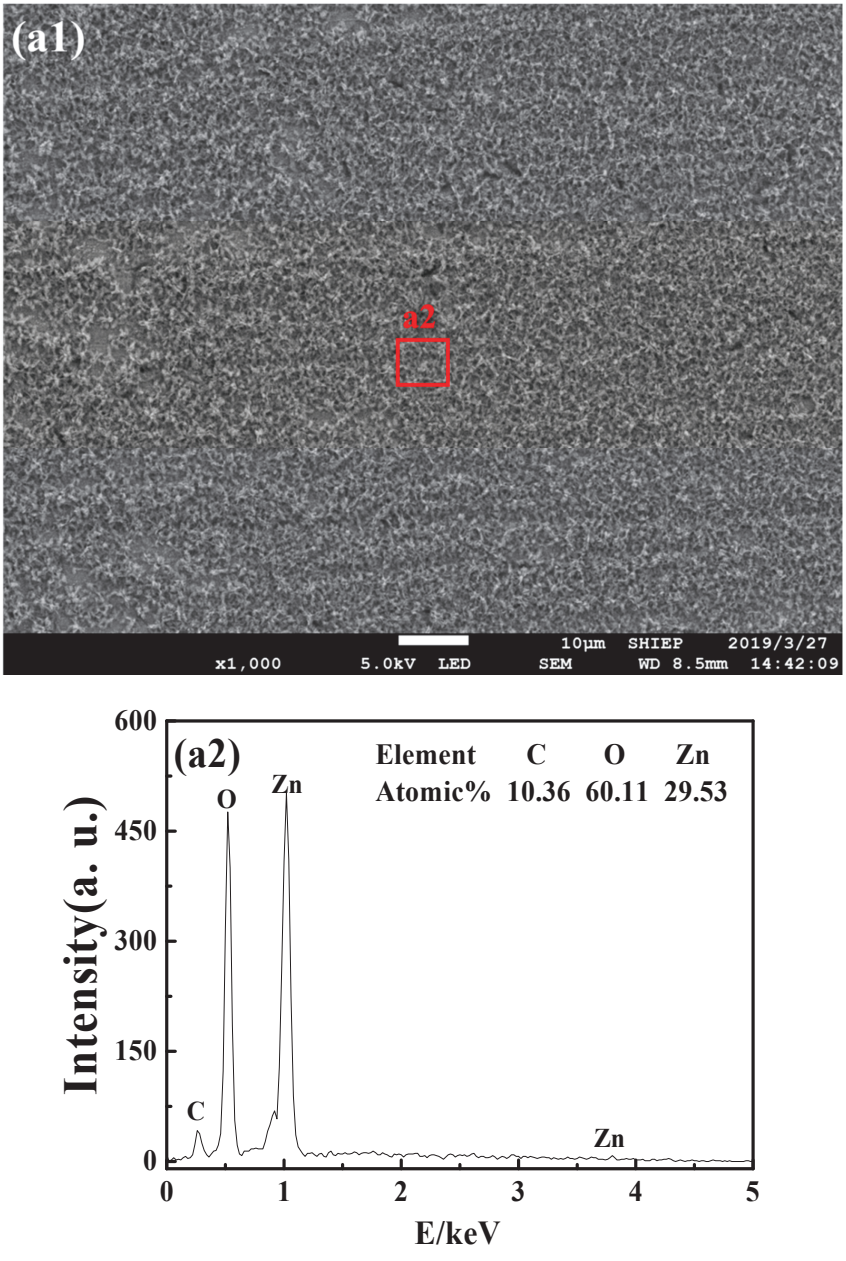

Figure 4. *Cont.*

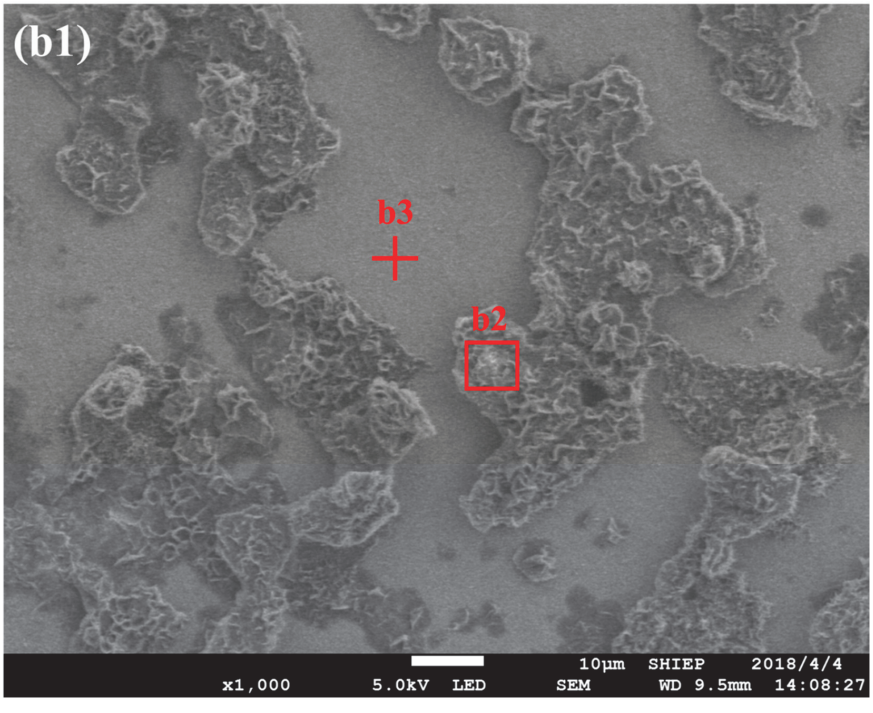

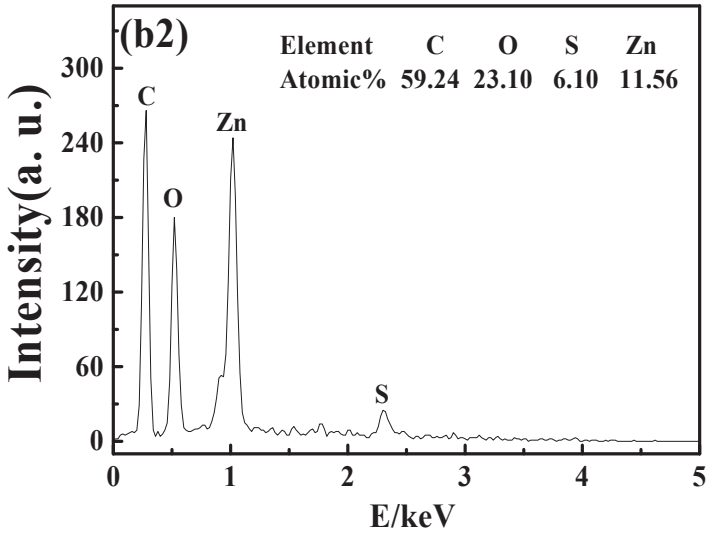

Figure 4. *Cont.*

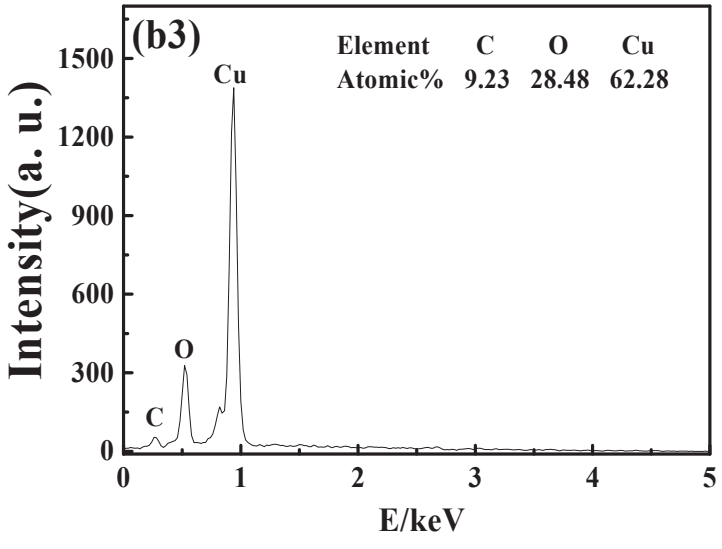

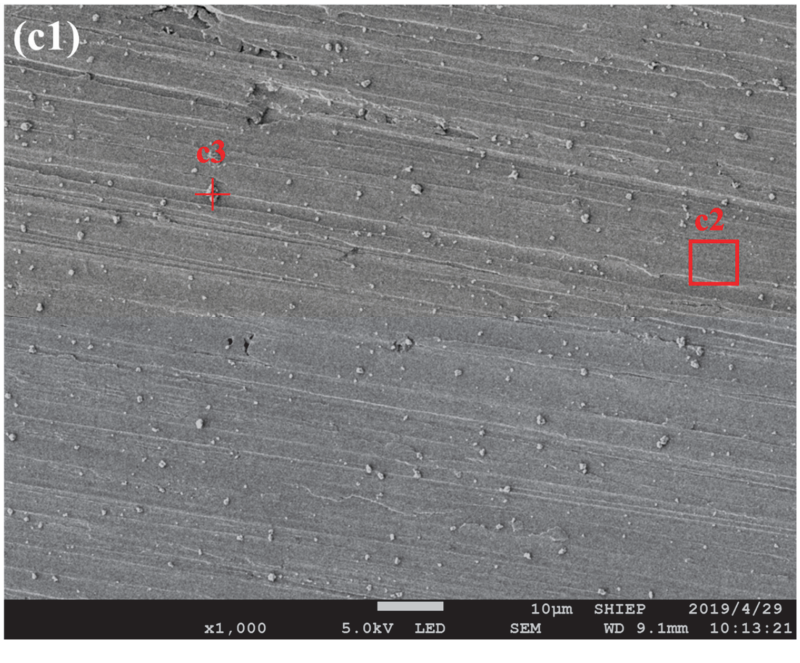

Figure 4. *Cont*.

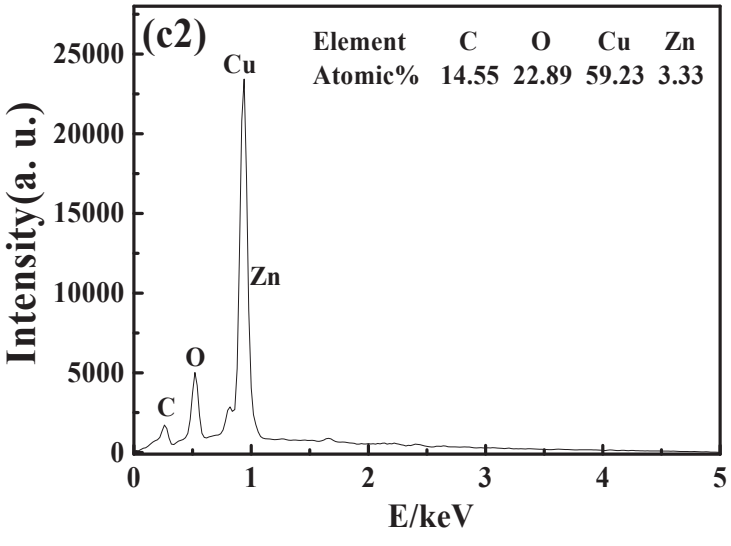

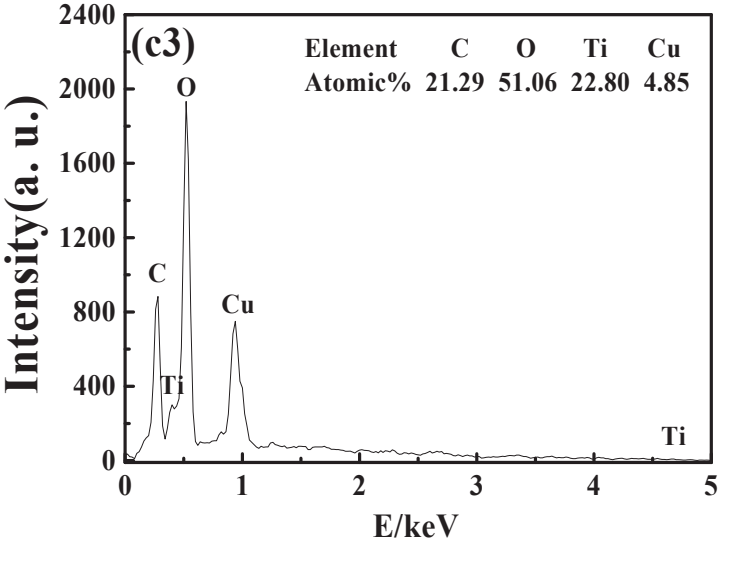

Figure 4. *Cont*.

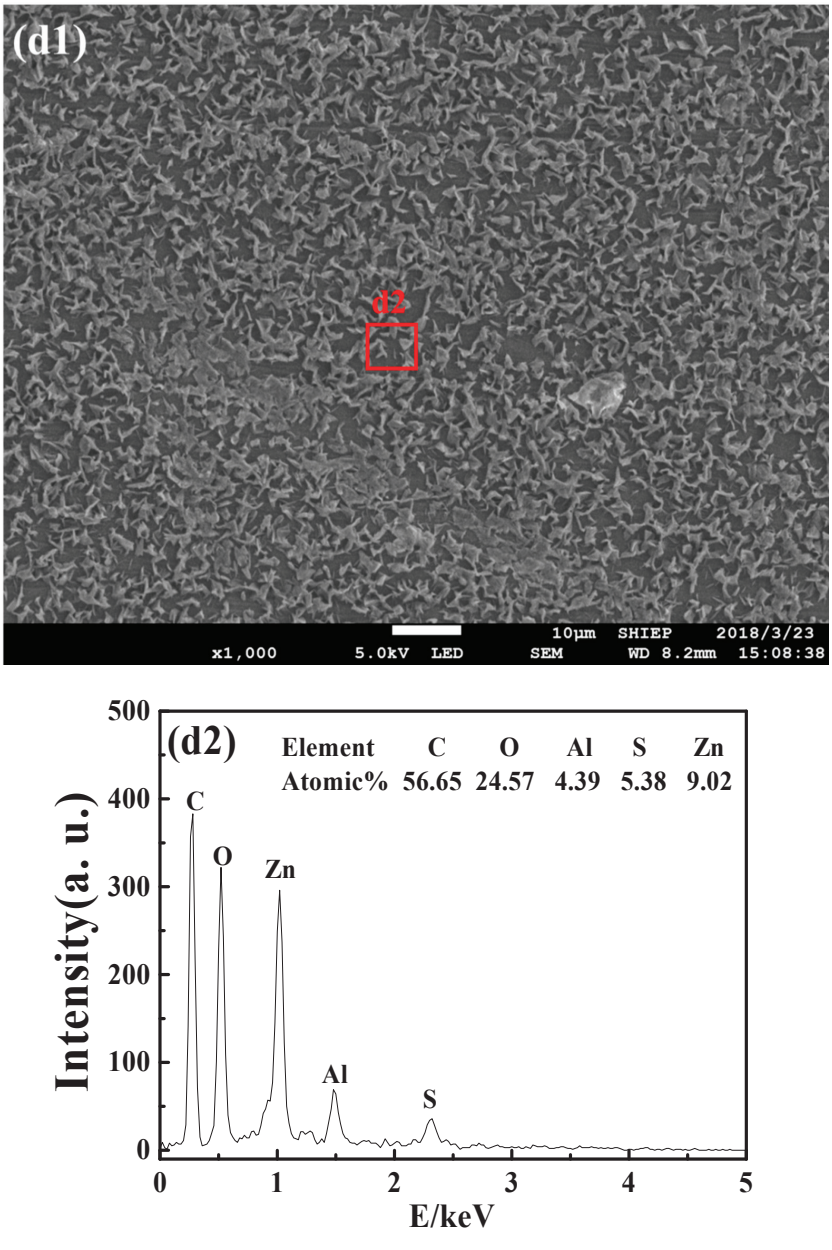

Figure 4. SEM photos and EDS results of the brass surface after immersion of 5 days in different media. (**a**) Simulated cooling water (SCW); (**b**) SCW-sodium dodecyl benzene sulfonate (SDBS); (**c**) SCW-SDBS-TiO_2 nanofluid; and (**d**) SCW-SDBS-Al_2O_3 nanofluid.

According to the above results, it can be seen that in SCW, the brass surface was mainly covered by loose corrosion products, which have poor protection for brass. In the SCW-SDBS medium, the positively charged brass surface [32] was protected by the adsorption film of SDBS, which improved the corrosion resistance of brass. In the SCW-SDBS-TiO_2 nanofluid, a small amount of TiO_2 nanoparticles

were adsorbed on the brass surface and no obvious corrosion products and SDBS adsorption film were found. SDBS was not easy to adsorb on the brass surface in this nanofluid, which should be due to the competitive adsorption between the negatively charged TiO_2 nanoparticles and the SDBS anions on the brass surface. The adhesion of the TiO_2 nanoparticles inhibited the formation of an SDBS adsorption film on the brass surface, so that SDBS exhibited almost no corrosion inhibition effect on brass. In the SCW-SDBS-Al_2O_3 nanofluid, the Al_2O_3 nanoparticles are positively charged and would not be adsorbed on the brass surface which is also positively charged. An SDBS adsorption film was easy to form on the brass surface in this nanofluid. Furthermore, the positively charged Al_2O_3 nanoparticles could be adsorbed on the negatively charged SDBS film, improving the protection performance of the SDBS film on brass [32]. In addition, Al_2O_3 nanoparticles can also improve the critical micelle concentration of SDBS [17], therefore the SDBS adsorption film was not easy to aggregate on the brass surface. Therefore, brass has the best corrosion resistance in the SCW-SDBS-Al_2O_3 nanofluid among the four test media.

4. Conclusions

SDBS was adopted as a dispersant to prepare the TiO_2 and Al_2O_3 nanofluids. The zeta potential of the two nanofluids containing 500 mg/L SDBS was −46.4 and −40.9 mV, respectively.

In SCW, the brass surface was covered by loose corrosion products and had poor corrosion resistance. In the SCW-SDBS medium, an SDBS adsorption film formed on the brass surface and improved the corrosion resistance of brass.

In the SCW-SDBS-TiO_2 nanofluid, a small amount of TiO_2 nanoparticles were adsorbed on the brass surface, and no obvious corrosion product and SDBS adsorption film were found. The adhesion of the negatively charged TiO_2 nanoparticles on the brass surface inhibited the adsorption of the SDBS anions, which reduced the R_f and R_{ct} values of the brass electrode. In this nanofluid, the corrosion current density (j_{corr}) of brass was larger, and the corrosion resistance of brass was close to that in SCW.

In the SCW-SDBS-Al_2O_3 nanofluid, the R_f and R_{ct} values of the brass electrode were the maximum and the corrosion current density (j_{corr}) was the minimum. The brass surface was covered with a relatively dense SDBS adsorption film containing a small number of Al_2O_3 nanoparticles. The positively charged Al_2O_3 nanoparticles promoted the formation of a denser SDBS adsorption film, which obviously improved the corrosion resistance of brass.

Author Contributions: Conceptualization, H.G.; data curation, S.X.; formal analysis, S.X.; funding acquisition, H.G.; investigation, S.X.; methodology, S.X.; project administration, S.X. and H.G.; resources, H.G.; supervision, H.G.; validation, S.X. and Y.Z. (Yi Zhang); writing-original draft, S.X.; writing-review and editing, S.X., H.G., Y.Z. (Yi Zhang), Y.S., F.G., X.H. and Y.Z. (Yuzeng Zhao). All authors have read and agreed to the published version of the manuscript.

Funding: This research was funded by the National Natural Science Foundation of China, grant number (grant number 51471104) and Science and Technology Commission of Shanghai Municipality (grant number 18DZ2204500).

Acknowledgments: The authors acknowledge the financial support of the National Natural Science Foundation of China (grant number 51471104) and Science and Technology Commission of Shanghai Municipality (grant number 18DZ2204500), and the Analysis and Testing Center of Shanghai University of Electric Power for SEM and XRD analysis.

Conflicts of Interest: The authors declare no conflict of interest.

References

1. Sidik, N.A.C.; Mohammed, H.A.; Alawi, O.A.; Samion, S. A review on preparation methods and challenges of nanofluids. *Int. Commun. Heat Mass Transf.* **2014**, *54*, 115–125. [CrossRef]
2. Hwang, Y.; Lee, J.-K.; Lee, C.H.; Jung, Y.; Cheong, S.; Lee, C.; Ku, B.; Jang, S. Stability and thermal conductivity characteristics of nanofluids. *Thermochim. Acta* **2007**, *455*, 70–74. [CrossRef]
3. Kumar, S.; Dinesha, P.; Gaggad, A.; Mehrotra, K. Performance investigation of an automotive car radiator operated with nanofluid based coolant. *Heat Transf. Res.* **2018**, *49*, 1527–1543. [CrossRef]

4. Zamzamian, A.; KeyanpourRad, M.; KianiNeyestani, M.; Jamal-Abad, M.T. An experimental study on the effect of Cu-synthesized/EG nanofluid on the efficiency of flat-plate solar collectors. *Renew. Energy* **2014**, *71*, 658–664. [CrossRef]
5. Bi, S.; Guo, K.; Liu, Z.; Wu, J. Performance of a domestic refrigerator using TiO_2-R600a nano-refrigerant as working fluid. *Energy Convers. Manag.* **2011**, *52*, 733–737. [CrossRef]
6. Raja, M.; Vijayan, R.; Dineshkumar, P.; Venkatesan, M. Review on nanofluids characterization, heat transfer characteristics and applications. *Renew. Sustain. Energy Rev.* **2016**, *64*, 163–173. [CrossRef]
7. Rashidi, A.; Amrollahi, A.; Lotfi, R.; Javaheryzadeh, H.; Rahimi, H.; Rahimi, A.R.; Jorsaraei, A. An investigation of electrochemical behavior of nanofluids containing MWCNT on the corrosion rate of carbon steel. *Mater. Res. Bull.* **2013**, *48*, 4438–4443. [CrossRef]
8. Celata, G.P.; D'Annibale, F.; Mariani, A.; Sau, S.; Serra, E.; Bubbico, R.; Menale, C.; Poth, H. Experimental results of nanofluids flow effects on metal surfaces. *Chem. Eng. Res. Des.* **2014**, *92*, 1616–1628. [CrossRef]
9. Fotowat, S.; Askar, S.; Ismail, M.; Fartaj, A. A study on corrosion effects of a water based nanofluid for enhanced thermal energy applications. *Sustain. Energy Technol. Assessments* **2017**, *24*, 39–44. [CrossRef]
10. Bubbico, R.; Celata, G.P.; D'Annibale, F.; Mazzarotta, B.; Menale, C. Experimental analysis of corrosion and erosion phenomena on metal surfaces by nanofluids. *Chem. Eng. Res. Des.* **2015**, *104*, 605–614. [CrossRef]
11. Nithiyanantham, U.; Grosu, Y.; González-Fernández, L.; Zaki, A.; Igartua, J.M.; Faik, A. Corrosion aspects of molten nitrate salt-based nanofluids for thermal energy storage applications. *Sol. Energy* **2019**, *189*, 219–227. [CrossRef]
12. Peng, H.; Ding, G.; Hu, H. Effect of surfactant additives on nucleate pool boiling heat transfer of refrigerant-based nanofluid. *Exp. Therm. Fluid Sci.* **2011**, *35*, 960–970. [CrossRef]
13. Yang, L.; Du, K.; Niu, X.; Yang, L.; Zhang, Y. An experimental and theoretical study of the influence of surfactant on the preparation and stability of ammonia-water nanofluids. *Int. J. Refrig.* **2011**, *34*, 1741–1748. [CrossRef]
14. Yang, L.; Du, K.; Zhang, X.-S. Influence factors on thermal conductivity of ammonia-water nanofluids. *J. Central South Univ.* **2012**, *19*, 1622–1628. [CrossRef]
15. Said, Z.; Sabiha, M.; Saidur, R.; Hepbasli, A.; Rahim, N.; Mekhilef, S.; Ward, T. Performance enhancement of a Flat Plate Solar collector using Titanium dioxide nanofluid and Polyethylene Glycol dispersant. *J. Clean. Prod.* **2015**, *92*, 343–353. [CrossRef]
16. Tantawy, A.H.; Soliman, K.A.; El-Lateef, H.M.A. Novel synthesized cationic surfactants based on natural piper nigrum as sustainable-green inhibitors for steel pipeline corrosion in CO_2-3.5%NaCl: DFT, Monte Carlo simulations and experimental approaches. *J. Clean. Prod.* **2020**, *250*, 119510. [CrossRef]
17. Sha, J.-Y.; Ge, H.; Wan, C.; Wang, L.-T.; Xie, S.-Y.; Meng, X.-J.; Zhao, Y.-Z. Corrosion inhibition behaviour of sodium dodecyl benzene sulphonate for brass in an Al_2O_3 nanofluid and simulated cooling water. *Corros. Sci.* **2019**, *148*, 123–133. [CrossRef]
18. Lee, S.; Choi, S.U.-S.; Li, S.; Eastman, J. Measuring Thermal Conductivity of Fluids Containing Oxide Nanoparticles. *J. Heat Transf.* **1999**, *121*, 280–289. [CrossRef]
19. Ismay, M.J.; Doroodchi, E.; Moghtaderi, B. Effects of colloidal properties on sensible heat transfer in water-based titania nanofluids. *Chem. Eng. Res. Des.* **2013**, *91*, 426–436. [CrossRef]
20. Asadi, A.; Asadi, M.; Siahmargoi, M.; Asadi, T.; Andarati, M.G. The effect of surfactant and sonication time on the stability and thermal conductivity of water-based nanofluid containing $Mg(OH)_2$ nanoparticles: An experimental investigation. *Int. J. Heat Mass Transf.* **2017**, *108*, 191–198. [CrossRef]
21. Xia, G.; Jiang, H.; Liu, R.; Zhai, Y. Effects of surfactant on the stability and thermal conductivity of Al_2O_3/de-ionized water nanofluids. *Int. J. Therm. Sci.* **2014**, *84*, 118–124. [CrossRef]
22. Wang, X.-J.; Zhu, D.-S.; Yang, S. Investigation of pH and SDBS on enhancement of thermal conductivity in nanofluids. *Chem. Phys. Lett.* **2009**, *470*, 107–111. [CrossRef]
23. Yang, L.; Du, K.; Zhang, X.S.; Cheng, B. Preparation and stability of Al_2O_3 nano-particle suspension of ammonia–water solution. *Appl. Therm. Eng.* **2011**, *31*, 3643–3647. [CrossRef]
24. Mehrali, M.; Sadeghinezhad, E.; Latibari, S.T.; Kazi, S.; Mehrali, M.; Zubir, M.N.M.; Metselaar, H.S.C. Investigation of thermal conductivity and rheological properties of nanofluids containing graphene nanoplatelets. *Nanoscale Res. Lett.* **2014**, *9*, 15. [CrossRef]
25. Kormann, C.; Bahnemann, D.W.; Hoffmann, M.R. Photolysis of chloroform and other organic molecules in aqueous TiO_2 suspensions. *Environ. Sci. Technol.* **1991**, *25*, 494–500. [CrossRef]

26. Tsai, W.-B.; Kao, J.-Y.; Wu, T.-M.; Cheng, W.T. Dispersion of Titanium Oxide Nanoparticles in Aqueous Solution with Anionic Stabilizer via Ultrasonic Wave. *J. Nanopart.* **2016**, *2016*, 6539581. [CrossRef]
27. Fan, H.; Li, S.; Zhao, Z.; Wang, H.; Shi, Z.; Zhang, L. Inhibition of brass corrosion in sodium chloride solutions by self-assembled silane films. *Corros. Sci.* **2011**, *53*, 4273–4281. [CrossRef]
28. Emregül, K.C.; Atakol, O. Corrosion inhibition of mild steel with Schiff base compounds in 1 M HCl. *Mater. Chem. Phys.* **2003**, *82*, 188–193. [CrossRef]
29. Ma, X.; Xu, L.; Wang, W.; Lin, Z.; Li, X. Synthesis and characterisation of composite nanoparticles of mesoporous silica loaded with inhibitor for corrosion protection of Cu-Zn alloy. *Corros. Sci.* **2017**, *120*, 139–147. [CrossRef]
30. Wang, D.; Xiang, B.; Liang, Y.; Song, S.; Liu, C. Corrosion control of copper in 3.5wt.% NaCl Solution by Domperidone: Experimental and Theoretical Study. *Corros. Sci.* **2014**, *85*, 77–86. [CrossRef]
31. Wu, K.; Ge, H.-H.; Wang, F.; Zhou, H.-W. Corrosion Behavior of Brass In TiO_2 Nanofluids. In Proceedings of the Materials Science and Engineering Conference Series 2017, Barcelona, Spain, 14 July–16 August 2017. [CrossRef]
32. Yuan, Q.; Ge, H.-H.; Sha, J.-Y.; Wang, L.-T.; Wan, C.; Wang, F.; Wu, K.; Meng, X.-J.; Zhao, Y.-Z. Influence of Al_2O_3 nanoparticles on the corrosion behavior of brass in simulated cooling water. *J. Alloy. Compd.* **2018**, *764*, 512–522. [CrossRef]

nanomaterials

MDPI

Article

Navigation of Silver/Carbon Nanoantennas in Organic Fluids Explored by a Two-Wave Mixing

Geselle García-Beltrán [1], Cecilia Mercado-Zúñiga [2], Christopher René Torres-SanMiguel [1], Martín Trejo-Valdez [3], Isaela Villalpando [4] and Carlos Torres-Torres [1,*]

[1] Sección de Estudios de Posgrado e Investigación, Escuela Superior de Ingeniería Mecánica y Eléctrica Unidad Zacatenco, Instituto Politécnico Nacional, Ciudad de México 07738, Mexico; ggarciab1102@alumno.ipn.mx (G.G.-B.); ctorress@ipn.mx (C.R.T.-S.)

[2] Departamento de Ingeniería de Materiales, Tecnológico de Estudios Superiores de Coacalco, Cabecera Municipal 55700, Mexico; cecilia@tesco.edu.mx

[3] Escuela Superior de Ingeniería Química e Industrias Extractivas, Instituto Politécnico Nacional, Ciudad de México 07738, Mexico; mtrejov@ipn.mx

[4] Centro de Investigación para los Recursos Naturales, Salaices 33941, Mexico; i.villalpando@cirena.org

* Correspondence: ctorrest@ipn.mx

Received: 4 August 2020; Accepted: 3 September 2020; Published: 21 September 2020

Abstract: Within this work are analyzed third-order nonlinear optical properties with a potential influence on the dynamic mechanics exhibited by metal/carbon nanofluids. The nanofluids were integrated by multiwall carbon nanotubes decorated with Ag nanoparticles suspended in ethanol or in acetone. Optical third-order nonlinearities were experimentally explored by vectorial two-wave mixing experiments with a Nd-YAG laser system emitting nanosecond pulses at a 532 nm wavelength. An optically induced birefringence in the metal/organic samples seems to be responsible for a significant modification in density and compressibility modulus in the nanosystems. The measured nonlinear refractive index was associated with a thermal process together with changes in density, compressibility modulus and speed of sound in the samples. Nanofluid diffusivity was studied to characterize the dynamic concentration gradients related to the precipitation of nanostructures in the liquid solutions. The evolution of the nanoparticle density suspended in the nanofluids was considered as a temporal-resolved probabilistic system. It is stated that the incorporation of Ag nanoparticles in carbon nanotubes produces strong mechanical changes in carbon-based nanofluids. According to numerical simulations and optical evaluations, immediate applications for developing dynamic nanoantennas optical logic gates and quantum-controlled metal/carbon systems can be contemplated.

Keywords: nonlinear optics; two-wave mixing; silver nanoparticles; carbon nanostructures; diffusivity; nanoantenas

1. Introduction

Photoinduced functions tailored by nonlinear optics and materials science correspond to an attractive field of research regarding the possibility to design ultrafast and low-dimensional applications. Nanostructured materials have emerged as a new generation of advanced materials with strong sensitivity to shape, size and distribution that determine their physical and chemical performance. In this direction, the inclusion of hybrid nanostructures in organic nanofluids has been related to an automatic enhancement in their third-order nonlinear optical effects.

Carbon nanotubes (CNTs) exhibit remarkable optical [1] and mechanical properties as the apparent density [2] and a notable Young modulus [3]. The peculiar morphology of CNTs consists of rolled-up structures of pure carbon with nanometric diameters and lengths of many microns. The structure

of CNTs allows their use as a support material for the dispersion and stabilization of metal and semiconductor nanoparticles (NPs) [4]. The decoration of CNTs allows for integrating the properties of metallic NPs in carbon structures, resulting in unique optical and mechanical properties [5]. In addition, Ag NPs stand out from other materials with plasmonic response because of their optical selectivity. Ag also provides a strong enhancement in plasmonic and absorption effects useful for optical processes [6]. Plasmonic interactions of Ag NPs could find applications as optical sensors or broadside nanoantenas [7]. Metallic NPs can act as optical antennae, due to their reception range and emission of optical radiation. The incorporation of metallic NPs on nanofluids can produce sharp-selective optical interactions; in particular, Ag NPs have a large third-order nonlinear optical response at wavelengths close to the absorption band of their surface plasmon resonance [8]. Ag colloidal solutions in organic liquids exhibit a large thermal-induced nonlinear refractive index [9]. Photoinduced energy transfer is a consequence of the high thermo-optic coefficient of organic fluids as ethanol [10]. In addition, the advantages of the functionalized CNTs stand out in the changes in physical properties that imply improvements in solubility and dispersion of carbon nanofluids [11]. Multiwall CNTs (MWCNTs) in nanofluids originate in an important change in effective thermal conductivity and viscosity [12]; however, it is important to consider the characteristics of the solvent [13]. Remarkable properties such as high thermal conductivity and high energy vaporization for ethanol and acetone are present in carbon nanofluids [14]. Many organic fluids have been useful in nanofluid applications due to their outstanding magnetic [15], thermal [16], and optical phenomena [17]. Carbon-based nanomaterials [18], metal NPs [19] and carbon-based nanofluids [20] exhibit a nonlinear optical response over a large wavelength range. In addition, the incorporation of plasmonic NPs in carbon nanostructures could be responsible for modifying optical nonlinearities induced by intense optical waves in nanofluids. Therefore, carbon nanofluids based on ethanol or acetone have high sensitivity to optical and mechanical effects [21]. Nanostructures with high nonlinear refractive index are of interest due their fascinating applications for developing all-optical switching devices. Progress in optical research has allowed the design of quantum systems based on Kerr nonlinearities that produce phase-changes dependent on optical irradiance [22]. Moreover, quantum optics has demonstrated several methods to generate optical nonlinearities in photons for developing optical gates [23], and the influence of optical waves on dynamics in nanofluids extends the possibility for exploring different remote or low-dimensional atmospheres.

The identification of optical nonlinearities exhibited by nanostructures in precipitation through nanofluids can be considered for teledetection or revelation of physical phenomena correlated with results obtained by laser scanning. Particular nonlinear optical parameters exhibited by nanofluids can present a strong influence in the density of their suspended NPs. The non-uniform speed of the nanoantenas can also be employed for the smart detection and identification of biofluids with biological conditions sensitive to the dynamics of the NPs [24].

With these motivations, the impact of this research mainly corresponds to the study of plasmonic nanoantenas with probabilistic logic functions controlled by dynamic nonlinear optical properties. Silver decorated MWCNTs suspended in organic nanofluids were evaluated. We analyzed third-order nonlinear optical phenomena and probabilistic effects based on diffusivity of the samples and the optical monitoring of concentration gradient associated with the particles suspended in the studied nanofluids. This work was devoted to further investigating potential probabilistic gate functions based on mechanical and Kerr nonlinearities exhibited by nanofluids. Analogic signals provided by nonlinear sensors are not preferable in respect to digital sensors in regard to the fact that observational errors usually cause excessive sensitivity to variations in environmental conditions. In this respect, we propose a logic gate system to identify the information provided by the nanostructures studied. A digital logical operation is defined in this work in terms of nonlinear optical signals in propagation through the nanoantenas in dynamic precipitation along the nanofluids. We consider that our strategy opens up an alternative for collecting information by nonlinear sensors and revelation of the evolution of nanofluids properties by probabilistic signal processing functions.

It is remarkable that silver decorated CNTs in an organic liquid solution can provide a hybrid nanofluid with optical nonlinearities improved by plasmonic phenomena. This work highlights that the third-order nonlinear optical behavior of metal/carbon nanofluids can be considered for developing electromagnetically controlled functions and dynamic nanoantennas.

2. Materials and Methods

2.1. Sample Preparation and Morphology Characterization

The MWCNTs growing process was carried out by the spray pyrolysis method. This growing method consists of setting a quartz tube inside a cylindrical oven at 850 °C. The quartz tube was fed with a toluene and ferrocene solution. Toluene molecules break down into carbon atoms and they are hexagonally arranged in the form of MWCNTs due to the presence of iron NPs derived from the decomposition of ferrocene [25]. Subsequently, MWCNTs were functionalized in 3:1 *v/v* mixture of 30 mL of 95–97% sulfuric and 10 mL of 65% nitric acid under sonication at 42 kHz for 15 min at room temperature. Functionalized MWCNTs were repeatedly washed in distilled water, centrifuged and dried in vacuum. Functionalization of MWCNTs with HNO_3/H_2SO_4 solution resulted in the formation of a surface associated with carbonyl, carboxyl, and hydroxyl functional groups. The metal decoration process of MWCNTs with Ag NPs was carried out by a chemical vapor deposition method. For each milligram of MWCNTs, 5.3 mg of Ag, 25 mL of dimethyl sulfoxide (DMSO) and 0.85 g of $AgNO_3$ were used. The samples were exposed to ultrasound for 10 min. The mixture was in continuous agitation at 120 RPM with a constant temperature of 60 °C for 30 min. After agitation, a solution was obtained due to the dissociation of the $AgNO_3$ precursor agent with the reducing agent DMSO. The samples were filtered and rinsed with acetone to remove the impurities. A filtering process was carried out in a vacuum, and then the samples were placed on a glass platform to be dried. The washing and filtering steps were repeated 4 times. Finally, to completely dry the samples, the glass platform was placed in a muffle at 200 °C for 30 min.

Previous results in comparative MWCNTs indicate that the influence of the inclusion of single-wall CNTs (SWCNTs) or noble metal NPs in MWCNTs importantly modulate their collective nonlinear optical response [26]. SWCNTs can present opposite nonlinear optical effects in respect to MWCNTs and Ag NPs can switch the physical mechanism responsible for multiphotonic absorption [27]. Hierarchical nanostructures with different concentration of metal NPs revealed that the coating of the tubes can be completed with a volume fraction of NPs in respect to the tubes of about 1:3 [28]. With these considerations, we designed our sample with the incorporation Ag NPs integrated in the MWCNTs as Ag-MWCNT samples.

Ag-MWCNTs were weighted to prepare the nanofluid samples measured in this work. Then, 8.2 mg of Ag-MWCNTs were suspended in an acetone solution with a volume of 2 mL. Comparatively, 8.2 mg of Ag-MWCNTs were suspended in an ethanol solution with a volume of 2 mL. Different concentrations of the nanostructures in the selected organic samples were analyzed. Here are described the conditions of the most representative results with heuristically chosen concentrations to better observe the optical nonlinearities without a strong depletion of the optical transmittance and a high signal to noise ratio.

In order to analyze the metal decoration and chemical composition in MWCNTs, field-emission scanning electron microscopy with energy-dispersive X-ray (SEM and EDX; JEOL JSM-6701F) studies were undertaken. High-resolution transmission electron microscopy (TEM) studies were carried out to confirm the multiwall nature of the CNTs studied.

2.2. Third-Order Optical Nonlinearities Explored by a Two-Wave Mixing

A two-wave mixing (TWM) technique was conducted in order to evaluate the third-order nonlinear optical response of the nanofluid samples. The schematic experimental setup for the superposition of the two coherent and polarized beams is illustrated in Figure 1. A Nd-YAG laser system (Continuum model SL II-10) with 4 ns of pulse duration and wavelength at 532 nm was used as an optical source.

The pump and probe beams with an optical irradiance relation of 1:10 were focused in the nanofluid sample S contained in a quartz cuvette with 1 mm thickness. The spot size of the focused beams was approximately 1 mm. The propagation vectors of the beams make a geometrical angle of 30° due to the beam splitter and the mirrors. A half-wave plate, λ/2, modifies the angle of the polarization plane of the incident pump beam. A PIN photodetector was used to measure the orthogonal polarization component of the incident probe beam transmitted through a polarizer by the influence of the pump beam. The maximum total optical irradiance of the probe beam in the sample was 2 MW/cm^2. The high-irradiance of the pump beams promotes the modification of the polarization state of the probe beam. Likewise, the modification of the polarization state of the beams results in changes in the transmittance of the probe beam in the TWM system.

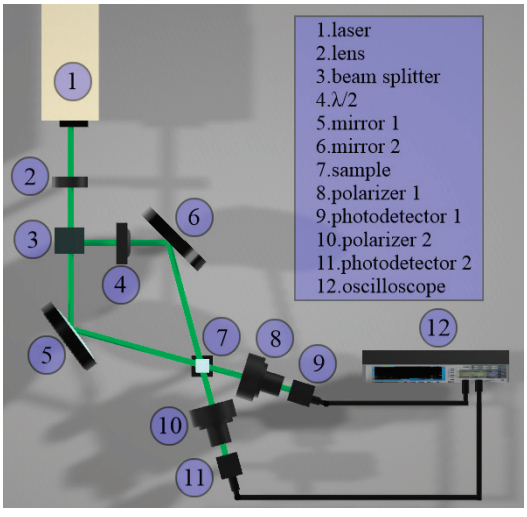

Figure 1. Scheme of the experimental setup of the two-wave mixing (TWM).

The electric fields in propagation through the samples can be described by considering the wave equation [29] as described in the supplementary material.

According to Equation (S3), the intensity-dependent refractive index can be significant for high-irradiance effects induced in a nonlinear material. For nanosecond pulses irradiating MWCNTs, the most likely physical mechanism responsible for the nonlinear refractive index, n_2, is the photothermal effect [30], and this third-order optical nonlinearity excited by an important photoinduced energy transfer can also be responsible for a local modulation in density in the irradiated sample [26].

Photoinduced Mechanical Response

Considering the optical Kerr effect (OKE) represented by Equation (S3), the density of a nonlinear optical medium can be modified. Then, from Equations (S3) and (S4), the change in mass density, $\Delta\rho_m$, coming from the OKE can be estimated by,

$$\Delta\rho_m = \left[\frac{(n_0 + n_2 I)^2 - 1}{(n_0 + n_2 I)^2 + 2} - \frac{n_0^2 - 1}{n_0^2 + 2}\right]\left[\frac{3M}{4\pi N_A \alpha}\right] \quad (1)$$

where n_0 is the weak-field refractive index, n_2 in the nonlinear refractive index, I refers to the intensity of the optical field, α is the polarizability, N_A is the Avogadro's number and M is the molecular weight of the chemical element.

In Equation (1), it is implicit that a change in irradiance generates a change in the refractive index. Explicitly, Equation (1) also describes that a change in the density of mass can be obtained as a function of irradiance in the sample.

In addition, the compressibility modulus, ΔY, can be estimated as a function of the speed of sound through the medium, v_a, and the change in density with dependence on the OKE:

$$\Delta Y = {v_a}^2 \left[\frac{(n_0 + n_2 I)^2 - 1}{(n_0 + n_2 I)^2 + 2} - \frac{n_0^2 - 1}{n_0^2 + 2} \right] \left[\frac{3M}{4\pi N_A \alpha} \right] \tag{2}$$

2.3. Effects of Difusivity in Plasmonic Nanoantennas

The second Fick law is a mathematical description of the evolution exhibited by a diffusion effect by a partial differential equation. This law is described by [31]:

$$\frac{\partial C}{\partial t} = D \frac{\partial^2 C}{\partial x^2} \tag{3}$$

where C is the concentration of the solute in the solvent, D is the diffusion coefficient, and x is the position of the particle. The solution of the differential equation corresponds to the probability at the coordinates of the particles x of the medium at each time t [32].

$$p(x,t) = \frac{1}{\sqrt{4\pi D t}} \exp\left(\frac{-x^2}{4Dt} \right) \tag{4}$$

In order to determine the diffusivity coefficient value D_{S1-S2}, where $S1$ is the solute, $S2$ is the solvent, the Wilke–Chang relation can be used [33]:

$$D_{S1-S2} = \delta \left[\frac{\varphi \sqrt{\vartheta M_{S2}}}{\Upsilon_{S2} (v_{S1})^{0.6}} \right] \tag{5}$$

where δ is a constant equivalent to 1.17×10^{-16}, ϑ is the association parameter of the fluid, M_{S2} is the molecular weight of the solvent, Υ_{S2} is the viscosity of the solvent, and v_{S1} is the atomic volume of the solute and φ is the temperature.

The particles of a nanofluid are in constant fluctuation. That means the absorption of a sample is modified as a function of the time related to the stability of the sample. A numerical fitting for describing the temporal dynamics of a nanofluid can be computed by considering:

$$y = a e^{-t/\tau} + b \tag{6}$$

where τ is the value of the independent variable time, y represents the absorbance, a is a constant and b is the point where the straight line cuts the vertical axis.

2.4. Probabilistic Signals Exhibited by Plasmonic Nanoantenas

In contrast to the classic digital recording of binary bits where only the values 0 and 1 can be present, the probabilistic bits refer to an overlap of values between 0 and 1. A probabilistic bit system is a two-dimensional complex vector space, and the state of a probabilistic bit, Ψ, can be represented by a complex vector in that space as follows:

$$\Psi = \Gamma|0\rangle + \Lambda|1\rangle \tag{7}$$

The configurations of the probabilistic bits increase infinitely due to coefficients that can be negative and with complex numbers. The probabilistic bits are characterized by the complex numbers Γ and Λ, which correspond to the probability of measuring a value of 0 and 1. Likewise, the notation

ket $|\rangle$ means input and the notation $\langle|$, means output. Since these coefficients can be imaginary, they cannot simply be interpreted as probabilities of their associated results. Then, the probability of measuring each state is given by [34],

$$|\Gamma|^2 + |\Lambda|^2 = 1 \tag{8}$$

The quantum logic gates can be represented by reversible operations between the quantum elements. A three probabilistic bits gate can be described as a controlled gate with inputs S1–3 and outputs O1–3. In this case, S1 corresponds to O1, S2 corresponds to S2 and S3 corresponds to O3. However, O3 changes its value if S1 and S2 are 1. It can be interpreted as a logic gate with 2 control probabilistic bits identified as S1 and S2. The truth table is shown in Table 1.

Table 1. Truth table related to three probabilistic bits.

Inputs			**Outputs**		
S1	S2	S3	O1	O2	O3
0	0	0	0	0	0
0	0	1	0	0	1
0	1	0	0	1	0
0	1	1	0	1	1
1	0	0	1	0	0
1	0	1	1	0	1
1	1	0	1	1	1
1	1	1	1	1	0

This gate is usually employed for simulating irreversible classic gates. Among its particularities, it can be mentioned that this gate is one of the most important classic gates, the NAND gate.

Different architectures based on carbon nanomaterials have demonstrated exceptional optical nonlinearities that can be tailored by their structure and morphology [35]. This particular physical empowering related to size, shape and chirality has been employed in MWCNT systems to design unusual metal/carbon nanohybrids assisted by decoration processes including plasmonic NPs [36]. It is worth mentioning that silver NPs present a sharp selective absorption band associated to their characteristic surface plasmon resonance close to 400 nm, while MWCNTs exhibit their characteristic resonance around 270 nm [27]. The integration of a double resonance characteristic by Ag NPs in MWCNTs seems to be attractive with advantages for visible laser driven logic gate functions and single-photon devices in the UV region of the electromagnetic spectrum. Optical nonlinearities exhibited by nanostructures in precipitation through nanofluids can be considered for remote sensing or laser scanning as a function of their dynamics. The use of MWCNTs decorated with Ag NPs has been chosen by considering that metallic NPs can act as nanoantenas with an enhanced reception and emission of optical radiation in nonlinear devices. The operation of nanoantenas is based on capturing an electromagnetic wave of a specific wavelength by an energy transfer. In our case, this nanoantenna response is considered to be plasmonic and achieved by the collective excitation of the electrons in the metal as a consequence of the strong interaction with the incident light. To improve metal light emitters, there is a coherent oscillation of the electrons confined to the surface of particular NPs. In Ag NPs, their absorption peak is maximum in the visible region of the electromagnetic spectrum. This response depends on factors such as the concentration of the NPs, spatial distribution, morphology and surrounding properties. The morphology of the studied nanostructures and their influence on optical properties with ethanol and acetone as background media was considered. The results corresponding to the absorption spectrum show that Ag NPs are attractive for applications in the visible range and close to UV.

3. Results

Figure 2 shows the characterization of MWCNTs in order to reveal the multiwall nature, functionalization, and decoration of the CNTs. Figure 2a shows a high-resolution TEM image of a representative section of MWCNT growth. Bright-field mode was chosen to observe in detail the cross-section multiwall nature of CNTs. TEM micrograph provides clear evidence of the formation of multilayer nanotubes during the toluene–ferrocene decomposition reaction, which is several microns in length. In addition, the TEM studies determined that the internal diameters are approximately 4 nm ± 5% and the external diameters are up to around 28 nm ± 2%. Moreover, the intermolecular distance between the carbon layers was 0.134 nm.

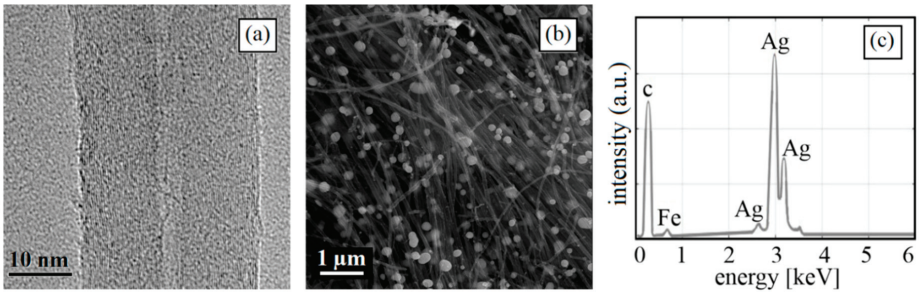

Figure 2. (**a**) A representative TEM micrograph of the studied carbon nanotubes (CNTs) confirming their multiwall nature. (**b**) SEM micrograph of representative regions of the samples. (**c**) Results of statistical EDX analysis for the studied silver decorated multiwall CNTs (Ag-MWCNTs).

SEM micrographs allowed the observation of the homogeneity of metal NPs incorporated to the MWCNT samples. Figure 2b shows the Ag NPs represented by quasi-circular white points in the extremes of MWCNTs. Ag NPs have an average size of approximately 60 nm ± 5%. Metal particles represent 30% of weight of MWCNTs. Correspondingly, from the image, it is possible to deduce that MWCNTs have a minimum length of 10 µm approximately.

Figure 2c depicts the elemental analysis of MWCNTs by the EDX technique. This analysis highlights the presence of carbon corresponding to MWCNT structure and iron appropriate of the synthesis process. There is also a notable presence of Ag NPs in the composition of the samples due to decoration process.

The UV-VIS absorption spectra of the samples prepared in ethanol and acetone with Ag-MWCNTs respectively are plotted in Figure 3.

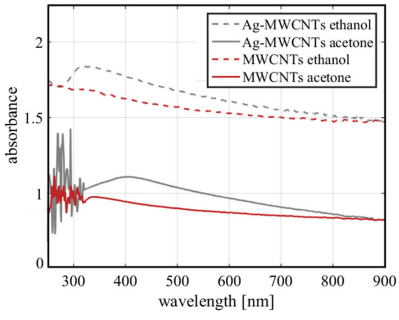

Figure 3. Typical UV-VIS absorption spectra of the studied nanofluids.

From the spectra shown in Figure 3, it is possible to observe an emerging band corresponding to the excitation of the surface plasmon resonance of the Ag NPs near to 400 nm. However, an interesting

point to highlight it is the influence of the geometry of the Ag NPs and the solvent in which they are suspended on the resonance spectral location [37]. The absorption band of pure acetone is located around 250 nm [38]. In the nanofluid spectrum shown in Figure 3, related to acetone, there is a high noise caused by phenomena related to scattering. The absorption bands for ethanol should be close to 340 nm. The peak in the absorption band associated with the π-π bond resonance exhibited by MWCNTs is located in the ultraviolet region, near to 270 nm. Nevertheless, the absorption peaks of the MWCNTs can move due to the polarity of the solvent [39]. On the other hand, the presence of MWCNTs agglomeration influences the absorption spectrum of the samples, such that, from the UV-VIS spectra, it can be identified that the sample in the acetone suspension has a lower absorption than the ethanol sample. So, from the previous points and from the experimental observations, we can conclude that MWCNTs present more agglomeration in ethanol suspensions than in acetone.

To further investigate the possibility to modulate the dynamic response of the probabilistic logic gate, no changes in nonlinear optical absorption were observed through monitoring single-beam transmittance as a function of irradiance. However, we analyzed the OKE of the samples by our TWM experiment described by Figure 1. The calibration of the system was performed by using a CS_2 sample. The TWM technique presents the potential to evaluate an induced birefringence promoted by the superposition of optical waves. From Figure 4, it is possible to observe experimental evidence of Kerr nonlinearities exhibited by Ag-MWCNT samples and a numerical fitting based on Equation (S1). The degenerated TWM method in a non-collinear pump-probe configuration was selected for measuring the nonlinear refractive index regarding the potential of this technique for identifying the physical mechanisms responsible for the optical Kerr effect [40]. Our analysis of Equation (S2) in Equation (S1) reveals that the fitting of numerical data is consistent with $X^{(3)}_{1212} = 0$, which corresponds to the isotropic nonlinear refractive index [29]. The expected thermal effect induced by nanosecond pulses in MWCNTs [30] matches our results. The error bar corresponds to about ±15%. A strong magnitude in $n_2 = 6.1 \times 10^{-12}$ cm^2/W was obtained for the Ag-MWCNTs in ethanol and $n_2 = 5.6 \times 10^{-12}$ cm^2/W for the Ag-MWCNTs in acetone.

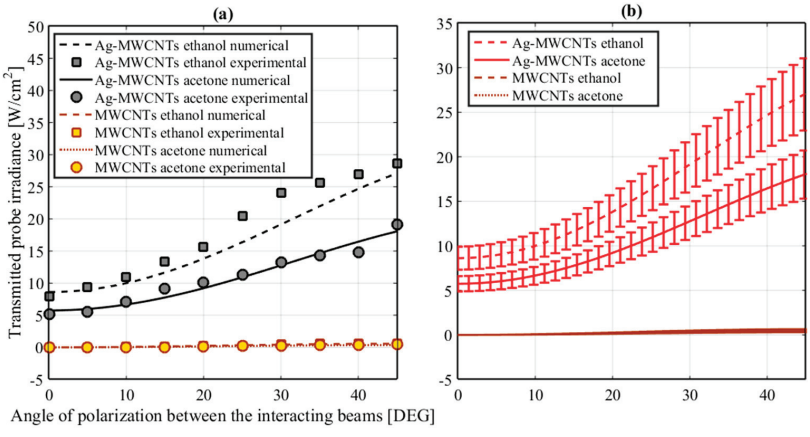

Figure 4. (**a**) Transmitted probe irradiance as a function of the angle between the planes of polarization of the incident beams in the nanofluids tested in the vectorial TWM. (**b**) Experimental error bars for (**a**).

The third-order optical susceptibility of pure ethanol and pure acetone is omitted in Figure 4. This consideration is valid because the nonlinear optical responses of ethanol and acetone [29] are lower than the nonlinear results for the samples measured in this work, and they present a nonlinearity at least three orders of magnitude lower.

In our TWM experiment, pump and probe beams had incident linear polarizations, and their superposition in the sample produces a modulation in irradiance featuring an interference fringe

pattern. The variation in irradiance along the sample automatically causes a modulation in nonlinear birefringence as a function of the change in refractive index given by $\Delta n = n_2 I$, with n_2 being the nonlinear refractive index and I the optical irradiance profile. Initially, the incident polarization of the probe beam is fixed but sensitive to the nonlinear birefringence induced by the pump beam. The polarization of the pump beam was rotated by a half-wave plate during the experiment in order to explore the vectorial nature of the nonlinear birefringence induced during the interaction of the beams. An analyzer with its transmission axis orthogonal to the incident polarization of the probe beam monitored the evolution of the polarization of the probe beam after passing the sample. The transmitted probe irradiance is directly related to the characteristic third-order optical nonlinearities of induced birefringence and multiphotonic absorption exhibited by the studied samples in the TWM [29].

The nonlinear optical response of nanofluids can be used for the harmonic generation of optical waves through coherent optical mixing. In contrast with nanosecond optical effects, ultrashort pulses can be suitable for observing ultrafast electronic nonlinearities, but the modeling of thermal mechanisms that can be induced by picosecond and femtosecond pulses, which is more complex for describing photothermal energy transfer. Nanosecond pulses involve enough time for thermal transport while the photoinduced effects correspond to a collective response exhibited by nanofluids deposited in thicker samples [41]. The potential to excite stronger nonlinear optical absorption effects closer to the absorption band of the surface plasmon resonance of the Ag NPs can be expected by using the third-harmonic of our Nd:YAG laser system [42]; but this consideration is also correlated with a potential inhibition in the nonlinear optical refraction effects according to Kramers-Kroning relations.

Figure 4b corresponds to the error bar of the measurements associated with the transmitted probe irradiance as a function of the relative angle between the plane of polarization of the incident beams in the samples. These bars exhibit an error of approximately ±15%. From the absence of an overlapping in the experimental data for the Ag-MWCNTs in acetone and ethanol and the MWCNTs can be guaranteed the clear signature of the different studied samples in this TWM experiment.

The inherent morphology, structure and geometric properties exhibited by nanostructures are responsible for the outstanding changes in their optical, electrical and thermal behavior. In this regard, the incorporation of Ag NPs in MWCNTs in film form can promote the switching of multi-photonic effects that is topic of this research in nanofluids, as comparatively has been demonstrated in nonlinear optical absorption processes measured by single-beam techniques [27]. The uniform and homogeneous distribution of the metallic decoration as well as the multi-wall nature of the tubes were guaranteed and analyzed in this work by SEM, TEM and X-ray studies.

Furthermore, the incorporation of Ag NPs in carbon nanostructures seems to cause an enhancement in the nonlinear optical properties in comparison with carbon nanostructures without decorations [27]. The enhancement in the third-order nonlinear optical response can be attributed to surface plasmon absorption effects of Ag NPs [43]. A nonlinear absorption coefficient and nonlinear refractive index are strongly dependent on the NP concentration in the solutions and the duration of pulses [44]. In addition, a fast photoresponse is characteristic in CNT-decorated samples [45].

In order to measure the stability of nanofluids, the optical absorption at 532 nm of nanofluids was monitored after a sonication process in the samples. The UV-VIS spectra were evaluated in a range of 0 to 5 min, in order to demonstrate the stability of the samples. Figure 5 shows the dependence on absorbance in the time from the samples. The numerical fitting for the experimental measurements was obtained by Equation (6). It is possible to observe the parameters a, τ and b, related to the behavior of the numerical fitting for each sample.

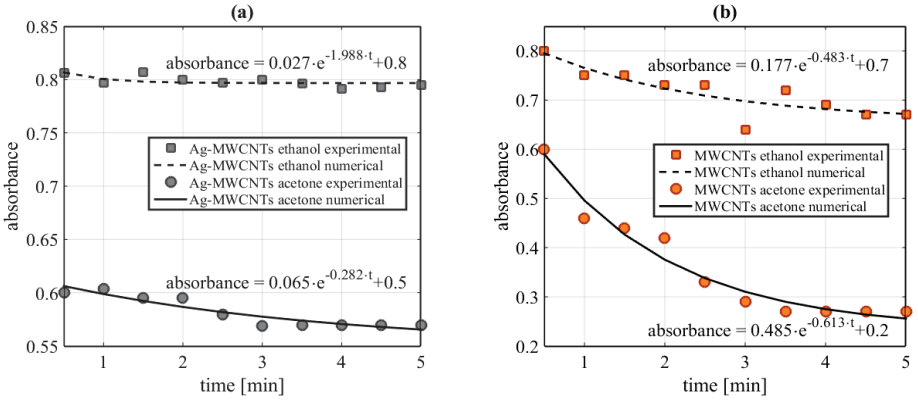

Figure 5. Time dependence of UV-VIS absorbance at 532 nm. (**a**) Ag-MWCNT samples, (**b**) MWCNT samples.

The stability of nanofluids is strongly dependent on the solution but also changes with the incorporation of the NPs in the carbon nanostructures [46]. It has also been demonstrated that the stability times of Ag NPs nanofluids are longer than others [47]. It is worth mentioning that the time-dependence stability of nanofluids strongly depends on the diffusion of the suspended NPs and the organic solvents.

The spatial distribution of molecules in a nanofluid is not homogeneous; this implies that there is a concentration gradient between two points in the medium. The diffusion phenomenon describes the concentration gradients with respect to time in the fluid. The concentration at the position of the particles in the medium at each instant of time obtained from Equation (4) is represented in Figure 6. The diffusion coefficient approximation was calculated from Equation (5) with $\Psi_{Ethanol} = 1.5$, $\Psi_{Acetone} = 1$, $M_{Ethanol} = 46.07$ g/mol, $M_{Acetone} = 58.08$ g/mol, $\vartheta_{Ethanol} = 1.074$ mPa·s, $\vartheta_{Ethanol} = 0.32$ mPa·s and $\nu_{Carbon} = 4.58$ cm^3/mol. The diffusion coefficient for carbon-acetone is 3×10^{-13} cm^2/s and that for carbon-ethanol is 9×10^{-14} cm^2/s. Time-dependence stability of the Ag-MWCNTs nanofluids strongly depends on the diffusion coefficient between the CNTs suspended and the ethanol or acetone solvents. The diffusion coefficient indicates an inverse relation in respect to the stability of the fluid. In order to verify the law of conservation of matter and energy in the diffusivity analysis, the area under the diffusivity curves was analyzed.

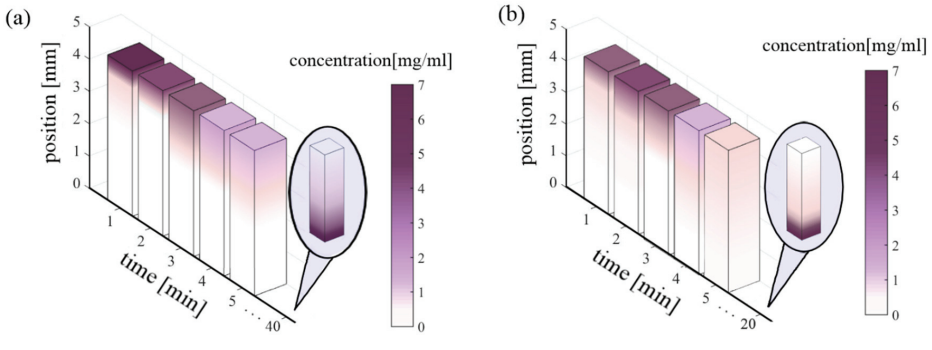

Figure 6. (**a**) Diffusivity of carbon nanostructures in ethanol. (**b**) Diffusivity of carbon structures in acetone.

Figure 6 shows the graphic representation of the diffusivity behavior of the samples in the quartz cuvettes. It can be noticed that the evolution of the concentration of nanostructures in ethanol and in

acetone is different. The results indicate that the particles can be easily dispersed in acetone suspensions. Diffusivity concentrations are indicative of fluid stability.

Regarding the experimental results, we consider that a probabilistic bit can be referred to an overlap of values associated with our samples. It was considered the value of the bits as the solute concentration suspended in the liquid samples. The logic states of the input's gate were defined by the probability of the position of the particles in the fluid tested by an optical signal. The values in the measurement of the gate outputs and the experimental setup gate are shown in Figure 7.

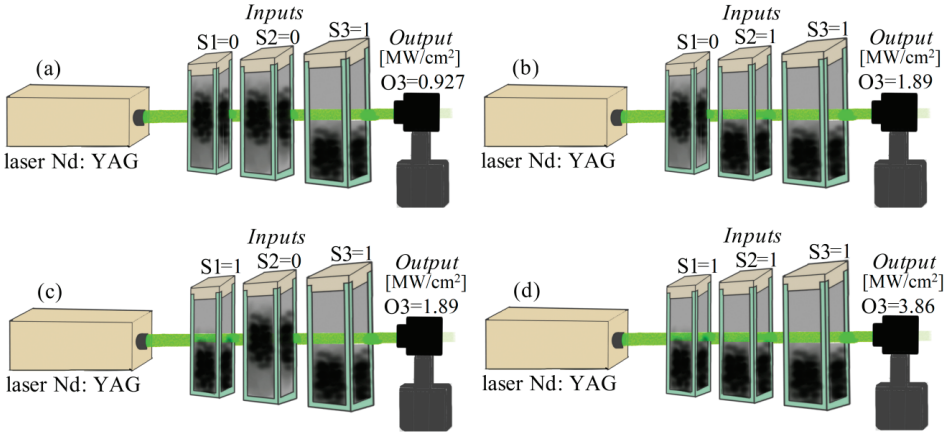

Figure 7. Experimental setup of the probabilistic gate in an AND configuration controlled by the particle position probabilities. The laser beam energy is absorbed by the CNTs position. (**a**) S1 = 0, S2 = 0; S3 = 1, O3 = 1 with 0.927 MW/cm^2, (**b**) S1 = 0, S2 = 1; S3 = 1, O3 = 1 with 1.89 MW/cm^2, (**c**) S1 = 1, S2 = 0; S3 = 1, O3 = 1 with 1.89 MW/cm^2 (**d**) S1 = 1, S2 = 1; S3 = 1, O3 = 0 with 3.86 MW/cm^2.

The logic states of the output were designated by the irradiance of the laser beam as shown in Figure 7. The logical value 1 was assigned to an optical irradiance lower than 2 MW/cm^2. Otherwise, the logical value is 0.

In addition, in Figure 7 the separation of the samples explored in different containers is schematized; the potential of the logic device can be extended to analyze a single nanofluid with diverse regions or thermodynamic properties of multiple phases.

A probabilistic bit simulation was performed by using the fuzzy set theory. Figure 8a shows the fuzzy interference process to obtain the output value of the beam energy due to the concentration and position of the particles suspended in the nanofluid.

The fuzzy logic process was structured by using rules to define the behavior of nanofluids. The rules were established by the input variables distance, concentration, and the output energy. The sets defined by the domain of concentration x were represented by ζ1, ζ2, ζ3, ζ4, ζ5. Over domain y, the position are d1, d2, d3, d4, d5, and the output over domain z are f1, f2, f3, f4, f5. The values of the domains represent the lowest, low, middle, high and higher level. Figure 8b shows a range of magnitudes of the domains in the fuzzy variables. For the fuzzification step, the peak values of the inputs were defined and the degree of belonging of the input variables to the associated fuzzy sets was determined. In this way, each input is fuzzified over all the belonging functions used in fuzzy rules.

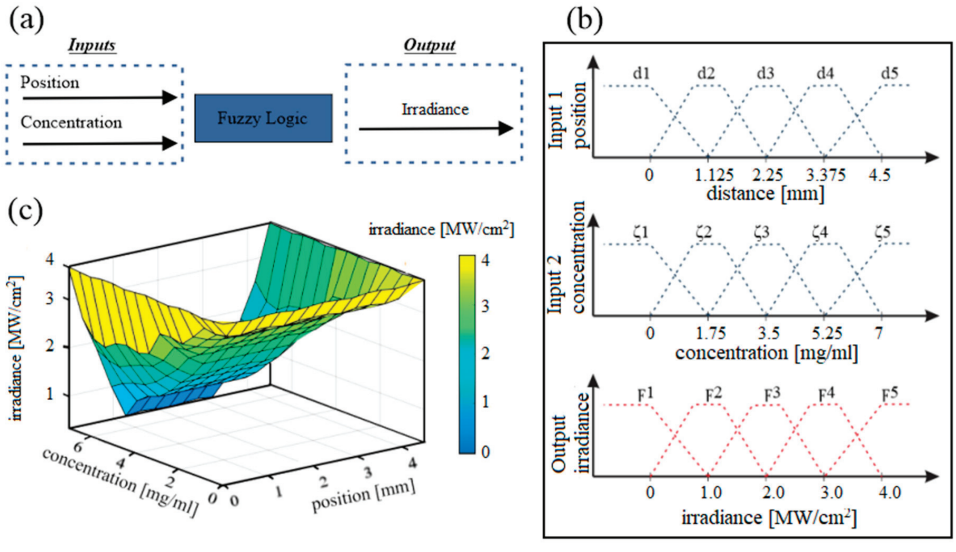

Figure 8. Graphic representation of fuzzy logic system. (**a**) diagram of system implemented; (**b**) parameter representation of the inputs and output variables for the fuzzy logic controller; (**c**) surface diagram of the fuzzy logic controller results for the nanofluid samples.

For the evaluation of the fuzzy rules, the AND operator was used by considering the generalized form of the T-norm intersection to obtain a belonging function þ, which is defined as follows:

$$\text{þ}\varrho \cap \complement(x) = T\left(\text{þ}\varrho(x), \text{þ}\complement(x)\right) \tag{9}$$

where ϱ and ∁ are fuzzy sets and x is the set variable.

In order to obtain the resulting values of the fuzzy logical system, the fuzzy set previously obtained is taken as an input to give an output value. The fuzzy controller receives the input data corresponding to the variables x_0 and y_0 by the Manmdani inference rules defined by:

$$\begin{aligned} \text{þ}\zeta'_1(z) &= \text{þ}\varrho_1(x_0) \cap \text{þ}\complement_1(y_0) \cap \text{þ}\zeta_1(z) \\ \text{þ}\zeta'_2(z) &= \text{þ}\varrho_2(x_0) \cap \text{þ}\complement_2(y_0) \cap \text{þ}\zeta_2(z) \\ &\vdots \\ \text{þ}\zeta(z) &= \text{þ}\zeta'_1(z) \cup \text{þ}\zeta'_2(z) \cup \ldots \text{þ}\zeta'_n(z) \end{aligned} \tag{10}$$

The belonging function values related to the input variables position and concentration are fuzzified. The minimum value between the belonging value of the input variables is calculated, in order to define the output set at the height of the smallest fuzzification value. The minimum belonging value of each rule is defined in order to limit the output set related to the energy of the beam. As a result, dimension sets are joined to calculate the membership function of the output set. The defuzzification of the sets is obtained by the following:

$$\text{Defuzzification} = \frac{\sum_{x=\varrho}^{\complement} \text{þ}\varrho(x)x}{\sum_{x=\varrho}^{\complement} \text{þ}\varrho(x)} \tag{11}$$

Figure 8c shows a superficial plot representing the fuzzy logic applied to the probabilistic bit system. The effect of the predictive diffuse system based on the behavior of the NPs suspended in the nanofluids and their impact on the optical irradiance of the system can be observed.

The results shown in Figure 8c demonstrate the effect of the input variables in the optical transmittance of the nanofluid. The relationship between the concentration and position of the NPs is also observed. The result of optical transmittance output shows that the maximum value mostly depends on the minimum concentration of the nanofluids which, at the same time, depends tightly on the diffusivity of the fluid.

The optical Kerr effect, described by the magnitude of n_2, can be associated with different physical mechanisms responsible for the third-order optical nonlinearity in a sample. In particular, molecular orientation, electronic polarization, electrostriction, magneto-optical phenomena or a thermal transfer can be related to a nonlinearity of the index [29]. In this aspect, a photothermal effect can be described as an optical Kerr effect that may be responsible for a change in density, as expressed by Equation (1). The change in the refractive index illustrated in Figures 9 and 10 is the result of a change in the concentration of the samples. By using Equation (1), the change in refractive index was estimated at concentrations between 10 and 100% w of Ag-MWCNTs. It is notable that the refractive index can be related to the density of the samples. The numerical data resulting from Equation (1) confirm that the optical nonlinearities generated by TWM are significant in the changes in the mechanical properties of the nanofluids. The behavior for the change in density of the samples with Ag-MWCNTs ethanol and acetone nanofluids was analyzed and the results are shown in Figure 9a,b.

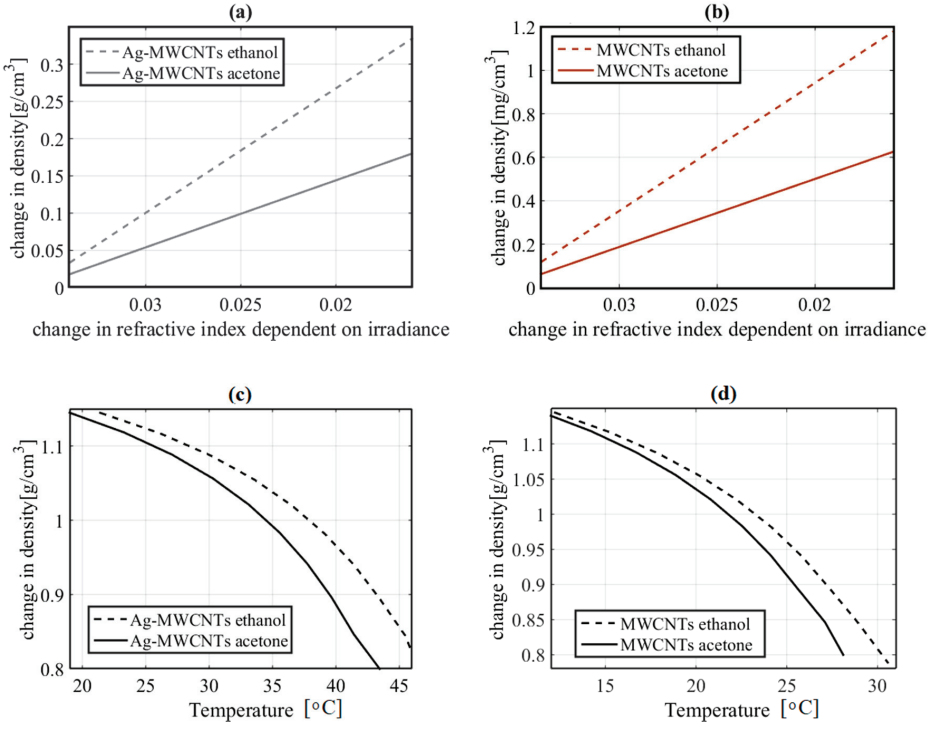

Figure 9. Numerical results of the induced change in density estimated by considering the change in refractive index in the nanofluids. (**a**) Ag-MWCNT samples, (**b**) MWCNT samples. Numerical results of the induced change in temperature estimated by the change in density in the nanofluids. (**c**) Ag-MWCNT samples, (**d**) MWCNT samples.

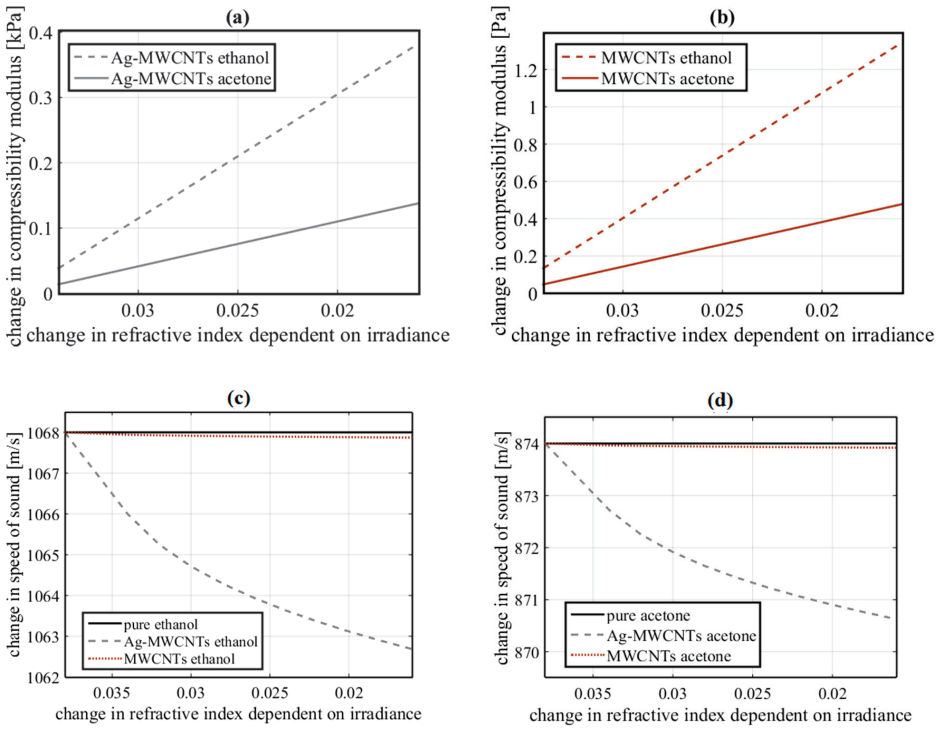

Figure 10. Numerical results of the induced change in compressibility modulus estimated by considering the experimental optical Kerr effect (OKE) in the nanofluids. (**a**) Ag-MWCNT samples, (**b**) MWCNT samples. (**c**) Change in the speed of sound due to Ag-MWCNT suspensions. (**d**) Change in the speed of sound due to MWCNT suspensions.

If the parameters described by the Lorentz–Lorenz relation are considered, it can be concluded that modification of the nanofluid density by dependence on optical irradiance must be present under high-optical irradiation. Figure 9c,d also shows the relation in temperature of the nanofluids considering the change in density.

Figure 10a,b shows the change in the compressibility modulus of the samples considering Equation (2). The changes in mechanical properties in the samples described by the Lorentz–Lorenz equation are caused by an induced nonlinear refractive index with dependence on optical irradiance and concentration of the samples. In the same way, an important contribution of different parameters such as the molecular weight of the chemical elements and the mean molecular polarizability of the samples ought to be considered.

Moreover, an approximation for the speed of sound through the Ag-MWCNTs nanofluids can be obtained by the compressibility modulus, and change in density. From the above, the numerical calculations require the calculus of density corresponding to elements that compose the sample. Density calculation was performed for suspensions with 2 mL of pure solvent, 0.0057 g to MWCNTs and 0.00246 g of metallic NPs. The previous weights correspond to 0.0082 g of Ag-MWCNTs with 30% of Ag NPs.

Figure 10 shows the change in the speed of sound of ethanol and acetone Ag-MWCNTs nanofluids. From Figure 10c, it is possible to observe the change in the speed of sound due to ethanol and acetone suspensions with MWCNTs without decorations. The result demonstrates that the addition of Ag-MWCNTs in nanofluids generates a higher change in the speed of sound of pure organic fluids. So, the refractive index of the Ag NPs adhered to the MWCNTs defines strong differences in the

mechanical behavior of nanofluids according to the optical nonlinearities of the samples. The control of the mechanooptic properties exhibited by the studied samples gives an advantage in the field of nanoantenas. If the density of the involved nanofluids is very low, the phenomenon could not be observable due to the absence of enough NPs in their vicinity of the nanoantenas. On the other hand, if the density is very high, it is possible that high-density agglomerations will appear, preventing the reaction of the electromagnetic field of the nanoantenas. Additionally, the excitation beam could be absorbed together with an induced nonlinear refractive index depending on the optical irradiance and the concentration of the samples. Consequently, optical nonlinearities find important areas of application in the field of nanoantenas, and the dynamic behavior of NPs can control discrete variables associated with the physical-chemical changes of nanofluids.

The local control of the temperature of plasmonic nanoantenas has been studied and good results have been obtained for Ag NPs; however, the operating temperatures for hybrid materials present different advantages compared to pure Ag NPs [48]. In Figure 9b,c, the modified temperature operating range due to density and optical irradiance dependency is shown. The dissipation of energy within the metallic NPs is an important factor in the performance of nanoantenas [49]. In this work, the concentration gradients with respect to time in the fluid indicate the dynamic stability of the proposed nanofluids. Due to the nature of the diffusivity presented in the samples studied, the design of UV-VIS nanoantenas with minimal energy dissipation can be contemplated in comparison to sensitive nanoantenas with infrared response [50]. In addition to good light absorption and energy dissipation, plasmonic NPs have been studied for applications related to sensors and nanoswitches by coupling light with the NPs [51]. The application of optical nanoantenas in binary logic operations has also been explored [52]. In this work, the advantages of the plasmonic properties of metallic NPs have been considered as well as the optomechanical properties exhibited by MWCNTs. Using a fuzzy logic system, it was possible to design an AND logic gate with probabilistic signals. The system was structured by rules defined by the behavior resulting from the diffusivity simulations, and the optical response exhibited by the studied nanofluids. The operating principles depend on controlled sets of NPs with not only specific optical and mechanical properties, but also with quantum properties.

4. Conclusions

This work highlights the importance of metal/carbon nanostructures to control probabilistic functions assisted by dynamic and nonlinear optical properties. Nanoantenas in a fluid featuring a probabilistic NAND logic gate were proposed by the assistance of mechanical and nonlinear optical properties. The evolution of mechano-optical signals in simple organic liquids was modulated by the incorporation of Ag decorated MWCNTs. The participation of Ag NPs incorporated in MWCNTs seems to cause strong changes in off-resonance nonlinear optical interactions. The plasmonic properties of the metal nanoparticles allow for increasing the emission and control in the optical response due to the excitation of the electrons of the metal structures. Optically induced variations in density, compressibility modulus and speed of sound in metal/carbon-based nanofluids were analyzed considering a dynamic OKE. The mechanical and optical properties exhibited by MWCNTs show advantages over other nanostructured materials with the same dimensions. Due to the morphology of the CNTs, it is possible to consider nanoantenas for wireless communication in GHz and THz. CNTs allow developments in quantum and molecular communications due to their high rates of electrical and thermal conductivity and mechanical moldability. The plasmonic behavior derived from the decoration of the MWCNTs can also function as an oscillator for frequency modulation. This work can be a base for future research related to dynamic nonlinear optical systems assisted by hybrid nanostructures.

Supplementary Materials: The following are available online at http://www.mdpi.com/2079-4991/10/9/1886/s1, Supplementary material.

Author Contributions: G.G.-B. carried out two-wave mixing measurements, numerical simulations of the mechanical phenomena and probabilistic logic gate design; C.M.-Z. is responsible for the preparation, decoration and morphology characterization of the samples; M.T.-V. contributed in the development of UV-VIS spectroscopic observations; C.R.T.-S. participated in discussions about the mechanical results; I.V. studied the evolution of the nanofluids during experiments; C.T.-T. elucidated and analyzed the dynamic influence of the nonlinear optical properties on the mechanical effects and designed the paper. The manuscript was written through contribution of all authors. All authors have read and agreed to the published version of the manuscript.

Funding: This research was funded by Consejo Nacional de Ciencia y Tecnología (CONACyT) (grant CB-2015-251201), Comisión de Operación y Fomento de Actividades Académicas, Instituto Politécnico Nacional (COFAA) and Instituto Politécnico Nacional (IPN) (SIP-2020).

Acknowledgments: The authors kindly acknowledge the financial support from the Instituto Politécnico Nacional, TESCo, COFAA-IPN, and Consejo Nacional de Ciencia y Tecnología. The authors are also thankful to the Central Microscopy facilities of the Centro de Nanociencias y Micro y Nanotecnología of Instituto Politécnico Nacional.

Conflicts of Interest: The authors declare no conflict of interest.

References

1. Nudrat, S.; Archana, Y.; Hasan, S.S. A review study of advances in the science and technology of carbon nanotubes. *J. Phys.* **2018**, *5*, 1–6.
2. Lehman, J.H.; Terrones, M.; Mansfield, E.; Hurst, K.E.; Meunier, V. Evaluating the characteristics of multiwall carbon nanotubes. *Carbon* **2011**, *49*, 2581–2602. [CrossRef]
3. Andalouci, A.; Roussigne, Y.; Farhat, S.; Cherif, S.M. Low frequency vibrations observed on assemblies of vertical multiwall carbon nanotubes by Brillouin light scattering: Determination of the Young modulus. *J. Phys. Condens. Matter* **2020**, *32*, 455701. [CrossRef] [PubMed]
4. Sezer, N. Dispersion stability of CNT and CNT/Metal-based nanofluids. In Proceedings of the ICTEA International Conference on Thermal Engineering, Doha, Qatar, 25–28 February 2018.
5. Kharisov, B.I.; Kharissova, O.V.; Ortiz Mendez, U.; De La Fuente, I.G. Decoration of carbon nanotubes with metal nanoparticles: Recent trends. *Synth. React. Inorg. Met.-Org. Nano-Met. Chem.* **2016**, *46*, 55–76. [CrossRef]
6. Wang, X.; Santschi, C.; Martin, O.J. Strong Improvement of Long-Term Chemical and Thermal Stability of Plasmonic Silver Nanoantennas and Films. *Small* **2017**, *13*, 1700044. [CrossRef]
7. Zhuo, X.; Yip, H.K.; Ruan, Q.; Zhang, T.; Zhu, X.; Wang, J.; Lin, H.Q.; Xu, J.B.; Yang, Z. Broadside nanoantennas made of single silver nanorods. *ACS Nano* **2018**, *12*, 1720–1731. [CrossRef]
8. Thomas, J.; Periakaruppan, P.; Thomas, V.; John, J.; Mathew, S.; Thomas, T.; Jose, J.; Rejeena, I.; Mujeeb, A. Morphology dependent nonlinear optical and photocatalytic activity of anisotropic plasmonic silver. *RSC Adv.* **2018**, *8*, 41288–41298. [CrossRef]
9. Al-Ani, S.A.; Elias, M.M.; Hamid, M.K. The effects of laser intensities on nonlinear properties for Ag nanoparticles colloid. *Iraqi J. Phys.* **2017**, *15*, 36–40.
10. Domenegueti, J.F.M.; Andrade, A.A.; Pilla, V.; Zilio, S.C. Simultaneous measurement of thermo-optic and thermal expansion coefficients with a single arm double interferometer. *Opt. Express* **2017**, *25*, 313–319. [CrossRef]
11. Mesgari, S.; Taylor, R.A.; Hjerrild, N.E.; Crisostomo, F.; Li, Q.; Scott, J. An investigation of thermal stability of carbon nanofluids for solar thermal applications. *Sol. Energy Mater. Sol. Cells* **2016**, *157*, 652–659. [CrossRef]
12. Omrani, A.N.; Esmaeilzadeh, E.; Jafari, M.; Behzadmehr, A. Effects of multi walled carbon nanotubes shape and size on thermal conductivity and viscosity of nanofluids. *Diam. Relat. Mater.* **2019**, *93*, 96–104. [CrossRef]
13. Li, Y.; Yang, L.; Yu, Q.; Yin, X.; Liu, X.; Huang, H.; Wang, H. Dispersion and stability of solvent-free multi-walled carbon nanotube nanofluids. *Part. Sci. Technol.* **2020**, *38*, 475–481. [CrossRef]
14. Karthikeyan, A.; Coulombe, S.; Kietzig, A.M. Wetting behavior of multi-walled carbon nanotube nanofluids. *Nanotechnology* **2017**, *28*, 105706. [CrossRef] [PubMed]
15. Hedayatnasab, Z.; Abnisa, F.; Daud, W.M. Review on magnetic nanoparticles for magnetic nanofluid hyperthermia application. *Mater. Des.* **2017**, *123*, 174–196. [CrossRef]
16. Rudyak, V.Y.; Minakov, A.V. Thermophysical properties of nanofluids. *Eur. Phys. J. E* **2018**, *41*, 15. [CrossRef] [PubMed]
17. Otanicar, T.; Hoyt, J.; Fahar, M.; Jiang, X.; Taylor, R.A. Experimental and numerical study on the optical properties and agglomeration of nanoparticle suspensions. *J. Nanopart. Res.* **2013**, *15*, 2039. [CrossRef]

18. Xu, S.; Wang, F.; Zhu, C.; Meng, Y.; Liu, Y.; Liu, W.; Tang, J.; Liu, K.; Hu, G.; Howe, R.C.T.; et al. Ultrafast nonlinear photoresponse of single-wall carbon nanotubes: A broadband degenerate investigation. *Nanoscale* **2016**, *8*, 9304–9309. [CrossRef]
19. Zhang, Y.X.; Wang, Y.H. Nonlinear optical properties of metal nanoparticles: A review. *RSC Adv.* **2017**, *7*, 45129–45144. [CrossRef]
20. Leal, N.N.; Brandão-Silva, A.C.; Fantini, C.; Hickmann, J.M.; Fonseca, E.J.; Alencar, M.A. Thermo-optical response of colloidal metallic and semiconducting single-walled carbon nanotubes. *Opt. Laser Technol.* **2019**, *116*, 315–321. [CrossRef]
21. Bhavitha, K.B.; Nair, A.K.; Perumbilavil, S.; Joseph, S.; Kala, M.S.; Saha, A.; Kalarikkal, N. Investigating solvent effects on aggregation behaviour, linear and nonlinear optical properties of silver nanoclusters. *Opt. Mater.* **2017**, *73*, 695–705. [CrossRef]
22. Hamedi, H.R.; Juzeliūnas, G. Phase-sensitive Kerr nonlinearity for closed-loop quantum systems. *Phys. Rev. A* **2015**, *91*, 053823. [CrossRef]
23. Hartmann, M.J. Quantum simulation with interacting photons. *J. Opt.* **2016**, *18*, 104005. [CrossRef]
24. Morales-Bonilla, S.; Martines-Arano, H.; Torres-Torres, D.; Ochoa-Ortega, G.; Carrillo-Delgado, C.; Trejo-Valdez, M.; Torres-Torres, C. Dynamic and plasmonic response exhibited by Au nanoparticles suspended in blood plasma and cerebrospinal fluids. *J. Mol. Liq.* **2019**, *281*, 1–8. [CrossRef]
25. Pinault, M.; Mayne-L'Hermite, M.; Reynaud, C.; Pichot, V.; Launois, P.; Ballutaud, D. Growth of multiwalled carbon nanotubes during the initial stages of aerosol-assisted CCVD. *Carbon* **2005**, *43*, 2968–2976. [CrossRef]
26. Torres-Torres, C.; Mercado-Zúñiga, C.; Martínez-González, C.L.; Martínez-Gutiérrez, H.; Rebollo, N.R.; Trejo-Valdez, M.; Vargas-García, J.R.; Torres-Martínez, R. Optical Kerr effect exhibited by carbon nanotubes and carbon/metal nanohybrid materials. *Phys. E* **2015**, *73*, 156–162. [CrossRef]
27. Mercado-Zúñiga, C.; Torres-Torres, C.; Trejo-Valdez, M.; Torres-Martinez, R.; Cervantes-Sodi, F.; Vargas-Garcia, J.R. Influence of silver decoration on the nonlinear optical absorption exhibited by multiwall carbon nanotubes. *J. Nanopart. Res.* **2014**, *16*, 2334. [CrossRef]
28. Morales-Bonilla, S.; Mercado-Zúñiga, C.; Campos-López, J.P.; Carrillo-Delgado, C.; Martínez-González, C.L.; Torres-Torres, C. Unidirectional Optical Kerr Transmittance in Hierarchical Carbon/Platinum Nanostructures. *Photonics* **2020**, *7*, 54. [CrossRef]
29. Boyd, R.W. *Nonlinear Optics*; Academic Press: Cambridge, MA, USA, 1992.
30. García-Merino, J.A.; Martínez-González, C.L.; Torres-SanMiguel, C.R.; Trejo-Valdez, M.; Martínez-Gutiérrez, H.; Torres-Torres, C. Photothermal, photoconductive and nonlinear optical effects induced by nanosecond pulse irradiation in multi-wall carbon nanotubes. *Mater. Sci. Eng. B* **2015**, *194*, 27–33. [CrossRef]
31. Ikeda, N.; Watanabe, S. *Stochastic Differential Equations and Diffusion Processes*; Elsevier: Amsterdam, The Netherlands, 2014.
32. Sivan, M.; Farago, O. Probability distribution of Brownian motion in periodic potentials. *Phys. Rev. E* **2018**, *98*, 052117. [CrossRef]
33. Miyabe, K.; Isogai, R. Estimation of molecular diffusivity in liquid phase systems by the Wilke–Chang equation. *J. Chromatogr. A* **2011**, *1218*, 6639–6645. [CrossRef]
34. Crespi, A.; Ramponi, R.; Osellame, R.; Sansoni, L.; Bongioanni, I.; Sciarrino, F.; Vallone, G.; Mataloni, P. Integrated photonic quantum gates for polarization qubits. *Nat. Commun.* **2011**, *2*, 566. [CrossRef] [PubMed]
35. Chu, H.; Li, Y.; Wang, C.; Zhang, H.; Li, D. Recent investigations on nonlinear absorption properties of carbon nanotubes. *Nanophotonics* **2020**, *9*, 761–781. [CrossRef]
36. De Aquino, B.R.H.; Neek-Amal, M.; Milošević, M.V. Unconventional two-dimensional vibrations of a decorated carbon nanotube under electric field: Linking actuation to advanced sensing ability. *Sci. Rep.* **2017**, *7*, 13481. [CrossRef]
37. Gezgin, S.Y.; Kepceoğlu, A.; Kılıç, H.Ş. An investigation of localised surface plasmon resonance (LSPR) of Ag nanoparticles produced by pulsed laser deposition (PLD) technique. *AIP Conf. Proc.* **2017**, *1815*, 030019.
38. Ibrahim, J.; Al Masri, M.; Veillas, C.; Celle, F.; Cioulachtjian, S.; Verrier, I.; Jourlin, Y. Condensation phenomenon detection through surface plasmon resonance. *Opt. Express* **2017**, *25*, 24189–24198. [CrossRef] [PubMed]
39. Ingalagondi, P.K.; Patil, O.; Sankarappa, T.; Hanagodimath, S.M. Spectroscopic studies of synthesized coumarins. *AIP Conf. Proc.* **2019**, *2100*, 020112.

40. Torres-Torres, C.; Reyes-Esqueda, J.A.; Cheang-Wong, J.C.; Crespo-Sosa, A.; Rodríguez-Fernández, L.; Oliver, A. Optical third order nonlinearity by nanosecond and picosecond pulses in Cu nanoparticles in ion-implanted silica. *J. Appl. Phys.* **2008**, *104*, 014306. [CrossRef]
41. Hamad, A.H. Effects of different laser pulse regimes (nanosecond, picosecond and femtosecond) on the ablation of materials for production of nanoparticles in liquid solution. In *High Energy and Short Pulse Lasers*; IntechOpen: Rijeka, Croatia, 2016; pp. 305–325.
42. Torres-Torres, C.; Peréa-López, N.; Reyes-Esqueda, J.A.; Rodríguez-Fernández, L.; Crespo-Sosa, A.; Cheang-Wong, J.C.; Oliver, A. Ablation and optical third order nonlinearities in Ag nanoparticles. *Int. J. Nanomed.* **2010**, *5*, 925–932. [CrossRef]
43. Zhang, L.; Lu, F.; Zhang, W.; Gao, K.; Xue, T.; Liu, M.; Mei, T. Plasmon-enhanced linear and second-order surface nonlinear optical response of silver nanoparticles fabricated using a femtosecond pulse. *Nanotechnology* **2019**, *31*, 035305. [CrossRef]
44. Maurya, S.K.; Rout, A.; Ganeev, R.A.; Guo, C. Effect of size on the saturable absorption and reverse saturable absorption in silver nanoparticle and ultrafast dynamics at 400 nm. *J. Nanomater.* **2019**, *2019*, 9686913. [CrossRef]
45. Manzoni, G.; Ponzoni, S.; Galimberti, G.; Scarselli, M.; Pulci, O.; Camilli, L.; Matthes, L.; Castrucci, P.; Pagliara, S. Ultrafast dynamics in unaligned MWCNTs decorated with metal nanoparticles. *Nanotechnology* **2016**, *27*, 235704. [CrossRef] [PubMed]
46. Yu, F.; Chen, Y.; Liang, X.; Xu, J.; Lee, C.; Liang, Q.; Tao, P.; Deng, T. Dispersion stability of thermal nanofluids. *Prog. Nat. Sci. Mater.* **2017**, *27*, 531–542. [CrossRef]
47. Li, D.; Fang, W.; Feng, Y.; Geng, Q.; Song, M. Stability properties of water-based gold and silver nanofluids stabilized by cationic gemini surfactants. *J. Taiwan Inst. Chem. Eng.* **2019**, *97*, 458–465. [CrossRef]
48. Chen, M.; He, Y.; Hu, Y.; Zhu, J. Local temperature control of hybrid plasmonic nano-antennas. *J. Quant. Spectrosc. Radiat. Transf.* **2019**, *225*, 50–57. [CrossRef]
49. Zurich, E.B. Gold, Copper, Silver and Aluminum Nanoantennas to Enhance Spontaneous Emission. *eps* **2009**, *40*, 20.
50. Cakmakyapan, S.; Lu, P.K.; Navabi, A.; Jarrahi, M. Ultrafast and broadband graphene photodetectors based on plasmonic nanoantennas. In Proceedings of the 2017 IEEE MTT-S, International Microwave Symposium, Honolulu, HI, USA, 4–9 June 2017; pp. 1861–1864.
51. Escoubas, L.; Carlberg, M.; Le Rouzo, J.; Pourcin, F.; Ackermann, J.; Margeat, O.; Berginc, G. Design and realization of light absorbers using plasmonic nanoparticles. *Prog. Quantum Electron.* **2019**, *63*, 1–22. [CrossRef]
52. Yang, Z.; Fu, Y.; Yang, J.; Hu, C.; Zhang, J. Spin-encoded subwavelength all-optical logic gates based on single-element optical slot nanoantennas. *Nanoscale* **2018**, *10*, 4523–4527. [CrossRef] [PubMed]

nanomaterials

MDPI

Review

Novel Nanofluidic Cells Based on Nanowires and Nanotubes for Advanced Chemical and Bio-Sensing Applications

Xin-Yi Zhu, Bo-Ran Wang, Yi Gu, Hao Zhu *, Lin Chen and Qing-Qing Sun

The State Key Laboratory of ASIC and System, School of Microelectronics, Fudan University, Shanghai 200433, China; 19112020059@fudan.edu.cn (X.-Y.Z.); 20112020032@fudan.edu.cn (B.-R.W.); 20112020008@fudan.edu.cn (Y.G.); linchen@fudan.edu.cn (L.C.); qqsun@fudan.edu.cn (Q.-Q.S.)
* Correspondence: hao_zhu@fudan.edu.cn; Tel.: +86-21-65647395

Abstract: Since the first introduction of one-dimensional nanochannels for single-molecule detection, there has been increasing interest in modern nanofluidic systems, such as chemical and biological sensing applications. Recently developed nanowires (NWs) and nanotubes (NTs) have received tremendous attention due to their unique geometrical, physical and chemical properties, which are very attractive in this field. Here, we review the recent research activities in the field of novel nanofluidic cells based on NWs and NTs. First, we give a brief introduction of this field. Then the common synthesis methods of NWs and NTs are summarized. After that, we discuss the working principle and sensing mechanism of nanofluidic devices, which is fundamental to the interaction between these nanostructures and small molecules. Finally, we present the NW- and NT-based devices for chemical and bio-sensing applications, such as gas sensing, pathogen detection, DNA sequencing, and so forth.

Keywords: nanowire; nanotube; nanofluidic cell; single molecule detection; chemical and bio-sensing

Citation: Zhu, X.-Y.; Wang, B.-R.; Gu, Y.; Zhu, H.; Chen, L.; Sun, Q.-Q. Novel Nanofluidic Cells Based on Nanowires and Nanotubes for Advanced Chemical and Bio-Sensing Applications. *Nanomaterials* **2021**, *11*, 90. https://doi.org/10.3390/nano11010090

Received: 4 December 2020
Accepted: 27 December 2020
Published: 3 January 2021

1. Introduction

Nanofluids are suspensions of basic liquids and nanoparticles, which provide a well transport environment for various ions, gases and bio-molecules. The development of nanofluidics has led to the preparation and optimization of many new engineering devices for biochemical sensor applications, such as gas sensing, protein and pathogen detection, DNA translocation and sequencing, etc. [1]. It was realized that the electronic devices should be further scaled down to the size of chemical molecules with enhanced performance to achieve biological applications. The emergence of various types of nanomaterial has enabled the preparation and application of nanochannels with adjustable structures and shapes [2,3]. In 1996, Kasianowicz et al. first reported the translocation of DNA through a α-hemolysin protein nanopore under an external electrical field [4]. Since then, other nanostructures have been extensively studied and provide a new platform for nanofluidic system. For example, the research on two-dimensional (2D) materials (graphene, MoS_2, BN, etc.) has greatly enriched and promoted the field of nanofluid ion transport [5]. Compared with nanopores or other nanofluidic channels, 2D nanofluidic channel systems with high flow rates are relatively easy and expandable to manufacture, which can be used for applications in bionic transmission and manipulation of ions, molecular screening, and energy conversion [6–8]. However, the currently reported research on the asymmetric ion transmission characteristics of the 2D nanofluidic homogeneous structure is still in its infancy, due to their problems of insufficient charge density and low rectification ratio [9].

Since carbon nanotubes (CNTs) were first synthesized, tremendous efforts have been made in the research field of one-dimensional (1D) materials, including the synthesis, properties, assembly and application [10]. So far, there has been significant research devoted to various solid nanowires and tubular forms, such as carbon, silicon, boron nitride, oxides (SiO_2, Al_2O_3, MoO_3, V_2O_5, TiO_2), chalcogenides (WS_2, MoS_2), and halides ($NiCl_2$).

Nanowires (NWs) and nanotubes (NTs) are seamless cylinders with high aspect ratios, and their structures and compositions lead to unique geometric, physical, and chemical properties. Taking advantage of their controllable diameters, high mechanical strength, high transmission efficiency, and easy planar integration, it has a potential to break through the limitations of traditional nanofluidic applications based on vertical nanoporous films and 2D nanomaterials [11]. From the basic physics research point of view, NTs and NWs provide an interesting system to test classical theory of nanofluid flow. On the other hand, they can be readily integrated into novel nanofluidic devices, which are further explored in single-molecule technique and future bio-chemical sensing applications. NW/NT-based nanofluidic cells sensitively record the nanoparticles and can effectively overcome existing challenges in conventional biological and chemical electronics. For example, a recognition probe fixed to the surface of the nanostructure selectively interacts with target analytes in solution, responding an electrical signal that reflects the concentration. In addition, ions or small molecules with charges can cause physical blockages of nanoscale channels during transport, which results in the measurable and identifiable electrical properties changes.

The core components of these nanofluidic devices are the quasi-1D nanostructures. First, NWs and NTs have the advantages of small geometrical size and high surface-to-volume ratio. This makes it possible to generate obvious electrical signals at ultralow concentrations, allowing the reduction of sample size and the miniaturization of sensors. Secondly, high quality NWs and NTs with uniform inner diameters, robustness, and non-porous smooth surfaces are attractive in the fields of nanoelectronics, optoelectronics, and biochemical sensing. Moreover, the well-defined internal and external surface as well as the sites at the ends can be easily modified, which is useful for ion and molecular detection, capture and manipulation.

This review is organized to emphasize the recent advances in novel nanofluidic cells based on NWs and NTs for advanced chemical and bio-sensing applications, updating the reports of previous works. We will briefly go through the synthesis methods of NWs and NTs in Section 2 and discuss the principles and sensing mechanisms of NW/NT-based nanofluidic devices in Section 3. Several representative advances in nanostructure-based nanofluidic biochemical sensors will be reviewed in Section 4. Based on the fact that there have been some excellent reviews for the research on NWs/NTs-based sensors [12–14], we also discussed about novel preparation methods, functional modifications, monitoring mechanisms, and correction schemes, which is of great significance to improve the sensing performance and overcome the limitations of biochemical sensors based on NWs/NTs nanofluidic cells. It should be noted that we will focus on the basic and latest progress in materials preparation, device mechanisms and applications, instead of covering all the work performed in this field.

2. Synthesis Approaches

There are two routes in realizing one-dimensional nanomaterials: top-down and bottom-up approaches. Bottom-up is a commonly used approach to synthesize the target structure at atomic or molecular level which makes it feasible to build new conceptual devices and functional systems. The early synthesis approaches of NWs and NTs are mainly achieved by vapor phase growth. In typical bottom-up processes, two basic steps of nucleation and growth are involved to form a solid crystal from a gas, liquid or solid phase. When the concentration of the growth unit is sufficiently high up to saturation, it will aggregate into small crystal nuclei through homogeneous nucleation and continue to grow into larger structures. The robust NWs/NTs and rationally designed nanofluidic cells have advantages in potential nanoelectronics, optoelectronics, and bio-chemical sensing applications. On the other hand, when developing a synthetic method of nanomaterials, attention should be paid to control the morphology, size, composition and uniformity of the products. This section reviews the synthesis approaches of NWs and NTs that have been commonly used and developed in recent years, such as vapor-liquid-solid (VLS) growth, membrane-templet synthesis and nanowire template approach.

2.1. Vapor-Liquid-Solid (VLS) Growth

Nanoparticle-catalyzed VLS growth is a widely used method for preparing NWs and NTs by gas phase reaction because of its simplicity and versatility. It was first proposed by Wagner in 1964 through the growth of microscopic Si whiskers [15]. Later, the research teams from Harvard University and Hong Kong University proposed the true nanoscale Si NWs [16]. Various single crystal forms of inorganic nanowires have been reasonably synthesized by VLS method with diameters on the order of nanometers [17,18]. The growth mechanism is shown in Figure 1a [15]. Generally, small droplets of metal catalyst (e.g., Au nanoparticles) are assembled or patterned on the solid substrate. Then, the carrier gas stream containing precursors is dissolved at elevated temperature to form alloy droplets. Once the reactants reach supersaturation, they will precipitate and form a solid-liquid interface, which will promote the anisotropic growth of crystals. Thereby the material preferentially grows in one direction and obtain one-dimensional nanostructure. Following the initial VLS mechanism studies, it has been extended to chemical vapor deposition (CVD) method [19–21], which can control the reactant sources, growth temperature and so on well during the synthesis process.

As for diameter of 1D nanostructures, it is typically proportional to the size of the catalyst since the alloy droplet used as a soft template is always at the tip. In addition, the average diameter of NWs depends on the growth temperature, growth time, gold layer thickness, flow rate, and so forth [22,23]. Terasako et al. have reported successful suppression over the enhancement of the average diameter as the growth temperature increases utilizing the alternate source supply technique [24]. Similarly, tapering of VLS grown NWs is a common phenomenon resulting from dynamics of the liquid droplet during growth and direct vs. growth on the sidewall (Figure 1b) [25]. Küpers et al. developed a novel two-step approach to realize an untapered morphology with high vertical yield [26]. NW diameters at the top and bottom gradually approach the same with the increasing of V/III flux ratios during the second growth step. The flux dependence of radial vs. growth was theoretically studied and the diffusion on the NW sidewalls was combined into the model to understand the tapering phenomenon. Dejarld et al. also studied the doping effect on the diameter of GaAs NW [27]. Be-doping was found to significantly reduce the diameter and increase the aspect ratio to 50:1, which greatly improves the performance of the optoelectronic devices.

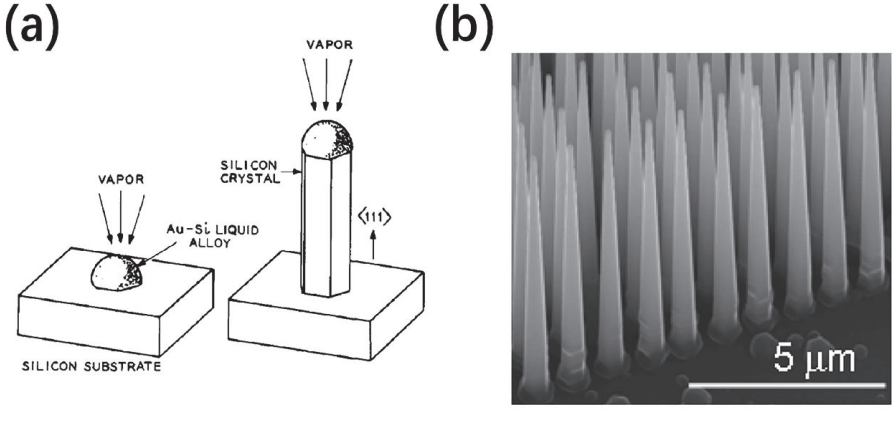

Figure 1. (**a**) Schematic illustration of the vapor-liquid-solid (VLS) growth method. Silicon crystal grows with liquid alloy at the tip [15]; (**b**) scanning electron microscope (SEM) image of SiNWs (nanowires) with significant tapering [25].

VLS growth allows NWs/NTs to be selectively grown at ordered positions of the substrate patterned by the catalyst, which reduces the introduction of impurities and pollution in the subsequent dispersion and arrangement [28–31]. Moreover, growth orientations

control is also highly desirable. It was found that the preferred growth direction is the one that minimizes the total free energy and can be influenced by diameters [32]. Recently, Wang et al. first demonstrated the surface-parallel growth of SiO_2 NWs by controlling mass transport [33]. The directional growth of SiO_2 NWs towards low SiO concentration was obtained at the position with high SiO concentration gradient. The incorporation of metallic catalyst in the synthetic NWs/NTs is another inevitable issue to be addressed which can introduce unwanted doping or impurities in the nanostructures. Floating catalysts (Mg–Fe–O species) and remote catalyzation methods have the potential to produce high purity BN NTs without post-treatment [34]. Finally, additional treatments are required to modify the electrical properties before assembly into suitable device structures and applications, which will be covered in the following sections.

2.2. Membrane-Template Synthesis

Membrane-template synthesis is a simple, low-cost approach for the preparation and assembly of 1D nanomaterials, which refers to copying the specific structure of a template into the product. A porous membrane is one of the basic hard templates, such as anodic aluminum oxide (AAO) membrane, track-etched polycarbonate (PC) membrane, and mesoporous silica. Among them, AAO membranes with higher porosity are usually used to prepare highly periodic arrays [35,36]. PC membranes are commonly available in a variety of pore sizes and larger dimensions, which is more suitable for biosensing applications [37]. In this method, the growth of nanomaterials was guided through nanopores of the membranes, using vapor deposition, electrodeposition, electrochemical deposition and other filling processes to synthesize desired materials. After that, the template can decompose and dissolve through the solvent or annealing.

Membrane-template synthesis has the characteristics of high periodicity, chemical stability and versatility. By controlling the diameter, spacing, and direction of the pores, a uniform, dense, and nearly parallel 1D nanomaterial matrix can easily be obtained (Figure 2a) [38–40]. The solid or hollow cylinders depend on the hole wall chemistry, deposition time and deposition method. Moreover, Three-dimensional NWs or NTs networks with precise spatial distribution, diameter and wall thickness have been prepared (Figure 2b) [41,42]. The improved method has been developed to synthesis AL-, Zn- doped TiO_2 nanotubes with uniform continuous composition control using PC membrane and atomic layer deposition (ALD) (Figure 2c) [43]. Another reproducible method is using alumina nano-trenches with single-wall NTs (SWNTs) as templates. CNTs were removed by O_2 reactive ion etching (RIE) following the area-selective ALD of alumina coating, which obtained predefined alumina membrane with nano-trenches that used as a mask to obtain sub-5 nm ZnO nanowires [44].

Despite the above characteristics, the membrane-template approach also has some intrinsic limitations. It becomes difficult to manipulate without order after being released from the membrane. There are two methods for producing ordered arrays onto the target substrate. The first is to prepare the template directly on the substrate, but the film thickness may be limited [45,46]. The other method involves the transfer method, which is complicated to operate and the membrane is fragile. An improved transfer method that allows the integration of dense NW arrays on almost any flat and curved substrate has been demonstrated [47]. A two-layer polymer (S1818 and PMMA A11) was used to prevent damage to the AAO membrane and the residue of organic contamination in pores. Secondly, the custom-designed nanopores membranes are very expensive or commercially unavailable. He et al. produced the membranes with desired nanopore size by oxygen plasma etching for the application of cell penetration and DNA infection (Figure 2d) [40]. The composite fiber melt-codrawing and bundling method was developed to prepared a well-controlled porous PMMA membrane with controlled structure size [39]. Unfortunately, the membrane-template approach relies on wet chemical reactions at low temperatures, resulting in a lack of layered crystal structures, poor morphology and porous walls.

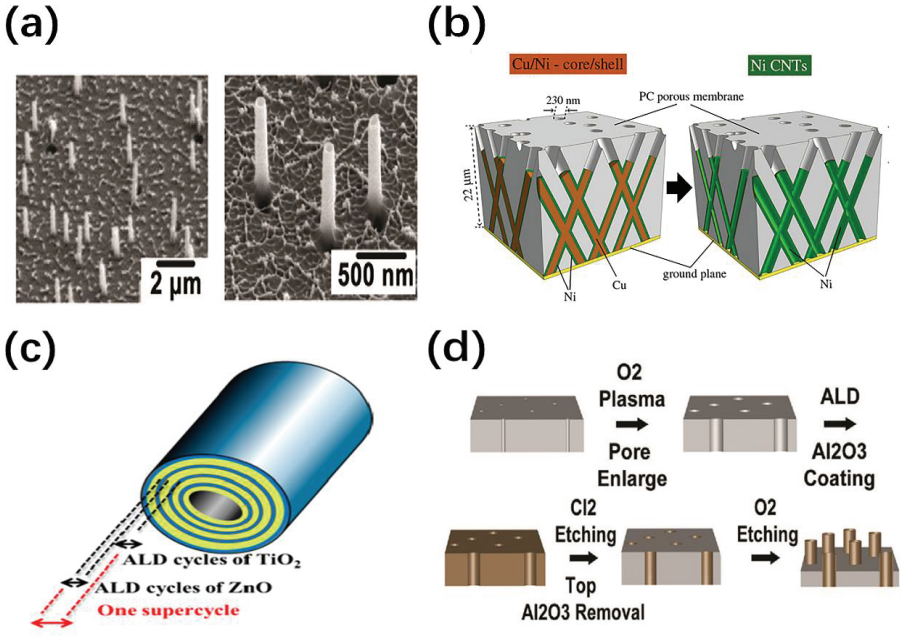

Figure 2. (**a**) SEM image of nanowires array [40]; (**b**) schematic illustration of 3-D Cu/Ni core/shell and Ni carbon nanotubes (CNTs) [41]; (**c**) schematic diagram of highly homogeneous Al- and Zn-doped TiO_2 nanotube by ALD with various cyclic sequences [43]; (**d**) schematic illustration of fabrication of nanostraws array using a track-etched polycarbonate membrane [40].

2.3. Nanowire Template Approach

A promising approach that uses nanowires as epitaxial growth substrates or sacrificial templates has been developed in recent years. In this approach, nanowires are converted into core-sheath structures through deposition or chemical methods and etch the cores subsequently [48]. There are various nanowires with different composition and size that can be used as stable templates. In addition, advanced conformal coating technologies such as CVD, ALD and sputtering allow epitaxial growth of various high-quality materials. The internal core can be selectively removed based on different chemical reactivities.

The NTs prepared by nanowire template approach have the smooth surface and lower porosity. The diameters can be tuned from 1 to 100 nm and the inner walls can easily covalently attach the desired receptors, which is attractive in biochemical sensing applications. Some deposition methods for the shell formation were developed to obtain a robust and clean crystal surface, which does not require a large volume of water or solvent, nor large energy and time. For example, high-quality few-layer molybdenum sulfide (MoS_2) nanotubes with good morphology control were synthesized by combining the nanowire template with the CVD process [49]. As shown in Figure 3a, SiO_2 NWs prepared and dispersed on silicon substrates are used as templates for depositing a thin film of MoS_2. The cores are stable in CVD process and are etched away in HF acid solution. Moreover, the sheathes maintain complete tubular structures and the number of MoS_2 layers can be reduced to four by shortening the growth time. Similarly, Zhang et al. prepared CdS nanotubes with tunable wall dimensions and optical microcavities through a simple thermal evaporation co-deposition technique using Sn nanowire templates [50].

On the other hand, the shell can be produced by chemical reactions [51]. Zhu et al. have developed a novel optimized process that can precisely control the inner diameter without involving dispersion, transfer and alignment steps, leading to robust, smooth

and clean nanotubes [52]. As shown in the Figure 3b, Self-assembled SiO_2 nanotubes are prepared from Si nanowires on a silicon-on-insulator (SOI) substrate through several oxidation and etching processes. The channel between the NTs and SOI substrates was open by dry etching, which is beneficial to the preparation of nanofluidic devices and biomedical applications. Furthermore, a single-phase tube with an accurate stoichiometric ratio is readily obtained. The chemical conversion of the template by gas- or vapor-phase avoids problems of the solid-phase reaction due to the reaction self-termination once the sacrificial template is exhausted. As an example, Sutter et al. converted sphalerite GaAs nanowires into single crystal cubic γ-Ga_2S_3 nanotubes by reacting with sulfur vapor [53]. The schematic reaction sequence is shown in Figure 3c, which involves the rapid diffusion of Ga ions through the growing sulfide shell. Ga_2S_3 is thicken and separated from the contracted GaAs core until the entire core is consumed.

In recent years, the nanowire template approach has been developed to the fabrication of various devices with specific functions. For example, the ultra-fine Pt nanotubes with 1 nm wall thickness and several microns length has been synthesized, which enhances the oxygen reduction reaction performance [54]. Insulin fibers have been introduced as a biological template, which allows the diameter of Pd NWs be reduced from 9 nm to less than 5 nm. The full decomposition of the fibers provided the necessary smooth surface for Pt deposition. In addition, highly active FeN_x modified CNTs are synthesized using ZnO nanowire templates [55]. As shown in Figure 3d, ZnO nanowires undergo in situ polymerization of dopamine under $FeCl_3$ environment and then pyrolyze in NH_3. The evaporation of Zn created sufficient pores on the CNTs and lead to high aspect area, which can be useful for the applications of sensors, catalysis, fuel cells, and so on.

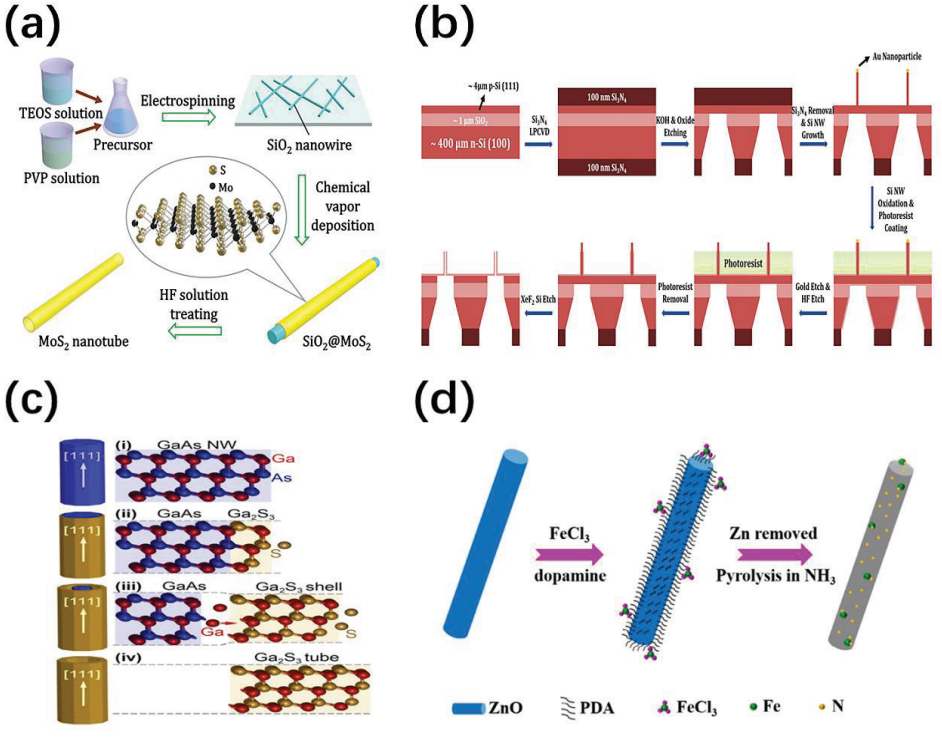

Figure 3. (**a**) Schematic illustration of MoS_2 nanotube synthesis [49]; (**b**) schematic illustration of preparation of SiO_2 nanotubes from Si nanowires on a SOI substrate [52]; (**c**) reaction schematic of the conversion of GaAs nanowires into single-crystalline γ-Ga_2S_3 nanotubes [53]; (**d**) schematic illustration of the fabrication of FeN_x modified CNT using ZnO nanowire template [55].

3. Device Mechanisms

The use of NTs and NWs provides a new platform for nanofluidic devices. Compared with planar semiconductor sensors, surface bonding with biochemical molecules affects the accumulation and depletion of carriers in the entire nanostructure, instead of just a small portion of it. This greatly improves the sensitivity and even realizes the possibility of detecting individual molecules, which is very attractive in chemical and bio-sensing. This chapter will give a brief overview focusing on the working mechanism and sensing principle of nanofluidic devices based on NWs and NTs.

3.1. Working Principle of Nanofluidic Cells Based on Nanowires/Nanotubes (NWs/NTs)

The ion-sensitive field-effect transistor (ISFET) is one of the most promising devices in nanofluidic system for biochemical sensing application. The channel composed of NW and NT has a large specific surface area and high sensitivity, and can perform charge sensing and label-free detection of species in nanofluids [56,57]. We first describe the working mechanisms of NW/NT-based ISFETs to better understand the principle of biochemical sensing. As illustrated in Figure 4a, the basic structure of NW-based ISFET is similar to metal-oxide-semiconductor field-effect transistor (MOSFET) except the metal gate which is replaced by a liquid-sensing region [57]. The liquid gate voltage is applied to the electrolyte via the reference electrode, which influences the change of carriers and the conductance of devices [58]. In addition, the specific or non-specific binding of charged molecules can also generate the electric field making it equivalent to the role of a gate. As the diameter of the NWs decreases, the surface interactions cause more significant electrochemistry changes in the NWs. After the functionalization of NWs, it is possible to detect the pH value (H^+ or OH^- ions) or selectively respond to the biochemical species (DNA, protein, gas, etc.) in nanofluid system [59]. On the other hand, nanotubes can not only provide the same function of sensing, but also serve as nanochannels to allow samples to flow through the interior. Due to the unique geometrical and electrical properties of NTs, it is extremely interesting to study the liquid and ion transport, as well as electrochemical detection of small molecules in nanofluids [60]. Hibst et al. integrated Si NTs into nanofluidic transistors in order to measure the ion diffusion of NaCl solution through NT, indicating that the fluid transmission in the nanoscale system can be simply considered by adjusting the diffusion coefficient [61]. As shown in Figure 4b, the NT-based ISFET consists of S/D electrical contact, fluidic supply and passivation layer covering (PDMS), in which the both ends of the Si NT are opened to connect two reservoirs.

However, the transport of water, ions and molecules through nanochannels is uniquely affected by special physical phenomena, including effects like electric double layer (EDL) and ion current rectification (ICR) [62]. ICR means that the ion current in one direction is greater than the other direction, and is determined by many factors, such as ion concentration, pH, surface charge density, curvature of channels, field effect modulation, etc. [63]. This asymmetric ion current is found in nanochannels and used to manufacture novel nanofluidic devices [64]. The control of ion transport rectification is usually achieved by functionalizing charged groups on the terminal or surface [65]. Compared with membrane-based nanopores, NTs with a better charge modification effect are more favorable nanochannels to increase the current rectification ratio. Take ion diode as an example, and the device structure and working mechanism are shown in Figure 4c,d [11]. Horizontally aligned nanotubes are employed as ion nanochannels, connecting two microchannels filled with nanofluidic. The mobile ions in the solution are driven by the voltage applied to both ends. ICR effect in the ion diode is caused by the accumulation or depletion of ion carriers. The oppositely charged polyelectrolytes are immobilized at the two terminals via strong physical absorption. The mobile cation and anion under the forward bias accumulate in the nanochannel by the electrostatic repulsion of both ends. In contrast, when a reverse bias is applied, the mobile ions are exhausted due to being attracted by the terminals. The increase and decrease of the overall conductance results in

the on and off states of the ion diode. It should be noted that the charge carriers here are the ions in nanofluidic, rather than electrons or holes.

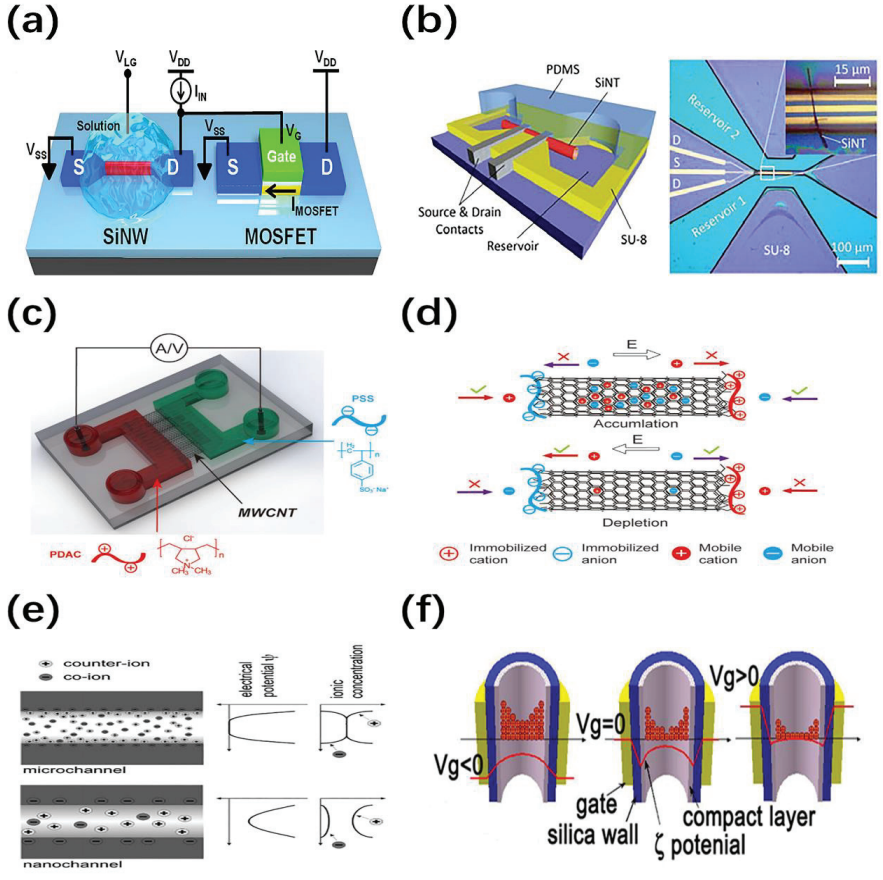

Figure 4. (**a**) Schematic illustration of a SiNW-based ion-sensitive field-effect transistor (ISFET) and a metal-oxide-semiconductor field-effect transistor (MOSFET) [57]; (**b**) schematic illustration of the SiNT-based ISFET device [61]; Schematic illustration of (**c**) the device structure and (**d**) working principle of a multi-walled carbon nanotubes (MWCNT) ionic diode filled with polyelectrolyte solutions (poly(diallyldimethylammonium chloride) (PSS) and poly(sodium 4-styrene-sulfonate) (PDAC)) [11]; (**e**) Schematic illustration of the ion environments and electric potential in microchannel and nanochannel [66]; (**f**) Schematic diagram of field-effect modulation of ion conductance in NT-based FETs [67].

In particular, a unipolar ion environment could appear in nanotubes [48]. The general mechanism is shown in Figure 4e, where the surface of the nanotube is modified by charged groups, and the charged ions in the fluidic are attracted or repelled by the surface charges [66]. In the microchannel, EDL is much smaller than the diameter and the electrostatic potential decays from the surface potential to zero. However, the size of one dimension in the nanochannel is smaller than the Debye length, which enhances the concentrated distribution of counter ions and non-zero central potential. Therefore, electrostatic control of ions or molecules can be achieved in the entire nanotube. Similar to MOSFETs, nanofluidic FETs based on nanotubes exhibit unipolar ion transport. The gate voltage is employed to control the ion concentration by adjusting the surface potential or charge. In addition, the channel doping level can be determined by the intrinsic surface charge. Fan et al. implemented NT-based FETs for the first time, which exhibited fast

field-effect modulation of ion conductance [67]. Figure 4f shows the schematic diagram, in which the surface of SiO_2 is usually negatively charged due to the presence of hydroxyl and SiO^-, thus the cations (k^+) in nanofluidic serve as the majority carriers. The positive and negative gate voltages cause the depletion and accumulation of the cations, respectively, leading to the *p*-type behavior.

The implementation of devices based on NWs and NTs suggests the feasibility of using electric field to control the transport of charged species in nanofluidic systems. Subsequent work can focus on the fabrication of nanosensors through the surface functionalization with probe molecules, which can specifically recognize chemical or biological molecular targets.

3.2. Sensing Mechanism of Biochemical Sensors Based on NW/NT Nanofluidic Cells

With the development of micro-nano technology, sensors have made great progress in terms of size, cost, sensitivity and speed by using novel nanomaterials and new mechanisms. Nanowires, nanotubes and other microarrays are served as sensor elements to fix target molecules on the surface or manipulate their transmission, which has been widely used in nanofluidic platforms. Due to the small diameter and large aspect ratio, nanofluidic transistors based on NWs or NTs can even achieve molecular sensing at extremely low concentrations with various detection mechanisms. Generally, the sensor response depends on changes in mechanical and electrical signals, as well as the charge of nanostructures and biomolecules caused by the surface adsorption, reaction or transport of target molecules. There are several basic principles involved during the sensing processes. For example, the electric field can be changed by the surface polarization effect during the molecular adsorption, and the reaction products produced by the enzyme and the substrate also influence it.

Electrical detection methods are usually used to reflect the concentration or translocation of chemical/biological molecules by monitoring the change of ion current in the nanochannel [68]. Nanopores have been used in single-molecule sensing for decades based on resistive pulse sensing mechanism. As shown in Figure 5a, when the particles pass through nanopores with comparable diameters, the ion current decreases transiently due to the blocking effect, which shows a broad prospect of rapid genome sequencing [69]. However, nanotubes with longer nanochannels and higher aspect ratios lead to a large number of blockade events and the interaction is more complicated, which also allows more obvious transient signals on the time scale. Fan et al. proposed an interaction model of charge effect and geometric effect to qualitatively explain the translocation of DNA molecules through nanotubes under different ion concentrations [70]. As shown in Figure 5b,c, charged molecules attract counter ions while repelling a portion of the volume of conductive ions. When the electrolyte concentration is lower than the critical concentration, the charge effect is stronger and will introduce more ion carriers. On the contrary, the volume effect is dominant and the ion conductance decreases. The ionic current encodes more biomolecule information such as charge, geometric characteristics and the evolution of DNA strand conformation through pulse duration, pulse amplitude and current attenuation characteristics, etc.

On the other hand, the nanostructure/electrolyte interface can be very sensitive to almost any specific surface reactions due to its large specific surface area which can provide more active centers. An individual molecule may induce significant changes in electronic properties in the following possible ways: (1) electrostatic gate control; (2) charge transfer; (3) charge scattering potential; (4) Schottky contact modulation [71,72]. For example, in oxygen gas sensing, the coverage of oxygen extracts electrons from the channel to form negatively charged oxygen ions (O^{2-}, O^- and $O_2{}^-$), which results in a change in the width of the charge depletion layer. The presence of reducing gases and oxidizing gases determines the desorption and adsorption of oxygen, respectively. Therefore, the changes in resistance and conductivity of a NW can be manifested [73–76]. The sensing mechanism of the acetone sensor is demonstrated in Figure 5d [77]. Acetone or ethanol react with surface

oxygen species and release electrons back into the conduction band of the nanostructure based on the following equations:

$$O_2(g) \rightarrow O_2(ads), \quad (1)$$

$$O_2(ads) + e^- \rightarrow O_2{}^-(ads), \quad (2)$$

$$O_2{}^- (ads) + e^- \rightarrow 2O^- (ads), \quad (3)$$

$$C_3H_6O(g) + 8O^- (ads) \rightarrow 3CO_2 + 3H_2O + 8e^-, \quad (4)$$

$$C_2H_5O + 6O^- (ads) \rightarrow 2CO_2 + 3H_2O(g) + 6e^-, \quad (5)$$

as a biosensor, the key point is the functionalization through the attachment of identification elements, which can be coupled with target analytes. The specific trapping of charged molecules is similar to the effect of applying a gate voltage, resulting in the accumulation and depletion of carriers. This was first applied in PH sensing that the conductance increased linearly with the pH value based on the mechanism of surface charge changes in the protonation and deprotonation procedures [78]. Biomolecules such as DNA, proteins, viruses, drugs, and neuronal signals have also been detected. Amorim reported that the cyclodextrin from biological enzyme products with hydroxyl groups tends to bind to the surface of SnO_2 nanowires, changing its electrical conductivity [79]. The nanowire biosensor exhibits different current responses under various cyclodextrin concentrations.

It is worth mentioning that various factors will affect the surface properties of nanostructures. As a result, complex working mechanisms require precise models and schemes for calibration. The research on Stern and diffusion is of great importance to improve the accuracy of target molecule detection. A method of experimentally extracting the Stern layer capacitance (C_{stern}) of Si NWs ISFET has been proposed which improves the development of ISFET-based biosensors [80]. So far, the commonly used detection mechanism is based on the drift of threshold voltage (V_{TH}) or the change of NWs conductance when binding target biomolecules. However, there is a limitation of potential sensing by the Debye screening of counter ions in the test solution. Schwartz et al. developed a novel impedance sensing approach for Si NWs ISFET devices for DNA detection [59]. This approach based on the transistor transfer function (TTF) has potential to achieve effective biosensing in physiological buffers. As shown in Figure 5e, the black and red curves show the TTFs of the original device and the device after the biomolecule combination, respectively, in which the estimated concentration of biomolecules can be calculated from the difference in cutoff frequencies. The inset of Figure 5e is a simplified input impedance model composed of a biomolecular layer and an oxide layer. The molecules are immobilized on the surface of the nanowire, which changes the input impedance and frequency dependence of the device. In Figure 5f, the single-stranded DNA layer on the surface of the Si NW has introduced certain surface charges. After DNA hybridization, the thickness of the biomolecule layer and the amount of DNA charge as well as the ion diffusion barrier have all changed, resulting in different input impedances (R_{BIO} and C_{BIO}).

On the other hand, NWs/NTs with enzyme-like activity is also a new type of nanozyme materials, which plays an important role in electrochemical biosensors for environmental and health monitoring [81]. Since the discovery of the peroxidase-like activity of Fe_3O_4 NPs, many research groups have devoted to the study of nanozymes [82]. NWs/NTs-based nanozyme immunoassay mainly performs three functions: target capture, magnetic separation, and color determination. In general, nanozymes catalyze the oxidation of a variety of chromogenic substrates in the presence of H_2O_2 to produce color reactions. This concept has been proven to detect H_2O_2 and other biomolecules such as glucose and lactic acid.

From the above analysis and reported work, the nanofluidic devices based on NTs and NWs are promising for the detection and sensing of chemical and biological species due to its real-time, label-free and ultra-high sensitivity advantages.

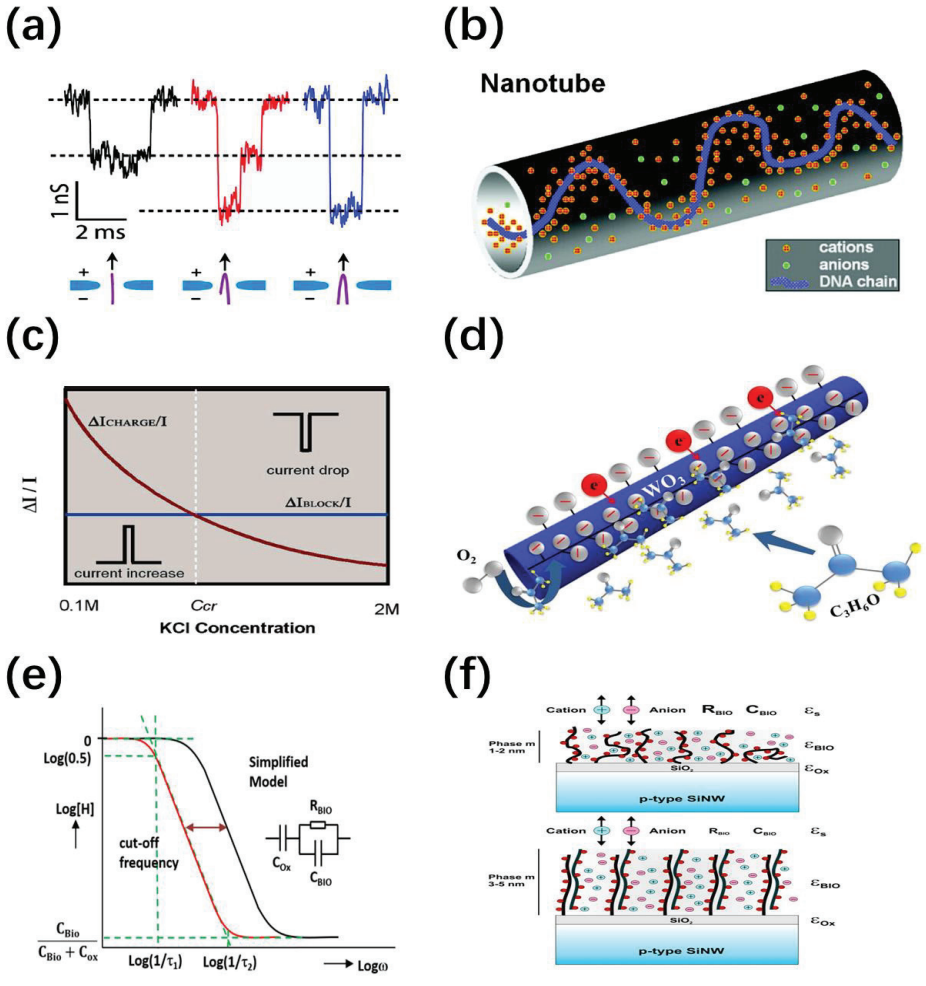

Figure 5. (**a**) Ion current response to the translocation of non-folded (black), partially folded (red), and fully folded (blue) DNA through a graphene nanopore [69]; (**b**) schematic illustration of the ionic distribution of counterions and co-ions in a nanotube with a DNA strand [70]; (**c**) schematic illustration of the current responses under different ion concentrations due to charge effect and blockade effect [70]; (**d**) schematic illustration of h-WO_3 nanotubes detecting acetone gas [77]; (**e**) the transistor transfer function (TTF) spectrums of the original (**left**) and after biomolecule combined (**right**) devices. The inset shows the simplified model of the input impedance of the device, which can be described as an Resistor-Capacitance element (R_{Bio} and C_{Bio}) of biomolecule layer in series with the gate oxide capacitance C_{Ox} [59]; (**f**) Schematic illustration of the attachment layers of single-stranded and double-stranded DNA molecules on the SiNW. The single-stranded DNA layer leads to a thin interface layer, where the negative charge introduces a certain surface charge density and forms an additional potential for ion diffusion. The charge composition of double-stranded DNA changes, resulting in a thicker layer, which allows ions more effectively diffuse to the oxide surface. The thickness of DNA layer, the diffusion of ions, the amount of DNA charges, and eventual changes in the dielectric constant ε_{BIO} will influence the biomolecule layer impedance, which allows for the expectation of the R_{Bio} and C_{Bio} values [59].

4. Device Applications for Chemical and Bio-Sensing

4.1. Chemical Sensing

4.1.1. Ion Sensing

Nanotubes have been proven both theoretically and experimentally to be effective nanofluidic channels, which can work at the molecular level for PH and ion sensing. A gold nanoparticle-modified SiNWs array-based sensor for highly sensitive and selectivity detection of mercury ion has been reported (Figure 6a,b), which plays a potential role in monitoring the quality of water [83]. Cao et al. have demonstrated the electrical response of single-walled carbon (SWCNT) to the concentration, pH and ion type of the ionic solution when exposed to electrolyte [84]. The presence of K^+ cations at low concentration inhibits the interaction of water with the inner surface of the CNT, thereby improving the gate control efficiency; while the higher ion concentration has a shielding effect on the gate voltage. In addition, the dependence of SWCNT with open ends on pH is opposite to that of unopened NTs or NWs, indicating their different pH sensing mechanisms.

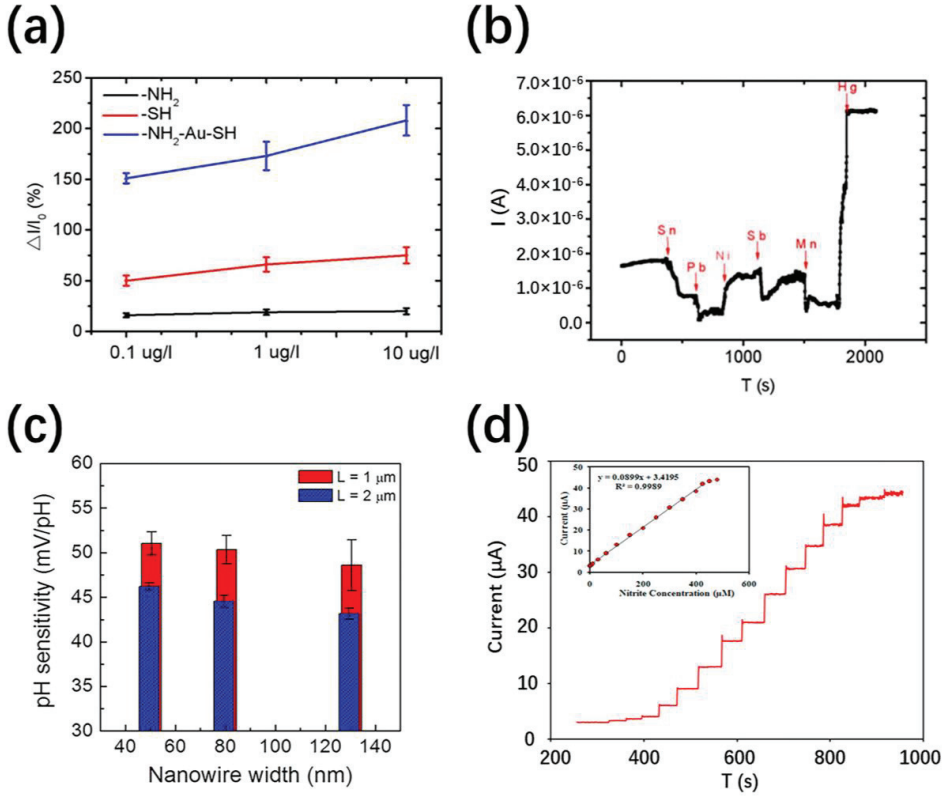

Figure 6. (**a**) $\triangle I/I_0$ as a function of mercury ion concentration for different modified SiNW devices [83]; (**b**) real-time current response to various metal ions of 10 $\mu g/L^{-1}$ [83]; (**c**) the pH sensitivity of nanowires with different widths and gate lengths (L) of Effects of 1 and 2 μm [85]; (**d**) the current response of the Ag/halloysite nanotube (HNT)/MoS_2-carbon paste electrode (CPE) to the nitrite with various concentrations. The inset shows the calibration curve of current versus nitrite concentration from 2 to 425 μM [86].

The widths and lengths of Si NWs also have an influence on pH sensing [58,85]. As shown in Figure 6c, the NWs with smaller width and longer length exhibit higher pH sensitivities. This can be understood by the overlap of the electric field concentration area in

the narrow channels and the small ratio between the source and drain electrode resistance and the total resistance in the long channels. More recently, Ghanei-Motlagh et al. demonstrated a new type of electrochemical sensor based on silver/halloysite nanotube/MoS_2 nanocomposite [86]. This shows a relatively fast response time, low detection limit and good anti-interference performance for nitrite sensing at low concentration levels. A linear amperometry response to the concentration of nitrite from 2 to 425 μM is presented in Figure 6d. Nanostructured materials and their composite materials are considered promising candidates in the field of electrochemical sensing.

4.1.2. Gas Sensing

Sensing and monitoring of various toxic gases such as H_2S, CO, NO_2, acetone, ethanol, etc. have become increasingly important in human life. NTs or NWs as sensing elements have great potential in high-precision gas sensing with high sensitivity, fast response, and good selectivity. As illustrated in Table 1, WO_3 nanostructures have proved to be efficient materials for ethanol detection [87]. Different structural morphologies such as WO_{3-x} nanowires, h-WO_3 nanowires, h-WO_3 nanorods and h-WO_3 nanotubes have also been prepared and tested [77]. As shown in Figure 7a,b, a relatively high sensitivity to acetone and ethanol have been observed in h-WO_3 nanotubes (Ra/Rg = 32 and 26, respectively). This is due to the inherent local crystal defects and oxygen vacancies of obtained ultrathin-walled NTs are conducive to the adsorption of oxygen molecules and target gases, hence improving the sensing performance. Actually, it is difficult for gas molecules to penetrate into the interior of NTs due to the large aspect ratio. Therefore, porous nanotubes are proposed to break through the limitation of NTs in gas sensing. Compared with general SnO_2 nanotubes, mesoporous SnO_2 nanotubes exhibit an enhanced response sensitivity for methanol with fast response and recovery times of 3 s and 6 s, respectively [88]. In the same year, Choi et al. prepared various nanostructures (nonporous ZnO NTs, porous ZnO NTs, and porous ZnO film) by adjusting the sputtering power through polyvinyl acetate (PVA) nanowire template approach for hydrogen sensing [89]. Compared with the other two structures, the response of porous ZnO NTs to hydrogen sensing has been significantly enhanced. This is because both the inner and outer surfaces form a depletion layer and effectively sense gases simultaneously.

Table 1. WO_3 sensors for ethanol detection reported in literature [86].

Materials	Concentration(ppm)	Response
WO_3	300	16.9
WO_3 nanoplates	400	~12
WO_3 hollow spheres	500	6.14
WO_3 nanotube bundles	400	~38

Noble metals and metal oxides have been demonstrated to modified the NWs or NTs to further improve the sensing performance. Pd-loaded In_2O_3 NW-like networks with excellent NO_2 gas sensitivity was synthesized by Huang et al. using CNTs templates [90]. As shown in Figure 7c,d, Pd–In_2O_3 NW-like network sensors have significantly higher response (Ra/Rg = 27), shorter response and recovery times (9 s and 28 s, respectively) to 5 ppm NO_2 at 110 °C. A synergy of electric and chemical effects is proposed to explain the influence of Pd loading. Choi et al. have experimentally coated Fe_2O_3 nanoparticles on the surface of SnO_2 nanowires for ethanol sensing, which leads to the 1.48–7.54 times enhanced sensitivities of at 300 °C [91]. The conductivity of NWs mainly depends on the barrier height, which is increased with the number of grain boundaries. This multi-network structure and heterogeneous structure have introduced many crystal grains and grain boundaries, which contribute to achieve better sensing performance. Furthermore, composite materials, doping and heterostructures can also alleviate some difficulties in gas sensing [92,93]. Nevertheless, there are some existing problems such as low recovery, poor

anti-interference, and insufficient sensitivity at room temperature, which need to be further developed in future gas-sensing technologies.

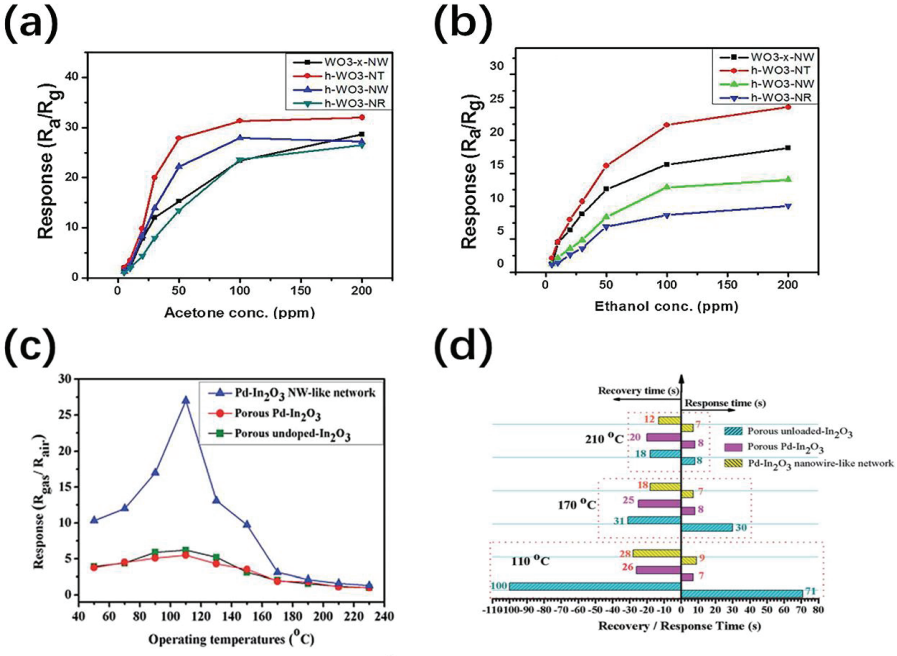

Figure 7. The response (R_a/R_g) of WO_{3-x} nanowire, h-WO_3 nanotube, h-WO_3 nanowire and h-WO_3 nanorod versus acetone (**a**) and ethanol (**b**) concentration [77]; (**c**) the response of porous unloaded-In_2O_3, porous Pd–In_2O_3 and Pd–In_2O_3 NW-like network under different temperatures to 5 ppm NO_2 [90]; (**d**) the response and recovery times of three samples to 5 ppm NO_2 at 110, 170 and 210 °C [90].

4.2. Bio-Sensing

4.2.1. Molecular Detection

In addition to chemical species, various biomolecules can also be detected by specific binding with recognition groups on the surface of nanostructures. Proteins, drugs, hormones, viruses and so on are usually analyzed by the changes of electronic properties or ionic current after the formation of antigen–antibody complexes on immunosensors. The translocation time of small molecules through NTs is longer than that of nanopores and their interaction with the hydrophobic inner wall is stronger, so that the basic sensor signals are more obvious and can be easily captured.

Recently, various research works have indicated that NTs/NWs-based nanofluidic devices are potential candidate for the detection of small biological molecules. Among them, the detection of pathogens plays an important role in the diagnosis and treatment of diseases. Multifunctional MWCNT-based magnetic fluorescent sensors have been fabricated by Liu et al., which shows high magnetic activity and fluorescence intensity linearly related to Vibrio alginolyticus (Va) concentration [94]. As shown in Figure 8a, after pretreatment of MWCNT, fluorescent reagent (Py) and antibody (Va-Ab) are used to recognize Va specifically, and non-specific adsorption of other strains was reduced by polyethylene glycol (PEG) modification. Moreover, electrochemical-based label-free sensing methods have been developed to improve the rapid, accurate and quantitative detection of pathogens. For example, Bhardwaj et al. demonstrated a paper-based immunosensor for the detection of foodborne virus [95]. In this work, Ab-SWCNT bio-conjugate simplifies the functionalization steps and improves the durability of the immunosensor. As shown

in Figure 8b,c, these Ab-SWCNT immunosensors exhibit high linear behavior and high selectivity for S. aureus. Additionally, a novel biomimetic nanosensor was prepared for the quantitative detection of biotoxins using CNT FET coated with red blood cell membrane (Figure 8d) [96]. By responding to the change of the charge distribution on the FET surface during the toxin-biofilm interaction, the detection limit is reduced to fM range with accurate concentration dependence. As for other small biomolecules, a glutamate biosensor based on chitosan-CNT-AuNW composite material was developed by Kitikul et al. [97]. The device shows ideal sensing characteristics in sensitivity, linearity and detection limit, which is widely used in flow injection analysis. Furthermore, a construct of Fe_2O_3/CNTs hybrid nanozyme has been prepared by ALD for dopamine detection [98]. CNTs with good activity provide a dispersibility support for the ultra-small nanoparticles (<1 nm) with adjustable size. Compared with other alternative nanozymes, this work shows better sensitivity with a limit of detection as low as 0.11 μM. Li et al. has developed a novel Asp/Ce NT-based colorimetric nanosensor for cysteine (Cys) [99]. The devices show high sensitivity and selectivity for Cys in H_2O_2-free and enzyme-free conditions due to the intrinsic oxidase-like activity of Asp/Ce NTs. This detection method is quite simple, effective and highly repeatable by reducing the interference from the environment.

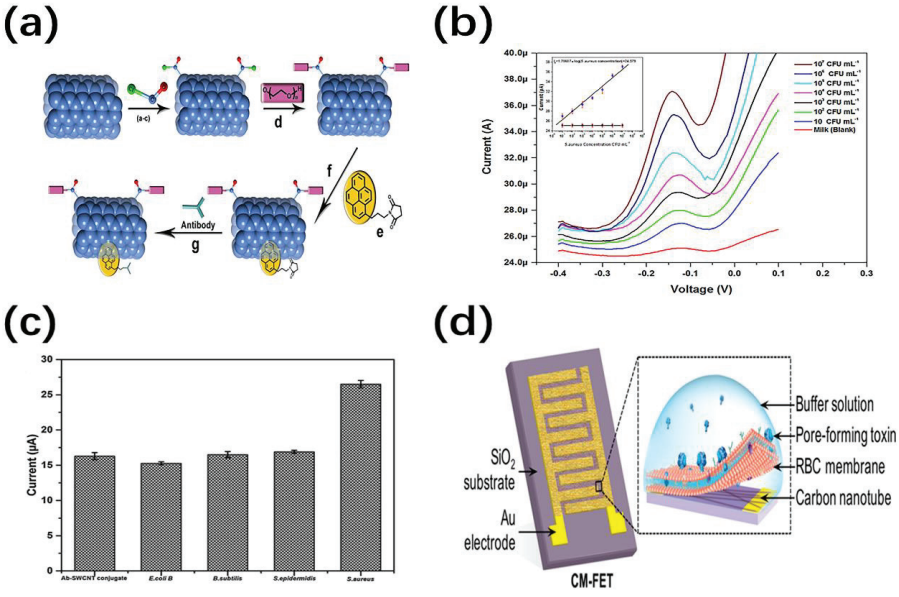

Figure 8. (**a**) Schematic illustration of the synthesis of modified MWCNT [94]; (**b**) the current versus voltage under different S. aureus concentrations from 10 to 10^7 colony-forming units (CFU) mL^{-1} in milk sample [95]; (**c**) the Histogram of selectivity for S. aureus vs. E. coli B, B. subtilis, and S. epidermidis [95]; (**d**) schematic illustration of the cell-membrane-coated CNT field-effect transistor (FET) [96].

4.2.2. DNA Sequencing

Well-designed NTs or NWs provide good opportunities for DNA real-time detection and sequencing [100]. It has been proven that single-stranded DNA can specifically and stably bind to the surface or the ends of functionalized NTs or NWs. Tahir et al. have been prepared the Zn-NPs loaded MWCNTs sensor with immobilized probe DNA strand [101]. During the hybridization process, the binding of a small amount of nucleic acid to the probe is converted into a directly measurable electrical signal. The electron doping of complementary DNA causes a great reduction in peak current, which shows three times higher selectivity compared to non-complementary DNA. It represents a simple and universal

detection method of DNA sequencing with enhanced response characteristics. In another example, Danielson et al. first employed a magnetron-sputter gas aggregation method to functionalize ZnO NWs with Au NPs for DNA detection at sub-nanomolar concentrations [102]. As shown in Figure 9, the attachment of the negatively charged DNA aptamer causes the carrier depletion of the nanowire and transforms it into Schottky-like behavior. The initial introduction of complementary DNA hybridization shows high sensitivity with ~1 μA current drop at 100 pM. In addition, passivation treatment by depositing a HfO_2 layer can alleviate the degradation of NWs exposed to aqueous solutions, which will produce a conductivity response similar to the negative charge signals. Recently, chemical resistance biosensors based on semiconductor SWCNTs (sc-SWCNTs) and nitrogen-doped MWCNTs (N-MWCNTs) have been compared for DNA sequencing derived from avian influenza virus H5N1 (Figure 10) [103]. The relatively higher sensitivity to the DNA target sequence was found in sc-SWCNTs with the lowest detection concentration down to 2 pm (20 pm in N-MWCNTs). This can be attributed to the Schottky barrier modulation effect at the CNT/metal interface, which exists only in semiconductor NTs but not in metallic NTs [104]. The amine groups on N-MW CNTs facilitate the adsorption of DNA probes while change the electronic properties of nanotubes.

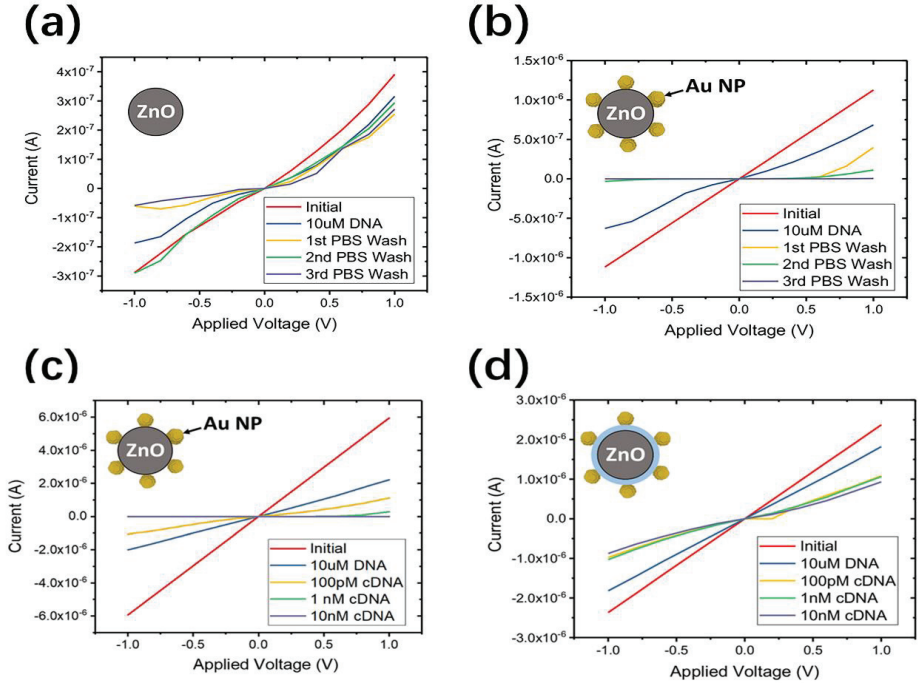

Figure 9. The response current-voltage curves of (**a**) bare, (**b**,**c**) Au NP decorated and (**c**) HfO_2 Passivated ZnO NW sensors with phosphate bufered solution (PBS) solution or cDNA exposure. HfO_2 passivation limits the change of NW conductivity with solution exposure (**c**), and AuNP modification maintains the sensitivity to DNA (**d**) [102].

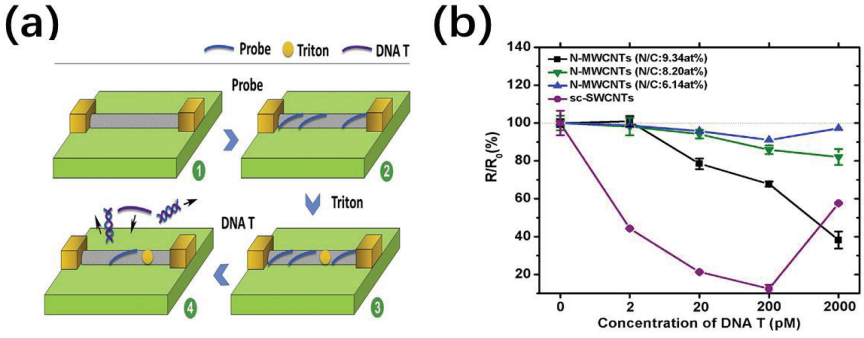

Figure 10. (**a**) Schematic illustration of the functionalization and sensing of the CNT-based biosensor [103]; (**b**) the response of N-doped MWCNTs with various N/C and sc-MWCNTs versus DNA concentration [103].

However, nucleic acid detection requires high ionic strength solutions to achieve high density of negative charges, which results in an undesirable small Debye length. To begin with, the electrostatic adsorption of DNA probes parallel to the NW surface was employed to overcome the limitation of Debye screening effect [105]. Alternatively, the surface functionalization of neutrally charged peptide nucleic acid (PNA) for gene sensing has also been demonstrated. The PNA probe-modified CNT device developed by Fortunati has realized direct measurement of DNA from genetically modified (GM) Soy, reaching the threshold level of soybean meal verification [106]. The enhanced sensitivity of CNTs can be attributed to the intrinsic characteristics of PNA, which provides high recognition efficiency. On the other hand, the compatibility of NWs/NTs-based ISFET sensor arrays with Complementary Metal Oxide Semiconductor (CMOS) technology allows them to be integrated on a large scale. Xu et al. comprehensively optimized the sensitivity of CMOS-ISFET to biomolecule-DNA based on the device design of size and bias [107]. The experiments and model show that it is an effective way to enhance the charge detection signal of the device, by biasing at near-threshold, reducing the channel-to-sensing area ratio and minimizing the double-layer capacitance of the sensing electrode.

5. Conclusions

With the advancement of micro-nano technology, people have been increasingly interested in the basic research of nanofluid transport at the nanoscale. The NWs and NTs introduced here as 1D nanostructured materials have unique properties, which are very attractive for advanced preparation and optimization of novel nanofluidic cells for chemical and biological sensing, especially for small molecule detection and DNA sequencing. The robust and uniform 1D nanostructures prepared by the improved synthesis methods have controllable morphology, size, composition and easily functionalized surfaces, which provide a foundation for the fabrication of nanofluidic devices and sensing applications.

Additionally, nanotubes as channels and sensor elements have large specific surface areas and there are special physical transport phenomena at the nanometer scale, such as ICR and a unipolar ion environment. Compared with nanopores, better electrostatic tuning in time and space makes nanofluidic devices based on NWs and NTs powerful tools for environmental analysis and molecular sensing. Similar to planar semiconductor sensors, NWs/NTs-based devices have been improved in terms of size, sensitivity, speed and specificity, which enable the detection and manipulation of few charged species and even single molecules. Various detection mechanisms have been employed like static control, charge transfer and charge scattering, etc. Most of them rely on the basic signal changes of the nanostructure when the target molecule interacts with the surface receptor

during the transfer process, which encodes molecular geometry, charge, concentration and other information through electronic or ionic current.

So far, there are still some limitations and challenges to be solved in NWs/NTs-based nanofluidic research for chemical and bio-sensing. To begin with, the main difficulty is the micro/nanofabrication technology in materials sorting and device fabrication, which limits the large-scale industrial production and applications. Moreover, high signal-to-noise ratio, low detection limit, and fast test analysis is another urgent problem to be solved. Hybrid detection mechanisms and accurate device models can be explored to reduce the noise and interference of functional devices. It is also possible to adopt novel devices structures and composite materials to improve response and selectivity. For example, incorporating multiple aligned or three-dimensional heterogeneous NWs/NTs into the devices may be an effective way. Further research should be conducted in material preparation, device fabrication and related applications. Nevertheless, the use of 1D nanostructure will deepen our understanding of the basic transport phenomena of nanofluids and open a new research paradigm in the areas of electronics, optoelectronics, chemistry and bio-sensing.

Author Contributions: Conceptualization, H.Z.; investigation, X.-Y.Z.; resources, B.-R.W. and Y.G.; writing—original draft preparation, X.-Y.Z.; writing—review and editing, H.Z.; project administration, L.C.; funding acquisition, Q.-Q.S. All authors have read and agreed to the published version of the manuscript.

Funding: This research was funded by the National Key Research and Development Program of China (2018YFB2202800), the National Natural Science Foundation of China (61904033) and the Science and Technology Commission of Shanghai Municipality (18JC1410300).

Institutional Review Board Statement: Not applicable.

Informed Consent Statement: Not applicable.

Data Availability Statement: The data presented in this study are available in article.

Conflicts of Interest: The authors declare no conflict of interest.

References

1. Hu, X.; Lu, D. Intensification of chemical separation engineering by nanostructured channels and nanofluidics: From theories to applications. *Chin. J. Chem. Eng.* **2019**, *27*, 1439–1448. [CrossRef]
2. Radha, B.; Esfandiar, A.; Wang, F.C.; Rooney, A.P.; Gopinadhan, K.; Keerthi, A.; Mishchenko, A.; Janardanan, A.; Blake, P.; Fumagalli, L.; et al. Molecular transport through capillaries made with atomic-scale precision. *Nature* **2016**, *538*, 222–225. [CrossRef] [PubMed]
3. Tunuguntla, R.H.; Henley, R.Y.; Yao, Y.C.; Pham, T.A.; Wanunu, M.; Noy, A. Enhanced water permeability and tunable ion selectivity in subnanometer carbon nanotube porins. *Science* **2017**, *357*, 792–796. [CrossRef] [PubMed]
4. Kasianowicz, J.J.; Brandin, E.; Branton, D.; Deamer, D.W. Characterization of individual polynucleotide molecules using a membrane channel. *Proc. Natl. Acad. Sci. USA* **1996**, *93*, 13770–13773. [CrossRef] [PubMed]
5. Surwade, S.P.; Smirnov, S.N.; Vlassiouk, I.V.; Unocic, R.R.; Veith, G.M.; Dai, S.; Mahurin, S.M. Water desalination using nanoporous single-layer graphene. *Nat. Nanotechnol.* **2015**, *10*, 459–464. [CrossRef]
6. Zhang, Z.; Yang, S.; Zhang, P.; Zhang, J.; Chen, G.; Feng, X. Mechanically strong MXene/Kevlar nanofiber composite membranes as high-performance nanofluidic osmotic power generators. *Nat. Commun.* **2019**, *10*, 2920. [CrossRef]
7. Mogg, L.; Zhang, S.; Hao, G.P.; Gopinadhan, K.; Barry, D.; Liu, B.L.; Cheng, H.M.; Geim, A.K.; Lozada-Hidalgo, M. Perfect proton selectivity in ion transport through two-dimensional crystals. *Nat. Commun.* **2019**, *10*, 4243. [CrossRef]
8. Li, Y.; Wu, Q.; Guo, X.; Zhang, M.; Chen, B.; Wei, G.; Li, X.; Li, X.; Li, S.; Ma, L. Laminated self-standing covalent organic framework membrane with uniformly distributed subnanopores for ionic and molecular sieving. *Nat. Commun.* **2020**, *11*, 599. [CrossRef]
9. Ji, D.; Wen, Q.; Cao, L.; Kang, Q.; Lin, S.; Zhang, X.; Jiang, L.; Guo, W. Electrokinetically Controlled Asymmetric Ion Transport through 1D/2D Nanofluidic Heterojunctions. *Adv. Mater. Technol.* **2019**, *4*, 1800742. [CrossRef]
10. Iijima, S. Helical Microtubules of Graphitic Carbon. *Nature* **1991**, *354*, 56–58. [CrossRef]
11. Peng, R.; Pan, Y.; Li, Z.; Zhang, S.; Wheeler, A.R.; Tang, X.; Liu, X. Ionotronics Based on Horizontally Aligned Carbon Nanotubes. *Adv. Funct. Mater.* **2020**, *30*, 2003177. [CrossRef]
12. Ambhorkar, P.; Wang, Z.; Ko, H.; Lee, S.; Koo, K.I.; Kim, K.; Cho, D.D. Nanowire-Based Biosensors: From Growth to Applications. *Micromachines* **2018**, *9*, 679. [CrossRef] [PubMed]
13. Pachauri, V.; Ingebrandt, S. Biologically sensitive field-effect transistors: From ISFETs to NanoFETs. *Essays Biochem.* **2016**, *60*, 81–90. [PubMed]

14. Smith, R.; Geary, S.M.; Salem, A.K. Silicon Nanowires and Their Impact on Cancer Detection and Monitoring. *ACS Appl. Nano Mater.* **2020**, *3*, 8522–8536. [CrossRef]
15. Wagner, R.S.; Ellis, W.C. Vapor-Liquid-Solid Mechanism Of Single Crystal Growth. *Appl. Phys. Lett.* **1964**, *4*, 89–90. [CrossRef]
16. Morales, A.M.; Lieber, C.M. A laser ablation method for the synthesis of crystalline semiconductor nanowires. *Science* **1998**, *279*, 208–211. [CrossRef]
17. Hu, P.; Dong, S.; Zhang, D.; Fang, C.; Zhang, X. Catalyst-assisted synthesis of core–shell SiC/SiO_2 nanowires via a simple method. *Ceram. Int.* **2016**, *42*, 1581–1587. [CrossRef]
18. Kaur, N.; Comini, E.; Zappa, D.; Poli, N.; Sberveglieri, G. Nickel oxide nanowires: Vapor liquid solid synthesis and integration into a gas sensing device. *Nanotechnology* **2016**, *27*, 205701. [CrossRef]
19. Ren, J.; Zhang, Y.; Li, J.; Tian, S.; Fei, T.; Li, H. Effects of deposition temperature and time on HfC nanowires synthesized by CVD on SiC-coated C/C composites. *Ceram. Int.* **2016**, *42*, 5623–5628. [CrossRef]
20. Haffner, T.; Zeghouane, M.; Bassani, F.; Gentile, P.; Gassenq, A.; Chouchane, F.; Pauc, N.; Martinez, E.; Robin, E.; David, S.; et al. Growth of Ge1−xSnx Nanowires by Chemical Vapor Deposition via Vapor-Liquid-Solid Mechanism Using GeH_4 and $SnCl_4$. *Phys. Status Solidi A* **2018**, *215*, 1700743. [CrossRef]
21. Wu, R.; Yang, Z.; Fu, M.; Zhou, K. In-situ growth of SiC nanowire arrays on carbon fibers and their microwave absorption properties. *J. Alloy. Compd.* **2016**, *687*, 833–838. [CrossRef]
22. Dong, S.; Hu, P.; Zhang, X.; Cheng, Y.; Fang, C.; Xu, J.; Chen, G. Facile synthesis of silicon nitride nanowires with flexible mechanical properties and with diameters controlled by flow rate. *Sci. Rep.* **2017**, *7*, 45538. [CrossRef] [PubMed]
23. Terasako, T.; Kawasaki, Y.; Yagi, M. Growth and morphology control of β-Ga_2O_3 nanostructures by atmospheric-pressure CVD. *Thin Solid Films* **2016**, *620*, 23–29. [CrossRef]
24. Terasako, T.; Kohno, K.; Yagi, M. Vapor-liquid-solid growth of SnO_2 nanowires utilizing alternate source supply and their photoluminescence properties. *Thin Solid Films* **2017**, *644*, 3–9. [CrossRef]
25. Krylyuk, S.; Davydov, A.V.; Levin, I. Tapering Control of Si Nanowires Grownfrom $SiCl_4$ at Reduced Pressure. *ACS Nano* **2010**, *5*, 656–664. [CrossRef]
26. Küpers, H.; Lewis, R.B.; Tahraoui, A.; Matalla, M.; Krüger, O.; Bastiman, F.; Riechert, H.; Geelhaar, L. Diameter evolution of selective area grown Ga-assisted GaAs nanowires. *Nano Res.* **2018**, *11*, 2885–2893. [CrossRef]
27. DeJarld, M.; Teran, A.; Luengo-Kovac, M.; Yan, L.; Moon, E.S.; Beck, S.; Guillen, C.; Sih, V.; Phillips, J.; Milunchick, J.M. The effect of doping on low temperature growth of high quality GaAs nanowires on polycrystalline films. *Nanotechnology* **2016**, *27*, 495605. [CrossRef]
28. Akbari, M.; Mohajerzadeh, S. Highly patterned growth of SnO_2 nanowires using a sub-atmospheric vapor–liquid–solid deposition. *J. Phys. D-Appl. Phys.* **2017**, *50*, 305104. [CrossRef]
29. Fan, H.J.; Werner, P.; Zacharias, M. Semiconductor nanowires: From self-organization to patterned growth. *Small* **2006**, *2*, 700–717. [CrossRef]
30. Kawaguchi, K.; Takahashi, T.; Okamoto, N.; Sato, M. Position-Controlled VLS Growth of Nanowires on Mask-Patterned GaAs Substrates for Axial GaAsSb/InAs Heterostructures. *Phys. Status Solidi A* **2018**, *215*, 1870015. [CrossRef]
31. Khayyat, M.M.; Wacaser, B.A.; Reuter, M.C.; Ross, F.M.; Sadana, D.K.; Chen, T.C. Nanoscale chemical templating of Si nanowires seeded with Al. *Nanotechnology* **2013**, *24*, 235301. [CrossRef] [PubMed]
32. Schmidt, V.; Senz, S.; Gosele, U. Diameter-dependent growth direction of epitaxial silicon nanowires. *Nano Lett.* **2005**, *5*, 931–935. [CrossRef] [PubMed]
33. Wang, J.; Westerbeek, E.Y.; van den Berg, A.; Segerink, L.I.; Shui, L.; Eijkel, J.C.T. Mass Transport Determined Silica Nanowires Growth on Spherical Photonic Crystals with Nanostructure-Enabled Functionalities. *Small* **2020**, *16*, 2001026. [CrossRef] [PubMed]
34. Wang, L.; Li, T.; Ling, L.; Luo, J.; Zhang, K.; Xu, Y.; Lu, H.; Yao, Y. Remote catalyzation for growth of boron nitride nanotubes by low pressure chemical vapor deposition. *Chem. Phys. Lett.* **2016**, *652*, 27–31. [CrossRef]
35. Li, Y.; Cheng, H.; Wang, N.; Zhou, Y.; Li, T. Magnetic and microwave absorption properties of Fe/TiO_2 nanocomposites prepared by template electrodeposition. *J. Alloy. Compd.* **2018**, *763*, 421–429. [CrossRef]
36. Zhang, C.; Chen, J.; Xu, L. Dual-templating approach to ordered mesoporous Pt nanowires with various morphologies. *Mater. Lett.* **2018**, *223*, 97–101. [CrossRef]
37. Narula, C.; Chauhan, R.P. Size dependent properties of one dimensional CdSe micro/nanostructures. *Physica B* **2017**, *521*, 381–388. [CrossRef]
38. Movsesyan, L.; Schubert, I.; Yeranyan, L.; Trautmann, C.; Eugenia Toimil-Molares, M. Influence of electrodeposition parameters on the structure and morphology of ZnO nanowire arrays and networks synthesized in etched ion-track membranes. *Semicond. Sci. Technol.* **2016**, *31*, 014006. [CrossRef]
39. Yang, B.; Niu, G.; Liu, X.-D.; Yang, Y.; He, W.; Zhu, Y.; Yu, B.; Zhou, X.-W.; Wu, W.-D. Preparation of size controllable porous polymethylmethacrylate template and Cu micro/nanowire arrays. *RSC Adv.* **2016**, *6*, 88656–88663. [CrossRef]
40. He, G.; Chen, H.-J.; Liu, D.; Feng, Y.; Yang, C.; Hang, T.; Wu, J.; Cao, Y.; Xie, X. Fabrication of Various Structures of Nanostraw Arrays and Their Applications in Gene Delivery. *Adv. Mater. Interfaces* **2018**, *5*, 1701535. [CrossRef]
41. De la Torre Medina, J.; da Camara Santa Clara Gomes, T.; Velazquez Galvan, Y.G.; Piraux, L. Large-scale 3-D interconnected Ni nanotube networks with controlled structural and magnetic properties. *Sci Rep* **2018**, *8*, 14555. [CrossRef] [PubMed]

42. Ruiz-Clavijo, A.; Caballero-Calero, O.; Martin-Gonzalez, M. Three-Dimensional Bi_2Te_3 Networks of Interconnected Nanowires: Synthesis and Optimization. *Nanomaterials* **2018**, *8*, 345. [CrossRef] [PubMed]
43. Su, C.Y.; Wang, L.C.; Liu, W.S.; Wang, C.C.; Perng, T.P. Photocatalysis and Hydrogen Evolution of Al- and Zn-Doped TiO_2 Nanotubes Fabricated by Atomic Layer Deposition. *Semicond. Sci. Technol.* **2018**, *10*, 33287–33295. [CrossRef] [PubMed]
44. Woo, J.Y.; Han, H.; Kim, J.W.; Lee, S.-M.; Ha, J.S.; Shim, J.H.; Han, C.-S. Sub-5 nm nanostructures fabricated by atomic layer deposition using a carbon nanotube template. *Nanotechnology* **2016**, *27*, 265301. [CrossRef] [PubMed]
45. Rabin, O.; Herz, P.R.; Lin, Y.M.; Akinwande, A.I.; Cronin, S.B.; Dresselhaus, M.S. Formation of Thick Porous Anodic Alumina Films and Nanowire Arrays on Silicon Wafers and Glass. *Adv. Funct. Mater.* **2003**, *13*, 631–638. [CrossRef]
46. Sander, M.S.; Gao, H. Aligned arrays of nanotubes and segmented nanotubes on substrates fabricated by electrodeposition onto nanorods. *J. Am. Chem. Soc.* **2005**, *127*, 12158–12159. [CrossRef]
47. Guiliani, J.; Cadena, J.; Monton, C. Template-assisted electrodeposition of Ni and Ni/Au nanowires on planar and curved substrates. *Nanotechnology* **2018**, *29*, 075301. [CrossRef]
48. Goldberger, J.; Fan, R.; Yang, P.D. Inorganic nanotubes: A novel platform for nanofluidics. *Acc. Chem. Res.* **2006**, *39*, 239–248. [CrossRef]
49. Jia, X.; Zhu, X.; Tian, W.; Ding, Y.; Tian, X.; Cheng, B.; Cheng, L.; Bai, S.; Qin, Y. Nanowire templated CVD synthesis and morphological control of MoS2 nanotubes. *J. Mater. Chem. C* **2020**, *8*, 4133–4138. [CrossRef]
50. Zhang, L.; Zhang, Y.; Guo, Y.; Wang, Y.; Liu, R.; Chen, B.; Zhong, H.; Zou, B. Growth of CdS nanotubes and their strong optical microcavity effects. *Nanoscale* **2019**, *11*, 5325–5329. [CrossRef]
51. Ishiyama, T.; Nakagawa, S.; Wakamatsu, T.; Fujiwara, N. Synthesis of β-$FeSi_2$ nanowires by using silicon nanowire templates. *AIP Adv.* **2018**, *8*, 085324. [CrossRef]
52. Zhu, H.; Li, H.; Robertson, J.W.F.; Balijepalli, A.; Krylyuk, S.; Davydov, A.V.; Kasianowicz, J.J.; Suehle, J.S.; Li, Q. Novel nanofluidic chemical cells based on self-assembled solid-state SiO_2 nanotubes. *Nanotechnology* **2017**, *28*, 435601. [CrossRef] [PubMed]
53. Sutter, E.; French, J.S.; Balgarkashi, A.; Tappy, N.; Fontcuberta, I.M.A.; Idrobo, J.C.; Sutter, P. Single-Crystalline gamma-Ga_2S_3 Nanotubes via Epitaxial Conversion of GaAs Nanowires. *Nano Lett.* **2019**, *19*, 8903–8910. [CrossRef] [PubMed]
54. Tao, L.; Yu, D.; Zhou, J.; Lu, X.; Yang, Y.; Gao, F. Ultrathin Wall (1 nm) and Superlong Pt Nanotubes with Enhanced Oxygen Reduction Reaction Performance. *Small* **2018**, *14*, 1704503. [CrossRef] [PubMed]
55. Li, Y.; Huang, H.; Chen, S.; Wang, C.; Ma, T. Nanowire-Templated Synthesis of FeNx -Decorated Carbon Nanotubes as Highly Efficient, Universal-pH, Oxygen Reduction Reaction Catalysts. *Chemistry* **2019**, *25*, 2637–2644. [CrossRef] [PubMed]
56. Jayakumar, G.; Asadollahi, A.; Hellström, P.E.; Garidis, K.; Östling, M. Silicon nanowires integrated with CMOS circuits for biosensing application. *Solid-State Electron.* **2014**, *98*, 26–31. [CrossRef]
57. Lee, J.; Jang, J.; Choi, B.; Yoon, J.; Kim, J.Y.; Choi, Y.K.; Kim, D.M.; Kim, D.H.; Choi, S.J. A Highly Responsive Silicon Nanowire/Amplifier MOSFET Hybrid Biosensor. *Sci. Rep.* **2015**, *5*, 12286. [CrossRef]
58. Lee, R.; Kwon, D.W.; Kim, S.; Kim, S.; Mo, H.-S.; Kim, D.H.; Park, B.-G. Nanowire size dependence on sensitivity of silicon nanowire field-effect transistor-based pH sensor. *Jpn. J. Appl. Phys.* **2017**, *56*, 124001. [CrossRef]
59. Schwartz, M.; Thanh Chien, N.; Xuan Thang, V.; Wagner, P.; Thoelen, R.; Ingebrandt, S. Impedimetric Sensing of DNA with Silicon Nanowire Transistors as Alternative Transducer Principle. *Phys. Status Solidi A* **2018**, *215*, 1700740. [CrossRef]
60. Guo, J.; He, J.; Zeng, B. Carbon Nanotube Based Nanopore and Nanofluidic Devices Towards Sensing Applications. *Curr. Nanosci.* **2016**, *12*, 421–428. [CrossRef]
61. Hibst, N.; Steinbach, A.M.; Strehle, S. Fluidic and Electronic Transport in Silicon Nanotube Biosensors. *MRS Adv.* **2016**, *1*, 3761–3766. [CrossRef]
62. Haywood, D.G.; Saha-Shah, A.; Baker, L.A.; Jacobson, S.C. Fundamental studies of nanofluidics: Nanopores, nanochannels, and nanopipets. *Anal. Chem.* **2015**, *87*, 172–187. [CrossRef] [PubMed]
63. Wang, M.; Meng, H.; Wang, D.; Yin, Y.; Stroeve, P.; Zhang, Y.; Sheng, Z.; Chen, B.; Zhan, K.; Hou, X. Dynamic Curvature Nanochannel-Based Membrane with Anomalous Ionic Transport Behaviors and Reversible Rectification Switch. *Adv. Mater.* **2019**, *31*, 1805130. [CrossRef] [PubMed]
64. Guan, W.; Fan, R.; Reed, M.A. Field-effect reconfigurable nanofluidic ionic diodes. *Nat. Commun.* **2011**, *2*, 506. [CrossRef] [PubMed]
65. Xiao, K.; Chen, L.; Zhang, Z.; Xie, G.; Li, P.; Kong, X.Y.; Wen, L.; Jiang, L. A Tunable Ionic Diode Based on a Biomimetic Structure-Tailorable Nanochannel. *Angew.Chem.Int. Ed.* **2017**, *56*, 8168–8172. [CrossRef] [PubMed]
66. Abgrall, P.; Nguyen, N.T. Nanofluidic devices and their applications. *Anal. Chem.* **2008**, *80*, 2326–2341. [CrossRef]
67. Fan, R.; Yue, M.; Karnik, R.; Majumdar, A.; Yang, P. Polarity switching and transient responses in single nanotube nanofluidic transistors. *Phys. Rev. Lett.* **2005**, *95*, 086607. [CrossRef]
68. Wilson, J.; Di Ventra, M. Single-base DNA discrimination via transverse ionic transport. *Nanotechnology* **2013**, *24*, 415101. [CrossRef]
69. Schneider, G.F.; Kowalczyk, S.W.; Calado, V.E.; Pandraud, G.; Zandbergen, H.W.; Vandersypen, L.M.K.; Dekker, C. DNA Translocation through Graphene Nanopores. *Nano Lett.* **2010**, *10*, 3163–3167. [CrossRef]
70. Fan, R.; Karnik, R.; Yue, M.; Li, D.Y.; Majumdar, A.; Yang, P.D. DNA translocation in inorganic nanotubes. *Nano Lett.* **2005**, *5*, 1633–1637. [CrossRef]
71. Roy, S.; Gao, Z. Nanostructure-based electrical biosensors. *Nano Today* **2009**, *4*, 318–334. [CrossRef]

72. Zhang, A.; Lieber, C.M. Nano-Bioelectronics. *Chem. Rev.* **2016**, *116*, 215–257. [CrossRef] [PubMed]
73. Rackauskas, S.; Barbero, N.; Barolo, C.; Viscardi, G. ZnO Nanowire Application in Chemoresistive Sensing: A Review. *Nanomaterials* **2017**, *7*, 381. [CrossRef] [PubMed]
74. Li, Z.; Li, H.; Wu, Z.; Wang, M.; Luo, J.; Torun, H.; Hu, P.; Yang, C.; Grundmann, M.; Liu, X.; et al. Advances in designs and mechanisms of semiconducting metal oxide nanostructures for high-precision gas sensors operated at room temperature. *Mater. Horiz.* **2019**, *6*, 470–506. [CrossRef]
75. Kondo, T.; Sato, Y.; Kinoshita, M.; Shankar, P.; Mintcheva, N.N.; Honda, M.; Iwamori, S.; Kulinich, S.A. Room temperature ethanol sensor based on ZnO prepared via laser ablation in water. *Jpn. J. Appl. Phys.* **2017**, *56*, 080304. [CrossRef]
76. Sun, P.; Cai, Y.; Du, S.; Xu, X.; You, L.; Ma, J.; Liu, F.; Liang, X.; Sun, Y.; Lu, G. Hierarchical α-Fe2O3/SnO2 semiconductor composites: Hydrothermal synthesis and gas sensing properties. *Sens. Actuator B-Chem.* **2013**, *182*, 336–343. [CrossRef]
77. Zeb, S.; Peng, X.; Yuan, G.; Zhao, X.; Qin, C.; Sun, G.; Nie, Y.; Cui, Y.; Jiang, X. Controllable synthesis of ultrathin WO3 nanotubes and nanowires with excellent gas sensing performance. *Sens. Actuator B-Chem.* **2020**, *305*, 127435. [CrossRef]
78. Cui, Y.; Wei, Q.Q.; Park, H.K.; Lieber, C.M. Nanowire nanosensors for highly sensitive and selective detection of biological and chemical species. *Science* **2001**, *293*, 1289–1292. [CrossRef]
79. Amorim, C.A.; Blanco, K.C.; Costa, I.M.; Vicente, E.F.; da S Petruci, J.F.; Contiero, J.; Leite, E.R.; Chiquito, A.J. Active-electrode biosensor of SnO2 nanowire for cyclodextrin detection from microbial enzyme. *Nanotechnology* **2020**, *31*, 165501. [CrossRef]
80. Choi, S.; Mo, H.-S.; Kim, J.; Kim, S.; Lee, S.M.; Choi, S.-J.; Kim, D.M.; Park, D.-W.; Kim, D.H. Experimental extraction of stern-layer capacitance in biosensor detection using silicon nanowire field-effect transistors. *Curr. Appl. Phys.* **2020**, *20*, 828–833. [CrossRef]
81. Mahmudunnabi, R.G.; Farhana, F.Z.; Kashaninejad, N.; Firoz, S.H.; Shim, Y.B.; Shiddiky, M.J.A. Nanozyme-based electrochemical biosensors for disease biomarker detection. *Analyst* **2020**, *145*, 4398–4420. [CrossRef] [PubMed]
82. Jiang, X.; Sun, C.; Guo, Y.; Nie, G.; Xu, L. Peroxidase-like activity of apoferritin paired gold clusters for glucose detection. *Biosens. Bioelectron.* **2015**, *64*, 165–170. [CrossRef] [PubMed]
83. Huang, Z.; Chen, S.; Wang, Y.; Li, T. Gold nanoparticle modified silicon nanowire array based sensor for low-cost, high sensitivity and selectivity detection of mercury ions. *Mater. Res. Express* **2020**, *7*, 035017. [CrossRef]
84. Cao, D.; Pang, P.; Liu, H.; He, J.; Lindsay, S.M. Electronic sensitivity of a single-walled carbon nanotube to internal electrolyte composition. *Nanotechnology* **2012**, *23*, 085203. [CrossRef]
85. Kwon, J.; Lee, B.H.; Kim, S.Y.; Park, J.Y.; Bae, H.; Choi, Y.K.; Ahn, J.H. Nanoscale FET-Based Transduction toward Sensitive Extended-Gate Biosensors. *ACS Sens.* **2019**, *4*, 1724–1729. [CrossRef]
86. Ghanei-Motlagh, M.; Taher, M.A. A novel electrochemical sensor based on silver/halloysite nanotube/molybdenum disulfide nanocomposite for efficient nitrite sensing. *Biosens. Bioelectron.* **2018**, *109*, 279–285. [CrossRef]
87. Song, C.; Li, C.; Yin, Y.; Xiao, J.; Zhang, X.; Song, M.; Dong, W. Preparation and gas sensing properties of partially broken WO_3 nanotubes. *Vacuum* **2015**, *114*, 13–16. [CrossRef]
88. Liu, H.; Wei, D.; Yan, Y.; Li, A.; Chuai, X.; Lu, G.; Wang, Y. Silver Nanowire Templating Synthesis of Mesoporous SnO_2 Nanotubes: An Effective Gas Sensor for Methanol with a Rapid Response and Recovery. *ChemistrySelect* **2018**, *3*, 7741–7748. [CrossRef]
89. Choi, K.-S.; Chang, S.-P. Effect of structure morphologies on hydrogen gas sensing by ZnO nanotubes. *Mater. Lett.* **2018**, *230*, 48–52. [CrossRef]
90. Huang, M.; Cui, Z.; Yang, X.; Zhu, S.; Li, Z.; Liang, Y. Pd-loaded In_2O_3 nanowire-like network synthesized using carbon nanotube templates for enhancing NO_2 sensing performance. *RSC Adv.* **2015**, *5*, 30038–30045. [CrossRef]
91. Choi, K.S.; Park, S.; Chang, S.-P. Enhanced ethanol sensing properties based on SnO2 nanowires coated with Fe_2O_3 nanoparticles. *Sens. Actuator B-Chem.* **2017**, *238*, 871–879. [CrossRef]
92. Huang, B.; Zhao, C.; Zhang, M.; Zhang, Z.; Xie, E.; Zhou, J.; Han, W. Doping effect of In_2O_3 on structural and ethanol-sensing characteristics of ZnO nanotubes fabricated by electrospinning. *Appl. Surf. Sci.* **2015**, *349*, 615–621. [CrossRef]
93. Kaur, N.; Comini, E.; Poli, N.; Zappa, D.; Sberveglieri, G. NiO/ZnO Nanowire-heterostructures by Vapor Phase Growth for Gas Sensing. *Procedia Eng.* **2016**, *168*, 1140–1143. [CrossRef]
94. Liu, Y.; Hu, J.; Sun, J.S.; Li, Y.; Xue, S.X.; Chen, X.Q.; Li, X.S.; Du, G.X. Facile synthesis of multifunctional multi-walled carbon nanotube for pathogen Vibrio alginolyticus detection in fishery and environmental samples. *Talanta* **2014**, *128*, 311–318. [CrossRef]
95. Bhardwaj, J.; Devarakonda, S.; Kumar, S.; Jang, J. Development of a paper-based electrochemical immunosensor using an antibody-single walled carbon nanotubes bio-conjugate modified electrode for label-free detection of foodborne pathogens. *Sens. Actuator B-Chem.* **2017**, *253*, 115–123. [CrossRef]
96. Gong, H.; Chen, F.; Huang, Z.; Gu, Y.; Zhang, Q.; Chen, Y.; Zhang, Y.; Zhuang, J.; Cho, Y.K.; Fang, R.H.; et al. Biomembrane-Modified Field Effect Transistors for Sensitive and Quantitative Detection of Biological Toxins and Pathogens. *ACS Nano* **2019**, *13*, 3714–3722. [CrossRef]
97. Kitikul, J.; Satienperakul, S.; Preechaworapun, A.; Pookmanee, P.; Tangkuaram, T. A Simple Flow Amperometric Electrochemical Biosensor Based on Chitosan Scaffolds and Gold Nanowires Modified on a Glassy Carbon Electrode for Detection of Glutamate in Food Products. *Electroanalysis* **2017**, *29*, 264–271. [CrossRef]
98. Yang, Y.; Li, T.; Qin, Y.; Zhang, L.; Chen, Y. Construct of Carbon Nanotube-Supported Fe_2O_3 Hybrid Nanozyme by Atomic Layer Deposition for Highly Efficient Dopamine Sensing. *Front. Chem.* **2020**, *8*, 564968. [CrossRef]
99. Li, Y.; Zhang, Z.; Tao, Z.; Gao, X.; Wang, S.; Liu, Y. A Asp/Ce nanotube-based colorimetric nanosensor for H_2O_2-free and enzyme-free detection of cysteine. *Talanta* **2019**, *196*, 556–562. [CrossRef]

100. Spain, E.; McCooey, A.; Joyce, K.; Keyes, T.E.; Forster, R.J. Gold nanowires and nanotubes for high sensitivity detection of pathogen DNA. *Sens. Actuator B-Chem.* **2015**, *215*, 159–165. [CrossRef]
101. Tahir, M.A.; Hameed, S.; Munawar, A.; Amin, I.; Mansoor, S.; Khan, W.S.; Bajwa, S.Z. Investigating the potential of multiwalled carbon nanotubes based zinc nanocomposite as a recognition interface towards plant pathogen detection. *J. Virol. Methods* **2017**, *249*, 130–136. [CrossRef] [PubMed]
102. Danielson, E.; Dhamodharan, V.; Porkovich, A.; Kumar, P.; Jian, N.; Ziadi, Z.; Grammatikopoulos, P.; Sontakke, V.A.; Yokobayashi, Y.; Sowwan, M. Gas-Phase Synthesis for Label-Free Biosensors: Zinc-Oxide Nanowires Functionalized with Gold Nanoparticles. *Sci. Rep.* **2019**, *9*, 17370. [CrossRef] [PubMed]
103. Fu, Y.; Romay, V.; Liu, Y.; Ibarlucea, B.; Baraban, L.; Khavrus, V.; Oswald, S.; Bachmatiuk, A.; Ibrahim, I.; Rümmeli, M.; et al. Chemiresistive biosensors based on carbon nanotubes for label-free detection of DNA sequences derived from avian influenza virus H5N1. *Sens. Actuator B-Chem.* **2017**, *249*, 691–699. [CrossRef]
104. Tang, X.; Bansaruntip, S.; Nakayama, N.; Yenilmez, E.; Chang, Y.-L.; Wang, Q. Carbon nanotube DNA sensor and sensing mechanism. *Nano Lett.* **2006**, *6*, 1632–1636. [CrossRef] [PubMed]
105. Bunimovich, Y.L.; Shin, Y.S.; Yeo, W.-S.; Amori, M.; Kwong, G.; Heath, J.R. Quantitative real-time measurements of DNA hybridization with alkylated nonoxidized silicon nanowires in electrolyte solution. *J. Am. Chem. Soc.* **2006**, *128*, 16323–16331. [CrossRef]
106. Fortunati, S.; Rozzi, A.; Curti, F.; Giannetto, M.; Corradini, R.; Careri, M. Novel amperometric genosensor based on peptide nucleic acid (PNA) probes immobilized on carbon nanotubes-screen printed electrodes for the determination of trace levels of non-amplified DNA in genetically modified (GM) soy. *Biosens. Bioelectron.* **2019**, *129*, 7–14. [CrossRef]
107. Xu, G.; Abbott, J.; Ham, D. Optimization of CMOS-ISFET-Based Biomolecular Sensing: Analysis and Demonstration in DNA Detection. *IEEE Trans. Electron Devices* **2016**, *63*, 3249–3256. [CrossRef]

nanomaterials

MDPI

Article

A New Thermal Conductivity Model and Two-Phase Mixed Convection of CuO–Water Nanofluids in a Novel I-Shaped Porous Cavity Heated by Oriented Triangular Hot Block

Amin Asadi [1,2], Maysam Molana [3], Ramin Ghasemiasl [4], Taher Armaghani [5,*], Mihail-Ioan Pop [6] and Mohsen Saffari Pour [7]

1 Institute of Research and Development, Duy Tan University, Da Nang 550000, Vietnam; aminasadi@duytan.edu.vn
2 Faculty of Natural Sciences, Duy Tan University, Da Nang 550000, Vietnam
3 Department of Mechanical Engineering, Wayne State University, Detroit, MI 48202, USA; molana@wayne.edu
4 Department of Mechanical Engineering, West Tehran Branch, Islamic Azad University, Tehran 14687-63785, Iran; ghasemiasl.r@wtiau.ac.ir
5 Department of Mechanical Engineering, Mahdishahr Branch, Islamic Azad University, Mahdishahr 35618-75915, Iran
6 Department of Mathematics, Babeş-Bolyai University, 400084 Cluj-Napoca, Brasov, Romania; popm.ioan@yahoo.co.uk
7 Department of Mechanical Engineering, Shahid Bahonar University of Kerman, Kerman 76169-13439, Iran; mohsensp@kth.se
* Correspondence: tarmaghani@msh-iau.ac.ir

Received: 9 September 2020; Accepted: 29 October 2020; Published: 7 November 2020

Abstract: This paper investigates the cooling performance of nanofluid (NF) mixed convection in a porous I-shaped electronic chip with an internal triangular hot block using Buongiorno's two-phase model. This type of cavity and hot block geometry has not been studied formerly. The NF was assumed to be a mixture of water and CuO nanoparticles (NP) up to 4% of volume concentration. As most published mathematical models for the thermal conductivity of NF give inaccurate predictions, a new predictive correlation for effective thermal conductivity was also developed with a high accuracy compared to the experimental data. The results showed that any increase in the NP volume concentration enhances the average Nusselt number ($\overline{Nu}$) and the normalized entropy generation, and reduces the thermal performance of the cavity in all orientations of the hot block. The maximum enhancement in cooling performance was 17.75% and occurred in the right-oriented hot block in the sand-based porous cavity. Furthermore, adding the NP to the base fluid leads to a more capable cooling system and enhances the irreversibility of the process.

Keywords: nanofluids; mixed convection; cooling; entropy generation; thermal conductivity; correlation

1. Introduction

Conventional cooling fluids typically yield relatively low performance and therefore they are unable to remove the desirable heat that the new industrial processes and equipment are generating. Today, most industries need a more efficient method of heat removal than the past. Thermal scientists have devised several innovative methods for cooling applications during the twentieth century, including but not limited to heat sinks, heat pipes, different types of heat exchangers, and so on. Nevertheless, none of them could attract the attention of the scientific community as much as the

nanofluids (NFs). NFs are relatively new type of heat transfer fluids with promising thermophysical properties. The ever-increasing number of the scientific publications and conferences as well as the industrial projects on the NF demonstrates the importance of this new category of cooling fluids.

NFs were introduced for the first time by Choi and Eastman [1] to enhance heat transfer of a cooling process. NFs are suspension of nanoscale particles in conventional heat transfer fluids like water, oil and ethylene glycol. This will enhance the thermophysical properties like density, viscosity, and thermal conductivity. Generally, NPs are synthesized from metals or oxides, as well as carbon nanotubes.

NF applications have been tried in a wide range of industrial processes and equipment including but not restricted to heat exchangers [2–6], nuclear reactors [7], medicine [8], automobiles [9,10], electronic chip cooling [11], renewable energies [12,13], heating and tempering processes [14–17], lubrication [18,19], combustion [20], etc. However, there are some other promising cooling technologies, which have attracted the attention of research communities, including but not restricted to phase change materials (PCMs) [21], electrocaloric effects [22], etc.

Enclosures also have different applications in a wide range of industries and equipment, such as cooling [23,24], Heating, Ventilation, and Air Conditioning (HVAC) [25], nuclear power [26], heat exchangers [27,28], renewable energies [29], etc.

Patterson and Imberger [30] simulated a differentially heated cavity under an unsteady natural convection. They also used a scale analysis to show that a number of initial flow types are possible. They realized that even though the steady state doesn't influence by the value of the Prandtl number, it is evident that the transient flows may depend strongly on this number.

Tiwari and Das [31] studied the heat transfer in a two-sided lid-driven square cavity using the NF, implementing a finite volume approach using the Semi-Implicit Method for Pressure Linked Equations (SIMPLE) algorithm. It has been found that the variation of the average Nusselt number $(\overline{Nu})$ is nonlinear with the solid volume fraction and the NPs are able to change the flow pattern of a fluid from free convection to the forced convection regime.

Chamkha et al. [32] studied the effects of heat sink and source and entropy generation on the Magnetohydrodynamics (MHD) mixed convection of copper-water NF in a lid-driven square porous enclosure with partial slip, numerically. Their results showed that the enhancement of the Hartmann number decreases the average Nu decreases considerably and NPs increase the entropy generation.

Al-Rashed et al. [33] et al. studied the effects of a hot elliptical centric cylinder, cavity angle and NP volume concentration in an inclined lid-driven cavity filled with water–alumina NF subjected to a mixed convection, numerically. They concluded that the Nu reduces with any increase in the Richardson number (Ri).

Mehmood et al. [34] investigated the alumina–water NF filled square porous cavity using a Koo-Kleinstreuer-Li (KKL) model in a mixed convection to examine how a nonlinear thermal radiation and inclined magnetic field can affect the heat and fluid field. To this end, a Darcy–Brinkman–Forchheimer extended model was employed to formulate the governing differential equations. They observed a growth in the maximum stream function with a rise in porosity and Da for a fixed value of Ri. They also found out an augmentation in maximum stream function value with a growth in thermal radiation parameter for free convection flows.

Baroon et al. [35] used a two-phase approach to simulate mixed convection and entropy generation in a lid-driven cavity with rotating cylinders filled by NF under a magnetic field. They found out that the heat transfer enhances with any reduction in the Hartmann number and Ri and any increase in the NP volume concentration. The presence of the cylinder and its angular velocity also improved the heat transfer. In addition, isothermal cylinders had a great impact on increasing heat transfer.

MHD mixed convection of the NF in an open C-shaped cavity was studied by Armaghani et al. [36]. Their enclosure was under constant magnetic field. NF entered the enclosure from the top right corner and exited from it from the bottom right corner. Eventually, they observed that with any increase in the aspect ratio of the enclosure, the heat transfer increases the local Nu by increasing the Ri.

The influence of partial slip on entropy generation and the MHD mixed convection in a square lid-driven porous enclosure saturated with a Cu–water NF was investigated by Chamkha et al. [37], numerically. Their results showed an augmentation in the heat generation/absorption parameter decreases the Nu. Also, when the volume fraction is raised, the Nu and entropy generation are reduced.

Armaghani et al. [38] studied numerically the water–alumina NF natural convection heat transfer and entropy generation in a baffled L-shaped cavity. They showed that increasing the Hartmann number reduces the entropy generation; however, the thermal performance increases. Increasing the aspect ratio raises heat transfer and thermal performance.

Mixed convection phenomena in a rectangular NF filled, non-Darcian porous enclosure with various wall speed ratios was studied by Nithyadevi et al. [39]. They implemented The Finite Volume Method (FVM) to solve transport equations for fluid and heat fields. In addition, the porous matrix was supposed to be rigid, containing with spherical, isotropic and homogeneous particles. They observed that dispersion of CuO NPs can enhance the heat transfer rate dramatically due to the impact of large thermal conductivity of the solid–fluid mixture in NF.

To the best knowledge of the authors, the heat transfer phenomenon of the NF in the I-shaped electronic chip has not been studied comprehensively. This paper investigates mixed convection heat transfer in an I-shaped porous enclosure filled with NF including an internal high temperature triangular solid block numerically using finite volume method. Two different porous media, sand and compact metallic powder, as well as different orientations of the internal hot block have been investigated. The CuO NP volume concentration in water was set in the range of 0 to 4 percent. This study implements Buongiorno's method with some assumptions, including laminar, incompressible, steady-state, homogenous, Newtonian NF, and a thermal equilibrium between NPs and the base fluid's molecules. To ensure that the prediction of effective thermal conductivity is accurate, a new predictive mathematical model with an acceptable accuracy is proposed. Using the second law of thermodynamics, entropy analysis, and thermal performance criteria, the best situation of the cavity consideration was determined.

2. Mathematic Modeling and Governing Equations

2.1. Problem Geometry

The geometry of the problem is shown in Figure 1. This was a lid-driven (bottom and upper lids) porous I-shaped enclosure saturated with water–CuO NF. The bottom and upper walls were moving in the right and left directions with a constant velocity of 10 m/s, respectively. All other walls were insulated. The temperatures of the cold and hot walls were set to 306 and 346 degrees Kelvin, respectively. As shown, the enclosure was made from porous media and included a hot triangular block at the geometric center. All shown scales are in centimeters. The problem was solved with four different cases of the hot block's orientation. The porous media also included two different materials: sand and compact metallic powder, which were considered separately.

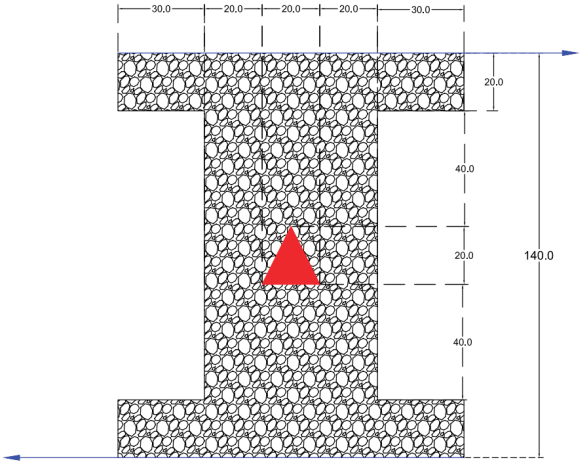

Figure 1. The problem geometry including a porous media with an internal hot block. All dimensions are in millimeters.

Figure 2 demonstrates the mesh network for the problem. Generally, all cases were meshed with two cells per millimeter. However, the number of cells per millimeter changed dramatically near to the hot block. It should be noted that the total cells of the mesh for up, down, left and right were 36,800, 48,000, 40,000 and 40,000, respectively.

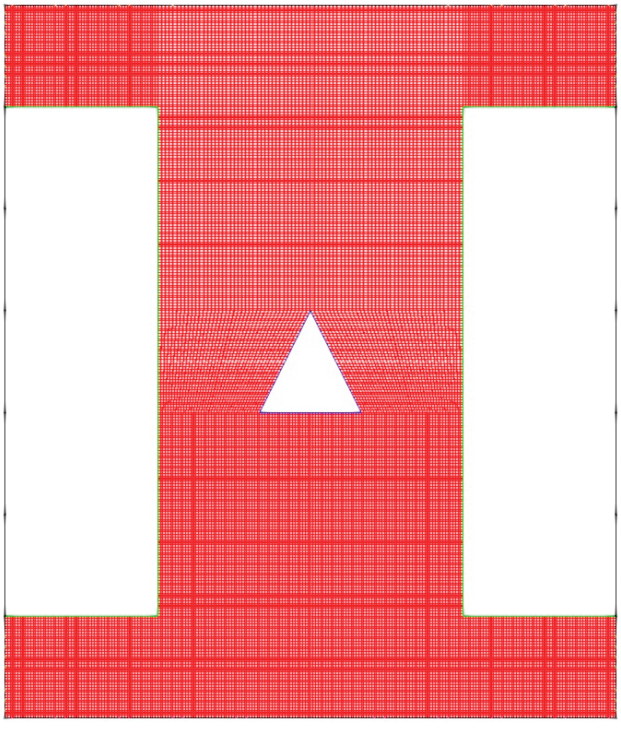

Figure 2. Mesh network for triangular hot block.

2.2. Material

The considered NF was CuO (copper oxide) produced by Iranshimi Company, Urmia, Iran. Such NPs are suspended in water as the base fluids up to 4% range of volume concentration. The mean diameter and NPs was assumed to be 29 nanometers and no surfactant was considered. Table 1 presents the reference values for different thermophysical properties of CuO NPs and water at the ambient conditions. The porous media were also considered to be made from sand and metallic powder with thermal conductivity of 3 W/m.K and 60 W/m.K, respectively. These two cases were solved separately. The porosity and diffusivity of the porous media for two cases were set to 0.4 and 10^{-8} m^2, respectively.

Table 1. Thermophysical properties of copper oxide nanoparticles (NPs) and water at the ambient conditions [40,41].

Material	Thermal Expansion (1/K)	Viscosity ($N.S/m^2$)	Thermal Conductivity (W/m.K)	Density (kg/m^3)	Heat Capacity (J/kg.K)
CuO	8.5×10^{-6}	-	18	6500	540
Water	2.07×10^{-4}	1.002×10^{-3}	0.598	998.3	4179

2.3. Governing Equations

Before going forward to describe the solution method, we need to take a look at the assumptions as follows: steady fluid flow, incompressible flow, laminar flow, two-dimensional flow, no chemical reactions, no viscous dissipation, no radiative heat transfer, and homogenous porous media.

To investigate the quality of the slip between the NPs and the base fluid's molecules, the conservation equations of mass and momentum are as follows:

The conservation of mass:

$$\nabla.\vec{V} = 0 \tag{1}$$

The conservation of momentum:

$$\nabla\left(\rho_{nf}\vec{V} \times \vec{V}\right) = -\left(\nabla\rho_{nf}\right)g.h - \nabla(P) + S \tag{2}$$

where S is the source term for porous media and is defined as:

$$S = -\left(\mu_{nf} \times d \times \vec{V} + \frac{\rho_{nf} \times f \times \vec{V}}{2}\right) \tag{3}$$

where d and f are the Darcy coefficient and Forchheimer coefficient, respectively. They are defined as follows [42]:

$$d = \frac{\varepsilon}{K} \tag{4}$$

$$f = \frac{3.5}{\sqrt{150} \times \sqrt{K} \times \varepsilon^{0.5}} \tag{5}$$

The conservation of energy for NF in a porous medium is as:

$$\rho_{nf} \times (1 - \beta_{nf}(T - T_0) \times C_{p,nf} \times V.\nabla T = \nabla\left(k_{eff}\right).\nabla T + \varepsilon\rho_{nf}C_{p,np} \times \left[D_B\nabla\varphi\nabla T + D_T\frac{\nabla T.\nabla T}{T}\right] \tag{6}$$

The NP volume concentration of NF should satisfy the equation below [42], in which $\vec{V}$, ε, k_{eff}, To and β are the vector of Darcy velocity, porosity, effective thermal conductivity of the porous media, the average temperature of the NF, and thermal expansion coefficient, respectively. Also, $C_{p,nf}$, φ, D_B, D_T, ρ, $C_{p,np}$ and μ are specific heat of NPs at the constant pressure, the NP volume concentration,

Brownian diffusion coefficient, thermophoresis coefficient, density of the NF, specific heat of NF at the constant pressure and dynamic viscosity of NF, respectively.

$$\frac{1}{\varepsilon}\vec{V}.\nabla\varphi = \nabla.\left[D_B\nabla\varphi + \frac{\nabla T}{T}\nabla\varphi\right] \tag{7}$$

where the Brownian diffusion coefficient and thermophoresis coefficient are defined by Equations (8) and (9), respectively [43,44]. In these equations, K_b, T, d_{np}, k_{bf} and k_{np} represent the Boltzmann constant, NF bulk temperature, mean diameter of the NPs, thermal conductivity of the base fluid and thermal conductivity of NPs, respectively.

$$D_B = \frac{K_b T}{3\pi\pi_{nf} d_{np}} \tag{8}$$

$$D_T = \left(\frac{0.26k_{bf}}{2k_{bf}+k_{np}}\right)\left(\frac{\mu_{nf}}{\rho_{nf}}\right)\varphi \tag{9}$$

We can calculate the total entropy generation using the Equation (10) [45].

$$S_{gen} = \left(\frac{k_{eff}}{T_0^2}\right)\times\left(\left(\frac{\partial T}{\partial x}\right)^2 + \left(\frac{\partial T}{\partial y}\right)^2\right) + \frac{\mu_{nf}}{KT_0}\times\left(u^2+v^2\right) + \frac{\mu_{nf}}{T_0}\times\left(2\left(\left(\frac{\partial u}{\partial x}\right)^2 + \left(\frac{\partial u}{\partial y}\right)^2\right)\right) + \left(\frac{\partial u}{\partial x} + \frac{\partial v}{\partial y}\right) \tag{10}$$

Integrating the effective thermal conductivity to the thermal conductivity of the base fluid times temperature gradient gives the average Nu as follows [45]:

$$\overline{Nu} = \int -\left(\frac{k_{eff}}{k_{bf}}\right)\times\left(\frac{\partial\theta}{\partial n}\right)dn \tag{11}$$

where, n is the direction perpendicular to the surface. Dimensionless temperature also is defined as Equation (12).

$$\theta = \frac{T - T_{cold}}{T_{hot} - T_{cold}} \tag{12}$$

To calculate the effective thermal conductivity of the porous media, we used the proportional equation as follows:

$$k_{eff} = \varepsilon k_{nf} + (1-\varepsilon)k_{solid} \tag{13}$$

where, k_{solid} and k_{nf} are the thermal conductivity of porous material and thermal conductivity of the NF. The density of NF also can be calculated as follows:

$$\rho_{nf} = \varphi\rho_{np} + (1-\varphi)\rho_{bp} \tag{14}$$

where, ρ_{np} and ρ_{bf} are the density of NPs and the density of the base fluid, respectively. To calculate the effective dynamic viscosity of NF, we used an empirical correlation [46]:

$$\frac{\mu_{nf}}{\mu_{bf}} = 1.475 - 0.319\varphi + 0.051\varphi^2 + 0.009\varphi^3 \tag{15}$$

The thermal expansion coefficient of NF could be determined using Equation (16).

$$\rho_{nf}\beta_{nf} = (1-\varphi)\rho_{bf} + \varphi\rho_{np}\beta_{np} \tag{16}$$

To find the enhancement achieved by the NF we used some concepts, including normalized Nu, normalized entropy generation, and thermal performance of the cavity [47], which are shown in Equations (17)–(19).

$$Nu^* = \frac{Nu}{Nu_0} \tag{17}$$

$$S^* = \frac{S_{gen}}{S_{gen,\,0}} \tag{18}$$

$$\eta = \frac{S_{gen}}{Nu} \tag{19}$$

where, Nu^*, S^*, η, Nu_0, $S_{gen,\,0}$ are the normalized Nu, normalized generation entropy, thermal performance of the cavity, the Nu of the base fluid, and entropy generation of the base fluid, respectively.

3. Proposing a New Correlation for CuO–Water Thermal Conductivity

To calculate the thermal effectivity of NF, we proposed a new predictive correlation based on the experimental data in the literature. To do so, we extracted 35,441 data on copper oxide-based NF thermal conductivity from the experimental studies [48–51] in order to correlate a new model. Then, we used the Gauss–Newton multivariable regression method and, after 31 iterations, the proposed Equation (20) resulted:

$$k_{eff} = k_{bf} \times \left(1 + 8.86068 \times \varphi \times \left(\frac{0.738066}{d_p}\right)^2\right) \tag{20}$$

where, k_{eff}, k_{bf}, φ, and d_p are effective thermal conductivity of NF (W/m.K), thermal conductivity of base fluid (W/m.K), NP volume concentration (%), and NP mean diameter (nm), respectively.

The average absolute error of the proposed correlation compared to the experimental data is 2.71%. To make sure about the validations of the proposed correlation, the predicted values are compared with an experimental study (Patel et al. [48]) represented in Figure 3. As shown, both data (experimental and predicted) show increasing values for the effective thermal conductivity with an increase in the NP volume concentration.

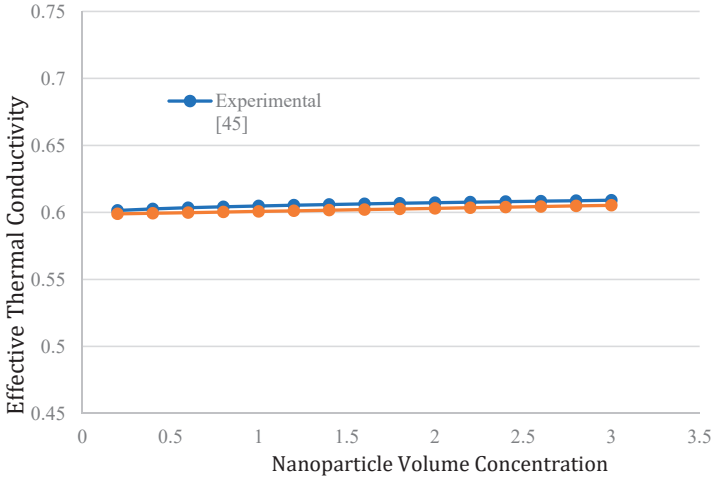

Figure 3. The comparison of the experimental data and predicted effective thermal conductivity by the proposed correlation against the NP volume concentration.

4. Numerical Method and Validation

Code Validation

The numerical method of the present work was validated in two steps with well-known references. First of all, we compared the results for air flowing in the cavity with the results of Davis [40]. Figure 4 shows the variations of the Nu versus the Ra (Ra) number in order to compare the results of the

numerical solution with the reference. The results demonstrate that the maximum error is 1.066%. Therefore, the numerical solution of the present work is as accurate at the first step.

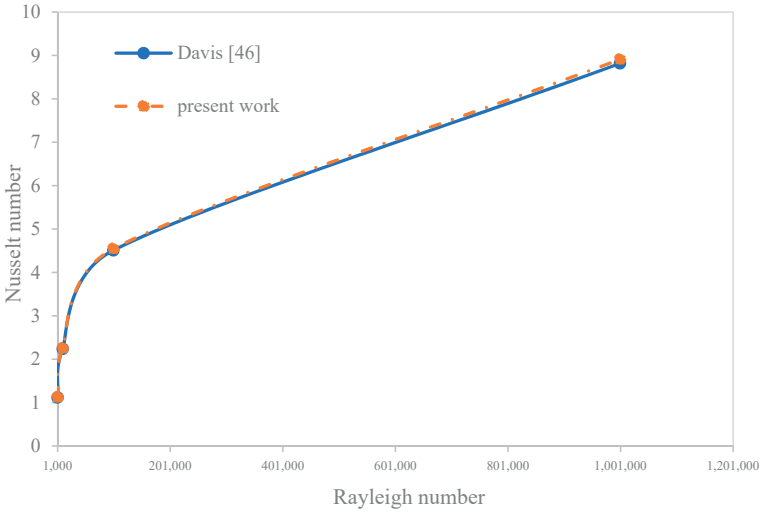

Figure 4. The comparison of the results of the present work with reference.

Then, we compared the results of the NF natural convection in a porous cavity with the experimental work of Nithiarasu et al. [42]. Table 2 shows the results of our numerical solution and comparison with the reference. It is clear that the present work gives very accurate results and the maximum error from the reference value is 1.069%. The error also decreases with any increase in the Ra number and porosity.

Table 2. The comparison of the results of the present study with the reference.

Test Number	Ra Number	Da	Porosity	Reference Nu [40]	Nu	Error
1	10^3	10^{-2}	0.4	1.008	1.0208	1.069%
2	10^6	10^{-4}	0.6	2.725	2.74106	0.589%
3	10^4	10^{-2}	0.9	1.64	1.65509	0.92%

An extensive mesh testing procedure was conducted using seven different meshes to obtain the appropriate grid size for the solution of the present problem considering constant parameters including the NP volume concentration and Ra number. Table 3 represents the obtained results for different size of meshes. Comparing the obtained numerical results of the average Nu, it was found that the value of the average Nu for 67,600 (260 × 260) elements showed a slight difference (0.32%) from the results calculated for other elements. Therefore, the grid size of 6218 nodes and 67,600 elements met the requirements of accurate solution with a proper grid independency for the present work.

Table 3. Grid independency test of the present work.

Test Number	NP Volume Concentration (%)	Ra Number	Reference Nu [44]	Mesh Size (Element Number)	Clock Time (Seconds)	Obtained Nu	Variation (%)
1	3	5.6×10^7	29.0769	140×140	334	29.2141	-
2	3	5.6×10^7	29.0769	160×160	651	28.8535	1.23
3	3	5.6×10^7	29.0769	180×180	940	28.5944	0.89
4	3	5.6×10^7	29.0769	200×200	1457	28.4005	0.67
5	3	5.6×10^7	29.0769	220×220	2209	28.2551	0.51
6	3	5.6×10^7	29.0769	240×240	3781	28.1401	0.40
7	3	5.6×10^7	29.0769	260×260	4247	28.0485	0.32

5. Results and Discussion

The obtained results will be presented in this section, including four orientations of the triangle and two porous media for different NP volume concentration from zero to 4%. Figure 5 shows the streamline contours of the 4% vol. NF in sand-based (left column) and metallic powder-based cavities (right column) with different orientations of the hot block. It seems that the contours are affected by the orientation of the hot block, especially for the left orientation. There are also more compact streamline contours for the NF in the metallic powder-based cavity.

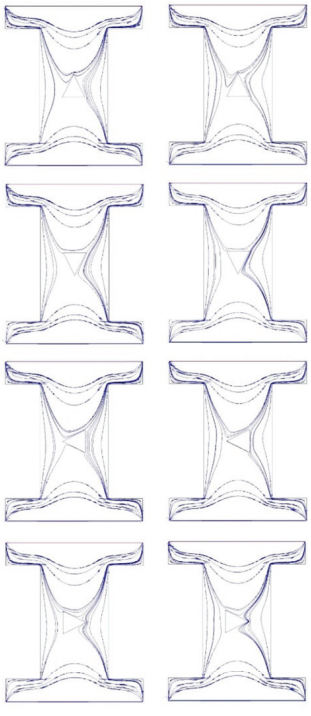

Figure 5. The streamline contours of the 4% vol. nanofluid (NF) in sand-based (**left column**) and metallic powder-based cavities (**right column**) with different orientations of the hot block.

Figure 6 also represents the temperature contours of the 4% vol. NF in sand-based (left column) and metallic powder-based (right column) cavities with different orientations of the hot block. It is found that the rotation of the hot block affects the temperature contours in both porous cavities.

Generally, there are higher temperatures in the metallic powder-based cavity than the sand-based cavity, due to the large difference in their thermal conductivities.

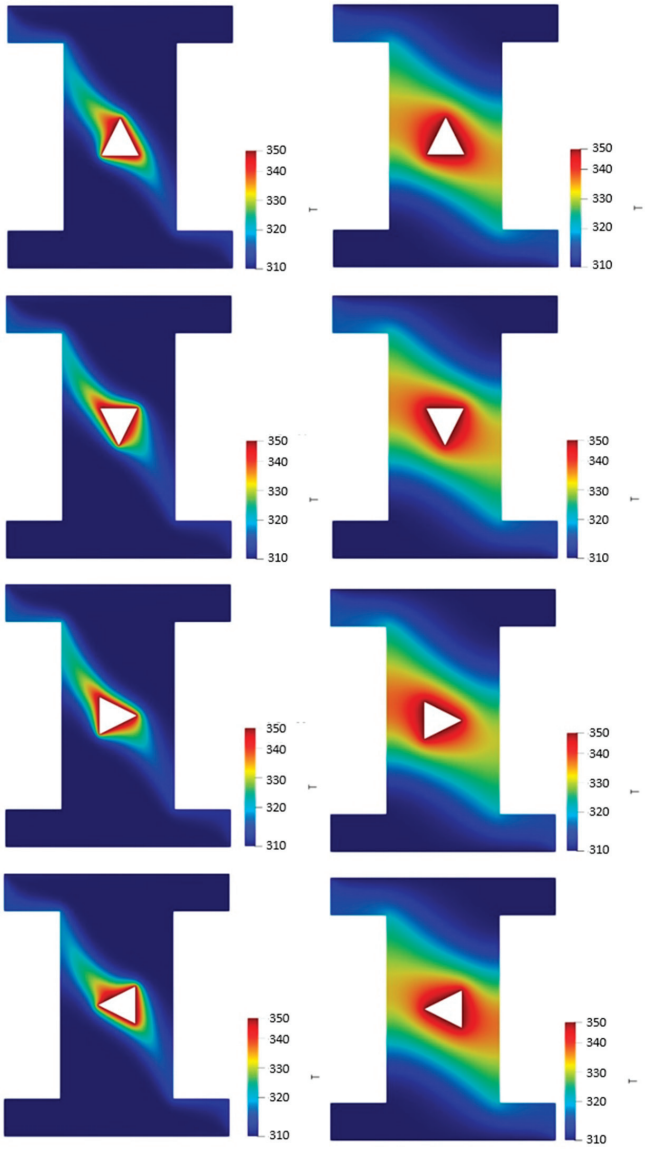

Figure 6. The temperature contours of the 4% vol. NF in sand-based (**left column**) and metallic powder-based cavities (**right column**) with different orientations of the hot block.

The entropy generation contours of the 4% vol. water-CuO NF in two different cavities including the sand-based (left column) and the metallic powder-based (right column) porous cavities with different orientations of the hot block are shown in Figure 7. It is clear that the entropy generation contours were affected by the different orientations of the hot block. However, changing the orientation did not change considerably the amount of the entropy and the elongation of the entropy contours.

It should be noted that the entropy generation contours for the metallic powder-based porous cavity were denser but more uniform than those of the sand-based porous cavity, in accordance with the temperature contours.

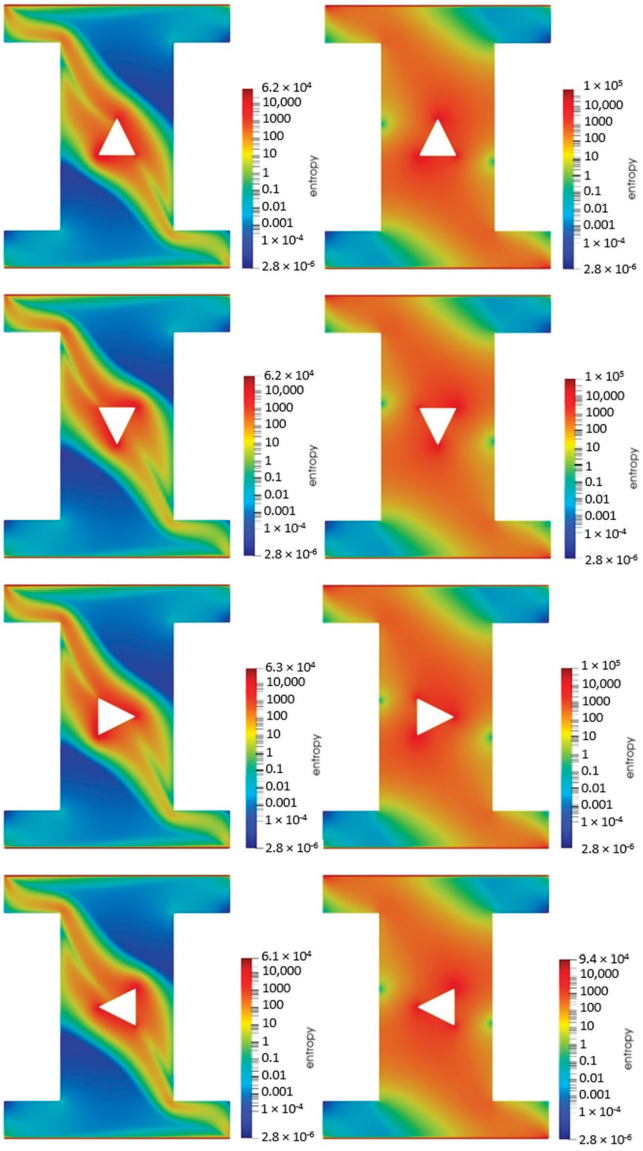

Figure 7. Entropy generation of the 4% vol. NF in two different cavities including the sand-based (**left column**) and the metallic powder-based (**right column**) porous cavities with different orientations of the hot block.

Figure 8 shows the NP distribution contours of the 4% vol. NF in two different cavities including the sand-based (left column) and the metallic powder-based (right column) porous cavities with different orientations of the hot block. The NP distribution contours in the sand-based porous cavity

show that there were more NPs below the hot block. The orientation of the hot block didn't change considerably the NP distribution contours, except for the left orientation. The different orientations also didn't change the NP distribution contours for the metallic powder-based porous cavity, except for the down orientation, which led to lower amount of NPs at the upper section of the cavity.

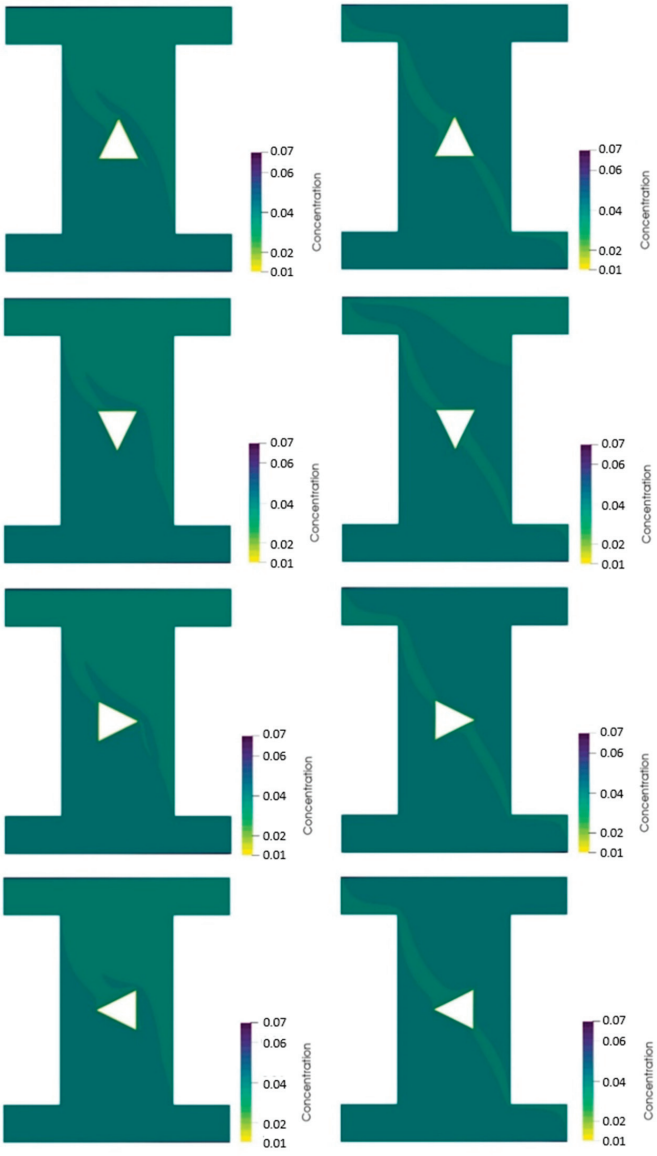

Figure 8. NP distribution contours of the 4% vol. NF in two different cavities including the sand-based (**left column**) and the metallic powder-based (**right column**) porous cavities with different orientations of the hot block.

Figure 9 shows the streamlines, temperature and entropy generation contours of the NF in the metallic powder-based porous cavity in the left, middle, and right columns, respectively for the

down-oriented hot block. The first, second and last row of Figure 9 is considered for the base fluid, 2% vol. and 4% vol. NF, respectively. It is shown that the streamlines were distributed symmetrically around the hot block and within the cavity for the base fluid. The streamlines were also aggregated at the left side of the hot block for more NP volume concentrations. Interestingly, there was no considerable difference between the temperature and the entropy generation contours for different NP volume concentrations.

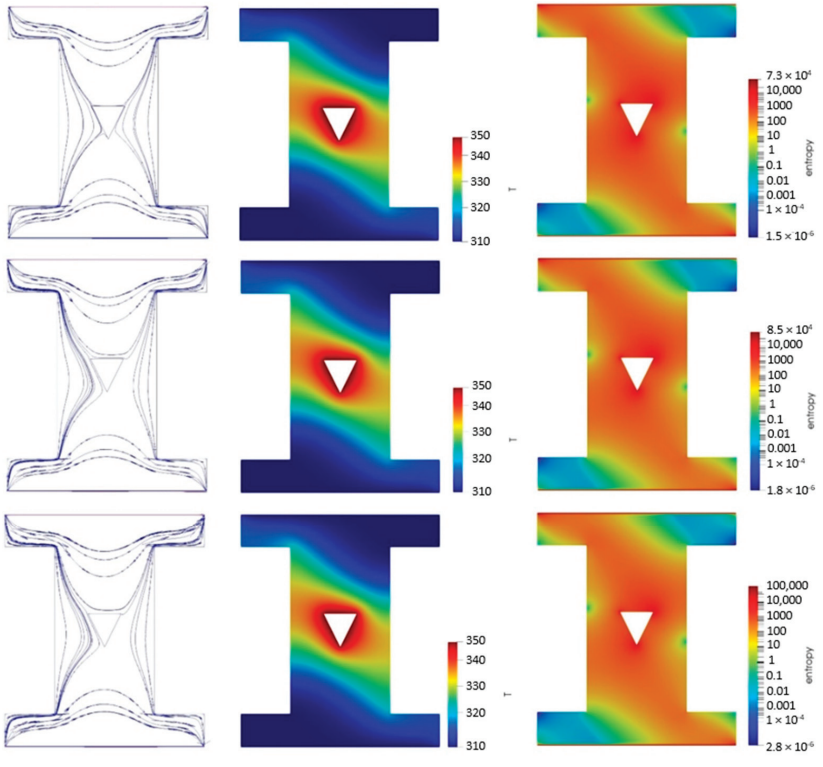

Figure 9. The streamlines (**left**), temperature (**middle**) and entropy generation (**right**) contours of the NF in the metallic powder-based porous cavity for the down-oriented hot block and the NP volume concentrations of 0% (**the first row**), 2% (**the middle row**) and 4% (**the bottom row**).

The average Nu as a function of the NP volume concentration and the orientation of the hot block for the sand-based porous cavity is shown in Figure 10. Generally, the average Nu rose continually with any increase in the NP volume concentration. However, the average Nu and its enhancement were higher for the right-oriented (17.75%), followed by up-oriented (11.00%), down-oriented (10.48%) and left-oriented (1.88%) hot block, respectively. Nevertheless, in all orientations of hot block, there was no considerable enhancement in the average Nu from 2% to 4% of the NP volume concentration, except the left-oriented hot block.

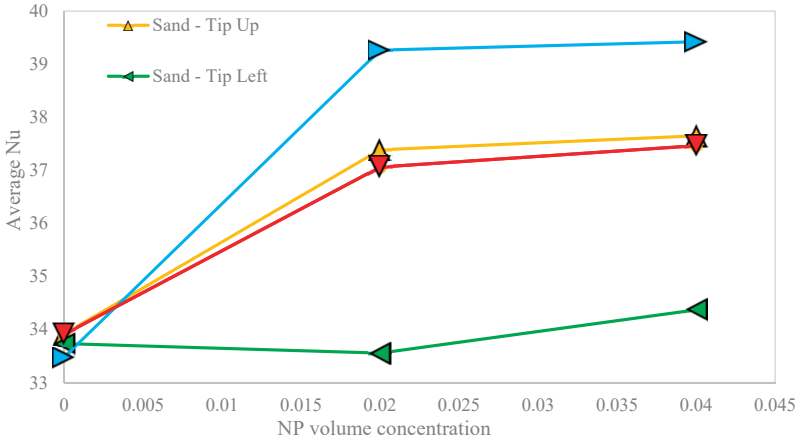

Figure 10. The variation of the average Nu versus the NP volume concentration for the sand-based porous cavity and different orientations of the hot block.

The variation of the average Nu versus the NP volume concentration for the metallic powder-based porous cavity and different orientations of the hot block is shown in Figure 11. Any increase in the NP volume concentration enhanced the average Nu, in all orientations of the hot block. Nevertheless, the enhancement in the average Nu was the maximum for the right-oriented hot block with 5.01%, followed by the down-oriented (4.85%), up-oriented (4.07%), and left-oriented (3.30%) hot block. It should be noted that the amount of the average Nu for the metallic powder-based porous cavity was roughly four times more than those of the sand-based porous cavity. The enhancement in the average Nu for the sand-based porous cavity was much more than those of the metallic powder-based porous cavity.

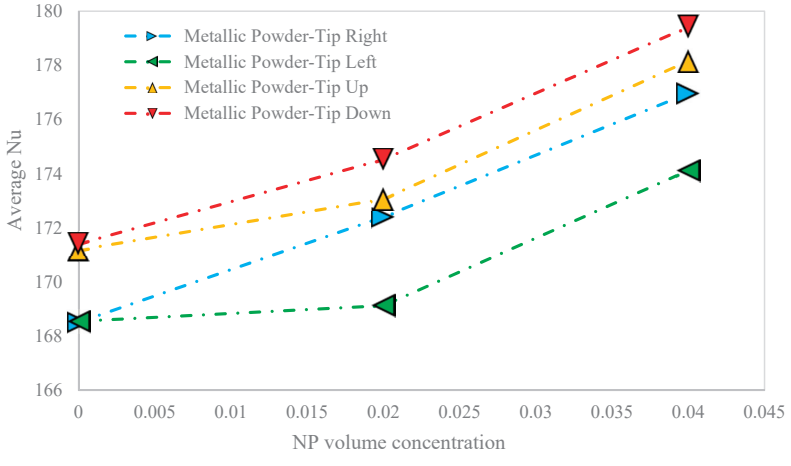

Figure 11. The variation of the average Nu versus the NP volume concentration for the metallic powder-based porous cavity and different orientations of the hot block.

The variation of the normalized Nu of the NF versus the NP volume concentration, in all cases is shown in Figure 12. The normalized Nu is defined as the ratio of the Nu to the Nu of the base fluids at the same conditions. It is obvious that there was a direct relationship between the normalized Nu

and the NP volume concentration, in all cases. The right-oriented hot block in the sand-based porous cavity yielded the higher value of the normalized Nu in all NP volume concentrations. Meanwhile, the left-oriented hot block gave the lowest normalized Nu in the two different porous cavities.

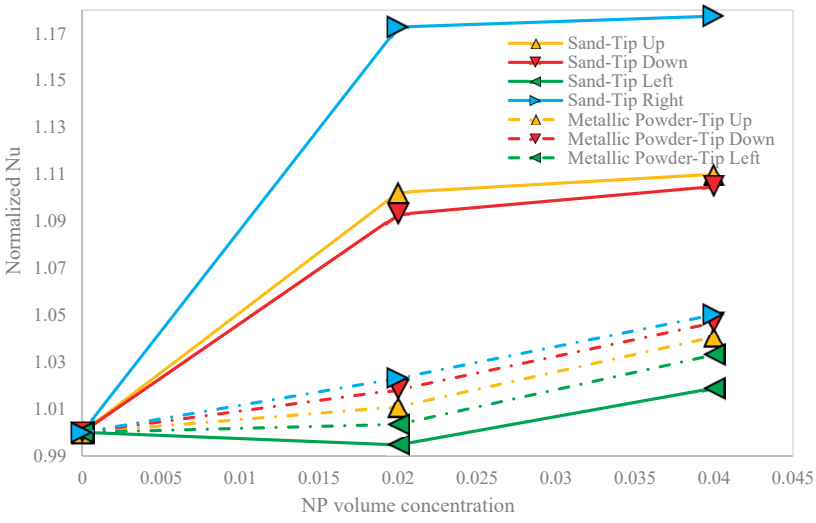

Figure 12. The variation of the normalized Nu of the NF versus the NP volume concentration, in all cases.

Figure 13 shows the normalized entropy generation against the NP volume concentration, in all cases. The normalized entropy generation is defined as the ratio of the entropy generation of the considered case to the entropy generation of the base fluid at the same conditions. Generally, any increase in the NP volume concentration led to a rise in the normalized entropy generation in all cases. Typically, the sand-based porous cavity gave more normalized entropy generation and, therefore, more irreversibility in the process. The right-oriented hot block in the sand-based porous cavity also yielded the highest value of the normalized entropy generation (1.035).

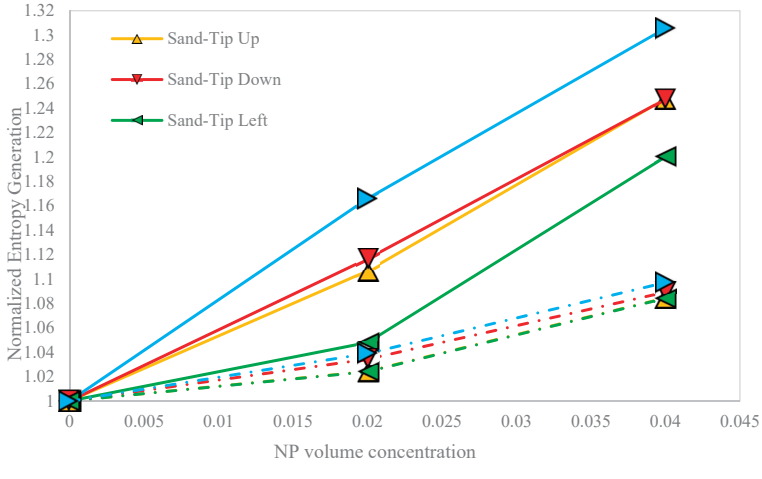

Figure 13. Normalized entropy generation against the NP volume concentration, in all cases.

Figure 14 also shows the thermal performance of the different porous cavities against the NP volume concentration in all cases. Thermal performance is the ratio of the normalized Nu versus the NP volume concentration and a higher thermal performance means that the Nu is achieved with less irreversibility. As it is shown, thermal performance of two porous cavities decreased with any increase in the NP volume concentration. It means that the cavity experienced more irreversibility in the process for NF than the base fluid to achieve the same Nu. Although adding the NP to the base fluid led to more Nu, it enhanced the irreversibility of the process. However, the maximum reduction in the thermal performance occurred in the left-oriented hot block in the sand-based porous cavity.

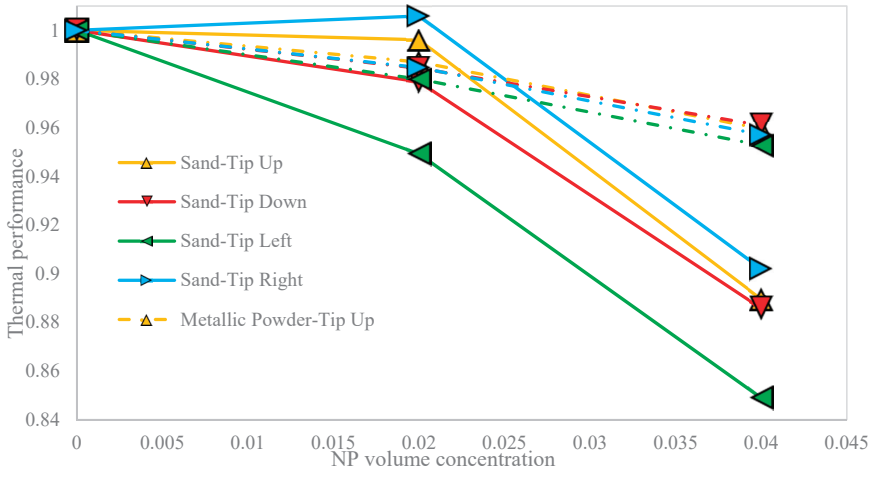

Figure 14. The thermal performance of the different porous cavities against the NP volume concentration in all cases.

6. Conclusions

The NF mixed convection in a porous I-shaped cavity was investigated numerically. The NF was assumed to be a mixture of water and CuO NPs up to 4% of volume concentration. A finite volume method was employed to solve the governing equations of eight cases as the combinations of four orientations of the internal triangular hot block, and two porous media: sand and compact metallic powder.

A new predictive correlation for effective thermal conductivity of the NF is proposed using the multivariable regression method based on the experimental data. It is shown that the proposed correlation predicted the effective thermal conductivity of the NF with a very low error compared to the experimental data. The major findings of the study are as follows:

1. The rotation of the hot block affected the temperature and entropy generation contours in both porous cavities.
2. Any increase in the NP volume concentration enhanced the average Nu, the cooling performance and the normalized entropy generation, and reduced the thermal performance of the cavity in all orientations of the hot block.
3. The average Nu for the metallic powder-based porous cavity was roughly four times more than that of the sand-based porous cavity.
4. The enhancement in the average Nu for the sand-based porous cavity was much more than that of the metallic powder-based porous cavity. The maximum enhancement in the average Nu was 17.75%.

5. The right-oriented hot block in the sand-based porous cavity yielded the higher value of the normalized Nu in all NP volume concentrations, while the left-oriented hot block gave the lowest normalized Nu in the two different porous cavities.
6. The sand-based porous cavity gave more normalized entropy generation and, therefore, more irreversibility in the process.
7. Adding the NP to the base fluid led to more Nu, enhancing the irreversibility of the process. However, the maximum reduction in the cooling performance occurred in the left-oriented hot block in the sand-based porous cavity.
8. The best and worst cooling performance was achieved with the 2% vol. NF in the sand-based right-oriented internal hot block and 4% vol. NF in the sand-based left-oriented internal hot block.

Author Contributions: A.A. and M.M. did the simulations, analyzed the work, and mainly wrote the paper, R.G. supervised the theoretical part, T.A. defined the project and mainly supervised the work. M.-I.P. and M.S.P. revised the manuscript and served as the advisors of the project. All authors have read and agreed to the published version of the manuscript.

Funding: This research received no external funding.

Conflicts of Interest: The authors declare no conflict of interest.

References

1. Choi, S.U.S.; Eastman, J.A. *Enhancing Thermal Conductivity of Fluids with Nanoparticles*; ASME: New York, NY, USA, 1995.
2. Molana, M. A Comprehensive Review on the Nanofluids Application in the Tubular Heat Exchangers. *Am. J. Heat Mass Transf.* **2016**, *3*, 352–381. [CrossRef]
3. Moradikazerouni, A.; Afrand, M.; Alsarraf, J.; Wongwises, S.; Asadi, A.; Nguyen, T.K. Investigation of a computer CPU heat sink under laminar forced convection using a structural stability method. *Int. J. Heat Mass Transf.* **2019**, *134*, 1218–1226. [CrossRef]
4. Mashayekhi, R.; Khodabandeh, E.; Akbari, O.A.; Toghraie, D.; Bahiraei, M.; Gholami, M. CFD analysis of thermal and hydrodynamic characteristics of hybrid nanofluid in a new designed sinusoidal double-layered microchannel heat sink. *J. Therm. Anal. Calorim.* **2018**, *122*, 1–11. [CrossRef]
5. Hoseinzadeh, S.; Sahebi, S.A.R.; Ghasemiasl, R. Effect of Al2O3/water nanofluid on thermosyphon thermal performance. *Eur. Phys. J. Plus* **2017**, *132*, 197. [CrossRef]
6. Banooni, S.; Zarea, H.; Molana, M. Thermodynamic and Economic Optimization of Plate Fin Heat Exchangers Using the Bees Algorithm. *Heat Transf. Asian Res.* **2014**, *43*, 427–446. [CrossRef]
7. Buongiorno, J.; Hu, L.-W.; Kim, S.J.; Hannink, R.; Truong, B.A.O.; Forrest, E. Nanofluids for enhanced economics and safety of nuclear reactors: An evaluation of the potential features, issues, and research gaps. *Nucl. Technol.* **2008**, *162*, 80–91. [CrossRef]
8. Tripathi, D.; Bég, O.A. A study on peristaltic flow of nanofluids: Application in drug delivery systems. *Int. J. Heat Mass Transf.* **2014**, *70*, 61–70. [CrossRef]
9. Kakavand, H.; Molana, M. A numerical study of heat transfer charcteristics of a car radiator involved nanofluids. *Heat Transf. Asian Res.* **2017**, *47*, 1–15. [CrossRef]
10. Molana, M. On the Nanofluids Application in the Automotive Radiator to Reach the Enhanced Thermal Performance: A Review. *Am. J. Heat Mass Transf.* **2017**, *4*, 168–187. [CrossRef]
11. Chamkha, A.J.; Molana, M.; Rahnama, A.; Ghadami, F. On the nanofluids applications in microchannels: A comprehensive review. *Powder Technol.* **2018**, *332*, 287–322. [CrossRef]
12. Rahbar, N.; Esfahani, J.A.; Asadi, A. An experimental investigation on productivity and performance of a new improved design portable asymmetrical solar still utilizing thermoelectric modules. *Energy Convers. Manag.* **2016**, *118*, 55–62. [CrossRef]
13. Dabiri, S.; Khodabandeh, E.; Poorfar, A.K.; Mashayekhi, R.; Toghraie, D.; Zade, S.A.A. Parametric investigation of thermal characteristic in trapezoidal cavity receiver for a linear Fresnel solar collector concentrator. *Energy* **2018**, *153*, 17–26. [CrossRef]
14. Izadi, S.; Armaghani, T.; Ghasemiasl, R.; Chamkha, A.J.; Molana, M. A comprehensive review on mixed convection of nanofluids in various shapes of enclosures. *Powder Technol.* **2018**, *343*, 880–907. [CrossRef]

15. Hoseinzadeh, S.; Sahebi, S.A.R.; Ghasemiasl, R.; Majidian, A.R. Experimental analysis to improving thermosyphon (TPCT) thermal efficiency using nanoparticles/based fluids (water). *Eur. Phys. J. Plus* **2017**, *132*, 197. [CrossRef]
16. Ghasemiasl, R.; Taheri, M.A.; Molana, M.; Raoufi, N. Experimental investigation of thermal performance of the graphene oxide–coated plates. *Heat Transf. Res.* **2020**, *49*, 519–532. [CrossRef]
17. Molana, M.; Zarrinderafsh, V.; Chamkha, A.J.; Rafizadeh, S.; Izadi, S. Magnetohydrodynamics convection in nanofluids-filled cavities: A review. *Heat Transf. Res.* **2020**, *49*, 1–26. [CrossRef]
18. Asadi, A.; Asadi, M.; Rezaei, M.; Siahmargoi, M.; Asadi, F. The effect of temperature and solid concentration on dynamic viscosity of MWCNT/MgO (20–80)–SAE50 hybrid nano-lubricant and proposing a new correlation: An experimental study. *Int. Commun. Heat Mass Transf.* **2016**, *78*, 48–53. [CrossRef]
19. Asadi, A.; Asadi, M.; Rezaniakolaei, A.; Rosendahl, L.A.; Wongwises, S. An experimental and theoretical investigation on heat transfer capability of Mg (OH) 2/MWCNT-engine oil hybrid nano-lubricant adopted as a coolant and lubricant fluid. *Appl. Therm. Eng.* **2018**, *129*, 577–586. [CrossRef]
20. Basu, S.; Miglani, A. Combustion and heat transfer characteristics of nanofluid fuel droplets: A short review. *Int. J. Heat Mass Transf.* **2016**, *96*, 482–503. [CrossRef]
21. Krašna, M.; Klemenčič, E.; Kutnjak, Z.; Kralj, S. Phase-changing materials for thermal stabilization and thermal transport. *Energy* **2018**, *162*, 554–563. [CrossRef]
22. Klemenčič, E.; Trček, M.; Kutnjak, Z.; Kralj, S. Giant electrocaloric response in smectic liquid crystals with direct smectic-isotropic transition. *Sci. Rep.* **2019**, *9*, 1721. [CrossRef]
23. Armaghani, T.; Ismael, M.A.; Chamkha, A.J.; Pop, I. Mixed Convection and Entropy Generation of an Ag-Water Nanofluid in an Inclined L-Shaped Channel. *Energies* **2019**, *12*, 1150. [CrossRef]
24. Abedini, A.; Emadoddin, S.; Armaghani, T. Numerical analysis of mixed convection of different nanofluids in concentric annulus. *Int. J. Numer. Methods Heat Fluid Flow* **2019**, *29*, 1506–1525. [CrossRef]
25. Alsabery, A.I.; Chamkha, A.J.; Hashim, I.; Siddheshwar, P.G. Effects of Nonuniform Heating and Wall Conduction on Natural Convection in a Square Porous Cavity Using LTNE Model. *J. Heat Transf.* **2017**, *139*, 122008. [CrossRef]
26. Burger, S.; Riciputi, L.R.; Turgeon, S.; Bostick, D.; McBay, E.; Lavelle, M. A high efficiency cavity ion source using TIMS for nuclear forensic analysis. *J. Alloys Compd.* **2007**, *444*, 660–662. [CrossRef]
27. Daloglu, A. Study on overall heat transfer coefficient for a rotating cavity type heat exchanger. *Int. Commun. Heat Mass Transf.* **1999**, *26*, 861–867. [CrossRef]
28. Rashad, A.M.; Mansour, M.A.; Armaghani, T.; Chamkha, A.J. MHD mixed convection and entropy generation of nanofluid in a lid-driven U-shaped cavity with internal heat and partial slip. *Phys. Fluids* **2019**, *31*, 42006. [CrossRef]
29. Marandi, O.F.; Ameri, M.; Adelshahian, B. The experimental investigation of a hybrid photovoltaic-thermoelectric power generator solar cavity-receiver. *Sol. Energy* **2018**, *161*, 38–46. [CrossRef]
30. Patterson, J.; Imberger, J. Unsteady natural convection in a rectangular cavity. *J. Fluid Mech.* **1980**, *100*, 65–86. [CrossRef]
31. Tiwari, R.K.; Das, M.K. Heat transfer augmentation in a two-sided lid-driven differentially heated square cavity utilizing nanofluids. *Int. J. Heat Mass Transf.* **2007**, *50*, 2002–2018. [CrossRef]
32. Chamkha, A.J.; Rashad, A.M.; Mansour, M.A.; Armaghani, T.; Ghalambaz, M. Effects of heat sink and source and entropy generation on MHD mixed convection of a Cu-water nanofluid in a lid-driven square porous enclosure with partial slip. *Phys. Fluids* **2017**, *29*, 52001. [CrossRef]
33. Al-Rashed, A.A.A.A.; Shahsavar, A.; Akbari, M.; Toghraie, D.; Akbari, M.; Afrand, M. Finite Volume Simulation of mixed convection in an inclined lid-driven cavity filled with nanofluids: Effects of a hot elliptical centric cylinder, cavity angle and volume fraction of nanoparticles. *Phys. A Stat. Mech. Appl.* **2019**, *527*, 1–17. [CrossRef]
34. Mehmood, K.; Hussain, S.; Sagheer, M. Numerical simulation of MHD mixed convection in alumina–water nanofluid filled square porous cavity using KKL model: Effects of non-linear thermal radiation and inclined magnetic field. *J. Mol. Liq.* **2017**, *238*, 485–498. [CrossRef]
35. Barnoon, P.; Toghraie, D.; Dehkordi, R.B.; Abed, H. MHD mixed convection and entropy generation in a lid-driven cavity with rotating cylinders filled by a nanofluid using two phase mixture model. *J. Magn. Magn. Mater.* **2019**, *483*, 224–248. [CrossRef]

36. Armaghani, T.; Esmaeili, H.; Mohammadpoor, Y.A.; Pop, I. MHD mixed convection flow and heat transfer in an open C-shaped enclosure using water-copper oxide nanofluid. *Heat Mass Transf.* **2018**, *54*, 1791–1801. [CrossRef]
37. Chamkha, A.J.; Rashad, A.M.; Armaghani, T.; Mansour, M.A. Effects of partial slip on entropy generation and MHD combined convection in a lid-driven porous enclosure saturated with a Cu–water nanofluid. *J. Therm. Anal. Calorim.* **2018**, *132*, 1291–1306. [CrossRef]
38. Armaghani, T.; Kasaeipoor, A.; Momayez, L.; Rashidi, M.M.; Mohammadpoor, Y. Entropy generation analysis of mixed convection with considering magneto-hydrodynamic effects in an open C-shaped cavity. *Therm. Sci.* **2018**, *23*, 112.
39. Nithyadevi, N.; Begum, A.S.; Oztop, H.F.; Abu-Hamdeh, N. Mixed convection analysis in heat transfer enhancement of a nanofluid filled porous enclosure with various wall speed ratios. *Int. J. Heat Mass Transf.* **2017**, *113*, 716–729. [CrossRef]
40. Mintsa, H.A.; Roy, G.; Nguyen, C.T.; Doucet, D. New temperature dependent thermal conductivity data for water-based nanofluids. *Int. J. Therm. Sci.* **2009**, *48*, 363–371. [CrossRef]
41. Nassan, T.H.; Heris, S.Z.; Noie, S.H. A comparison of experimental heat transfer characteristics for Al2O3/water and CuO/water nanofluids in square cross-section duct. *Int. Commun. Heat Mass Transf.* **2010**, *37*, 924–928. [CrossRef]
42. Nithiarasu, P.; Ravindran, K. A new semi-implicit time stepping procedure for buoyancy driven flow in a fluid saturated porous medium. *Comput. Methods Appl. Mech. Eng.* **1998**, *165*, 147–154. [CrossRef]
43. Seetharamu, K.N.; Sundararajan, T. Natural convective heat transfer in a fluid saturated variable porosity medium. *Pergamon. Inf. J. Heat Man Tramfir.* **1997**, *40*, 16.
44. Buongiorno, J. A non-homogeneous equilibrium model for convective transport in flowing nanofluids. *Heat Transf. Eng.* **2005**, *128*, 1–9.
45. Armaghani, T.; Ismael, M.A.; Chamkha, A.J. Analysis of entropy generation and natural convection in an inclined partially porous layered cavity filled with a nanofluid. *Can. J. Phys.* **2016**, *95*, 238–252. [CrossRef]
46. Nguyen, C.T.; Desgranges, F.; Roy, G.; Galanis, N.; Maré, T.; Boucher, S.; Mintsa, H.A. Temperature and particle-size dependent viscosity data for water-based nanofluids–Hysteresis phenomenon. *Int. J. Heat Fluid Flow* **2007**, *28*, 1492–1506. [CrossRef]
47. Ismael, M.A.; Armaghani, T.; Chamkha, A.J. Mixed convection and entropy generation in a lid-driven cavity filled with a hybrid nanofluid and heated by a triangular solid. *Heat Transf. Res.* **2018**, *49*, 17. [CrossRef]
48. Patel, H.E.; Sundararajan, T.; Das, S.K. An experimental investigation into the thermal conductivity enhancement in oxide and metallic nanofluids. *J. Nanoparticle Res.* **2010**, *12*, 1015–1031. [CrossRef]
49. Azmi, W.H.; Sharma, K.V.; Mamat, R.; Alias, A.B.S.; Misnon, I.I. Correlations for thermal conductivity and viscosity of water based nanofluids. *IOP Conf. Ser. Mater. Sci. Eng.* **2012**, *36*, 012029. [CrossRef]
50. Li, C.H.; Peterson, G.P. Experimental investigation of temperature and volume fraction variations on the effective thermal conductivity of nanoparticle suspensions (nanofluids). *J. Appl. Phys.* **2006**, *99*, 084314. [CrossRef]
51. De Davis, G. Natural convection of air in a square cavity: A bench mark numerical solution. *Int. J. Numer. Methods Fluids* **1983**, *3*, 249–264. [CrossRef]

nanomaterials

MDPI

Article

Computational Study of Heat Transfer inside Different PCMs Enhanced by Al_2O_3 Nanoparticles in a Copper Heat Sink at High Heat Loads

Nadezhda S. Bondareva, Nikita S. Gibanov and Mikhail A. Sheremet *

Laboratory on Convective Heat and Mass Transfer, Tomsk State University, Tomsk 634050, Russia; bondarevans@mail.tsu.ru (N.S.B.); gibanov@mail.tsu.ru (N.S.G.)

* Correspondence: sheremet@math.tsu.ru; Tel.: +7-3822-529740

Received: 5 January 2020; Accepted: 3 February 2020; Published: 7 February 2020

Abstract: The cooling of electronic elements is one of the most important problems in the development of architecture in electronic technology. One promising developing cooling method is heat sinks based on the phase change materials (PCMs) enhanced by nano-sized solid particles. In this paper, the influence of the PCM's physical properties and the concentration of nanoparticles on heat and mass transfer inside a closed radiator with fins, in the presence of a source of constant volumetric heat generation, is analyzed. The conjugate problem of nano-enhanced phase change materials (NePCMs) melting is considered, taking into account natural convection in the melt under the impact of the external convective cooling. A two-dimensional problem is formulated in the non-primitive variables, such as stream function and vorticity. A single-phase nano-liquid model is employed to describe the transport within NePCMs.

Keywords: nanoparticles; phase change material; natural convection; high heat loads

1. Introduction

The advent of electronic technologies with increased power and expanding their scope is ongoing on continuously and a large role in the development of technology in recent decades has been played by heat removal systems. The requirements for a heat sink depend not only on capacities but they are also associated with geometric parameters. High heat dissipation in a small volume requires a high effective heat capacity of the system and intensive heat dissipation. In addition, it is often required that the entire system occupies a small volume. To increase performance, metal radiators are filled with phase change materials (PCMs), which not only allows for the extension of the operating time of the device. When the melting point is reached, a large amount of energy is spent on melting at a constant temperature, which allows the use of such materials for both thermal control and thermal energy storage systems [1–4]. In such systems, PCMs significantly reduce the operating temperature and make it possible to increase thermal electrical efficiency of a photovoltaic/thermal system [1,5–8]. Adding materials with a low melting point to building structures can reduce energy costs for air conditioning systems and reduce temperature fluctuations associated with daily thermal cycles [9–12].

To accelerate the heat transfer processes inside the PCM, various nanoadditives with high thermal conductivity can be used. For the present, there are a large number of scientific studies devoted to the effect of nanoparticles on the melting processes, which note both a positive effect on heat transfer and a negative one [13–16]. The effect of adding nanoparticles depends on many factors, including the thermal and geometric properties of the system, as well as the thermophysical properties of the materials [17].

In [15], thermal energy storage based on coconut oil with CuO nanoparitcles was analyzed. It was experimentally shown that melting occurs faster when nanoparticles are added. In [16], RT35HC

enhanced by Al_2O_3 nanoadditives was used to lower the operating temperatures of the photovoltaic panel. It was shown that the use of a PCM heat sink can reduce the surface temperature by 34 °C at high heat fluxes, while the addition of nanoparticles to the PCM further reduces the temperature by 4.5 °C.

A numerical study of n-octadecane melting inside a closed copper radiator in the presence of a source with volumetric heat generation showed that the addition of nanoparticles can slightly reduce the temperature in the source at low concentrations (Φ = 1%), but at high nanoparticle concentrations, the melt circulation rate can be decreased by 57% ($\Phi \geq 3\%$), which can lead to an increase in the temperature of the element [18].

In experimental study [13], the melting of n-octadecane with TiO_2 nanoparticles (titanium oxide) inside the rectangular cavity heated from the side wall at a constant heat flux and thermally insulated on other sides was considered. The mass fraction of nanoparticles ranged from 0% to 4%. It was shown that at q″ = 10,000 W/m^2, the addition of 1, 2, and 4 wt % nanoparticles leads to a decrease in the quasi-steady Nusselt number by more than 10%, 36%, and 40%, respectively. This is related to the fact that natural convection plays a large role in heat transfer. However, an increase in viscosity leads to a decrease in the intensity of convective heat and mass transfer and an increase in thermal conductivity does not compensate for the effect of viscosity increasing. Heat transfer in the phase change materials is complicated by the presence of a moving border. Many studies have been shown that, at the initial stage, conductive heat transfer dominates in the region, however, with the growth of the melt region, an intensive regime of natural convection develops [18–21].

Nanoparticles have a complex effect on the processes of heat and mass transfer in liquids. On the one hand, there is an increase in the effective thermal conductivity of the suspension with increasing in conductive heat transfer. On the other hand, an increase in the melt viscosity affects hydrodynamics and can significantly reduce convective heat transfer. There are many numerical and experimental studies on the performance of heat sinks based on nano-enhanced phase change materials (NePCMs). In some of these studies, a positive effect of nanoparticles on heat transfer is noted, and, in others, there is a decrease in heat sink performance at high concentrations of nanoparticles. These two effects play a decisive role in the effectiveness of using nanoadditives. The intensity of thermal processes in a nano-enhanced PCM is determined not only by the parameters of the system and thermal conditions but also by the properties of base fluid and nano-sized particles. The melting temperature of the material is one of the determining factors in the heat transfer regimes for the system. This is evidenced by the studies devoted to the analysis of the influence of the PCM melting point on the efficiency of using heat sink [22,23]. Using the melting latent heat of materials allows for the absorption of a large amount of energy reaching the melting point.

Phase change materials with different melting points were used in experimental study [22]. The paraffin wax (T_m = 56–58 °C, L_m = 173.6 kJ/kg), n-eicosane (T_m = 36.5 °C, L_m = 237.4 kJ/kg), RT–54 (T_m = 54 °C, L_m = 200 kJ/kg), RT–44 (T_m = 44 °C, L_m = 250 kJ/kg), RT–35HC (T_m = 35 °C, L_m = 240 kJ/kg), and SP–31 (T_m = 31 °C, L_m = 210 kJ/kg) were employed for analysis. Heat transfer in a PCM-based pin-finned heat sink alumina radiator was studied under different heat loads. It was shown that at the highest considered power, the material with a high melting point RT–54 is turned out to be the most suitable. It should be also noted that at low critical temperatures (T = 45 °C) it is more efficient to use SP-31. At critical temperatures of T_{cr} = 60 °C, paraffin wax with T_f = 56–58 °C turned out to be the most effective one.

In [23], the performance of an alumina heat sink with two different PCMs, namely, n-eicosane and 1-hexadecanol, was studied. The authors showed that, to increase the productivity of the heat sink, the PCM with the highest melting point was preferable. It was also noted that, when using a PCM with a low T_m, the heat sink performance increases at low operation temperature. Thus, the choice of PCM should be based on the operating conditions of the device, technical requirements, power, and other parameters. In [24], three different PCMs in finned heat sink were considered. The investigation showed an evolution of heat sink temperature for different PCMs. When the temperature of the phase

transition is reached, the melting process begins, and the temperature, at the same time, reaches a constant level and practically does not change. The higher melting temperature of the material, the more the radiator heats up before the phase transition, accompanied by intense absorption of energy, begins. After the material has completely melted, the temperature in the region starts to rise again. Here, the latent heat of melting plays a large role, which affects the effective heat capacity of the heat sink and, therefore, the duration of the process.

In this paper, five different phase change materials with different melting points in the range from 28 to 81 °C with Al_2O_3 nanoparticles in a closed metal radiator to cool the source of constant volumetric heat release at high heat loads were considered. The two-dimensional problem of conjugated natural convection, taking into account phase transitions, was formulated in dimensionless variables such as the stream function, vorticity, and temperature with the smoothing of the jump in internal energy at the boundary of the phase transition. As a working liquid, the following PCMs were selected: n-octadecane, Capric acid, Lauric acid, RT–50, RT–80.

2. Mathematical Model

Figure 1 shows the model of the region under consideration, namely, a closed metal rectangular profile with dimensions of $L \times H$, where L = 3.0 cm and H = 1.5 cm, and internal metal fins, between which the PCM enhanced by Al_2O_3 nanoparticles is located. A rectangular source of constant volumetric heat generation with the properties of silicon with a total power of 400 W per meter length is located under the metal profile.

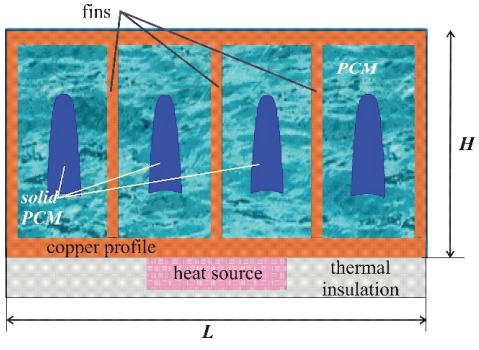

Figure 1. Domain of interest.

The temperature of the «source–heat sink» system at the initial time coincided with the ambient temperature T_0 = 23 °C, which was considered constant. As the external boundary conditions, the following relations were set: the upper and side boundaries of the radiator were cooled by air convective cooling with a constant heat transfer coefficient γ = 20 W/(m^2·K), and the remaining boundaries were considered to be heat-insulated. Natural convection in a viscous melt has been described using the Boussinesq approximation. A nano-enhanced phase change material was considered as a single-phase medium with constant thermophysical properties.

The equations of natural thermogravitational convection in the melt have the following form [18]:

$$\frac{\partial u}{\partial x} + \frac{\partial v}{\partial y} = 0 \tag{1}$$

$$(\rho_l)_{nm}\left(\frac{\partial u}{\partial t} + u\frac{\partial u}{\partial x} + v\frac{\partial u}{\partial y}\right) = -\frac{\partial p}{\partial x} + (\mu_l)_{nm}\left(\frac{\partial^2 u}{\partial x^2} + \frac{\partial^2 u}{\partial y^2}\right) \tag{2}$$

$$(\rho_l)_{nm}\left(\frac{\partial v}{\partial t} + u\frac{\partial v}{\partial x} + v\frac{\partial v}{\partial y}\right) = -\frac{\partial p}{\partial y} + (\mu_l)_{nm}\left(\frac{\partial^2 v}{\partial x^2} + \frac{\partial^2 v}{\partial y^2}\right) + (\rho_l\beta_l)_{nm}g(T - T_m) \tag{3}$$

The energy equations for an NePCM, taking into account the phase boundary, are written separately for solid and liquid phases [18]:

$$\frac{\partial h}{\partial t} = (k_s)_{nm}\left(\frac{\partial^2 T}{\partial x^2} + \frac{\partial^2 T}{\partial y^2}\right) \tag{4}$$

$$\frac{\partial h}{\partial t} + u\frac{\partial h}{\partial x} + v\frac{\partial h}{\partial y} = (k_l)_{nm}\left(\frac{\partial^2 T}{\partial x^2} + \frac{\partial^2 T}{\partial y^2}\right) \tag{5}$$

The interface motion satisfies the Stefan condition $\left[k\frac{\partial T}{\partial n}\right] = -L_F V_n$. In the metal case with fins and the heater, the conduction equations with the source term Q were solved [18]:

$$\frac{\partial T}{\partial t} = k_1\left(\frac{\partial^2 T}{\partial x^2} + \frac{\partial^2 T}{\partial y^2}\right) \tag{6}$$

$$(\rho c)_2\frac{\partial T}{\partial t} = k_2\left(\frac{\partial^2 T}{\partial x^2} + \frac{\partial^2 T}{\partial y^2}\right) + Q \tag{7}$$

Partial differential equations of natural convection together with the energy equations for the heat sink and heat source before the computational procedures were formulated in dimensionless non-primitive variables, such as stream function and vorticity. As the temperature scale $\Delta T = 60\ ^\circ\mathrm{C}$ was set so that the dimensionless temperature was determined as $\Theta = (T - T_m)/\Delta T$, where T_m is the melting point of a PCM and as a length scale, the radiator height $L = 1.5$ cm was chosen, hence, $X = x/L$, $Y = y/L$. The value of the velocity scale was chosen $V_0 = \sqrt{g\beta\Delta TL}$ and the dimensionless values of time, stream function, and vorticity were determined, respectively, from the following relations: $\tau = tV_0/L$, $\Psi = \psi/LV_0$, $\Omega = \omega L/V_0$.

As a result of transformations, the following equations were obtained for NePCM [18]:

$$\frac{\partial^2 \Psi}{\partial X^2} + \frac{\partial^2 \Psi}{\partial Y^2} = -\Omega \tag{8}$$

$$\frac{\partial \Omega}{\partial \tau} + U\frac{\partial \Omega}{\partial X} + V\frac{\partial \Omega}{\partial Y} = \frac{\mu_{nm}/\mu_l}{(\rho_l)_{nm}/\rho_l}\sqrt{\frac{Pr}{Ra}}\left(\frac{\partial^2 \Omega}{\partial X^2} + \frac{\partial^2 \Omega}{\partial Y^2}\right) + \frac{(\rho_l\beta_l)_{nm}/(\rho_l\beta_l)}{(\rho_l)_{nm}/\rho_l}\frac{\partial \Theta}{\partial X} \tag{9}$$

$$\zeta(\varphi)\left[\frac{\partial \Theta}{\partial \tau} + U + V\frac{\partial \Theta}{\partial Y}\right] + \frac{\rho_{nm}L_{nm}}{\rho_f L_f}\cdot Ste\cdot\left[\frac{\partial \varphi}{\partial \tau} + U\frac{\partial \varphi}{\partial X} + V\frac{\partial \varphi}{\partial Y}\right] = \frac{\xi(\varphi)}{\sqrt{Ra\cdot Pr}}\left(\frac{\partial^2 \Theta}{\partial X^2} + \frac{\partial^2 \Theta}{\partial Y^2}\right). \tag{10}$$

In the energy equation, the smoothing function $\varphi(T)$ is used, which determines the volume fraction of the melt and varies from 0 to 1 during the transition from solid material to melt, whereby a smooth transition of the enthalpy and thermophysical parameters of the material, expressed in functions $\zeta(\varphi)$ and $\xi(\varphi)$, was determined:

$$\varphi = \begin{cases} 0, & T < T_m - \eta \\ \frac{T-(T_m-\eta)}{2\eta}, & T_m - \eta \le T \le T_m + \eta \\ 1, & T > T_m + \eta \end{cases} \tag{11}$$

The energy equations, taking into account the volumetric heat generation for the source and profile, are as follows:

$$\frac{\partial \Theta}{\partial \tau} = \frac{\alpha_1/\alpha_0}{\sqrt{Ra\cdot Pr}}\left(\frac{\partial^2 \Theta}{\partial X^2} + \frac{\partial^2 \Theta}{\partial Y^2}\right) \tag{12}$$

$$\frac{\partial \Theta}{\partial \tau} = \frac{\alpha_2/\alpha_0}{\sqrt{Ra\cdot Pr}}\left(\frac{\partial^2 \Theta}{\partial X^2} + \frac{\partial^2 \Theta}{\partial Y^2} + Os\right) \tag{13}$$

The dimensionless equations contain the following dimensionless complexes, which are determined by the geometry parameters, thermal properties of the system, and the medium, as well as the properties of materials, which will be presented below: Rayleigh number $Ra = \frac{g\beta\Delta TL^3}{\nu\alpha_l}$, Prandtl number $Pr = \nu_l/\alpha_l$, Stefan number $Ste = L_f/(c_l\Delta T)$, Ostrogradsky number $Os = QL^2/(k_2\Delta T)$, and the Biot number $Bi = \gamma L/k$.

The single energy equation was formulated for solid and liquid phases in a temperature formulation using the smoothing function φ, and it was solved without highlighting the melting front. Hydrodynamic equations were solved in a region with moving boundaries, which position at each time step was determined by isotherms obtained at this time step.

At the initial time $\tau = 0$, the temperature in the entire system is coincided with the ambient temperature $\Theta = \Theta_{out}$, and since the material was in the solid state, the values of the stream function and vorticity were equal to zero ($\Psi = 0$, $\Omega = 0$). Boundary conditions in the dimensionless form for the presented statement of the conjugate problem are as follows:

- at the boundaries between system elements:

  at the border of the heat source: $k_1 \frac{\partial\Theta_1}{\partial Y} = k_2 \frac{\partial\Theta_2}{\partial Y}$;

  at the profile surface: $k_0 \frac{\partial\Theta_0}{\partial Y} = k_1 \frac{\partial\Theta_1}{\partial Y}$;
- at the outer borders:

  $0 \le X \le 2$, $Y = 1$: $\frac{\partial\Theta}{\partial Y}\Big|_M = -Bi(\Theta_M - \Theta_{out})$;

  $X = 0$ and $X = 2$, $0 \le Y \le 1$: $\frac{\partial\Theta}{\partial Y}\Big|_0 = -Bi(\Theta_0 - \Theta_{out})$ and $\frac{\partial\Theta}{\partial Y}\Big|_N = -Bi(\Theta_N - \Theta_{out})$;

  at $X = 0.6$ and $X = 1.4$, $-0.2 \le Y \le 0$ and $0.6 \le X \le 1.4$, $Y = -0.2$: $\frac{\partial\Theta}{\partial\overline{n}} = 0$.

The dimensionless ambient temperature Θ_{out} for each material was different, as it was determined by the melting temperature of the material and the temperature scale.

- The boundary conditions for the Poisson Equation (8) and vorticity Equation (9) $\Psi = 0$, $\Omega = -\nabla^2\Psi$ were applied for all solid boundaries of the melt region, including interphase. The transition conditions of the thermophysical properties of the material were expressed through a smoothing function:

$$\zeta(\varphi) = \frac{(\rho_s c_s)_{nm}}{\rho_l c_l} + \varphi\left(\frac{(\rho c)_{nm}}{\rho_l c_l} - \frac{(\rho_s c_s)_{nm}}{\rho_l c_l}\right) \tag{14}$$

$$\xi(\varphi) = \frac{(k_s)_{nm}}{k_l} + \varphi\left(\frac{k_{nm}}{k_l} - \frac{(k_s)_{nm}}{k_l}\right) \tag{15}$$

The numerical solution to Equations (8)–(13) was obtained on the basis of the finite difference method [25–28]. To discretize the convective terms in vorticity (Equation (9)) and energy (Equation (10)), we used the Samarskii monotonic difference scheme, and the diffusion terms in all equations were approximated based on the central differences with a second order of accuracy. The Poisson difference equation for the stream function was solved by the successive over-relaxation method. Samarskii local one-dimensional difference scheme for the approximation of the vorticity and energy equations was applied. Using this described method, the developed computational code was verified, employing the experimental data for the gallium melting. A numerical algorithm was applied in solving the problem of gallium melting in a rectangular region and showed good agreement with experimental results [29] (see Figure 2).

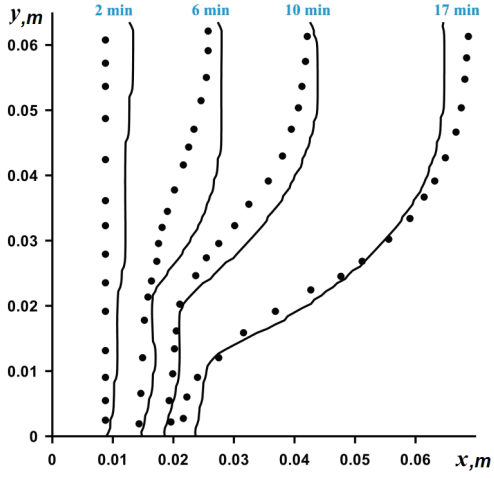

Figure 2. Comparison of obtained numerical data (solid line) and experimental data (dots) [29].

It should be noted that for the phase change problems, the presence of a moving boundary requires the use of a more detailed mesh. In the present study, a grid with 481 × 201 nodes was taken. Solving melting problems are time-consuming, due to the fact that the melting and solidification processes occur much more slowly than hydrodynamic processes. Therefore, problems associated with phase transitions are solved, as a rule, in the two-dimensional approximation. Moreover, using the non-primitive variables "stream function and vorticity" with the finite difference method allows for a reduction in the computational time due to both a smaller number of governing equations compared with the primitive variables "velocity and pressure" and an absence of the global iterations that are used, e.g., in the finite volume method with SIMPLE-like algorithms.

As for the considered two-dimensional problem, it is assumed that the third size is greater than L, and such an approach characterizes an opportunity to analyze 2D problem because the heat transfer rate will be similar to the 3D data. A comparison between 2D and 3D models for convective heat transfer has been performed earlier in [30–33].

Thus, the results of 2D and 3D models for magnetohydrodynamic (MHD) natural convection in a cavity were compared in [31]. The transverse elongation in the parallelepiped was varied from 0.2 to 5. A comparison of the obtained data for different models showed that the influence of the side walls decreases with the lengthening of the cavity and, as a result, 3D laminar natural convection can be replaced by 2D data for the heat transfer rate and fluid flow in the central part of the cavity. A study of the melting of n-octadecane in the cubic cavity (see [33]) showed that the isotherms in the middle cross section of the cube slightly differ from the two-dimensional model, while neglecting differences can be found in the flow structures for 2D and 3D models.

Therefore, the present analysis can be performed using the two-dimensional approximation.

3. Thermophysical Properties of the System Components

The system under consideration consisted of a volumetric heat generation source with silicon properties combined with the closed copper radiator with copper finning. As the nanoadditives the Al_2O_3 particles with diameter $d = 59 \times 10^{-9}$ m were chosen, the properties of these system components are presented in Table 1.

Table 1. Properties of nanoparticles and other materials.

Material	k, W/(m·K)	c, J/(kg·K)	ρ, kg/m^3	β, K^{-1}
Aluminum oxide (nanoparticles) ($d = 59 \times 10^{-9}$ m) [34]	36	765	3600	7.8×10^{-6}
Copper (radiator)	401	385	8900	–
Silicon (heat source)	148	714	2330	–

Five different PCMs were considered in the present study in the range of melting temperatures from 28 to 81 °C. The considered PCM properties are presented in Table 2.

Table 2. Properties phase change materials.

Phase Change Material	T_m, °C	L_f, kJ/kg	k_s/k_l, W/(m·K)	ρ_s/ρ_l, kg/m^3	c_s/c_l, J/(kg·K)	μ, Pa·s	β, K^{-1}
n-octadecane [35]	28.05	241	0.39/ 0.157	814/ 770	1900/ 2200	3.8×10^{-3}	8.5×10^{-4}
Capric acid [36]	32	152.7	0.372/0.153	1018/888	1900/2400	2.7×10^{-3}	10^{-3}
Lauric acid [37]	46	187.2	0.16/0.14	940/885	2180/2390	8×10^{-3}	8×10^{-4}
RT–50 [38]	49	168	0.2	780	2000	4.8×10^{-3}	6×10^{-4}
RT–80 [34]	81	175	0.2	920/770	2400/1800	7.2×10^{-3}	10^{-3}

As a model for describing nanoparticles suspended in a phase change material, a single-phase model, which assumes a uniform particle distribution in the volume, was applied. The properties of NePCM were considered constant within one phase. The density of NePCM was determined by the densities of the corresponding components and the mass concentration Φ of nanoparticles:

$$(\rho_l)_{nm} = (1-\Phi)\rho_l + \Phi\rho_{np}$$
$$(\rho_s)_{nm} = (1-\Phi)\rho_s + \Phi\rho_{np}$$

In turn, the volumetric heat capacity and the coefficient of thermal volume expansion were determined similarly:

$$(\rho_l c_l)_{nm} = (1-\Phi)(\rho_l c_l) + \Phi\left(\rho_{np} c_{np}\right)$$
$$(\rho_s c_s)_{nm} = (1-\Phi)(\rho_s c_s) + \Phi\left(\rho_{np} c_{np}\right)$$

In this study, the thermal conductivity model [39] for nanofluids, which takes into account the influence of particle size, concentration, and base fluid properties, was used. The authors proposed a correlation in which the effective thermal conductivity is the following sum: $k_{eff} = k_{static} + k_{Brownian}$ where k_{static} has been found from the Maxwell equation, and the additional term $k_{Brownian}$ corresponds to the Brownian motion of particles:

$$(k_l)_{nm} = k_l \frac{k_{np} + 2k_l - 2\left(k_l - k_{np}\right)\Phi}{k_{np} + 2k_l + \left(k_l - k_{np}\right)\Phi} + 5 \cdot 10^4 \beta_\lambda \Phi \rho_l c_l \sqrt{\frac{\kappa T}{\rho_{np} d_{np}}} f(T, \Phi)$$

where the Brownian motion of the molecules in the melt represented as the second term was taken into account, the thermal conductivity in a solid material was respectively determined from the Maxwell's relation:

$$k_{nm} = k_l \frac{k_{np} + 2k_l - 2\left(k_l - k_{np}\right)\Phi}{k_{np} + 2k_l + \left(k_l - k_{np}\right)\Phi}$$

Here, $\kappa = 1.381 \cdot 10^{-23} J/K$ is the Boltzmann constant. In [40], the new empirical correlations for β and $f(T,\Phi)$ were obtained experimentally considering nanoparticles of Al_2O_3, ZnO, and CuO. Correlations $\beta_\lambda = 8.4407(100\Phi)^{-1.07304}$ and the function $f(T, \Phi)$:

$$f(T,\Phi) = \left(2.817 \cdot 10^{-2}\Phi + 3.917 \cdot 10^{-3}\right)\frac{T}{T_0} + \left(-3.0669 \cdot 10^{-2}\Phi - 3.91123 \cdot 10^{-3}\right),\ T_0 = 273\ ^\circ K$$

were obtained for nanoparticles of Al_2O_3 for the following concentration range: $1\% \le \Phi \le 10\%$.

The melt viscosity was determined as [41]: $\mu_{nm} = 0.983 \cdot e^{12.959\Phi}\mu_f$.

The latent heat decreased with the increasing concentration of nanoparticles:$L_{nm} = \frac{(1-\Phi)\rho_f L_f}{\rho_{nm}}$.

4. Results and Discussion

Figure 3 shows the average source temperature versus time for five different PCMs: n-octadecane with a melting point of 28.05 °C, capric acid with a melting point of 32 °C, lauric acid with a melting point of 46 °C, RT–50 with a melting point of 49 °C, and RT–80 with a melting point of 81 °C for various nanoparticles loadings. In each case, it can be seen that the temperature increases evenly, while the temperature graph has two inflections corresponding to the beginning of the melting of the material and the end of the melting process. Exceeding the melting temperature is accompanied by the intense absorption of energy, which causes the temperature to rise more slowly.

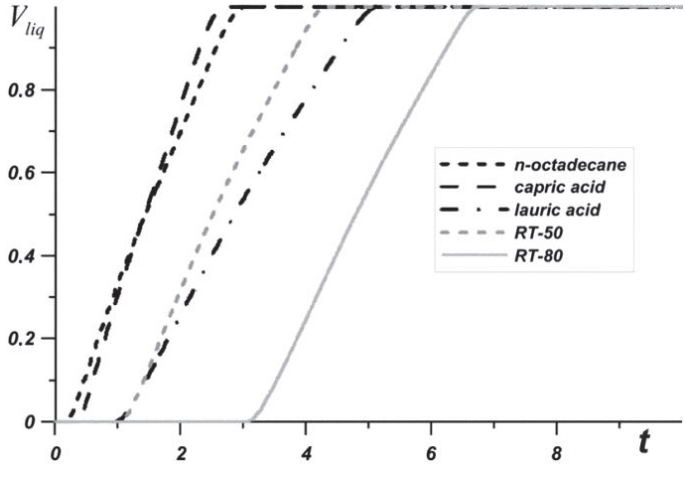

Figure 3. Liquid volume fraction versus time.

The phase change material with the lowest melting point begins to melt first, and during the entire melting process, the temperature in the source is lower when using an n-octadecane-based heat sink compared to other materials. However, this material melts very quickly and the temperature of paraffin rises rapidly. However, the source heats to 60 °C longer in the case of the n-octadecane-based heat sink. The remaining materials begin to melt later. It is worth noting that for n-octadecane, capric acid, and RT–50, the temperature in the source differs by no more than 6 degrees. Capric acid and RT–50 have low latent heat and therefore melt faster than n-octadecane and lauric acid, respectively.

Later than the others, RT–80 begins to melt, so for some time the temperature in the source is higher than in other cases (see Figure 4), however, by the end of the melting process, the temperature difference in the source reaches 8–11 degrees compared to n-octadecane, capric acid and RT–50. The heat source cooled by the lauric acid reaches a temperature of 80 °C later than other considered materials. It is worth noting that after four minutes of heating, the lowest temperature is observed in

the heat sink based on the lauric acid. This PCM has the smallest one of the largest latent heat values and a sufficiently high heat capacity both in the solid state and in the melt.

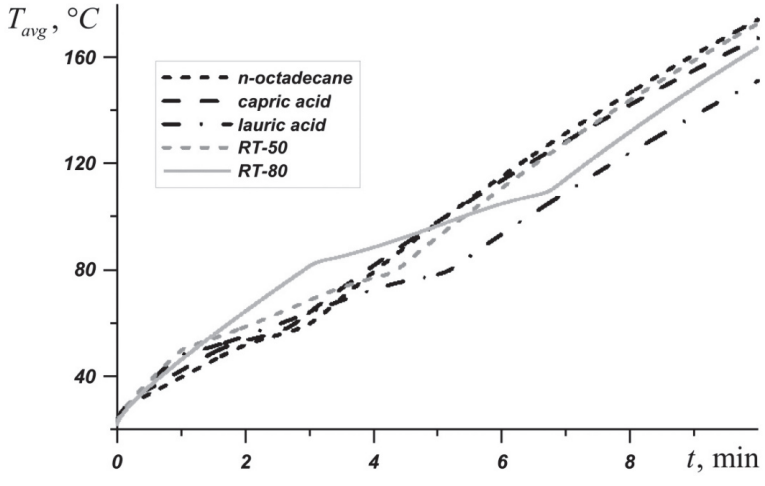

Figure 4. Average source temperature for five different phase change materials (PCMs).

Natural convection develops in the liquid material due to the temperature difference between the inner surface of the profile and the movable boundary of the yet-molten material. Figure 5 shows the temperature fields and streamlines for lauric acid at various nanoparticle loadings, and for each case, the maximum value of the stream function and the average source temperature at a given time are presented. At the initial time intervals around each solid region, two narrow convective cells develop along the vertical walls. The closed form of the radiator contributes to the rapid heat dissipation inside the highly heat-conducting casing; therefore, the heat spreads evenly around the perimeter. The maximum values of the stream function decrease with an increase in the concentration of nanoparticles, however, the melt region expands faster, due to the fact that thermal conductivity prevails at this stage. The intensification of conductive heat transfer leads to a slight decrease in the source temperature, this effect is weak and the temperature at time t = 3 min differs by only 0.47 °C for 2% and 6%.

With the development of natural convection and a decrease in the solid region, the heated melt of lauric acid accumulates in the upper part. A cold downward flow descends to the lower slab, where the material is melted later and the cores of the circulation cells are located below. At the time t = 5 min, when the material almost melted, the opposite effect is observed, namely, the higher mass fraction of nanoparticles, the higher average temperature of the source. The expansion of the melt region and a constant increase in the temperature of the metal surface lead to the intensification of mass transfer, which can be seen from the maximum values of the stream function $|\Psi|_{max}$. The effect of natural convection on temperature fields begins to prevail in NePCM. In this way, an increase in the melt viscosity due to the addition of nanoadditives critically affects the cooling process. In addition, the presence of nanoparticles in the material reduces its latent heat, which also accelerates the melting process (see Figure 6) and reduces the overall effective heat capacity of the system after 5 min from the start of source operating.

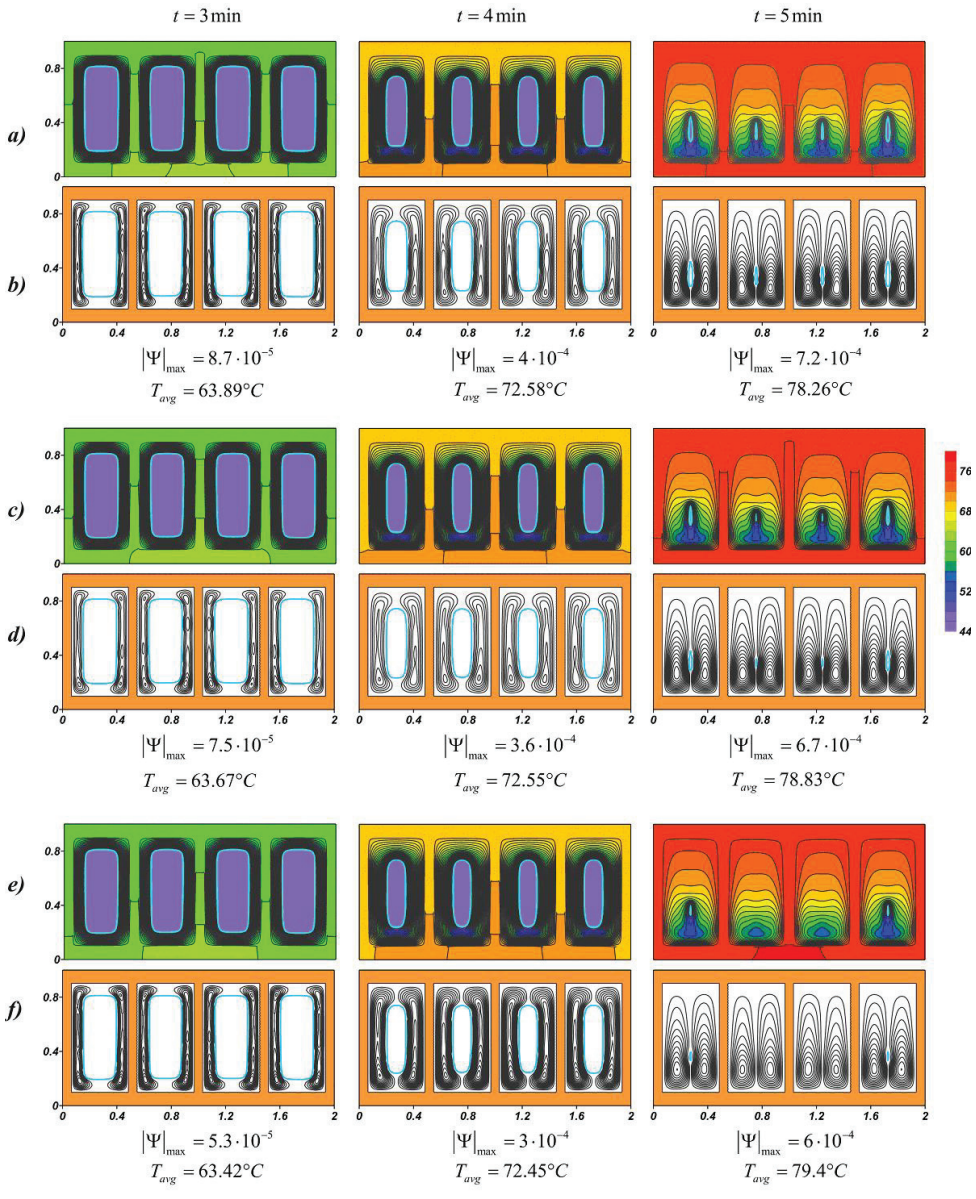

Figure 5. Temperature fields and streamlines for lauric acid at different time moments: (**a**,**b**) $\Phi = 2\%$; (**c**,**d**) $\Phi = 4\%$; (**e**,**f**) $\Phi = 6\%$.

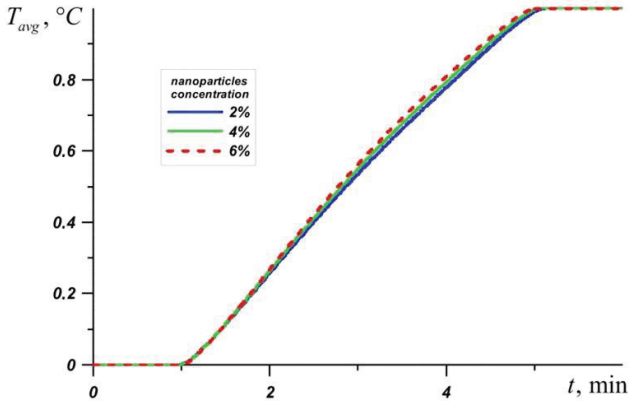

Figure 6. Liquid volume fraction versus time for lauric acid.

RT–80 has the highest melting point of all the phase change materials under consideration, so the temperature of the source quickly reaches 80 °C in this case. Figure 7 shows the change in the maximum value of the stream function at Φ = 0%, Φ = 2%, and Φ = 6%. Before the four minutes from the moment the source is turned on, the system heats up to the melting temperature of RT–80. This is followed by a monotonic increase in $|\Psi|_{max}$ and the influence of nanoparticles increases over time. The addition of nano-sized particles of Φ = 6% reduces $|\Psi|_{max}$ by about 1.5 times or more.

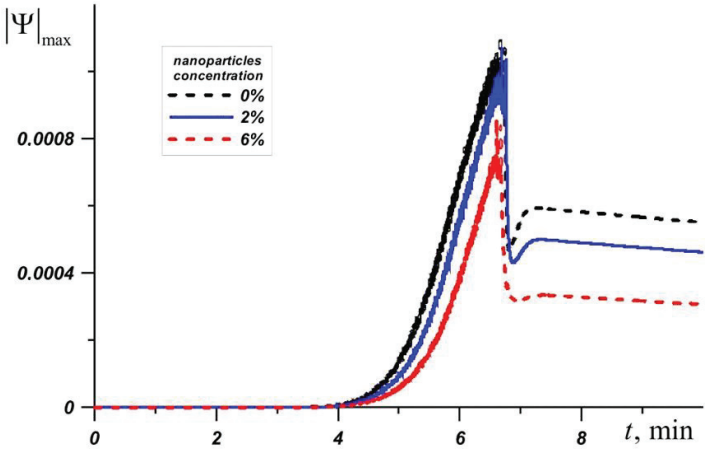

Figure 7. Maximum value of the stream function for RT-80 at different nanoparticle concentrations.

It should be noted that the addition of nanoparticles to the material does not lead to a significant decrease in the heater temperature. In the cases under consideration, at specific points in time, the temperature in the source decreases by no more than 1.5 °C with an increase in the concentration of nanoparticles, which is a relatively small difference in the considered thermal conditions. A high concentration of nanoparticles significantly reduces the intensity of the circulation of the melt, which leads to a decrease in the intensity of heat transfer. At the same time, the material melts faster due to a decrease in latent melting energy. Thus, an increase in the efficiency of the heat sink is observed only at a 2% concentration. At higher concentrations, the heater temperature decreases slightly, or vice versa, which leads to a decrease in heat transfer between the source and the heat sink (Figure 8).

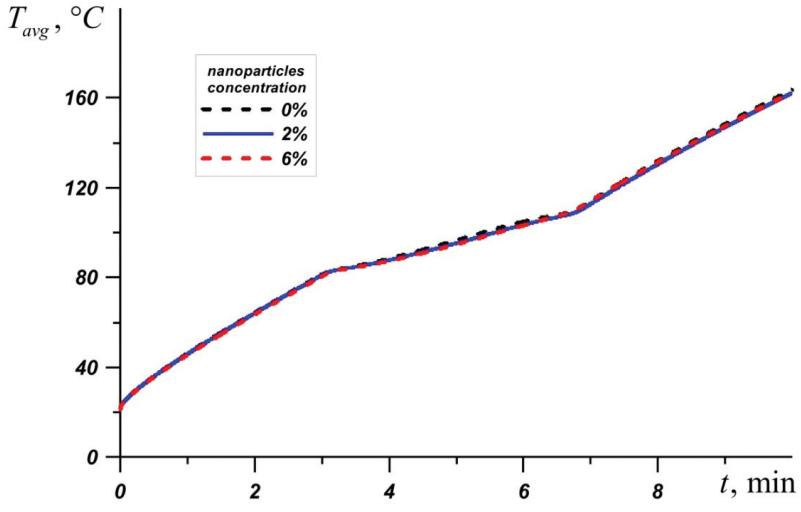

Figure 8. Average source temperature for RT-80 at different nanoparticle concentrations.

The temperature fields shown in Figure 9 at the time t = 3 min present wide-spaced isotherms in the radiator and more densely located isotherms in the material on the inner surface of the profile, indicating a faster heat distribution in the radiator compared to the nano-enhanced material. When heating solid paraffin wax, before the phase transition, the temperature difference of the source for pure paraffin and paraffin with nanoparticle concentrations of 6% reaches 0.87 °C. When the radiator temperature exceeds 81 °C and the melting process begins, the effect of adding the nanoparticles increases, namely, the temperature difference for pure material and NePCM at Φ = 6% increases to 1.79 °C. After the melt volume reaches 100%, the average temperature of the source grows more rapidly. Due to convective heat and mass transfer, the lowest temperatures are observed in the lower part of the melt region. Moreover, in the case of Φ = 2%, the isotherms in the melt are less condensed to the walls, which indicate a more intense conductive heat transfer, as a result of which the observed T_{avg} is lower by 1.35 °C at time t = 7 min and at higher mass particle concentrations. An increase in viscosity strongly affects the thermal processes in the system, namely, a 43% decrease in $|\Psi|_{max}$ is accompanied by an increase in the average temperature of the source. The average heater temperature at Φ = 6% was only 0.12 °C lower than in the case of pure paraffin and at the same time by 1.23 °C higher than at Φ = 2%. Thus, paraffin with 2 wt % nanoparticles shows the best results. With the disappearance of the unmelted material, the maximum values of the stream function sharply decrease up to two times.

An inclusion of nanoparticles to the material leads to an increase in the melt viscosity and an improvement of conductive heat transfer. Figure 10 shows a graph of the average source temperature for three different PCMs at different concentrations of nanoadditives. At different stages of heating and different PCMs, nanoparticles give different effects for heat transfer processes. It can be seen that the most effective concentration of Al_2O_3 is Φ = 2%, which is most noticeable on the temperature graph T_{avg} for n-octadecane. For RT–80, at the initial stages and during heating until the material is completely melted, the lowest temperatures are observed at a high concentration of nanoparticles Φ = 6%. However, after the melt volume reaches 100%, the PCM with 2% particle addition is most effective.

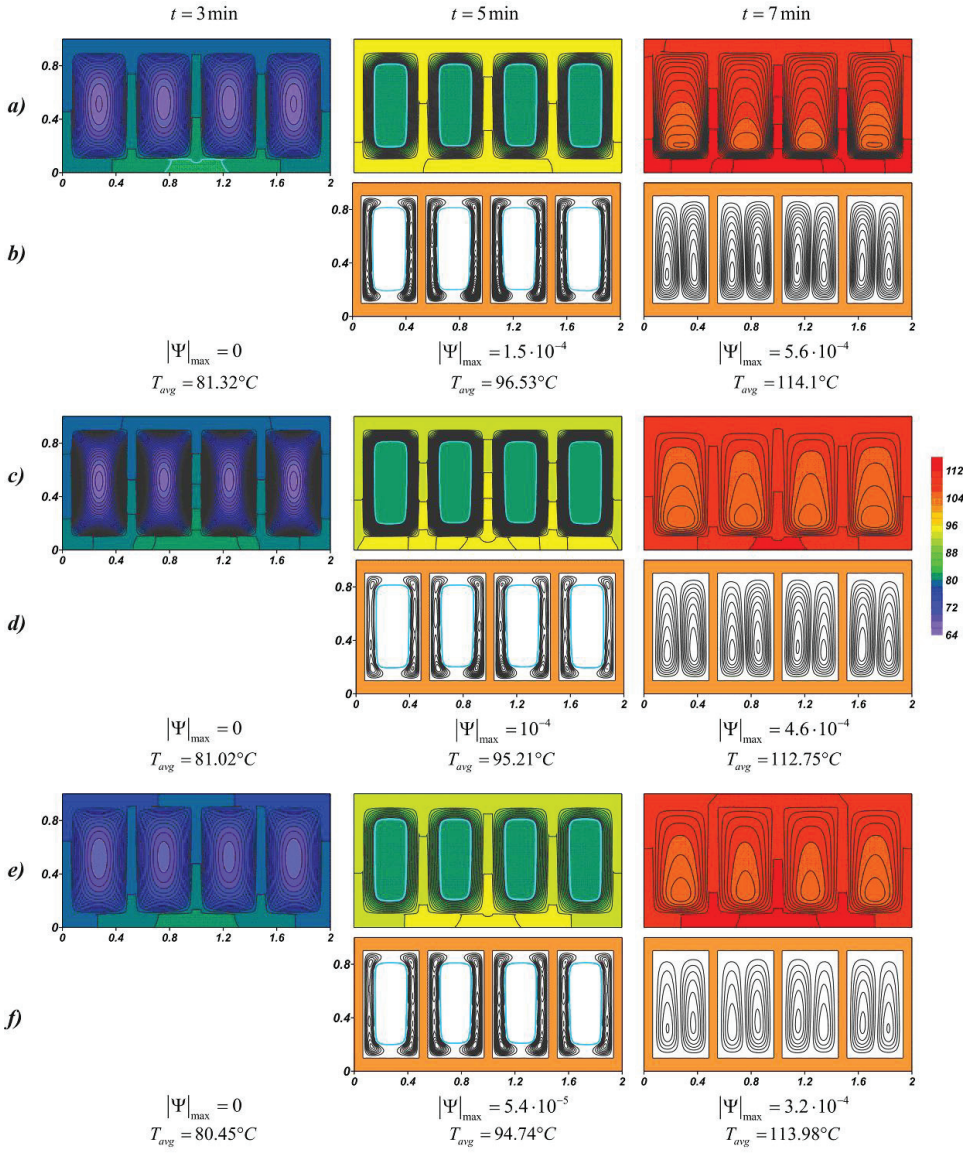

Figure 9. Temperature fields and streamlines for RT-80 at different time moments: (**a**,**b**) Φ = 0%; (**c**,**d**) Φ = 2%; (**e**,**f**) Φ = 6%.

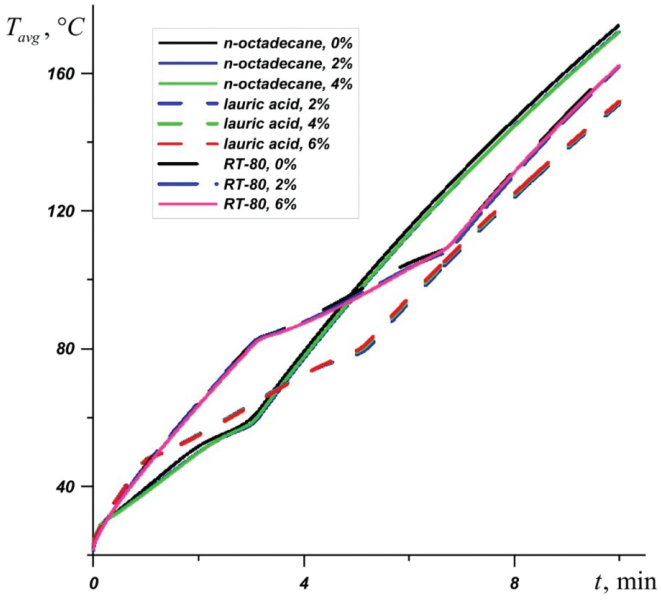

Figure 10. Evolution of average temperature in the source for n-octadecane, lauric acid, and RT-80 for different percentages of nanoparticles.

5. Conclusions

A numerical study of the effect of the Al_2O_3 nanoparticles on heat and mass transfer inside a closed system consisting of a volumetric heat generation element and an NePCM-based heat sink at high heat loads was carried out. The thermal characteristics of the system, including the position of the interface, the melt volume, the average temperature in the source, and the temperature distributions at fixed time points for five different materials (n-octadecane, Capric acid, Lauric acid, RT-50, and RT-80) were obtained. An analysis of the results showed that n-octadecane, lauric acid, and RT-80 are the most effective for cooling at high heat generations. Since n-octadecane begins to melt earlier than the other materials reviewed, the average temperature in the source at the initial minutes of heating is less than in other cases. However, the PCM with a melting point of 28.05 °C melts rather quickly, after which the heating element rapidly heats up. At critical temperatures above 70 °C, in the framework of the problem under consideration, lauric acid with a melting point of 46 °C is the most suitable phase change material, since after four minutes of melting of this material, the lowest temperatures are observed in the heat source.

An addition of nanoparticles has a small effect on the productivity of the heat sink and can reduce the temperature in the source by only 1.5 °C, however, for the five materials considered, depending on the heat and mass transfer conditions in the system, it can have both positive and negative effects. The most effective concentration, with which the ratio of the effects of increasing thermal conductivity and increasing viscosity was the most suitable is $\Phi = 2\%$. An increase in the mass fraction of particles from 2% to 6% leads to a significant weakening of the convective circulation of the melt and can lead to a decrease in the critical operating time.

Author Contributions: N.S.B. and M.A.S. conceived the main concept. N.S.B., N.S.G. and M.A.S. contributed to the investigation and data analysis. N.S.B. and M.A.S. wrote the manuscript. All authors contributed in writing the final manuscript. All authors have read and agreed to the published version of the manuscript.

Funding: This work was supported by the Russian Foundation for Basic Research and Administration of Tomsk Region of Russian Federation (grant No. 19-48-703034).

Conflicts of Interest: The authors declare no conflict of interest.

Nomenclature

Bi	the Biot number
c	specific heat, J K^{-1} kg^{-1}
d	diameter, m
g	gravitational acceleration, m s^{-2}
H	cavity height, m
h	specific enthalpy, J kg^{-1}
k	thermal conductivity, W K^{-1} m^{-1}
L	cavity length, m
L_m	fusion energy or latent heat of melting, J kg^{-1}
Os	Ostrogradsky number
p	pressure, Pa
Pr	Prandtl number
Q	heat transfer rate per unit of volume, W m^{-3}
Ra	Rayleigh number
Ste	Stefan number
t	time, s
T	temperature, K
T_m	melting temperature
u, v	velocity components in Cartesian coordinate along x and y, m s^{-1}
U, V	dimensionless velocity components
x, y	Cartesian coordinate, m
X, Y	dimensionless Cartesian coordinates
Greek Symbols	
α	thermal diffusivity, m^2 s^{-1}
β	coefficient of thermal expansion, K^{-1}
γ	heat transfer coefficient, $WK^{-1}m^{-2}$
η	smoothing parameter (or melting temperature range), K
Θ	dimensionless temperature
μ	dynamic viscosity, Pa s
ν	kinematic viscosity, m^2 s^{-1}
ρ	density, kgm^{-3}
τ	dimensionless time
Φ	nanoparticles volume fraction
φ	volume fraction of the melt
ψ	stream function, m^2 s^{-1}
Ψ	dimensionless stream function
ω	vorticity, s^{-1}
Ω	dimensionless vorticity
Subscripts	
0	initial condition or ambient
1	radiator
2	heater
l	liquid
m	melting
nm	nanomaterial
np	nanoparticle
s	solid

References

1. Al-Waeli, A.H.A.; Chaichan, M.T.; Sopian, K.; Kazem, H.A.; Mahood, H.B.; Khadom, A.A. Modeling and experimental validation of a PVT system using nanofluid coolant and nano-PCM. *Sol. Energy* **2019**, *177*, 178–191. [CrossRef]
2. Sheikholeslami, M.; Lohrasbi, S.; Ganji, D.D. Numerical analysis of discharging process acceleration in LHTESS by immersing innovative fin configuration using finite element method. *Appl. Therm. Eng.* **2016**, *107*, 154–166. [CrossRef]
3. Li, W.; Zhang, D.; Jing, T.; Gao, M.; Liu, P.; He, G.; Qin, F. Nano-encapsulated phase change material slurry (Nano-PCMS) saturated in metal foam: A new stable and efficient strategy for passive thermal management. *Energy* **2018**, *165*, 743–751. [CrossRef]
4. Huang, H.; Wang, Z.; Zhang, H.; Dou, B.; Huang, X.; Liang, H.; Goula, M.A. An experimental investigation on thermal stratification characteristics with PCMs in solar water tank. *Sol. Energy* **2019**, *177*, 8–21. [CrossRef]
5. Nehari, T.; Benlekkam, M.; Nehari, D.; Youcefi, A. The Effect of Inclination on the Passive cooling of the solar PV panel by using Phase change Material. *Int. J. Renew. Energy Res.* **2016**, *6*, 1434–1441.
6. Atkin, P.; Farid, M.M. Improving the efficiency of photovoltaic cells using PCM infused graphite and aluminium fins. *Sol. Energy* **2015**, *114*, 217–228. [CrossRef]
7. Stropnik, R.; Stritih, U. Increasing the efficiency of PV panel with the use of PCM. *Renew. Energy* **2016**, *97*, 671–679. [CrossRef]
8. Kibria, M.A.; Saidur, R.; Al-Sulaiman, F.A.; Aziz, M.M.A. Development of a thermal model for a hybrid photovoltaic module and phase change materials storage integrated in buildings. *Sol. Energy* **2016**, *124*, 114–123. [CrossRef]
9. Tyagi, V.V.; Buddhi, D. PCM thermal storage in buildings: A state of art. *Renew. Sustain. Energy Rev.* **2007**, *11*, 1146–1166. [CrossRef]
10. Lee, K.O.; Medina, M.A.; Raith, E.; Sun, X. Assessing the integration of a thin phase change material (PCM) layer in a residential building wall for heat transfer reduction and management. *Appl. Energy* **2015**, *137*, 699–706. [CrossRef]
11. Castell, A.; Martorell, I.; Medrano, M.; Pe'rez, G.; Cabeza, L.F. Experimental study of using PCM in brick constructive solutions for passive cooling. *Energy Build.* **2010**, *42*, 534–540. [CrossRef]
12. Evola, G.; Marletta, L.; Sicurella, F. A methodology for investigating the effectiveness of PCM wallboards for summer thermal comfort in buildings. *Build. Environ.* **2013**, *59*, 517–527. [CrossRef]
13. Motahar, S.; Alemrajabi, A.A.; Khodabandeh, R. Experimental investigation on heat transfer characteristics during melting of a phase change material with dispersed TiO_2 nanoparticles in a rectangular enclosure. *Int. J. Heat Mass Transf.* **2017**, *109*, 134–146. [CrossRef]
14. Leong, K.Y.; Rahman, M.R.A.; Gurunathan, B.A. Nano-enhanced phase change materials: A review of thermo-physical properties, applications and challenges. *J. Energy Storage* **2019**, *21*, 18–31. [CrossRef]
15. Al-Jethelah, M.; Tasnim, S.H.; Mahmud, S.; Dutta, A. Nano-PCM filled energy storage system for solar-thermal applications. *Renew. Energy* **2018**, *126*, 137–155. [CrossRef]
16. Abdelrahman, H.E.; Wahba, M.H.; Refaey, H.A.; Moawad, M.; Berbish, N.S. Performance enhancement of photovoltaic cells by changing configuration and using PCM (RT35HC) with nanoparticles Al_2O_3. *Sol. Energy* **2019**, *177*, 665–671. [CrossRef]
17. Elsayed, A.O. Numerical study on performance enhancement of solid–solid phase change materials by using multi-nanoparticles mixtures. *J. Energy Storage* **2015**, *4*, 106–112. [CrossRef]
18. Bondareva, N.S.; Sheremet, M.A. Effect of nano-sized heat transfer enhancers on PCM-based heat sink performance at various heat loads. *Nanomaterials* **2019**, *10*, 17. [CrossRef]
19. Dhaidan, N.S.; Khodadadi, J.M.; Al-Hattab, T.A.; Al-Masha, S.M. Experimental and numerical investigation of melting of phase change material/nanoparticle suspensions in a square container subjected to a constant heat flux. *Int. J. Heat Mass Transf.* **2013**, *66*, 672–683. [CrossRef]
20. Ho, C.J.; Gao, J.Y. An experimental study on melting heat transfer of paraffin dispersed with Al_2O_3 nanoparticles in a vertical enclosure. *Int. J. Heat Mass Transf.* **2013**, *62*, 2–8. [CrossRef]
21. Kousksou, T.; Mahdaoui, M.; Hlimi, M.; El Alaiji, R.; El Rhafiki, T. Latent energy storage: Melting process around heating cylinders. *Case Stud. Therm. Eng.* **2016**, *8*, 128–140. [CrossRef]

22. Ashraf, M.J.; Ali, H.M.; Usman, H.; Arshad, A. Experimental passive electronics cooling: Parametric investigation of pin-fin geometries and efficient phase change materials. *Int. J. Heat Mass Transf.* **2017**, *115*, 251–263. [CrossRef]
23. Fan, L.-W.; Xiao, Y.-Q.; Zeng, Y.; Fang, X.; Wang, X.; Xu, X.; Yu, Z.-T.; Hong, R.-H.; Hu, Y.-C.; Cen, K.-F. Effects of melting temperature and the presence of internal fins on the performance of a phase change material (PCM)-based heat sink. *Int. J. Therm. Sci.* **2013**, *70*, 114–126. [CrossRef]
24. Wang, X.-Q.; Yap, C.; Mujumdar, A.S. A parametric study of phase change material (PCM)-based heat sinks. *Int. J. Therm. Sci.* **2008**, *47*, 1055–1068. [CrossRef]
25. Bondareva, N.S.; Buonomo, B.; Manca, O.; Sheremet, M.A. Performance of the finned nano-enhanced phase change material system under the inclination influence. *Int. J. Heat Mass Transf.* **2019**, *135*, 1063–1072. [CrossRef]
26. Bondareva, N.S.; Buonomo, B.; Manca, O.; Sheremet, M.A. Heat transfer inside cooling system based on phase change material with alumina nanoparticles. *Appl. Therm. Eng.* **2018**, *144*, 972–981. [CrossRef]
27. Bondareva, N.S.; Sheremet, M.A. Conjugate heat transfer in the PCM-based heat storage system with finned copper profile: Application in electronics cooling. *Int. J. Heat Mass Transf.* **2018**, *124*, 1275–1284. [CrossRef]
28. Bondareva, N.S.; Sheremet, M.A. Effect of inclined magnetic field on natural convection melting in a square cavity with a local heat source. *J. Magn. Magn. Mater.* **2016**, *419*, 476–484. [CrossRef]
29. Gau, C.; Viskanta, R. Melting and solidification of a pure metal on a vertical wall. *J. Heat Transf.* **1986**, *108*, 174–181. [CrossRef]
30. Martyushev, S.G.; Sheremet, M.A. Conjugate natural convection combined with surface thermal radiation in a three-dimensional enclosure with a heat source. *Int. J. Heat Mass Transf.* **2014**, *73*, 340–353. [CrossRef]
31. Bondareva, N.S.; Sheremet, M.A. Influence of uniform magnetic field on laminar regimes of natural convection in an enclosure. *Thermophys. Aeromech.* **2015**, *22*, 203–216. [CrossRef]
32. Bondareva, N.S.; Sheremet, M.A. Natural convection heat transfer combined with melting process in a cubical cavity under the effects of uniform inclined magnetic field and local heat source. *Int. J. Heat Mass Transf.* **2017**, *108*, 1057–1067. [CrossRef]
33. Bondareva, N.S.; Sheremet, M.A. 3D natural convection melting in a cubical cavity with a heat source. *Int. J. Therm. Sci.* **2017**, *115*, 43–53. [CrossRef]
34. Hosseinizadeh, S.F.; Tan, F.L.; Moosania, S.M. Experimental and numerical studies on performance of PCM-based heat sink with different configurations of internal fins. *Appl. Therm. Eng.* **2011**, *31*, 3827–3838. [CrossRef]
35. Casano, G.; Piva, S. Experimental and numerical investigation of a phase change energy storage system. *J. Phys. Conf. Ser.* **2014**, *501*, 012012. [CrossRef]
36. Kant, K.; Shukla, A.; Sharma, A. Heat transfer studies of building brick containing phase change materials. *Sol. Energy* **2017**, *155*, 1233–1242. [CrossRef]
37. Fadl, M.; Eames, P. A numerical investigation into the heat transfer and melting process of lauric acid in a rectangular enclosure with three values of wall heat flux. *Energy Procedia* **2019**, *158*, 4502–4509. [CrossRef]
38. Hosseini, M.J.; Ranjbar, A.A.; Sedighi, K.; Rahimi, M. A combined experimental and computational study on the melting behavior of a medium temperature phase change storage material inside shell and tube heat exchanger. *Int. J. Heat Mass Transf.* **2012**, *39*, 1416–1424. [CrossRef]
39. Koo, J.; Kleinstreuer, C. A new thermal conductivity model for nanofluids. *J. Nanopart. Res.* **2004**, *6*, 577–588. [CrossRef]
40. Vajjha, R.S.; Das, D.K. Experimental determination of thermal conductivity of three nanofluids and development of new correlations. *Int. J. Heat Mass Transf.* **2009**, *52*, 4675–4682. [CrossRef]
41. Vajjha, R.S.; Das, D.K.; Namburu, P.K. Numerical study of fluid dynamic and heat transfer performance of Al_2O_3 and CuO nanofluids in the flat tubes of a radiator. *Int. J. Heat Fluid Flow* **2010**, *31*, 613–621. [CrossRef]

nanomaterials

MDPI

Article

Thermal Convection of Nanoliquid in a Double-Connected Chamber

Ioan Pop [1,*], Mikhail A. Sheremet [2] and Teodor Groşan [1]

[1] Department of Applied Mathematics, Babeş-Bolyai University, Cluj-Napoca 400084, Romania; trgosan@math.ubbcluj.ro

[2] Laboratory on Convective Heat and Mass Transfer, Tomsk State University, Tomsk 634050, Russia; sheremet@math.tsu.ru

* Correspondence: popm.ioan@yahoo.co.uk

Received: 19 February 2020; Accepted: 16 March 2020; Published: 23 March 2020

Abstract: Thermogravitational convective thermal transmission, inside a square differentially-heated chamber with a nanoliquid, has been examined in the presence of internal adiabatic or a thermally-conducting solid body. A single-phase nanoliquid approach is employed, based on the experimentally-extracted relations for nanofluid heat conductivity and dynamic viscosity. The governing equations have been written using non-primitive parameters such as stream function and vorticity. Such approach allows a decrease in computational time due to a reduction of equation numbers. One of the main challenges in such a technique is a determining the stream function magnitude at the inner body walls. A solution of this problem has been described in detail in this paper. Computational scrutinizing has been performed by employing the finite difference technique. The mesh sensitivity analysis and comparison with theoretical and experimental results of other researchers have been included. An influence of the Rayleigh number, nanoparticles concentration, internal block size, heat conductivity ratio and non-dimensional time on nanofluid motion and energy transport has been studied.

Keywords: nanoparticles; natural convection; conjugate heat transfer; heat-conducting block

1. Introduction

The investigation of heat-driven liquid motion and energy transfer in chambers is a significant subject due to its huge applications in practice, including thermal collectors, thermal exchangers, microelectronic gears, phenomena within buildings and many others [1,2]. Now there are many published papers and books on thermal convection within chambers. For example, a great review on thermal convective energy transport can be found in [3], where the complex nature of free convection phenomena in enclosures is discussed. An analysis is presented for two-dimensional (2D) convection flow, subjected by the buoyancy force on the liquid in a domain. Major efforts are directed to the various motion modes that can happen and the energy transport across the liquid area between the two flat parallel vertical surfaces. The rectangular chamber topic is considered as the most wide-spread benchmark task in numerical liquid flow and energy transport literature. This not only arises from theoretical benchmark data, but also for its practical applications where both, the liquid circulation and energy transport are within the chamber.

Nanoliquids play an essential role in energy transport applications with promising parameters that can be managed. Nanosuspensions have significant properties that allow performing analysis by many scientists to model new thermal systems for various practical applications. Mono-nanoliquids, created using a single sort of nanoadditives, have essential benefits due to defining nanoliquids, which is the combination of tiny-sized solid particles in conventional fluids, many experimental and numerical investigations have demonstrated use of these kind of liquids. Choi [4] studied the process of

suspending nano-sized solid particles in the host liquid and considered this liquid as a nanoliquid. The most essential feature of nanoliquid is that coagulation can be stopped. The homogeneous distribution of solid particles and introduction of necessary surfactant can stop the formation of set of conglutinated particles (Babu et al. [5]). Many investigations about energy transport intensification using nanoliquids have been published. Papers and books on energy transport in nanoliquids can be found in [6–21].

The objective of this research is to computationally scrutinize the free convective energy transport of nanofluid in a differentially-heated chamber, having internal blocks, using the mathematical nanofluid model based, on single-phase nanofluid approach. We have described, in detail, a technique for the definition of stream function magnitude at an inner body surface in a double-connected domain. It should be noted that the present paper deals with an analysis of heat transfer performance of nanoliquid in a cavity with internal solid block. Such problem can be found in the case of optimization of the electronics cooling system, where the electronic cabinet includes different solid blocks. In the case of simple geometry an investigation of the internal body size and thermal conductivity has been conducted for various nanoadditives concentration. Moreover, nowadays scientists use primitive variables for analysis to solve convective heat transfer problems, within multi-connected domains, and as a result, there are have been no problems with the definition of the velocity at internal solid block surface. In the case of non-primitive variables, such as stream function and vorticity, it is necessary to develop a special algorithm for definition of the stream function at internal solid block surface, and such algorithm has been developed in the present study. It is well-known that employing the non-primitive variables reduces the number of governing equations, and as a result, the computational time. By using this developed method, it is possible to conduct an effective analysis of the velocity and temperature fields within electronic cabinet having adiabatic of heat-conducting solid block. Different structure of the inner body can be used for an intensification of the convective heat transfer under the influence of nano-sized particles volume fraction.

2. Mathematical Model

It is important to consider the transient natural convective heat transport in 2D differentially-heated nanoliquid chamber of height L in the presence of inner adiabatic or thermally-conducting block. It is supposed that the left border is hot with temperature T_h, whilst the right border is cold with temperature T_c. The horizontal boundaries are thermally insulated $(\partial T/\partial \overline{y}) = 0$ (Figure 1). For the description of the transport processes within a nanoliquid the single-phase model with effective parameters is used. Such approach illustrates that the nanoadditives are uniformly included in the host liquid. Moreover, using the single-phase model with experimentally-based correlations for physical properties is more effective in comparison with two-phase nanoliquid models and experimental data [22,23].

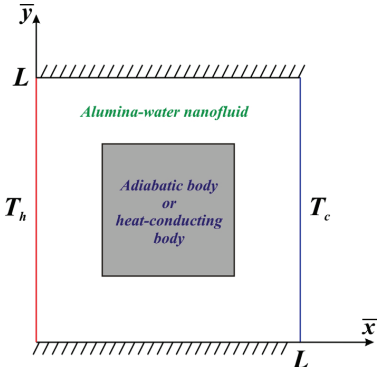

Figure 1. Sketch of the problem.

Using the Boussinesq approach, the basic equations managing these phenomena can be formulated in dimensional form as [24]:

$$\frac{\partial \overline{u}}{\partial \overline{x}} + \frac{\partial \overline{v}}{\partial \overline{y}} = 0 \tag{1}$$

$$\rho_{nf}\left(\frac{\partial \overline{u}}{\partial t} + \overline{u}\frac{\partial \overline{u}}{\partial \overline{x}} + \overline{v}\frac{\partial \overline{u}}{\partial \overline{y}}\right) = -\frac{\partial \overline{p}}{\partial \overline{x}} + \mu_{nf}\left(\frac{\partial^2 \overline{u}}{\partial \overline{x}^2} + \frac{\partial^2 \overline{u}}{\partial \overline{y}^2}\right) \tag{2}$$

$$\rho_{nf}\left(\frac{\partial \overline{v}}{\partial t} + \overline{u}\frac{\partial \overline{v}}{\partial \overline{x}} + \overline{v}\frac{\partial \overline{v}}{\partial \overline{y}}\right) = -\frac{\partial \overline{p}}{\partial \overline{y}} + \mu_{nf}\left(\frac{\partial^2 \overline{v}}{\partial \overline{x}^2} + \frac{\partial^2 \overline{v}}{\partial \overline{y}^2}\right) + (\rho\beta)_{nf} g(T - T_c) \tag{3}$$

$$(\rho c)_{nf}\left(\frac{\partial T}{\partial t} + \overline{u}\frac{\partial T}{\partial \overline{x}} + \overline{v}\frac{\partial T}{\partial \overline{y}}\right) = k_{nf}\left(\frac{\partial^2 T}{\partial \overline{x}^2} + \frac{\partial^2 T}{\partial \overline{y}^2}\right). \tag{4}$$

In the case of internal heat-conducting block an additional heat conduction equation has been included in the following form [25]:

$$(\rho c)_s \frac{\partial T}{\partial t} = k_s\left(\frac{\partial^2 T}{\partial \overline{x}^2} + \frac{\partial^2 T}{\partial \overline{y}^2}\right). \tag{5}$$

Additional relations for the considered problem are:

$$\begin{gathered} t = 0\text{: } \overline{u} = \overline{v} = 0,\ T = T_c \text{ at } 0 \le \overline{x} \le L,\ 0 \le \overline{y} \le L; \\ t > 0\text{: } \overline{u} = \overline{v} = 0,\ T = T_h \text{ at } \overline{x} = 0,\ 0 \le \overline{y} \le L; \\ \overline{u} = \overline{v} = 0,\ T = T_c \text{ at } \overline{x} = L,\ 0 \le \overline{y} \le L; \\ \overline{u} = \overline{v} = 0,\ \tfrac{\partial T}{\partial \overline{y}} = 0 \text{ at } \overline{y} = 0,\ L,\ 0 \le \overline{x} \le L \\ \overline{u} = \overline{v} = 0,\ \tfrac{\partial T}{\partial \overline{n}} = 0 \text{ at internal adiabatic block} \\ \begin{cases} T_{nf} = T_s \\ k_{nf}\frac{\partial T_{nf}}{\partial \overline{n}} = k_s\frac{\partial T_s}{\partial \overline{n}} \end{cases} \text{at internal heat-conducting block} \end{gathered} \tag{6}$$

The nanoliquid properties are [24,26]:

$$\rho_{nf} = (1 - \phi)\rho_f + \phi\rho_p \tag{7}$$

$$(\rho c)_{nf} = (1 - \phi)(\rho c)_f + \phi(\rho c)_p \tag{8}$$

$$(\rho\beta)_{nf} = (1 - \phi)(\rho\beta)_f + \phi(\rho\beta)_p. \tag{9}$$

The nanoliquid thermal conductivity was defined using the experimental data [27]:

$$k_{nf} = k_f\left(1 + 2.944\phi + 19.672\phi^2\right). \tag{10}$$

in the case of nanoliquid dynamic viscosity the following correlation was used [27]:

$$\mu_{nf} = \mu_f\left(1 + 4.93\phi + 222.4\phi^2\right). \tag{11}$$

These correlations are valid for $1\% \le \phi \le 4\%$.
The non-dimensional parameters are used,

$$\begin{gathered} x = \overline{x}/L,\ y = \overline{y}/L,\ \tau = V_0 t/L,\ u = \overline{u}/V_0,\ v = \overline{v}/V_0,\ \theta = (T - T_c)/(T_h - T_c), \\ \psi = \overline{\psi}/(V_0 L), \quad \omega = \overline{\omega} L/V_0, \quad V_0 = \sqrt{g\beta(T_h - T_c)L} \end{gathered} \tag{12}$$

and employing the non-dimensional stream function ψ, which is determined as $u = \partial\psi/\partial y$ and $v = -\partial\psi/\partial x$, as well as non-dimensional vorticity ω ($\omega = \partial v/\partial x - \partial u/\partial y$) we obtain:

$$\frac{\partial^2\psi}{\partial x^2} + \frac{\partial^2\psi}{\partial y^2} = -\omega \tag{13}$$

$$\frac{\partial\omega}{\partial\tau} + u\frac{\partial\omega}{\partial x} + v\frac{\partial\omega}{\partial y} = \frac{\mu_{nf}}{\mu_f}\frac{\rho_f}{\rho_{nf}}\sqrt{\frac{Pr}{Ra}}\left(\frac{\partial^2\omega}{\partial x^2} + \frac{\partial^2\omega}{\partial y^2}\right) + \frac{(\rho\beta)_{nf}}{\rho_{nf}\beta_f}\frac{\partial\theta}{\partial x} \tag{14}$$

$$\frac{\partial\theta}{\partial\tau} + u\frac{\partial\theta}{\partial x} + v\frac{\partial\theta}{\partial y} = \frac{1}{\sqrt{Ra\cdot Pr}}\frac{k_{nf}}{k_f}\frac{\left(\rho c_p\right)_f}{\left(\rho c_p\right)_{nf}}\left(\frac{\partial^2\theta}{\partial x^2} + \frac{\partial^2\theta}{\partial y^2}\right). \tag{15}$$

In the case of internal heat-conducting solid body we should add to the previous system of equations the following non-dimensional heat conduction equation:

$$\frac{\partial\theta}{\partial\tau} = \frac{1}{\sqrt{Ra\cdot Pr}}\frac{k_s}{k_f}\frac{(\rho c)_f}{(\rho c)_s}\left(\frac{\partial^2\theta_s}{\partial x^2} + \frac{\partial^2\theta_s}{\partial y^2}\right). \tag{16}$$

Initial and boundary relations for the obtained equations are:

$$\begin{gathered}
\tau = 0\text{: } \psi = 0,\ \omega = 0,\ \theta = 0.5 \text{ at } 0 \le x \le 1,\ 0 \le y \le 1;\\
\tau > 0\text{: } \psi = 0,\ \frac{\partial\psi}{\partial x} = 0,\ \theta = 1 \text{ at } x = 0,\ 0 \le y \le 1;\\
\psi = 0,\ \frac{\partial\psi}{\partial x} = 0,\ \theta = 0 \text{ at } x = 1,\ 0 \le y \le 1;\\
\psi = 0,\ \frac{\partial\psi}{\partial y} = 0,\ \frac{\partial\theta}{\partial y} = 0 \text{ at } y = 0,\ 1,\ 0 \le x \le 1\\
\psi = \gamma,\ \frac{\partial\psi}{\partial n} = 0,\ \frac{\partial\theta}{\partial n} = 0 \text{ at internal adiabatic block}\\
\psi = \gamma,\ \frac{\partial\psi}{\partial n} = 0,\ \begin{cases} \theta_{nf} = \theta_s \\ \frac{k_{nf}}{k_s}\frac{\partial\theta_{nf}}{\partial n} = \frac{\partial\theta_s}{\partial n} \end{cases} \text{ at internal heat-conducting solid block}
\end{gathered} \tag{17}$$

$$\tau > 0\text{: } \psi = \gamma,\ \frac{\partial\psi}{\partial n} = 0,\ \frac{\partial\theta}{\partial n} = 0 \text{ at internal adiabatic block} \tag{18}$$

$$\tau > 0\text{: } \psi = \gamma,\ \frac{\partial\psi}{\partial n} = 0,\ \begin{cases} \theta_{nf} = \theta_s \\ \frac{k_{nf}}{k_s}\frac{\partial\theta_{nf}}{\partial n} = \frac{\partial\theta_s}{\partial n} \end{cases} \text{ at internal heat-conducting solid block} \tag{19}$$

Here $Ra = \frac{g(\rho\beta)_f\left(\rho c_p\right)_f(T_h - T_c)L^3}{\mu_f k_f}$ is the Rayleigh number, $Pr = \frac{\left(\mu c_p\right)_f}{k_f}$ is the Prandtl number, additional factors in vorticity Equation (14) are $\frac{\mu_{nf}}{\mu_f}\frac{\rho_f}{\rho_{nf}} = \frac{1+4.93\phi+222.4\phi^2}{1-\phi+\phi\rho_p/\rho_f}$, $\frac{(\rho\beta)_{nf}}{\rho_{nf}\beta_f} = \frac{1-\phi+\phi(\rho\beta)_p/(\rho\beta)_f}{1-\phi+\phi\rho_p/\rho_f}$, a factor in energy Equation (15) is $\frac{k_{nf}}{k_f}\frac{(\rho c)_f}{(\rho c)_{nf}} = \frac{1+2.944\phi+19.672\phi^2}{1-\phi+\phi(\rho c)_p/(\rho c)_f}$, while $\frac{k_{nf}}{k_s} = \left(1 + 2.944\phi + 19.672\phi^2\right)K$ is a factor for temperature boundary condition of forth kind in Equation (19). Here $K = k_f/k_s$ is the heat conductivity ratio.

As a result, the boundary-value problem of thermogravitational convection in a double-connected domain having isolated internal body includes Equations (13)–(15), with conditions (17) and (18), while for the internal thermally-conducting solid body, Equations (13)–(16) need to be solved with additional relations (17) and (19).

For description of the overall energy transfer the local Nusselt number at heated wall was defined as,

$$Nu = -\frac{k_{nf}}{k_f}\frac{\partial\theta}{\partial x}\Big|_{x=0} \tag{20}$$

and the average Nusselt number $\left(\overline{Nu}\right)$ can be considered as:

$$\overline{Nu} = \int_0^1 Nu\, dy. \tag{21}$$

3. Numerical Technique

The written governing Equations (13)–(16), with additional relations (17)–(19), were worked out by the finite difference technique [8]. The steady solution was defined as a solution of the time-dependent problem. A discretization of the convective members was performed by Samarskii monotonic scheme [28] and for the diffusive members the central differences were employed. The parabolic Equations (14)–(16) were worked out using the Samarskii locally one-dimensional scheme [28]. The obtained set of linear equations was worked out by the Thomas algorithm. The stream function equation was approximated using the central differences for the second derivatives. The received set of linear equations was worked out by the successive over relaxation technique. The computations were stopped when the residuals for the stream function get bellow 10^{-7}.

For definition of the stream function magnitude at the inner body boundary the special procedure was used [29]. Namely, we introduce the condition that the pressure p should be single-valued along the internal block surface. This condition is expressed by:

$$\int \frac{\partial p}{\partial \eta}\, d\sigma = 0. \tag{22}$$

Here η is the unit tangential vector along the boundary, σ is the internal block surface.

Taking into account the considered domain of interest (Figure 1) we can define the internal block surface presented in Figure 2:

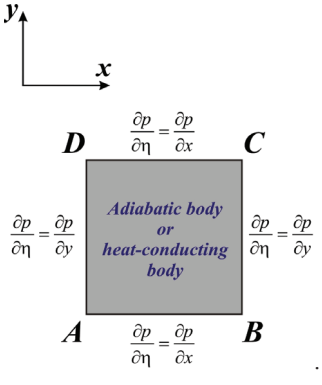

Figure 2. Surface of the internal body.

Using governing Equations (2) and (3) in non-dimensional form as well as non-slip boundary conditions for velocity at internal block surface, $\partial p/\partial \eta$ can be defined as:

$$\frac{\partial p}{\partial x} = \frac{\mu_{nf}}{\mu_f}\frac{\rho_f}{\rho_{nf}}\sqrt{\frac{Pr}{Ra}}\frac{\partial^2 u}{\partial y^2} \tag{23}$$

$$\frac{\partial p}{\partial y} = \frac{\mu_{nf}}{\mu_f}\frac{\rho_f}{\rho_{nf}}\sqrt{\frac{Pr}{Ra}}\frac{\partial^2 v}{\partial x^2} + \frac{(\rho\beta)_{nf}}{\rho_{nf}\beta_f}\theta. \tag{24}$$

Taking into account the condition (22) we have:

$$\int_{\sigma} dp = \int_{A}^{B} \frac{\partial p}{\partial x}\, dx + \int_{B}^{C} \frac{\partial p}{\partial y}\, dy + \int_{C}^{D} \frac{\partial p}{\partial x}\, dx + \int_{D}^{A} \frac{\partial p}{\partial y}\, dy = 0. \tag{25}$$

Introducing Equations (23) and (24) in (25) we have:

$$\int_{A}^{B} \frac{\partial \omega}{\partial y}\, dx - \int_{B}^{C} \frac{\partial \omega}{\partial x}\, dy + \int_{C}^{D} \frac{\partial \omega}{\partial y}\, dx - \int_{D}^{A} \frac{\partial \omega}{\partial x}\, dy = \frac{(\rho\beta)_{nf}}{(\rho\beta)_{f}} \frac{\mu_f}{\mu_{nf}} \sqrt{\frac{Ra}{\mathrm{Pr}}} \left(\int_{B}^{C} \theta\, dy + \int_{D}^{A} \theta\, dy \right). \tag{26}$$

Using Equation (26) and interpreting the correlation between vorticity at internal body surface and stream function, the considered value can be found. Such technique was used in the present study for determining the stream function magnitude at inner body boundary.

4. Validation

The created numerical code was verified employing the numerical results of Karki et al. [30] for convective heat transfer in a square cavity with isothermal vertical walls and centered thermally-insulated body. Figures 3 and 4 demonstrate a good concordance for considered isolines for different *Ra* in comparison with numerical data of Karki et al. [30].

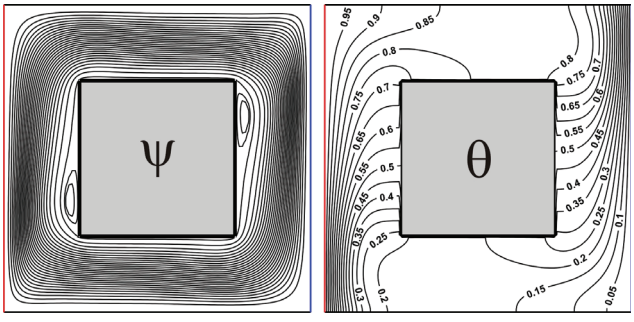

Figure 3. Isolines of ψ and θ for $Ra = 10^5$, $\delta = 0.5$.

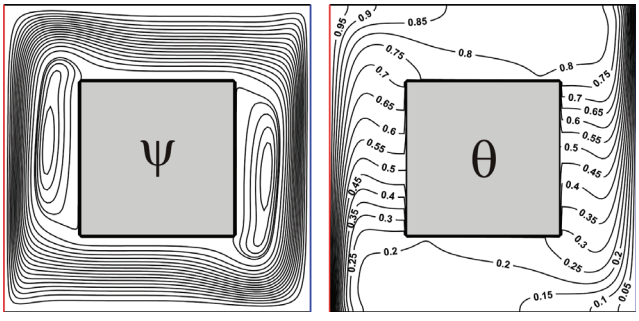

Figure 4. Isolines of ψ and θ for $Ra = 10^6$, $\delta = 0.5$.

The second benchmark problem was free convective energy transport in a rectangular chamber with two bottom border-mounted adiabatic blocks [31]. Figure 5 presents a very good concordance for the average *Nu* at the hot boundary compared with data of Ben-Nakhi and Chamkha [31].

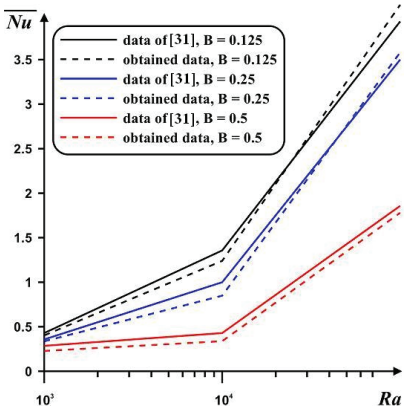

Figure 5. Mean *Nu* at hot border compared with computations [31] for different heights of the obstacles (B) and Rayleigh numbers.

The third benchmark problem was free convective energy transport of Al_2O_3-H_2O nanoliquid inside a differentially-heated chamber. Table 1 illustrates a very good concordance for the mean *Nu* at heated wall, in dependence on the nanoadditives concentration, in comparison with experimental results [27].

Table 1. Values of mean *Nu* at hot border.

φ	*Ra*	*Pr*	Experimental Data [27]	Present Study
0.01	7.74547×10^7	7.0659	32.2037	30.6533
0.02	6.6751180×10^7	7.3593	31.0905	30.5038
0.03	5.6020687×10^7	7.8353	29.0769	30.2157

A mesh independence test was performed employing four different grid parameters (100 × 100, 200 × 200, and 400 × 400) for $Ra = 10^5$, $Pr = 6.82$, $\phi = 0.02$, $\delta = 0.5$. Using Figure 6 it is possible to conclude that the deviations of the average *Nu* for 200 × 200 and 400 × 400 are negligible (at about 1.5%). Therefore, a uniform grid of 200 × 200 was used for investigations.

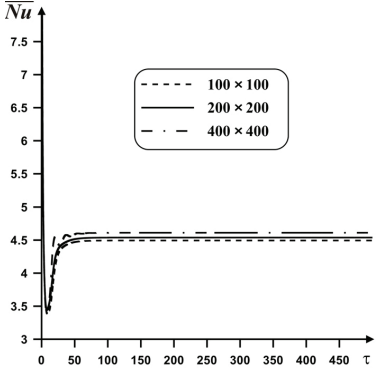

Figure 6. Time profiles of average *Nu* for various mesh parameters.

5. Results and Discussion

Computational investigations have been conducted for Rayleigh number (Ra = 10^4–10^6), the nanoadditives concentration (ϕ = 0.0–0.04), internal body size (δ = 0.3–0.7), and a thermal conductivity ratio (K = 10^{-3}–1). Effects of the mentioned characteristics on circulation field, temperature field and profiles of Nu are presented in Figures 7–15.

Figure 7 demonstrates the considered isolines within the cavity having internal adiabatic block for various Ra. In the case of small magnitude of the buoyancy force (see Figure 7a) one global circulation can be found reflecting an appearance of upstream flows next to the left hot boundary and downstream circulations at the right cold boundary. Temperature field illustrates a formation of heat conduction regime over and under the internal block, where temperature isolines are parallel to vertical boundaries. At the same time, isotherms near the isothermal walls characterize low intensive circulation. A rise of Ra (see Figure 7b) reflects more intensive liquid motion with an appearance of thin temperature boundary layers near the vertical borders. Isolines of stream function present a formation of weak recirculations zones near the internal block, namely, close to the left bottom corner and close to the right upper corner. This considered heat transfer mode demonstrates less intensive cooling and heating of the cavity from isothermal walls. Further increment of the buoyancy force bulk results in an expansion of secondary vortices close to the internal body surface. Such circulations reflect the temperature stratification in these zones, where heating occurs from the top portion till the lower part. An addition of nanoadditives (ϕ = 0.04) leads to a reduction of liquid circulation strength, while more essential difference in isotherms can be found for low values of Ra (see Figure 7a). As a result an inclusion of nanoparticles allows enhancing the heat conduction regime.

In the case of internal heat-conducting solid body (see Figure 8) flow structures and temperature patterns are changed. Regardless of the Rayleigh number the global circulation formed within the chamber is the same like presented in Figure 7, but the temperature field and secondary vortices have another structure. Thus, isotherms characterize the temperature change within the internal solid block from the left and right sides, where internal isotherm (θ = 0.5) is almost parallel to vertical walls.

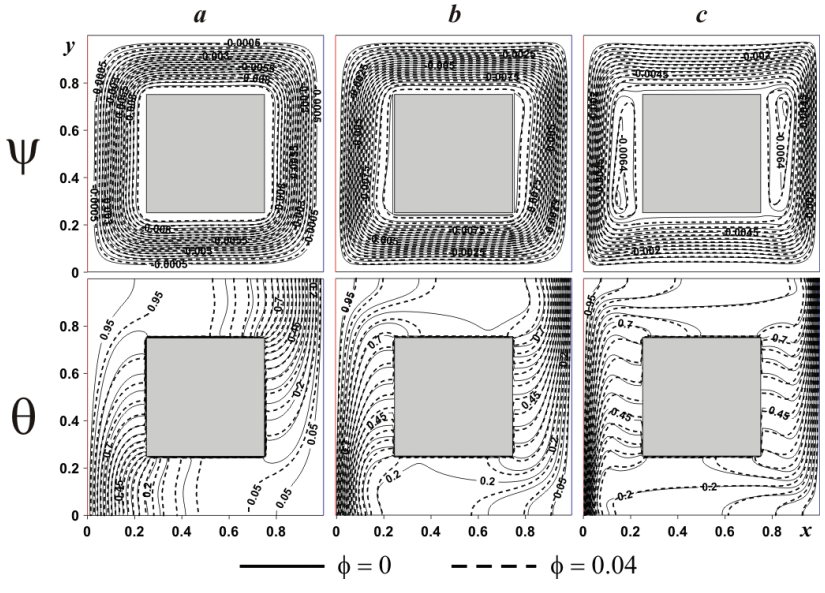

Figure 7. Isolines of ψ and θ for adiabatic internal body at δ = 0.5 and different Ra and ϕ:(**a**)—Ra = 10^4, (**b**)—Ra = 10^5, (**c**)—Ra = 10^6.

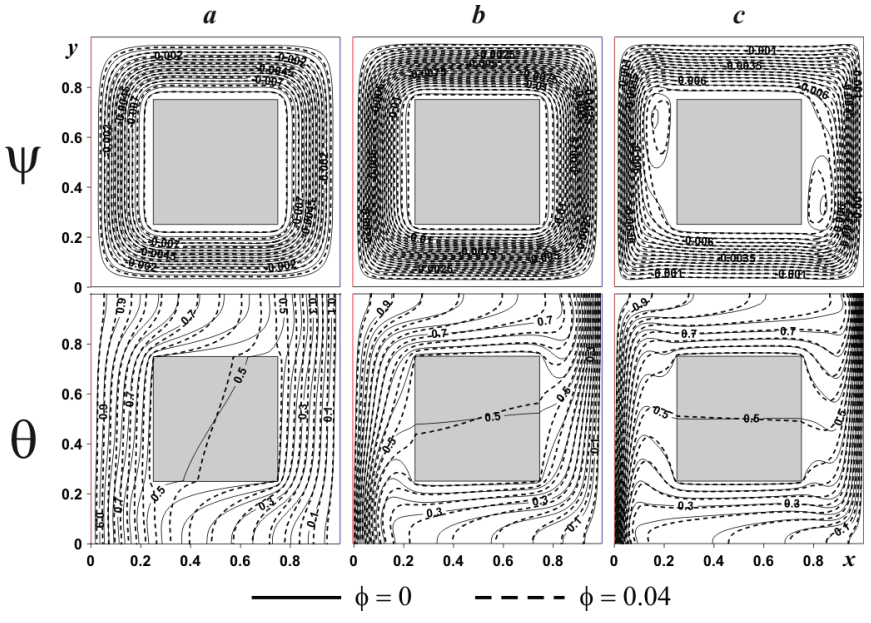

Figure 8. Isolines of ψ and θ for heat-conducting internal body at $\delta = 0.5$ and different Ra and ϕ: (**a**)—$Ra = 10^4$, (**b**)—$Ra = 10^5$, (**c**)—$Ra = 10^6$.

In the case of $Ra = 10^5$ isotherms within the internal solid body become parallel to horizontal walls illustrating heating from the top till bottom, while the cooling process occurs in the opposite direction. Also, a stronger circulation characterizes a diminution of the boundary layers thickness, due to the interaction between the hot and cold fluxes. It is interesting to note that a consideration of internal heat-conducting body characterizes a vanishing of the weak recirculations near the block surface for $Ra = 10^5$ mentioned for adiabatic case and for $Ra = 10^6$ these vortices have another shape and location of cells. It is worth noting that strong upstream flow close to the left border and a strong downstream one near the right boundary lead to formation of clockwise circulations far from the origin of these flows. An absence of such strong flows in the case of adiabatic block allows forming vortices elongate along the vertical walls of the internal block.

Figure 9 demonstrates the behavior of the local and mean Nu at hot border with Ra, thermal conductivity ratio and time. An increment of Ra characterizes a raise of the local Nu. An interaction of the hot and cold heat fluxes near the lower portion of the left border reflects a presence of high Nu values in this zone. A rise of y-coordinate illustrates a decrease of Nu. Moreover, with Ra the maximum value of Nu approaches the left boundary. Value $K = \infty$ reflects the presence of internal adiabatic body. A growth of the heat conductivity of internal body material characterizes a diminution of the temperature drop in the lower portion and a rise of this temperature difference in the upper zone. The time dependence of the average Nusselt number (Figure 9b) demonstrates a fast reaching the steady state value. An increment of Ra reflects a rise of time for the steady state. A diminution of the heat conductivity ratio from adiabatic case ($K = \infty$) till high internal body material thermal conductivity reflects a reduction of the mean Nu. Therefore, in the case of adiabatic internal body one can reveal the maximum energy transport strength.

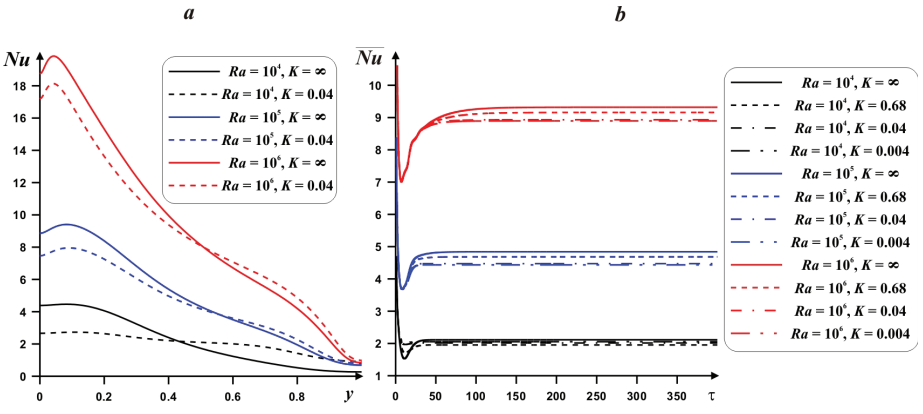

Figure 9. Local *Nu* profiles (**a**) and time-dependent mean *Nu* profiles (**b**) for $\delta = 0.5$, $\phi = 0.02$ and different *Ra* and *K*.

A reduction in the mean *Nu* with nanoadditives is presented in Figure 10. It is possible to intensify the energy transport with ϕ only for low *Ra*, where heat conduction is a dominated energy transport mode. Also, only for this regime, the heat transfer enhancement can be found with a rise of the internal body material thermal conductivity for the case of high nanoparticles concentration.

Effect of the internal body size on streamlines and isotherms for adiabatic and heat-conducting blocks is presented in Figures 11 and 12. In the case of adiabatic internal block (Figure 11), an increment of δ results in the attenuation of convective motion with a formation of secondary circulations near the internal body surface. A growth of the internal block size from $\delta = 0.3$ till $\delta = 0.5$ characterizes an elongation of secondary vortices near the solid block surface, while for $\delta = 0.7$ these vortices are decreased essentially. At the same time, an increment of δ reflects a vertical displacement of the left eddy core in negative *y*-coordinate direction, while the right eddy core displaces vertically in positive *y*-coordinate direction. Temperature fields illustrate the thermal stratification. Moreover, the presence of the adiabatic body divides the temperature isolines into two parts and these two parts are similar to the original isotherms without a solid body. The addition of nanoparticles reflects a modification of temperature field near the horizontal walls, while streamlines are differed in the zone of secondary vortices.

In the case of internal heat-conducting block (see Figure 12), an introduction of solid block characterizes also a rise in size of two secondary vortices but in the top portion of the left body boundary and near the bottom portion of the right body boundary. The reason for such a difference between adiabatic and heat-conducting bodies was discussed above. Moreover, for $\delta \leq 0.5$ heating/cooling of the internal block occurs in vertical direction, while for $\delta = 0.7$, temperature profiles can be found within the solid block that are not parallel to horizontal walls. The addition of nanoparticles reduces the convective flow strength due to a growth of nanofluid viscosity (see Equation (11)). Significant difference in isotherms can be found within the solid body due to different heat fluxes at solid body surface.

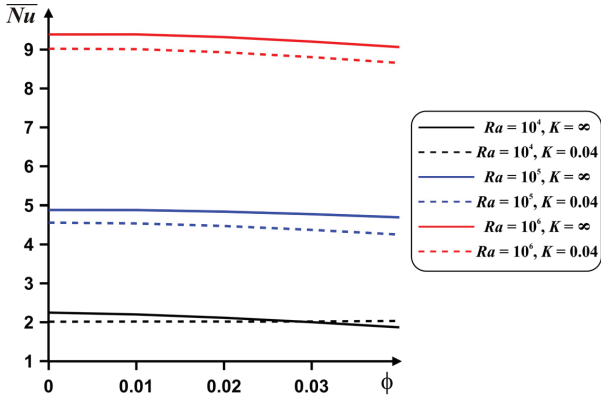

Figure 10. Dependences of the mean *Nu* on ϕ, *Ra* and *K* for $\delta = 0.5$.

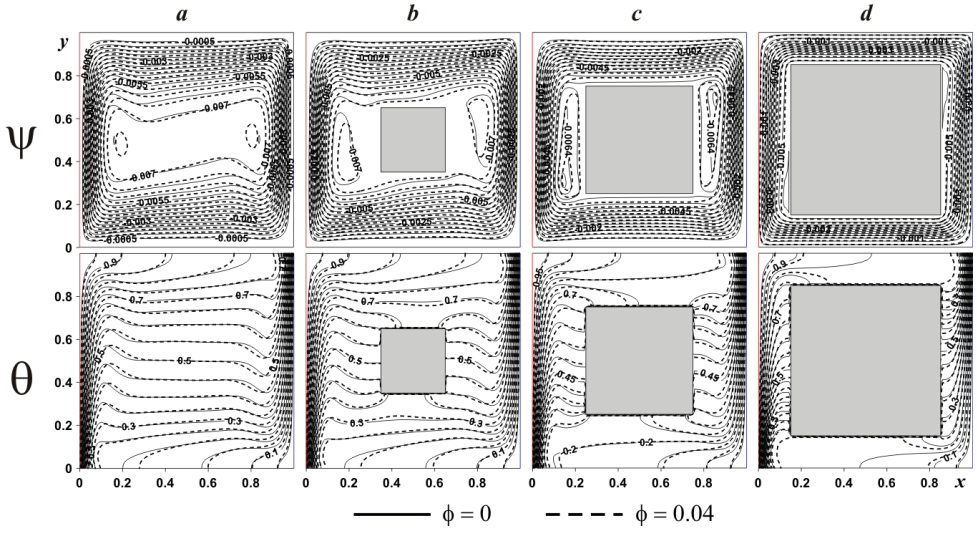

Figure 11. Isolines of ψ and θ for adiabatic internal body at $Ra = 10^6$ and different δ and ϕ: (**a**)—$\delta = 0.0$, (**b**)—$\delta = 0.3$, (**c**)—$\delta = 0.5$, (**d**)—$\delta = 0.7$.

Effect of internal block size and heat conductivity ratio on *Nu* and $\overline{Nu}$ is demonstrated in Figure 13. As it has been described above, a rise of the heat conductivity of solid block material results in a diminution of the mean *Nu*. At the same time, the growth of the solid block size illustrates a rise of the temperature drop at the lower portion of the heated wall and an increment of the internal block material thermal conductivity results in strong diminution of local *Nu* at the lower portion of left border. The internal body length has a non-monotonic impact on the mean *Nu*. Therefore, it is possible to reveal an optimal magnitude of δ for high value of $\overline{Nu}$. At the same time, a rise of δ characterizes more essential impact of *K* on the mean *Nu*.

Diminution of the mean *Nu* with nanoadditives concentration is presented in Figure 14. More essential reduction can be found for high value of the internal block material thermal conductivity. In this case for $\delta = 0.5$ we have maximum $\overline{Nu}$.

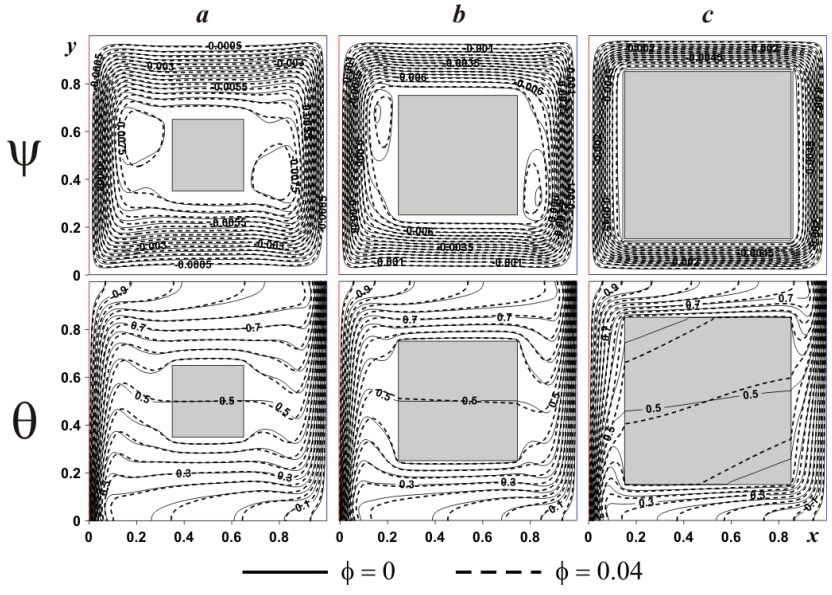

Figure 12. Isolines of ψ and θ for heat-conducting internal body at $Ra = 10^6$ and different δ and ϕ: (**a**)—$\delta = 0.3$, (**b**)—$\delta = 0.5$, (**c**)—$\delta = 0.7$.

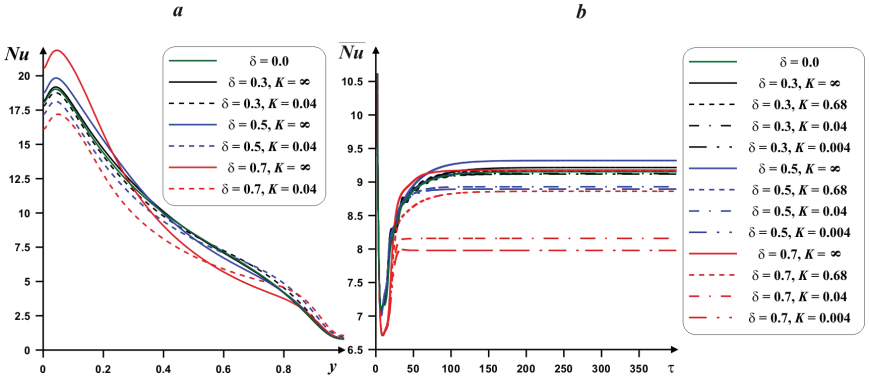

Figure 13. Local *Nu* profiles (**a**) and time-dependent mean *Nu* profiles (**b**) for $Ra = 10^6$, $\phi = 0.02$ and different δ and K.

An impact of the heat conductivity ratio on the considered isolines is shown in Figure 15. A reduction of this parameter illustrates modification of temperature field, where one can reveal a rise of the temperature wave speed within the solid block and as a result a density of isotherms rises near the solid block surface. At the same time, a reduction and displacement of the secondary convective cells cores occur with a decrement of K.

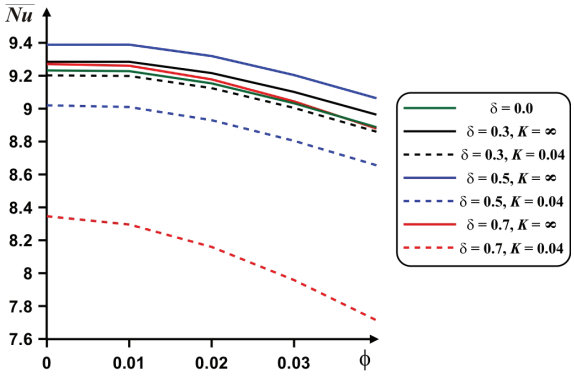

Figure 14. Dependences of the mean Nu on ϕ, δ and K for $Ra = 10^6$.

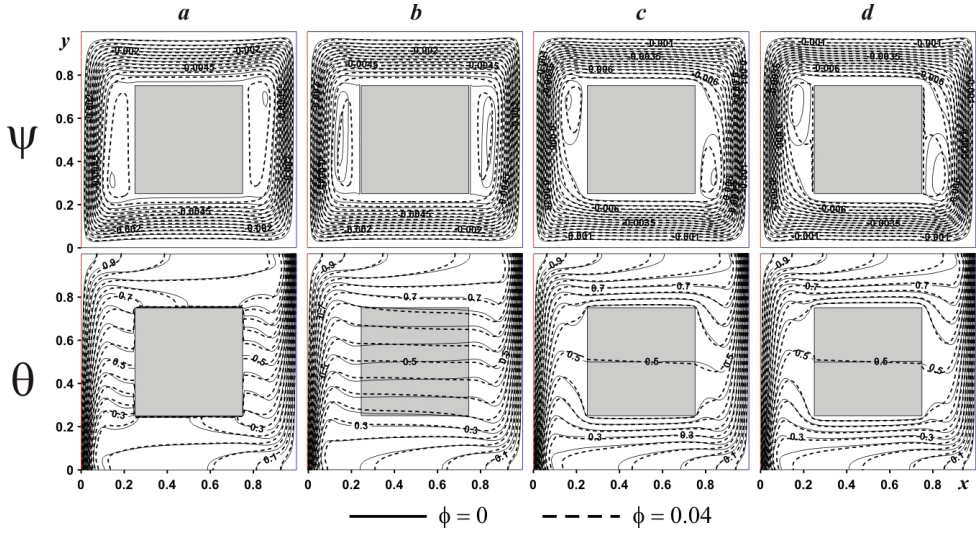

Figure 15. Isolines of ψ and θ for heat-conducting internal body at $Ra = 10^6$ and different K and ϕ: (**a**)—$K = \infty$, (**b**)—$K = 0.68$, (**c**)—$K = 0.04$, (**d**)—$K = 0.004$.

6. Conclusions

Numerical investigation of thermogravitational convection inside a differentially-heated domain with inner adiabatic or thermally-conducting block has been performed. Investigations have been carried out using the developed computational code based on the non-primitive variables. The detailed description of the numerical procedure for the determining the stream function magnitude the inner body surface has been provided. It should be noted that using the non-primitive variables decreases the number of governing equations due to an exclusion of the pressure field from the momentum equation. Such an approach results in the reduction of computational time. Therefore, using the non-primitive variables allows reducing computational time for various problems. In the case of present study the effective numerical algorithm has been developed for the multi-connected domains. This algorithm has been employed to investigate conjugate natural convection inside the differentially-heated chamber filled with a nanosuspension.

As a result, an analysis of the Rayleigh number, thermal conductivity ratio, internal block size, and nano-additives concentrations has been conducted. It has been ascertained that:

- a decrease in heat conductivity ratio from adiabatic case until high internal body material thermal conductivity illustrates a reduction of the mean Nu;
- an internal block size has a non-monotonic impact on the mean Nu. Therefore, it is possible to reveal an optimal value of δ (0.5 for the present analysis) for high value of $\overline{Nu}$. A rise of δ illustrates stronger impact of K on $\overline{Nu}$;
- an increment of the nanoadditives concentration characterizes the energy transport degradation, while it is possible to enhance the energy transport with ϕ only for low Ra, where thermal conduction is a dominated thermal transmission mode.

The performed analysis allows intensifying the heat transfer within the chamber in the case of optimal selection of the inner block size, thermal conductivity of this block material and concentration of nano-sized additives within the host fluid.

The developed numerical algorithm and computational code will be used in future for analysis of the cooling effect in the case of heat-generating internal solid block that can be considered an electronic chip within the electronic cabinet. Moreover, the developed computational technique will be used for an investigation of the effects of several internal heat-generating blocks in order to optimize the location of such an element inside the electronic cabinet. The mentioned analysis will be conducted in the case of a single or hybrid nanoliquid impact.

Author Contributions: M.A.S., I.P. and T.G. conceived the main concept. M.A.S. contributed to the investigation and data analysis. All authors have read and agreed to the published version of the manuscript.

Funding: This work of Mikhail A. Sheremet was supported by the Russian Science Foundation (Project No. 17-79-20141).

Conflicts of Interest: The authors declare no conflict of interest.

Nomenclature

c	heat capacity
g	gravity force acceleration
K	heat conductivity ratio
k	heat conductivity
L	length and height of the chamber
Nu	local Nusselt number
$\overline{Nu}$	average Nusselt number
p	non-dimensional pressure
$\overline{p}$	dimensional pressure
Pr	Prandtl number
Ra	Rayleigh number
T	dimensional temperature
t	dimensional time
T_c	cold boundary temperature
T_h	hot boundary temperature
u, v	non-dimensional velocity projections
$\overline{u}$, $\overline{v}$	dimensional velocity projections
V_0	dimensional reference velocity
x, y	non-dimensional Cartesian coordinate
$\overline{x}$, $\overline{y}$	dimensional Cartesian coordinates

Greek symbols

β	heat expansion parameter
δ	non-dimensional size of the internal solid block
θ	non-dimensional temperature
μ	dynamic viscosity
ρ	density
ρc	thermal capacitance
$\rho\beta$	buoyancy parameter
τ	non-dimensional time
γ	non-dimensional magnitude of the stream function at inner body borders
ϕ	nano-sized particles volume fraction
$\overline{\psi}$	stream function
ψ	non-dimensional stream function
$\overline{\omega}$	dimensional vorticity
ω	non-dimensional vorticity

Subscripts

c	cold
f	fluid
h	hot
nf	nanofluid
p	(nano)particle
s	solid

References

1. Hussein, A.K.; Ashorynejad, H.R.; Sivasankaran, S.; Kolsi, L.; Shikholeslami, M.; Adegun, I.K. Modeling of MHD natural convection in a square enclosure having an adiabatic square shaped body using Lattice Boltzmann method. *Alex. Eng. J.* **2016**, *55*, 203–214. [CrossRef]
2. Miroshnichenko, I.V.; Sheremet, M.A. Turbulent natural convection heat transfer in rectangular enclosures using experimental and numerical approaches: A review. *Renew. Sustain. Energy Rev.* **2018**, *82*, 40–59. [CrossRef]
3. Ostrach, S. Natural convection in enclosures. *Adv. Heat Transf.* **1972**, *8*, 161–227.
4. Choi, S.U.S. Enhancing thermal conductivity of fluids with nanoparticles. In Proceedings of the 1995 ASME International Mechanical Engineering Congress and Exposition, San Francisco, CA, USA, 12–17 November 1995; pp. 99–105.
5. Babu, J.A.R.; Kumar, K.K.; Rao, S.S. State-of-art review on hybrid nanofluids. *Renew. Sustain. Energy Rev.* **2017**, *77*, 551–565. [CrossRef]
6. Das, S.K.; Choi, S.U.S.; Yu, W.; Pradeep, Y. *Nanofluids: Science and Technology*; Wiley: Hoboken, NJ, USA, 2008.
7. Minkowycz, W.J.; Sparrow, E.M.; Abraham, J.P. *Nanoparticle Heat Transfer and Fluid Flow*; CRC Press: New York, NY, USA, 2013.
8. Shenoy, A.; Sheremet, M.; Pop, I. *Convective Flow and Heat Transfer from Wavy Surfaces: Viscous Fluids, Porous Media and Nanofluids*; CRC Press: New York, NY, USA, 2016.
9. Nield, D.A.; Bejan, A. *Convection in Porous Media*, 5th ed.; Springer: New York, NY, USA, 2017.
10. Bozhko, A.A.; Suslov, S.A. *Convection in Ferro-Nanofluids: Experiments and Theory*; Springer: New York, NY, USA, 2018.
11. Buongiorno, J.; Venerus, D.C.; Prabhat, N.; McKrell, T.; Townsend, J.; Christianson, R.; Tolmachev, Y.V.; Keblinski, P.; Hu, L.; Alvarado, J.L.; et al. A benchmark study on the thermal conductivity of nanofluids. *J. Appl. Phys.* **2009**, *106*, 1–14. [CrossRef]
12. Kakaç, S.; Pramuanjaroenkij, A.A. Review of convective heat transfer enhancement with nanofluids. *Int. J. Heat Mass Transf.* **2009**, *52*, 3187–3196. [CrossRef]
13. Manca, O.; Jaluria, Y.; Poulikakos, D. Heat transfer in nanofluids. *Adv. Mech. Eng.* **2010**, *2010*, 380826. [CrossRef]

14. Abouali, O.; Ahmadi, G. Computer simulations of natural convection of single phase nanofluids in simple enclosures: A critical review. *Appl. Therm. Eng.* **2012**, *36*, 1–13. [CrossRef]
15. Mahian, O.; Kianifar, A.; Kalogirou, S.A.; Pop, I.; Wongwises, S. A review of the applications of nanofluids in solar energy. *Int. J. Heat Mass Transf.* **2013**, *57*, 582–594. [CrossRef]
16. Mahian, O.; Kolsi, L.; Amani, M.; Estelle, P.; Ahmadi, G.; Kleinstreuer, C.; Marshall, J.S.; Taylor, R.A.; Abu-Nada, E.; Rashidi, S.; et al. Recent advances in modeling and simulation of nanofluid flows-part I: Fundamental and theory. *Phys. Rep.* **2019**, *790*, 1–48. [CrossRef]
17. Mahian, O.; Kolsi, L.; Amani, M.; Estelle, P.; Ahmadi, G.; Kleinstreuer, C.; Marshall, J.S.; Taylor, R.A.; Abu-Nada, E.; Rashidi, S.; et al. Recent advances in modeling and simulation of nanofluid flows-part II: Applications. *Phys. Rep.* **2019**, *791*, 1–60. [CrossRef]
18. Minea, A.A. Numerical studies on heat transfer enhancement and synergy analysis on few Metal oxide water based nanofluids. *Int. J. Heat Mass Transf.* **2015**, *89*, 1207–1215. [CrossRef]
19. Minea, A.A.; Lorenzini, G. A numerical study on ZnO based nanofluids behavior on natural convection. *Int. J. Heat Mass Transf.* **2017**, *114*, 286–296. [CrossRef]
20. Sheikholeslami, M.; Ganji, D.D. Nanofluid convective heat transfer using semi analytical and numerical approaches: A review. *J. Taiwan Inst. Chem. Eng.* **2016**, *65*, 43–77. [CrossRef]
21. Groşan, T.; Sheremet, M.A.; Pop, I. Heat transfer enhancement in cavities filled with nanofluids. In *Advances in Heat Transfer Fluids: From Numerical to Experimental Techniques*; Minea, A.A., Ed.; CRC Press: New York, NY, USA, 2017; pp. 267–284.
22. Saghir, M.Z.; Ahadi, A.; Yousefi, T.; Farahbakhsh, B. Two-phase and single phase models of flow of nanofluid in a square cavity: Comparison with experimental results. *Int. J. Therm. Sci.* **2016**, *100*, 372–380. [CrossRef]
23. Miroshnichenko, I.V.; Sheremet, M.A.; Oztop, H.F.; Abu-Hamdeh, N. Natural convection of alumina-water nanofluid in an open cavity having multiple porous layers. *Int. J. Heat Mass Transf.* **2018**, *125*, 648–657. [CrossRef]
24. Bondareva, N.S.; Sheremet, M.A.; Oztop, H.F.; Abu-Hamdeh, N. Entropy generation due to natural convection of a nanofluid in a partially open triangular cavity. *Adv. Powder Technol.* **2017**, *28*, 244–255. [CrossRef]
25. Sheremet, M.A. The influence of cross effects on the characteristics of heat and mass transfer in the conditions of conjugate natural convection. *J. Eng. Thermophys.* **2010**, *19*, 119–127. [CrossRef]
26. Sheremet, M.A.; Pop, I.; Oztop, H.F.; Abu-Hamdeh, N. Natural convection of nanofluid inside a wavy cavity with a non-uniform heating: Entropy generation analysis. *Int. J. Numer. Methods Heat Fluid Flow* **2017**, *27*, 958–980. [CrossRef]
27. Ho, C.J.; Li, W.K.; Chang, Y.S.; Lin, C.C. Natural convection heat transfer of alumina-water nanofluid in vertical square enclosures: An experimental study. *Int. J. Therm. Sci.* **2010**, *49*, 1345–1353. [CrossRef]
28. Bondarenko, D.S.; Sheremet, M.A.; Oztop, H.F.; Ali, M.E. Natural convection of Al_2O_3/H_2O nanofluid in a cavity with a heat-generating element. Heatline visualization. *Int. J. Heat Mass Transf.* **2019**, *130*, 564–574. [CrossRef]
29. Shulepova, E.V.; Sheremet, M.A.; Oztop, H.F.; Abu-Hamdeh, N. Mixed convection of Al_2O_3–H_2O nanoliquid in a square chamber with complicated fin. *Int. J. Mech. Sci.* **2020**, *165*, 105192. [CrossRef]
30. Karki, P.; Yadav, A.K.; Perumal, D.A. Study of adiabatic obstacles on natural convection in a square cavity using lattice Boltzmann method. *J. Therm. Sci. Eng. Appl.* **2019**, *11*, 034502. [CrossRef]
31. Ben-Nakhi, A.; Chamkha, A.J. Natural convection in inclined partitioned enclosures. *Heat Mass Transf.* **2006**, *42*, 311–321. [CrossRef]

nanomaterials

MDPI

Article

Cooling Performance of a Novel Circulatory Flow Concentric Multi-Channel Heat Sink with Nanofluids

Ravindra Jilte [1], Mohammad H. Ahmadi [2,*], Ravinder Kumar [1], Vilas Kalamkar [3] and Amirhosein Mosavi [4,5,6,7,*]

1 Department of Mechanical Engineering; Lovely Professional University, Phagwara, Punjab-14411, India; rdjilte@gmail.com (R.J.); rav.chauhan@yahoo.co.in (R.K.)
2 Faculty of Mechanical Engineering, Shahrood University of Technology, POB- Shahrood 3619995161, Iran
3 Department of Mechanical Engineering, Visvesvaraya National Institute of Technology, Nagpur 440010, India; vilas.kalamkar@gmail.com
4 Kalman Kando Faculty of Electrical Engineering, Obuda University, 1034 Budapest, Hungary
5 Institute of Structural Mechanics (ISM), Bauhaus-Universität Weimar, 99423 Weimar, Germany
6 Thuringian Institute of Sustainability and Climate Protection, 07743 Jena, Germany
7 Faculty of Civil Engineering, Technische Universität Dresden, 01069 Dresden, Germany
* Correspondence: mohammadhosein.ahmadi@gmail.com (M.H.A.); Amir.mosavi@kvk.uni-obuda.hu (A.M.)

Received: 28 December 2019; Accepted: 27 February 2020; Published: 31 March 2020

Abstract: Heat rejection from electronic devices such as processors necessitates a high heat removal rate. The present study focuses on liquid-cooled novel heat sink geometry made from four channels (width 4 mm and depth 3.5 mm) configured in a concentric shape with alternate flow passages (slot of 3 mm gap). In this study, the cooling performance of the heat sink was tested under simulated controlled conditions.The lower bottom surface of the heat sink was heated at a constant heat flux condition based on dissipated power of 50 W and 70 W. The computations were carried out for different volume fractions of nanoparticles, namely 0.5% to 5%, and water as base fluid at a flow rate of 30 to 180 mL/min. The results showed a higher rate of heat rejection from the nanofluid cooled heat sink compared with water. The enhancement in performance was analyzed with the help of a temperature difference of nanofluid outlet temperature and water outlet temperature under similar operating conditions. The enhancement was ~2% for 0.5% volume fraction nanofluids and ~17% for a 5% volume fraction.

Keywords: heat sink; mini-channels; liquid cooling; nanofluid; cooling performance

1. Introduction

Miniaturization of electronic devices faces heat rejection problems. Advancement in fabricating these devices has resulted in them becoming smaller in size. Such devices produce a large heat generation in a smaller volume. It necessitates an effective cooling arrangement for maintaining the operating temperature within a safe range [1]. Uses of heat sinks with micro/mini-channels have emerged as a feasible solution, which was first proposed by Tukerman and Pease [2]. Among the possible working fluids investigated, air cooling is unable to meet the increasing demand for high heat removal rates. Electronic and IT applications demand a compact, more efficient, and an adequately designed effective cooling system that is capable of sustainable longevity. Generally, these electronics systems are cooled with either air or liquid (water, glycol, etc.) [3]. Microchannel liquid cooling can be advantageous [4].

Many investigations have reported on hydraulic and thermal behavior as well as heat transfer augmentations. The different heat-transfer augmented techniques in micro/mini-channels for single-phase cooling devices were reviewed by Steinke and Kandlikar [5].An investigation was

performed on a water-cooled offset strip fin enhanced microchannel heat exchanger and this was shown to perform better when compared with straight continuous channel walls [6]. Khameneh et al. [7] carried out a numerical study on laminar flow and forced convective heat transfer in water-cooled rectangular-shaped microchannel sections that had specific hydraulic diameters and distinct geometric configurations. Aspect ratio and hydraulic diameter affected the heat transfer rate of microchannels. Hasan et al. [8] analyzed the performance of a microchannel heat exchanger and presented results which took into consideration the different shapes and sizes of the channels. Xie et al. [4] performed a numerical study on mini-channel heatsinks subjected to a constant heat flux wall condition. In narrow and deep channels, the heat transfer performance was improved with a relatively high-pressure drop. Jiang and Ruina [9] reported that, in mini-fin structures, the convective heat transfer coefficient increased 9–21-fold for water and 12–38-fold for air, compared to the empty plate channel. Ahmed [10] conducted a numerical study on grooved microchannel heatsinks to analyze the effect of geometrical specifications on laminar convective heat transfer. Trapezoidal grooved microchannel heatsinks (MCHSs) have the optimum thermal design compared to rectangular and triangular grooved MCHSs. Choi et al. [11] conducted numerical analysis on microchannel water blocks with pass variations. The heat transfer rate accompanied by higher values of pressure drop were observed in two-pass samples. Jajja et al. [12] experimentally investigated the influence of fin spacing in different heat sinks for effective thermal management. Liu and Jianlin [13] numerically analyzed the fluid flow and thermal characteristics of mini-channel heatsinks with non-uniform inlets. The total thermal resistance of the mini-channel heat sink was reduced by 9.9% to 13.1% using non-uniform baffles. Aliabadi et al. [14] experimentally studied the cooling performance of a sinusoidal wavy mini-channel heat sink and examined the effect of geometrical parameters and working fluids and observed the effective thermal performance compared to a straight mini-channel heatsink. Lee et al. [15] suggested that a continuum-based approach can be applied to estimate the heat transfer in microchannels. The use of a serpentine microchannel (with a square cross-section) to characterize slug flow behavior has been reported by Cairone et al. [16]. Under critical heat flux conditions, heat rejection from heat sink utilizing water as the heat transfer media can be further enhanced with nanofluids [17].

Many studies have been carried out citing nanofluid usage in heat transfer enhancement [18–20]. Among these, Choi et al. [21] introduced the concept of nanofluid and presented that thermal conductivity of base fluid can be increased with the addition of nanoparticles of sizes less than 100 nm [22]. The use of such nanofluids in mini-channel heat sinks (MCHSs) has been reported in some studies. Ho et al. [23] carried out forced convective cooling of MCHSs with Al_2O_3–water nanofluid and found that it enhanced heat transfer. Koo and Kleinstreuer [24] suggested nanofluid selection should be based on higher Prandtl numbers, high-volume concentrations of nanoparticles, and a high aspect ratio of microchannels to avoid nanoparticle accumulation. Jang and Choi [25] found that MCHS performance was enhanced by 10% for a water-diamond nanofluid compared with pure water. Ijam and Saidur [26] analytically investigated the effect of nanoparticle concentration and Reynolds number in MCHSs.

Based on the studies above, most of the investigations were carried out on the characteristics of heat transfer and fluid flow in circular or rectangular straight mini-channel heat sinks. Only a few experimental or numerical studies are currently available with regards to spiral or concentric channels, but there is no research currently available which has reported on a multi-circular mini-channel heat sink. In this work, thermal performance of a concentric channel heat sink with an alternate slot for the fluid flow is presented.

2. Circulatory Flow Multi-Channel Heat Sink

A heat sink was modified to create a circulatory flow of cooling media. It contained four concentric channels (width 4 mm and depth 3.5 mm) with alternate opening slots (Figure 1). The cooling fluid was fed centrally to the heat sink to facilitate higher heat removal. An electronic device such as a processor generates more heat at the center, whereas peripheral portions or parts can dissipate heat to

the surroundings. Cooling liquid from the inlet pipe entered centrally, and the flow bifurcated after passing through the first slot or opening. The liquid then flowed through the first channel again and then bifurcated after it passed through the second slot. The outlet for circulating liquid was provided at the outer periphery. The interior view of the heat sink (as shown in Figure 1) was made of copper and sealed on top with a copper plate. This top cover was provided with an inlet pipe which allowed the flow of inlet water through the channel. The geometrical dimensions of concentric circulatory flow heat sink are listed in Table 1.

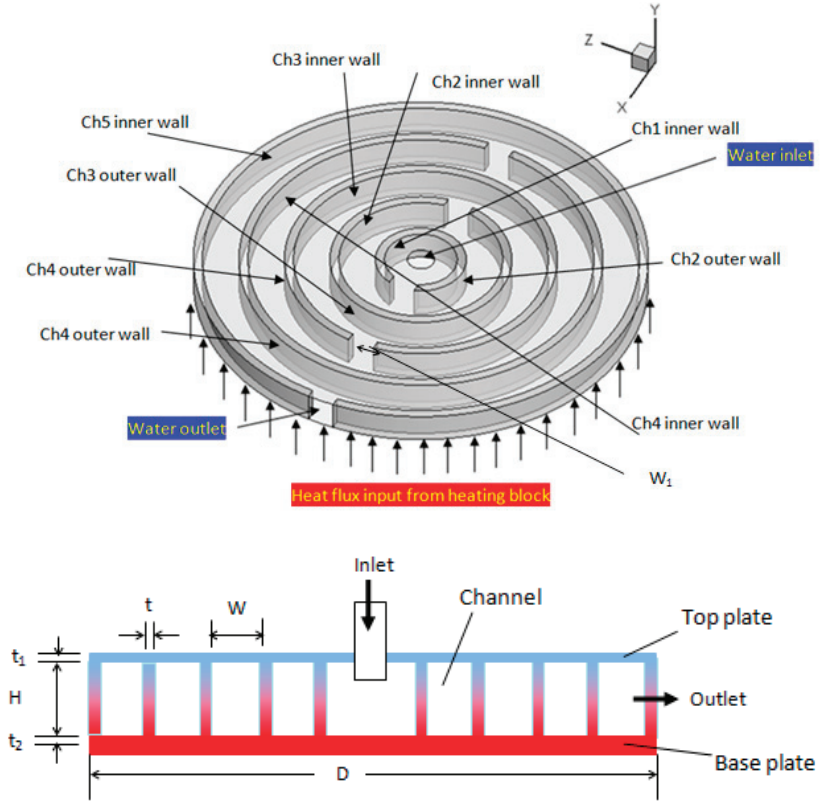

Figure 1. Proposed circulatory flow multi-channel heat sink.

Table 1. Specifications of the heat sink.

Parameters	Size, mm
Diameter of heat sink (D)	50
Height of channel (H)	3.5
Width of channel (W)	4
Thickness of channel wall (t)	1
Thickness of heat sink base plate (t_2)	2
Thickness of heat sink cover plate (t_1)	1
Total height of heat sink ($H + t_1 + t_2$)	5.5
Flow passage slot for the water to flow (W_1)	3
Dimensions of the water outlet duct ($W_1 \times H$)	3×3.5
Width of the slots (passage)	3

The copper plate of required dimensions is used as heat sink material (Figure 2a). Due to the miniature size of the heat sink, it is fabricated using CNC machining (Figure 2b). In this study, cooling performance of the heat sink has tested under simulated controlled conditions. The electronic device that dissipates heat and needs cooling is replaced with equivalent heating block illustrated in Figure 3. The heating block majorly comprised of nichrome plate heaters placed directly beneath the lower surface of the heat sink. The amount of heat flow through this heater can regulated through different knob settings of the dimmerstat. The wattage of the electrical input is computed based on measured value of current and voltage. The heating block is provided with insulation to avoid heat losses to the surroundings. The experimental set up is assisted with instruments for measuring surface temperature of heat sink, inlet and outlet cooling liquid temperature, mass flow measurement, voltmeter and ammeter for voltage and current measurement, dimmerstat for wattage control, and control valves. Set up is created for continuous operation under steady-state conditions with the help of flow from water tank.

(**a**) (**b**)

Figure 2. Heat sink during fabrication: (**a**) copper plate; (**b**) interior view of heat sink with channels.

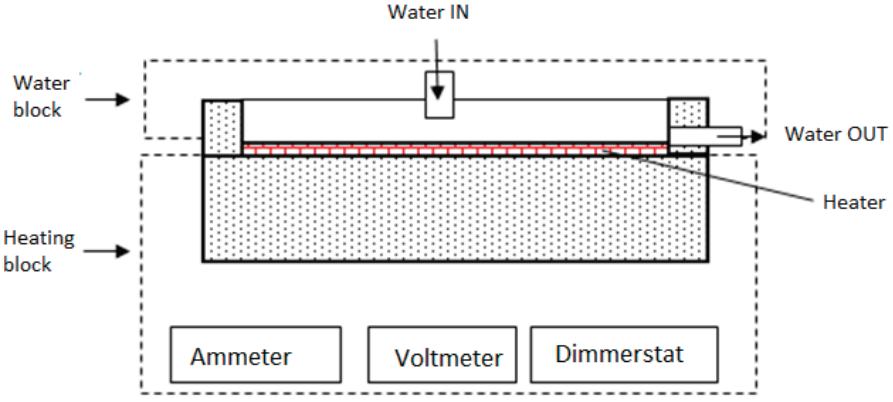

Figure 3. Arrangement showing water and heating.

During the experiment, a constant input power of 50 W was supplied to the heating block. The bottom wall temperature of the heating block was recorded after the attainment of steady-state conditions. Experiments were conducted at different flow rates. A set of three trials were conducted to check reproducibility of the experimental data.

3. Numerical Modelling

3.1. Geometry

The present numerical work aimed at providing an insight into thermal performance throughout the flow direction. The limitation of installing temperature sensors in a mini-channel restricts the provision of any details on channel-to-channel heat removal. As a result, the three-dimensional modeling and meshing were created using software package GAMBIT 2.3.16 as shown in Figure 4. CFD Software package FLUENT 6.3.26 was used to perform numerical computations.

Figure 4. Three-dimensional geometry meshed model.

3.2. Nanofluid Properties

In this investigation, Al_2O_3 nanoparticles were used due to their ability to enhance heat transfer. The thermophysical properties of base fluid (water) and nanoparticles (Al_2O_3) are listed in Table 2.

Table 2. Properties of base fluid and nanoparticles.

Properties	Pure Water	Alumina (Al_2O_3)
Mass density, kg/m^3	995.81	3880
Specific heat, J/kgK	4178	765
Thermal conductivity, W/mK	0.6172	40
Viscosity, kg/ms	0.0008034	–

For a lesser volume fraction of nanoparticles in the base fluid, the nanofluid can be treated as a single-phase, homogenous liquid. Nanofluid properties depend on the percentage of nanoparticles used in the base fluid. The thermophysical properties of nanofluids are calculated by the following equations:

Density [27–29]:

$$\rho_{nf} = (1 - \varnothing)\rho_b + \varnothing\rho_p \quad (1)$$

Viscosity, Einstein'sequation [30]:

$$\mu_{nf} = \mu_{nf}(1 + 2.5\varnothing) \tag{2}$$

Thermal conductivity [31–33]:

$$k_{nf} = \left[\frac{k_p + 2k_{bf} + 2\left(k_p - k_{bf}\right)(1+\beta)^3\varnothing}{k_p + 2k_{bf} - 2\left(k_p - k_{bf}\right)(1+\beta)^3\varnothing}\right]k_{bf} \tag{3}$$

where β is taken as 0.1 [34].

Specific heat [34,35]:

$$\left(\rho C_p\right)_{nf} = (1-\varnothing)\left(\rho C_p\right)_{bf} + \varnothing\left(\rho C_p\right)_p \tag{4}$$

where ϕ denotes volume fraction of nanoparticles and subscript *nf*, *bf*, *p* denotes nanofluid, basefluid and particle, respectively.

3.3. Governing Equation and Boundary Conditions

The nanofluid was taken as single-phase fluid and subjected to the following flow assumptions: steady state, incompressible, laminar, and constant properties. The governing equations for solving flow conditions are given below [36]: Continuity equation:

$$\nabla(\rho v) = 0 \tag{5}$$

Momentum equation:

$$\nabla(\rho v v) = -\nabla P + \nabla(\mu \nabla v) \tag{6}$$

Energy equation for the fluid:

$$\nabla\left(\rho v C_p T\right) = \nabla(k \nabla T) \tag{7}$$

Energy equation for the solid wall:

$$\nabla(k \nabla T) = 0 \tag{8}$$

Boundary conditions:

Heat sink walls are subjected to no-slip boundary conditions, whereas the inlet and the outlet of the domain are given as velocity inlet and pressure outlet, respectively. As shown in Figure 1, the lower bottom surface of the heat sink was heated at a constant heat flux condition based on dissipated power of 50 and 70 W.

3.4. Numerical Scheme and Validation

The control volume-based approach was adopted for solving governing equations (Equations (6)–(9). The SIMPLE algorithm was chosen for pressure-velocity coupling. A steady-state laminar model was used for the analysis, and the convergence criteria for residuals of continuity and velocity equations were of the order of 10^{-6}. For the energy equation, they were of the order of 10^{-9}. The results were obtained once the solutions were converged. Figure 4 shows the plot of surface temperature and water outlet temperature measured experimentally as described in Section 2. The area-weighted surface and water outlet temperatures were obtained at similar flow conditions and were plotted in Figure 5. It was observed that numerical results were in good agreement with the experimental data and, therefore, the present numerical scheme should be adopted for further study to give insights into heat transfer.

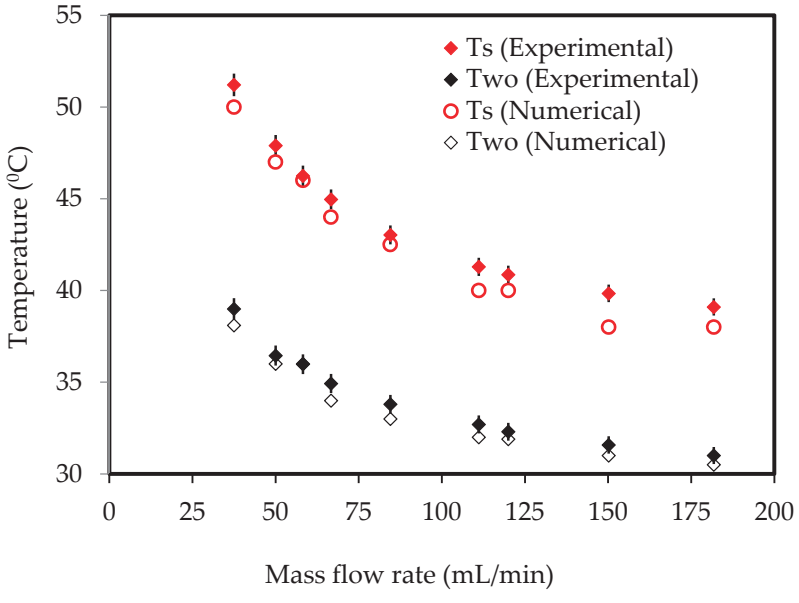

Figure 5. Validation of the numerical model adopted for the analysis.

4. Discussion

The cooling performance of the heat sink was carried out at heat generation rates of 50 and 70 W. Under each heating condition, heat dissipation was computed out for four different flow rates at 30 to 180 mL/min. The computational results are presented below.

4.1. Flow Field in Heat Sink

Due to the miniature size involved in the mini-/microchannel heat sink and difficulty in sensor placement, flow field and temperature distribution were difficult to measure experimentally. The post-processing tools available in computational software allowed detailed flow-field analysis. Figures 6–9 show sample contours of temperature for a heat generation rate of 50W. Temperature flow fields were analyzed at depths of 0.1 mm and 0.5 mm from the base surface of the heat sink. It can be observed that the temperature of the cooling fluid increased along the flow direction. At the center of the heat sink, cooling fluid was at its lowest temperature. It collected heat from the heat sink as it passed through different channels. It was observed that the fluid layers adjacent to the solid bottom wall collected heat by conduction, whereas other fluid layers above underwent forced convective heat transfer. The temperature fields developed in the heat sink were also analyzed at different flow rates. It was observed that lower flow rates were not adequate in maintaining a lower heat sink temperature. At a lower flow rate, there could be potential danger of obtaining a temperature that is beyond that of safe operation. The maximum local temperature (~77°C) attained at a low flow rate (Figure 6) can be reduced to 58°C (Figure 7), 49.31°C (Figure 8), and 44.61 °C (Figure 9) for flow rates of 60, 120, and 180 mL/min, respectively.

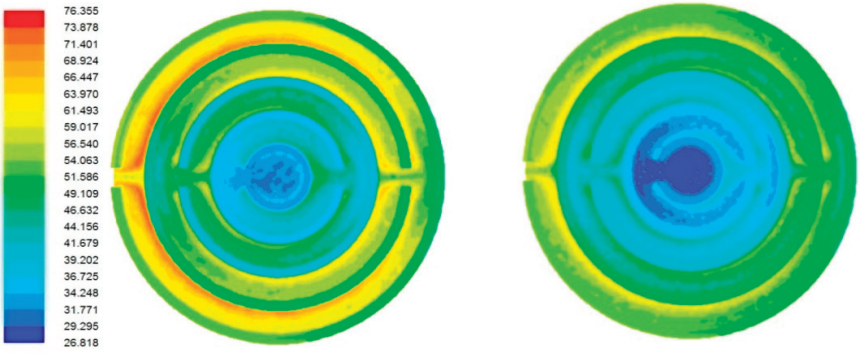

Figure 6. Contours of the temperature field in the heat sink for a flow rate of 30 mL/min.

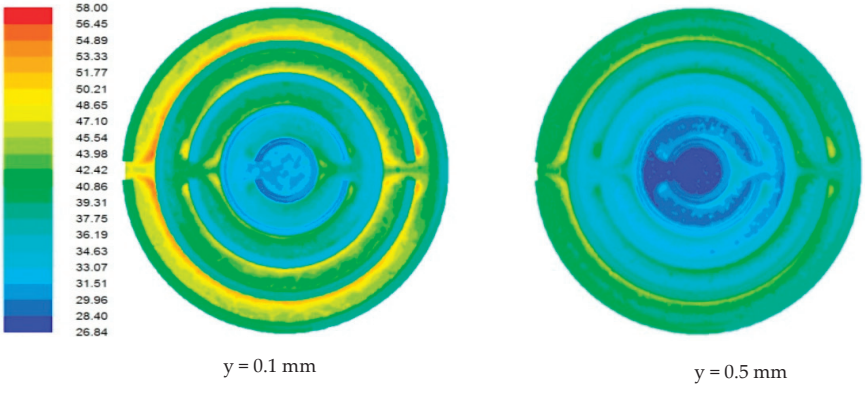

Figure 7. Contours of the temperature field in the heat sink for a flow rate of 60 mL/min.

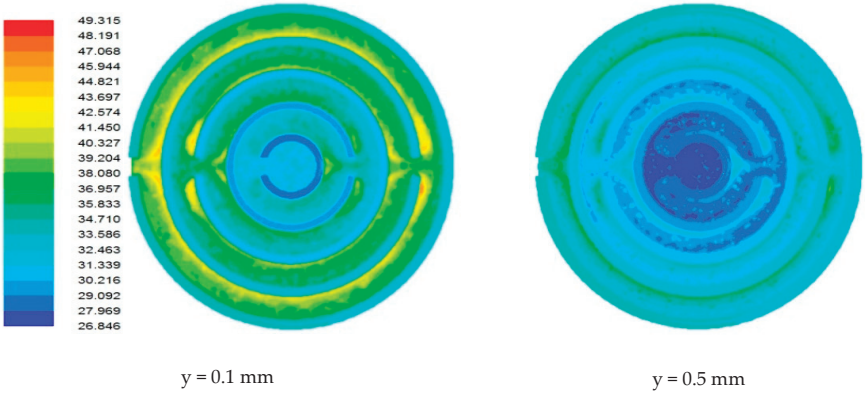

Figure 8. Contours of the temperature field in the heat sink for a flow rate of 120 mL/min.

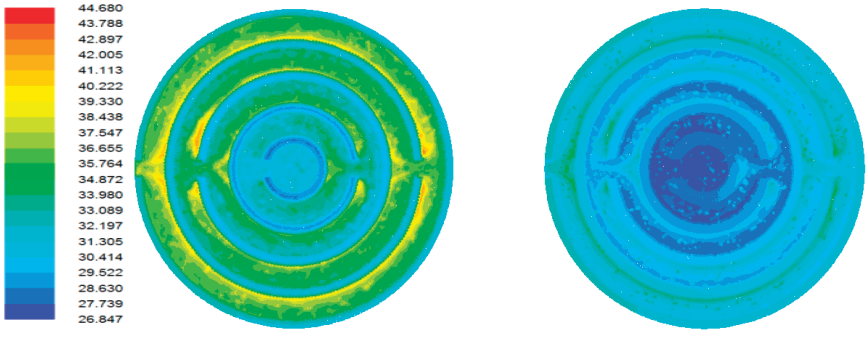

Figure 9. Contours of the temperature field in the heat sink for a flow rate of 180 mL/min.

4.2. Heat Transfer Enhancement with Nanofluids

The fluid outlet temperature was considered to analyze the device's cooling performance. Initially, the heat sink was cooled with water for different flow rates and taken as base for its comparison with nanofluid. The computations were carried out for different volume fractions of nanoparticles, namely 0.5%, 1%, 3%, and 5%. The following two temperature differences were compared:

$$\left.\begin{aligned} \Delta T &= T_{f,out} - T_{f,in} \\ dT &= T_{nf,out} - T_{bf,out} \end{aligned}\right\} \tag{9}$$

where $T_{f,out}$ is the liquid outlet temperature, $T_{f,in}$ is the liquid inlet temperature, $T_{nf,out}$ is the nanofluid outlet temperature, and $T_{\mathrm{bf,out}}$ is the water outlet temperature. The results are plotted in Figures 10 and 11.

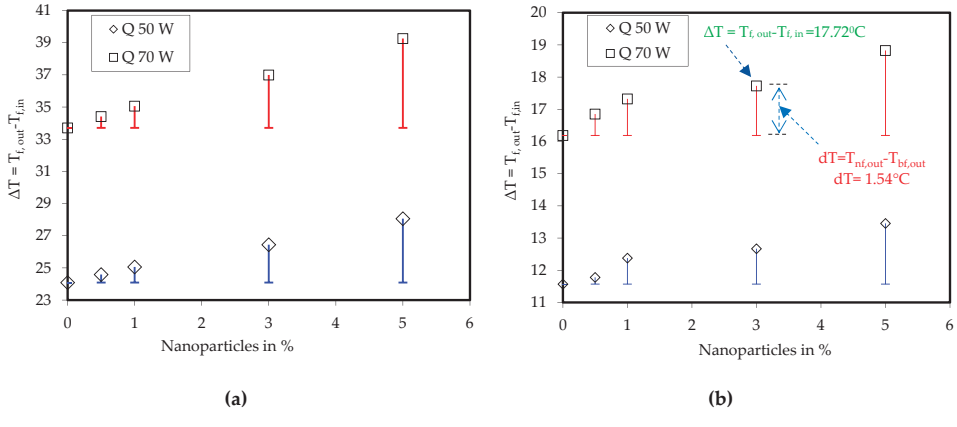

Figure 10. Temperature difference between liquid outlet and liquid inlet and its comparison with base fluid at (**a**) 30 mL/min, (**b**) 60 mL/min.

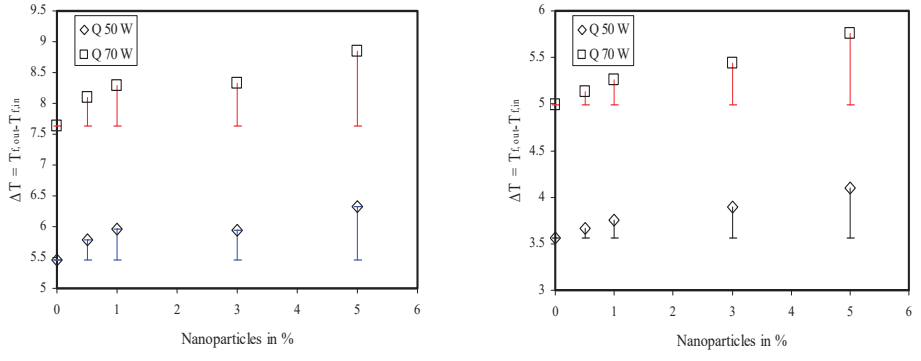

Figure 11. Temperature difference between liquid outlet and liquid inlet and its comparison with base fluid at (**a**) 120 mL/min, (**b**) 180 mL/min.

The computed data were analogous to the experimental observation shown earlier in Figure 5. The liquid outlet temperature was reduced when the liquid flow rate was increased and, therefore, ΔT also reduced the constant liquid inlet temperature. At a low mass flow rate of 30 mL/min and when Q = 50 W, ΔT was approximately 24 °C. Under this condition, the nanoparticle addition in the base fluid enhanced ΔT. The use of nanoparticles increased dT by 0.5 °C to ~3.97 °C for nanoparticles volume concentrations of 0.5% and 5%.Similarly, for the same flow rate of 30 mL/min and Q = 70 W, ΔT was approximately 34 °C. The nanofluid raised dT by 0.7 °C to ~5.55 °C for nanoparticles volume concentrations of 0.5% and 5%. The other computational results are plotted in Figure 11.

5. Conclusions

In the present work, modified heat sink geometry was introduced for heat dissipation from electronic devices. The cooling performance of the proposed heat sink was compared with Al_2O_3–water nanofluids. The conclusion can be summarized as follows:

(1) The maximum local temperature (~77 °C) attained at a low flow rate (30 mL/min) can be reduced to 58, 49.31, and 44.61 °C for flow rates of 60, 120, and 180 mL/min, respectively.

(2) At a lower mass flow rate of 30 mL/min and Q = 50 W, the temperature difference between water outlet temperature and water inlet temperature was approximately 24 °C. This reduced to ~4 °C as the mass flow was increased to 180 mL/min.

(3) A higher rate of heat generation of around 70 W produced a water outlet temperature of ~34 °C for a water flow rate of 30 mL/min. This was reduced to ~5 °C when the water flow was increased.

(4) Heat rejection rate enhanced with nanofluid usage. The enhancement was calculatedby measuring the temperature difference of nanofluid outlet temperature and water outlet temperature under similar operating conditions. The enhancement was ~2% for 0.5% volume fraction nanofluids to ~17% for a 5% volume fraction.

Author Contributions: Conceptualization, R.J. and R.K.; methodology, M.H.A.; software, R.J.; validation, R.J.; formal analysis, V.K.; investigation, R.J. and M.H.A; resources, R.J.; data curation, V.K.; writing—original draft preparation, R.J.; writing—review and editing, M.H.A. and A.M.; visualization, R.K.; supervision, M.H.A and A.M. All authors have read and agreed to the published version of the manuscript.

Funding: This research received no external funding.

Acknowledgments: We acknowledge the support of the German Research Foundation (DFG) and the Bauhaus-Universität Weimar within the Open-Access Publishing Programme. We also acknowledge the financial support of this work by the Hungarian State and the European Union under the EFOP-3.6.1-16-2016-00010 project and the 2017-1.3.1-VKE-2017-00025 project.

Conflicts of Interest: The authors declare no conflict of interest.

References

1. Kalteh, M.; Abbassi, A.; Saffar-Avval, M.; Frijns, A.; Darhuber, A.; Harting, J. Experimental and numerical investigation of nanofluid forced convection inside a wide microchannel heat sink. *Appl. Therm. Eng.* **2012**, *36*, 260–268. [CrossRef]
2. Tuckerman, D.B.; Pease, R.F.W. High-performance heat sinking for VLSI. *IEEE Electron. Device Lett.* **1981**, *2*, 126–129. [CrossRef]
3. Wang, B.X.; Peng, X.F. Experimental investigation on liquid forced-convection heat transfer through microchannels. *Int. J. Heat Mass Transfer.* **1994**, *37*, 73–82. [CrossRef]
4. Xie, X.L.; Liu, Z.J.; He, Y.L.; Tao, W.Q. Numerical study of laminar heat transfer and pressure drop characteristics in a water-cooled mini channel heat sink. *Appl. Therm. Eng.* **2009**, *29*, 64–74. [CrossRef]
5. Steinke, M.E.; Kandlikar, S.G. Review of single-phase heat transfer enhancement techniques for application in microchannels, mini-channels and microdevices. *Heat Technol.* **2004**, *22*, 3–11.
6. Steinke, M.E.; Kandlikar, S.G. Single-phase liquid heat transfer in plain and enhanced Micro-channels. In Proceedings of the ICNMM2006, Fourth International Conference on Nanochannels, Microchannels and Minichannels, Limerick, Ireland, 19–21 June 2006.
7. Khameneh, P.M.; Mirzaie, I.; Pourmahmoud, N.; Majidyfar, S. A numerical study of single-phase forced convective heat transfer with flow friction in microchannels. *Int. J. Eng. Trans. A* **2012**, *25*, 79–87. [CrossRef]
8. Hasan, M.I.; Rageb, A.A.; Yaghoubi, M.; Homayoni, H. Influence of channel geometry on the performance of counter flow microchannel heat exchanger. *Int. J. Therm. Sci.* **2009**, *48*, 1607–1618. [CrossRef]
9. Jiang, P.; Xu, R. Heat transfer and pressure drop characteristics of mini-fin structures. *Int. J. Heat Fluid Flow* **2007**, *28*, 1167–1177. [CrossRef]
10. Ahmed, H.E.; Ahmed, M.I. Optimum thermal design of triangular, trapezoidal and rectangular grooved microchannel heat sinks. *Int. Commun. Heat Mass Transfer* **2015**, *66*, 47–57. [CrossRef]
11. Choi, J.T.; Kwon, O.K. A numerical study of the heat transfer and fluid flow micro-channeled water block for computer CPU cooling. *J. Mech. Sci. Technol.* **2015**, *25*, 2657–2663. [CrossRef]
12. Saad, A.J.; Wajahat, A.; Hafiz, M.; Aysha, M. Water cooled mini-channel heat sinks for microprocessor cooling: Effect of fin spacing. *Appl. Therm. Eng.* **2014**, *64*, 76–82.
13. Liu, J. Numerical study on performances of mini-channel heat sinks within-uniform inlets. *Appl. Therm. Eng.* **2016**, *9*, 856–864. [CrossRef]
14. Khoshvaght-Aliabadi, M.; Sahamiyan, M.; Hesampour, M.; Sartipzadeh, O. Experimental study on cooling performance of sinusoidal–wavy minichannel heat sink. *Appl. Therm. Eng.* **2016**, *9*, 50–61. [CrossRef]
15. Lee, P.-S.; Garimella, S.; Liu, D. Investigation of heat transfer in rectangular microchannels. *Int. J. Heat Mass Transfer* **2008**, *48*, 1688–1704. [CrossRef]
16. Cairone, F.; Gagliano, S.; Bucolo, M. Experimental study on the slug flow in a serpentine microchannel. *Exp. Therm. Fluid Sci.* **2016**, *76*, 34–44. [CrossRef]
17. Fazeli, S.A.; Hashemi, S.M.H.; Zirakzadeh, H.; Ashjaee, M. Experimental and numerical investigation of heat transfer in a miniature heat sink utilizing silica nanofluid. *Superlattices Microstruct.* **2012**, *51*, 247–264. [CrossRef]
18. Lee, S.; Choi, S.U.S.; Li, S.; Eastman, J.A. Measuring thermal conductivity of fluids containing oxide nanoparticles. *ASME J. Heat Transfer* **1999**, *121*, 280–289. [CrossRef]
19. Wang, B.X.; Zhou, L.P.; Peng, X.F. A fractal model for predicting the effective thermal conductivity of liquid with suspension of nanoparticles. *Int. J. Heat Mass Transfer* **2003**, *46*, 2665–2672. [CrossRef]
20. Koo, J.; Kleinstreuer, C. A new thermal conductivity model for nanofluids. *J. Nanopart. Res.* **2004**, *6*, 577–588. [CrossRef]
21. Choi, S.U.S.; Zhang, Z.G.; Yu, W.; Lockwood, F.E.; Grulke, E.A. Anomalous thermal conductivity enhancement in nanotube suspensions. *Appl. Phys. Lett.* **2001**, *7*, 2252–2254. [CrossRef]
22. Duangthongsuk, W.; Wongwises, S. Comparison of the effects of measured and computed thermophysical properties of nanofluids on heat transfer performance. *Exp. Therm. Fluid Sci.* **2010**, *34*, 616–624. [CrossRef]
23. Ho, C.J.; Wei, L.C.; Li, Z.W. An experimental investigation of forced convective cooling performance of a microchannel heat sink with Al_2O_3/water nanofluid. *Appl. Therm. Eng.* **2010**, *30*, 96–103. [CrossRef]

24. Koo, J.; Kleinstreuer, C. Laminar nanofluid flow in micro heat-sinks. *Int. J. Heat Mass Transfer* **2005**, *48*, 2652–2661. [CrossRef]
25. Jang, S.P.; Choi, S. Cooling performance of a microchannel heat sink with nanofluids. *Appl. Therm. Eng.* **2006**, *26*, 2457–2463. [CrossRef]
26. Ijam, A.; Saidur, R. Nanofluid as a coolant for electronic devices (cooling of electronic devices). *Appl. Therm. Eng.* **2012**, *32*, 76–82. [CrossRef]
27. Pak, B.C.; Cho, Y.I. Hydrodynamic and heat transfer study of dispersed fluids with submicron metallic oxide particles. *Exp. Heat Transfer* **1998**, *11*, 151–170. [CrossRef]
28. Khanafer, K.; Vafai, K. A critical synthesis of thermophysical characteristics of nanofluids. *Int. J. Heat Mass Transf.* **2011**, *54*, 4410–4428. [CrossRef]
29. Ghasemi, B.; Aminossadati, S.M. Natural convection heat transfer in an inclined enclosure filled with a water-CuO nanofluid. *Numer. Heat Transfer Part A* **2009**, *55*, 807–823. [CrossRef]
30. Einstein, A. *Investigation on the Theory of Brownian Movement*; Courier Corporation: New York, NY, USA, 1956.
31. Heris, S.Z.; Esfahany, M.N.; Etemad, S.G. Experimental investigation of convective heat transfer of Al_2O_3/water nanofluid in circular tube. *Int. J. Heat Fluid Flow* **2007**, *28*, 203–210. [CrossRef]
32. Yu, W.; Choi, S.U.S. The role of international layers in the enhanced thermal conductivity of nanofluids: A renovated Maxwell model. *J. Nanopart. Res.* **2003**, *5*, 167–171. [CrossRef]
33. Trisaksri, V.; Wongwises, S. Critical review of heat transfer characteristics nanofluids. *Renew Sustain. Energy Rev.* **2007**, *11*, 512–523. [CrossRef]
34. Ghasemi, B.; Aminossadati, S.M. A numerical study on the forced convection of laminar nanofluid in a micro channel with both slip and no slip conditions. *Numer. Heat Transfer Part A* **2011**, *59*, 114–129.
35. Xuan, Y.; Roetzel, W. Conceptions for heat transfer correlation of nanofluids. *Int. J. Heat Mass Transf.* **2000**, *43*, 3701–3707. [CrossRef]
36. Yang, Y.-T.; Lai, F.-H. Numerical study of heat transfer enhancement with the use of nanofluids in radial flow cooling system. *Int. J. Heat Mass Transf.* **2010**, *53*, 5895–5904. [CrossRef]

nanomaterials

MDPI

Article

Configuration and Optimization of a Minichannel Using Water–Alumina Nanofluid by Non-Dominated Sorting Genetic Algorithm and Response Surface Method

Ali Akbar Ahmadi [1], Masoud Arabbeiki [2], Hafiz Muhammad Ali [3], Marjan Goodarzi [4] and Mohammad Reza Safaei [5,6,*]

1 Department of Mechanical Engineering, Isfahan University of Technology, Isfahan 84156-83111, Iran; ali.akb.ahmadi@gmail.com
2 Department of Mechanical Engineering, Payame Noor University, Tehran 19395-3697, Iran; m.arabbeiki@yahoo.com
3 Mechanical Engineering Department, King Fahd University of Petroleum and Minerals, Dhahran 31261, Saudi Arabia; hafiz.ali@kfupm.edu.sa
4 Sustainable Management of Natural Resources and Environment Research Group, Faculty of Environment and Labour Safety, Ton Duc Thang University, Ho Chi Minh City 700000, Vietnam; marjan.goodarzi@tdtu.edu.vn
5 Institute of Research and Development, Duy Tan University, Da Nang 550000, Vietnam
6 Faculty of Electrical—Electronic Engineering, Duy Tan University, Da Nang 550000, Vietnam
* Correspondence: mohammadrezasafaei@duytan.edu.vn; Tel.: (+1)-502-657-9981

Received: 31 March 2020; Accepted: 28 April 2020; Published: 8 May 2020

Abstract: Nanofluids in minichannels with various configurations are applied as cooling and heating fluids. Therefore, it is essential to have an optimal design of minichannels. For this purpose, a square channel with a cylinder in the center connected to wavy fins at various concentrations of an Al_2O_3 nanofluid is simulated using the finite volume method (FVM). Moreover, central composite design (CCD) is used as a method of design of experiment (DOE) to study the effects of three input variables, namely the cylinder diameter, channel width, and fin radius on the convective heat transfer and pumping power. The impacts of the linear term, together with those of the square and interactive on the response variables are determined using Pareto and main effects plots by an ANOVA. The non-dominated sorting genetic algorithm-II (NSGA-II), along with the response surface methodology (RSM) is applied to achieve the optimal configuration and nanofluid concentration. The results indicate that the effect of the channel width and cylinder diameter enhances about 21% and 18% by increasing the concentration from 0% to 5%. On the other hand, the pumping power response is not sensitive to the nanofluid concentration. Besides, the channel width has the highest and lowest effect on the heat transfer coefficient (HTC) and pumping power, respectively. The optimization for a concentration of 3% indicates that in Re = 500 when the geometry is optimized, the HTC enhances by almost 9%, while the pumping power increases by about 18%. In contrast, by increasing the concentration from 1% to 3%, merely an 8% enhancement in HTC is obtained, while the pumping power intensifies around 60%.

Keywords: ANOVA; geometrical optimization; nanofluid; non-dominated sorting genetic algorithm; response surface methodology

1. Introduction

Nanofluids are nanoparticle suspensions dispersed in a host fluid, usually including water, oil, and ethylene glycol. Nanofluids, which are extremely useful with remarkable thermal properties,

are innovative fluids with various applications in the industry. Hence, it has been exciting for many scholars [1,2]. Several studies have been conducted, and it is still undergoing at universities and research centers in this field. Additionally, many scientists have also reviewed and classified the studies performed in this area [3,4]. In recent years, minichannels and microchannels have attracted much attention, and scholars have investigated the combination of different configurations using nanofluids as cooling or heating fluids [5,6]. A summary of the studies on the employment of nanofluids in various shapes is presented in Table 1.

Furthermore, research has been conducted to predict [7–9] and optimize [10–12] the desired performance of nanofluids in multiple conditions. It should be noted that a few studies have been conducted on the optimization of configuration to obtain the conditions with the expected thermohydraulic attributes. Nanofluids promise thermal fluids. However, heat transfer can be intensified by employing nanofluids and using an optimized configuration simultaneously.

In the case of single-objective problems, the main target of solving problems is to improve the index of single performance so that either the maximum or the minimum value utterly indicates the outcome quality [13]. Nevertheless, in several conditions, relying on merely one index in an optimization problem to evaluate a hypothetical response would not be possible. Therefore, there is a need for defining more than one objective function or index to then optimize all of them simultaneously. The non-dominated sorting genetic algorithm-II (NSGA-II) is a standard algorithm used in intelligence optimizations. The suggested method by Box and Wilson, namely the response surface methodology (RSM), is a mathematical and statistical approach that can be employed for studying the effects of diverse input variables at various levels.

Moreover, RSM utilizes a design such as a central composite design (CCD) to fit a model [14]. The efficiency of the model could be verified by checking the tools provided by an analysis of variance (ANOVA). The Pareto and main effects plots could be employed to assess the impact of the input variables on the response variables.

Table 1. Studies on employing nanofluids in different configurations.

Researchers	Nanofluid Type	Configuration Type	Main Results
Ahmadi et al. [5]	Water-Al_2O_3	Minichannel with cylinder, No fin, wavy fin, flat fin	Nanofluid concentration increment: thermal conductivity improvement. Heat transfer enhancement: 199.6%. Decreasing particles size: HTC increases
Bahiraei and Heshmatia [15]	Water-Ag	A liquid block heat sink	Using nanofluid at φ = 1% and Re = 500: temperature reduces by 2.21 °C with the least entropy of 56.2%. Increasing concentration from 0% to 1% at Re = 1500: convective HTC enhancement of 15.2%
Bahiraei et al. [16]	Water-CMC/TiO_2	C shaped minichannel Straight minichannel	Concentration and Re increment: frictional entropy generation increases; thermal entropy generation decreases.
Liu et al. [17]	Water-Al_2O_3	curved duct	Al_2O_3 nanoparticle in a curved duct increase the convective heat transfer. Nanoparticle shape affects the convective heat transfer of nanofluid. Nanoplatelets show the highest convective heat transfer and pressure drop among all other shapes.

Table 1. *Cont.*

Researchers	Nanofluid Type	Configuration Type	Main Results
Bahiraei et al. [18]	hybrid nanofluid containing coated Fe_3O_4/CNT	Double-tube heat exchanger	Maximum heat transfer enhancement: 53.8%
Ghasemi et al. [19]	Water-Al_2O_3	minichannel heat sink	Nanofluid concentration increment: thermal resistance decreases. Thermal performance factor enhancement at *Re* 490 and φ = 1.5%: 1.24
Bahiraei and Majd [20]	Water-Al_2O_3	Triangular minichannel	*Re* increases from 100 to 500 at φ = 5%: HTC enhances by 56%. At φ = 5%, *Re* increment from 100 to 300: the thermal entropy generation rate decreases by 29.7%.
Bergman [21]	Water-Al_2O_3	minichannel heat sinks	Nanofluids are not useful in this application due to minimal enhancement.

Many studies performed RSM to model the thermophysical properties of nanofluids [22–24]. However, a limited number of them applied optimization in configuration while employing a nanofluid as a working fluid [25–27]. Kumar and Dinesha [28] optimized the thermal characteristics of heat transfer improvement in a double pipe heat exchanger using RSM. Rashidi et al. [29] optimized the flow of a nanofluid around an equilateral triangular obstacle in which the optimum conditions for the maximum heat transfer rate and the minimum drag coefficient were predicted using RSM. The multi-objective optimization of the corrugated tube with a loose-fit twisted tape through RSM is done to correlate the Reynold number, twisted ratio, and clearance ratio with the Nusselt number ratio, friction factor ratio, and overall heat transfer performance to estimate the optimum design range of a heat exchanger [30,31]. The optimization of the viscosity and thermal conductivity of the Al_2O_3/water, CuO/water, SiO_2/water, and ZnO/water nanofluids is performed using RSM and NSGA-II, in which the thermal conductivities of the $Al_2O_{3/}$water and CuO/water nanofluids determine the maximum increment at different temperatures and volume fractions [32]. It also should be noted that the current optimization method can be used for entropy generation [33].

According to the review of the relevant literature, it is concluded that using a nanofluid enhances the HTC [34–36]. In contrast, nanofluids not only improve the convective heat transfer but also intensify the pressure loss and, consequently, the pumping power [37,38]. Several studies have been conducted on employing nanofluids in various configurations [39–41]. However, a few studies are carried out to employ the nanofluid in an optimized configuration. The objective of this research is to perform a method for multi-objective optimization of configuration of a minichannel while having the Al_2O_3/water nanofluid using the NSGA-II algorithm. This nanofluid is widely employed in this area and has many applications. The mathematical models for predicting the maximum HTC and minimum pumping power of the nanofluid are presented using an ANOVA.

2. Material and Methods

The present numerical research is to study the heat transfer and pressure drop of the water and nanofluid flow containing Al_2O_3 nanoparticles in a square channel with a cylinder in the center, consisting of a fin with a constant heat flux condition (see Figure 1a). To simulate the laminar flow regime in a constant mass flow rate of 0.03 Kg/s, the finite volume method (FVM) is applied. Furthermore, the constant uniform heat flux on the channel wall is considered as a thermal boundary condition (see Figure 1b). A numerical investigation is carried out for the nanofluid with concentrations of 0% to 5% through a straight channel. Also, the basic dimension of minichannel is tabulated in Table 2.

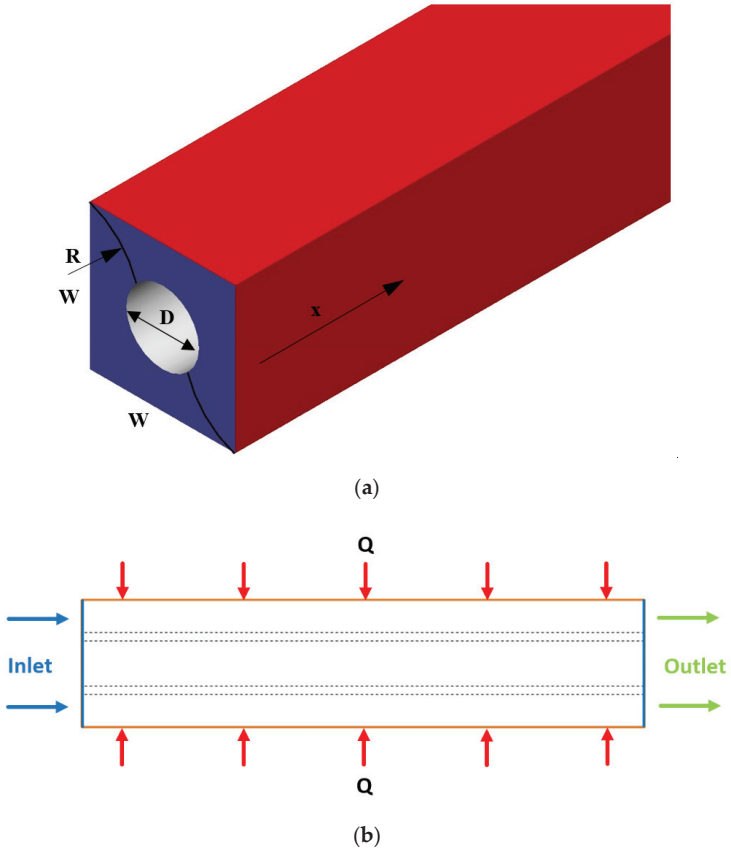

Figure 1. The study case: (**a**) isometric view of the channel with an inner cylinder and with a wavy fin; (**b**) side view.

Table 2. Description of the under-study channel, basic dimensions.

L (m)	W (mm)	D (mm)	R (mm)
3	50	50	25

2.1. Multi-Objective Optimization

2.1.1. Design of Experiments

To reduce the number of tests, time, and cost, the design of experiments (DOE) is an essential tool to solve multi-variable engineering problems. Further, CCD is a second-order design in which merely three levels of every variable are needed. CCD provides a survey on the effects of each variable and their interaction throughout the responses by means of fewer experimental runs compared with a full-factorial model. Additionally, CCD can be used to predict and optimize responses [42]. In the current study, the CCD consists of 15 numerical experiments at three independent input variables, including cylinder diameter, channel width, and fin radius with three levels. The design space for each input variable is based on the design limitations; therefore, the possible range is selected. Table 3 demonstrates the actual values of the three independent variables. The experimental layout, which is implemented in the current study in actual form, is tabulated in Table 4.

Table 3. The design space for each input variable.

Input Variable	Symbol	Lower Bound	Basic Value	Upper Bound
Cylinder diameter (mm)	D	22.5	25	27.5
Channel width (mm)	W	45	50	55
Fin radius (mm)	R	21	28.5	36

Table 4. Experimental layout.

Expt. No.	Cylinder Diameter (mm)	Channel Width (mm)	Fin Radius (mm)
1	25	50	28.5
2	22.5	50	28.5
3	27.5	50	28.5
4	25	45	28.5
5	25	55	28.5
6	25	50	21
7	25	50	36
8	22.5	45	21
9	27.5	45	21
10	22.5	55	21
11	27.5	55	21
12	22.5	45	36
13	27.5	45	36
14	22.5	55	36
15	27.5	55	36

2.1.2. Response Surface Methodology

The RSM is widely adopted as a statistical approach applied for experimental purposes. The RSM performs by conducting a statistical design of the experiments, followed by assessing the coefficients in the mathematical model, and by predicting the responses and sufficiency examining of the model. In the RSM, the quantitative interaction pattern response variables and independent variables can be equally interpreted. The flowchart of the RSM is demonstrated in Figure 2.

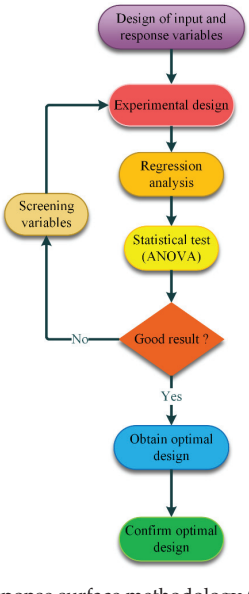

Figure 2. The response surface methodology (RSM) flowchart.

A second-order polynomial equation is assigned to the numerical results that in its general form is

$$Y = \beta_0 + \sum_{i=1}^{k} \beta_i X_i + \sum_{i=1}^{k} \beta_{ii} X_i^2 + \sum_{i=1}^{k} \sum_{i \neq j=1}^{k} \beta_{ij} X_i X_j + \varepsilon \quad (1)$$

where Y assigns a response, X_i and X_j are the independent variables, β_0 is the constant coefficient, the coefficient of the linear term together with those of the quadratic and the interaction are considered as β_i, β_{ii}, and β_{ij}, respectively, k denotes the number of independent variables that in this study are equal to 3, and ε is used for error [43].

2.1.3. NSGA-II Algorithm

The NSGA-II is known as the secondary type of NSGA algorithm. Both types of NSGA are generated based on the genetic algorithm and extracted from the evolution theory of Darwin as well as genetic science. These two algorithms utilize the rule of "survival of the fittest" on responses to problems, intending to achieve proper outcomes. In the initial type of the algorithm, the users are supposed to find the suitable quantity through changing the σ shared in different problems. However, to avoid any accumulation of population members and support of every level of design interval, the subprogram of the crowding distance (CD) is used in the second version of NSGA.

Through the optimization with two objective functions, the allocated value of the CD to each chromosome is precisely equal to the perimeter of a rectangular created by the next and previous chromosomes. The magnitude of the CD of each population member, in comparison with the next and former members, together with the first and last population members, is calculated based on Equation (2) [7].

$$d_{ij} = \frac{\left| f_1^k - f_1^j \right|}{f_1^{max} - f_1^{min}},\ d_{ik} = \frac{\left| f_2^k - f_2^j \right|}{f_2^{max} - f_2^{min}},\ CD_i = d_{ij} + d_{ik} \quad (2)$$

The process of optimization is in a way that the N numbers of the primary populations are firstly generated by random. Then, the values of the objective functions are calculated for the primary population, and these members are classified, and their CD is specified. Parents are selected based on their rank and CD scale through the binary tournament selecting method, crossover, and mutation operators that are used on them. This new population is combined with the prior population, and the sorting operation is repeated. Between the total available populations, which their members are even more than the primary population, the N numbers of the population's upper members are chosen for the other generation. Upper fronts are initially determined to select the population of the other generation. Then, if by selecting another front, the number of population members gets more than the N, an adequate number of that front is selected based on the CD scale.

The flowchart of NSGA-II is illustrated in Figure 3. The optimization method utilizes the RSM to assign the function of fitness, as shown in Figure 3. Besides, new operators, namely, mutation and crossover, are applied for the populations generating. By the end, the process of optimization would be finalized with the condition of some iterations.

2.2. Governing Equations

For modeling the laminar flow, the Navier–Stokes equations are employed to solve the performance of the fluid. As a result, the governing equations at the steady-state flow are as below [44]:

Mass conservation:

$$\nabla \cdot (\rho_{nf} V_{nf}) = 0 \quad (3)$$

Momentum conservation:

$$\nabla \cdot (\rho_{nf} V V_{nf} V_{nf}) = -\nabla P_{nf} + \nabla \cdot (\mu_{nf} \nabla V_{nf}) \quad (4)$$

Energy conservation:

$$\nabla \cdot (\rho_{nf} V_{nf} C_{p,nf} T_{nf}) = \nabla \cdot (k_{nf} \nabla T_{nf}) \quad (5)$$

where ρ (kg m^{-3}) and k (W m^{-1} K^{-1}) represent the density and thermal conductivity, respectively. μ (N m^{-2} s) and C_p (J kg^{-1} K^{-1}) show the dynamic viscosity and the specific heat, respectively. Meanwhile, V (m s^{-1}), T (K), and P (N m^{-2}) are the velocity, temperature, and pressure, respectively.

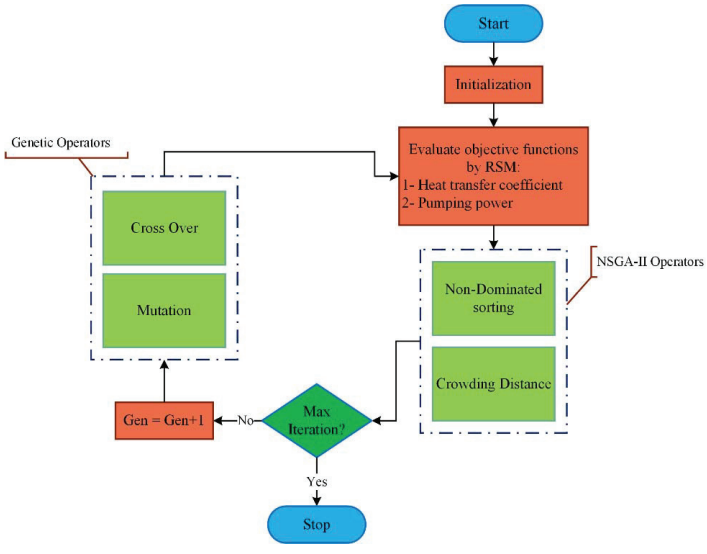

Figure 3. Flowchart of the non-dominated sorting genetic algorithm-II (NSGA-II).

2.3. Nanofluid Properties

The base fluid is water with temperature-dependent properties. Its viscosity is calculated via Equation (6) [45]. Further, Equation (7) calculates the thermal conduction of water, while its density and specific heat are evaluated by Equations (8) and (9), respectively [1].

$$\mu_{bf} = 0.00002414 \times 10^{\left(\frac{247.8}{(T-140)}\right)} \quad (6)$$

$$k_{bf} = 2.33417 - 0.0328575T + 0.000185702T^2 \quad (7)$$

$$\rho_{bf} = 753.2 + 1.88T - 3.570 \times 10^{-3} T^2 \quad (8)$$

$$c_{p,bf} = -29664.8 + 403.224T - 1.78895T^2 + 0.00349982T^3 - 0.00000254434T^4 \quad (9)$$

To assess the density and specific heat of the nanofluid, Equations (10) and (11) are used, respectively [1].

$$\rho_{nf} = (1-\varphi)\rho_{bf} + \varphi\rho_p \quad (10)$$

$$c_{p,nf} = \frac{\varphi\rho_p c_{p,p} + (1-\varphi)\rho_{bf} c_{p,bf}}{\rho_{nf}} \quad (11)$$

The nanofluid viscosity is attained by employing the below model [46]:

$$\frac{\mu_{nf}}{\mu_{bf}} = 1 + 1631\left(\frac{\varphi}{1-\varphi}\right)^{2.8} \quad (12)$$

Vajha and Das [47] offered Equation (13) to evaluate the thermal conductivity of the nanofluid. This model consists of two terms, which are demonstrated in Equations (14) and (15). The first and second terms, respectively, denote the static and dynamic part of the model. Equation (15) is for the Brownian motion of the nanoparticles.

$$k_{nf} = \frac{k_p + 2k_{bf} - 2\left(k_{bf} - k_p\right)\varphi}{k_p + 2k_{bf} + \left(k_{bf} - k_p\right)\varphi} k_{bf} + 5 \times 10^4 \beta \varphi \rho_{bf} c_{pbf} \sqrt{\frac{kT}{\rho_b d_p}} f(T, \varphi) \tag{13}$$

$$f(T, \varphi) = (2.8217 \times 10^{-2}\varphi + 3.917 \times 10^{-3})(\frac{T}{T_0}) + (-3.0669 \times 10^{-2}\varphi + 3.91123 \times 10^{-3}) \tag{14}$$

$$\beta = 8.4407(100\varphi)^{(-1.07304)};\ 1\% \le \varphi \le 100\%,\ 298K \le T \le 363\text{K} \tag{15}$$

T_0 is equal to 273 K and indicates the reference temperature [48].

The properties of the aluminum oxide particles are presented in Table 5 [48].

Table 5. Thermophysical properties of the Al_2O_3 nanoparticles [48].

Properties	k (W/mK)	ρ (kg/m^3)	Cp (kJ/kgK)
Value	36	3600	765

2.4. Boundary Conditions

A laminar and steady-state flow of the nanofluid with a uniform velocity and temperature profile with different concentrations (the inlet temperature is 25 °C) is considered. A constant and uniform heat flux, as much as 200 W/m^2 is applied as the thermal condition on the channel walls. Furthermore, the relative pressure is set to zero at the outlets of the channel (Figure 1b). Also, the no-slip condition is considered on the walls. The boundary conditions are described in mathematical forms as follows:

At the inlets: $T = T_0$, $v = v_0$;

At the outlets: $P_{gage} = 0$;

At the walls: $v = 0$.

Equation (16) evaluates the Reynolds number as follows:

$$Re = \frac{4\dot{m}}{\pi D_h \mu} \tag{16}$$

where $\dot{m}$ denotes the mass flow rate, and D_h is the hydraulic diameter calculated by applying Equation (17).

$$D_h = \frac{4W^2 - \pi D^2}{4W + \pi D} \tag{17}$$

To evaluate the HTC, the Equation (16) is applied [48].

$$h = \frac{q''}{T_w - T_m} \text{ and } T_m = \frac{T_{in} + T_{out}}{2} \tag{18}$$

The temperatures of the fluid are T_{in} and T_{out} in the outlet and inlet, respectively. Furthermore, q'' denotes the heat flux applied to the channel wall, and T_w and T_m indicate the average wall temperature and the average fluid temperature, respectively.

To evaluate the pumping power, Equation (19) is applied.

$$P = Q\Delta\text{P} \tag{19}$$

where Q represents the rate of fluid flow, and ΔP indicates the pressure loss.

2.5. Numerical Solution

The control volume method is used to solve the present case numerically. To couple the pressure and velocity, the SIMPLE algorithm is employed. Moreover, the second-order upwind scheme is utilized to solve the continuity, momentum, and energy equations. For all variables, the minimum divergence criteria are assumed to be 10^{-5}.

2.6. Grid Generation and Grid Independency

For evaluating the mesh independency, the effect of different grids on the HTC at the channel exit is assessed. According to Figure 4, finer cells along the radius to the walls are employed where gradients are high. Water enters the channel at a temperature of 25 °C and Re = 500, as shown in Figure 1, and the properties are calculated by Equations (6)–(9). A constant heat flux of 200 W/m^2 is applied to the channel walls. The HTC at the channel exit is achieved by the different elements represented in Table 6. It is seen in Table 6 that minifying grids more than 2673173 have no noticeable effect on the HTC. Hence, this grid is adopted for further simulation in the current study.

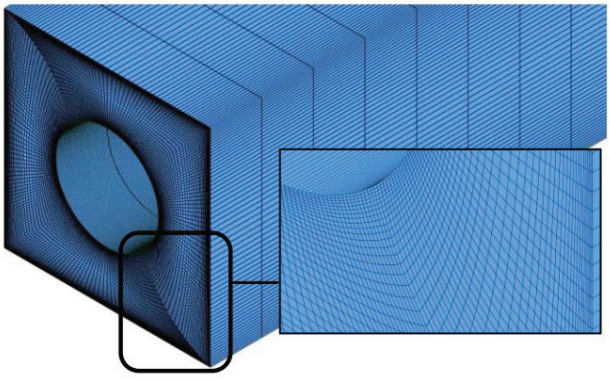

Figure 4. Channel gridding.

Table 6. Cell number studied in mesh independent study.

Grid	Cell Number	HTC	Error
Grid 1	191185	116.979	-
Grid 2	1004566	116.198	−0.7%
Main Grid	2673173	115.962	−0.2%
Grid 4	4276219	115.961	0.0%

3. Results and Discussion

3.1. Validation

For the validation of the current simulation, the numerical results are evaluated with the correlation presented by Sieder–Tate [49] and the experimental data from Reference [50] for laminar flow with the constant wall temperature boundary condition. Laminar water flows in a 1-m long tube with a 6 mm diameter under the constant wall temperature condition, and the achieved results are shown in Figure 5. According to Figure 5, the almost same response from the simulation of the data from the experimental and theoretical study [49,50] highlights the accuracy of the current simulation.

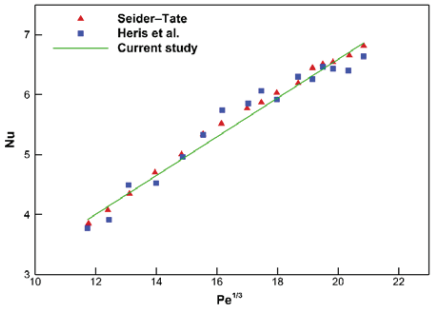

Figure 5. Comparison between the current simulation and those reported by Sieder–Tate [49] and Heris et al. [50] for water at the constant wall temperature.

3.2. DOE Results

The HTC and pumping power are selected as the two response variables in every design of an experiment's numerical simulation, including water-based and nanofluids in the concentration of 1%, 3%, and 5%. The magnitude of every response variable is tabulated in Table 7.

Table 7. Response values.

Expt. No.	φ = 0%		φ = 1%		φ = 3%		φ = 5%	
	h (W/m^2K)	Pumping Power ($\times 10^{-5}$) (W)	h (W/m^2K)	Pumping Power ($\times 10^{-5}$) (W)	h (W/m^2K)	Pumping Power ($\times 10^{-5}$) (W)	h (W/m^2K)	Pumping Power ($\times 10^{-5}$) (W)
1	234.25	7.51	233.25	7.77	229.48	8.23	231.08	8.61
2	230.88	6.26	229.26	6.47	225.67	6.84	228.58	7.12
3	238.96	9.17	237.25	9.52	232.90	10.11	235.671	10.58
4	326.87	13.88	322.41	14.51	316.59	15.56	342.95	16.36
5	214.40	4.37	213.19	4.52	209.85	4.77	213.48	4.98
6	234.75	7.51	233.09	7.78	229.06	8.24	231.79	8.61
7	233.91	7.51	232.32	7.78	228.23	8.24	231.04	8.61
8	315.36	11.08	311.46	11.56	306.31	12.36	329.19	12.97
9	348.94	17.88	343.25	18.72	335.09	20.10	365.94	21.17
10	208.90	3.79	208.00	3.91	206.16	4.10	209.72	4.26
11	220.94	5.14	218.75	5.33	215.41	5.66	218.62	5.89
12	306.55	11.09	303.94	11.56	299.16	12.37	319.85	12.98
13	344.78	17.88	339.14	18.72	331.36	20.10	361.57	21.17
14	208.18	3.80	207.80	3.92	205.83	4.09	209.75	4.26
15	220.48	5.13	218.00	5.32	215.29	5.65	218.33	5.88

3.3. Analysis of Variance

An analysis of variance is employed to assess the data using the least square method. All required ANOVA assumptions consisting of case independence, normality of residuals distribution, and equality of variances are analyzed to determine the goodness of the fitted model. Therefore, the residual plots are drawn, as shown in Figures 6 and 7. The regression coefficient of the linear term, in addition to those of the quadratic and interaction, existed in the fitted model, and their impacts are assessed. All terms of the fitted model are verified utilizing their probability magnitudes at a 95% confidence level (p-value < *0.05*). To acquire the best model, the adjusted coefficient of determination (R^2_{adj}) is applied to assess the efficiency of the models. Once the ultimate model is reached, the main effect plots are performed to illustrate the effects of the input variables on the responses. The value of R^2_{adj} for each response is tabulated in Table 8.

Table 8. The percentage of the adjusted coefficient of determination for each response.

Concentration	HTC	Pumping Power
0%	99.44	99.60
1%	99.54	99.59
3%	99.59	99.58
5%	99.54	99.58

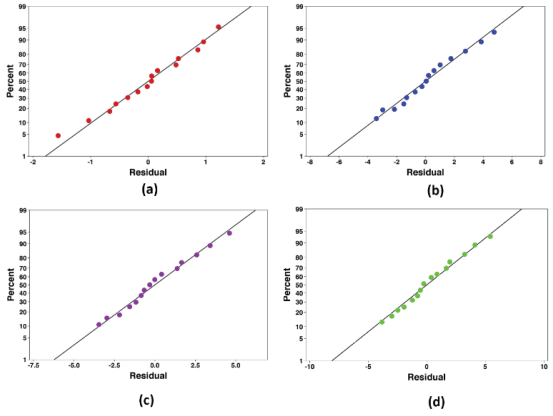

Figure 6. Normal probability plot of the residuals for the heat transfer coefficient (HTC), (**a**): φ = 0%, (**b**): φ = 1%, (**c**): φ = 3%, and (**d**): φ = 5%.

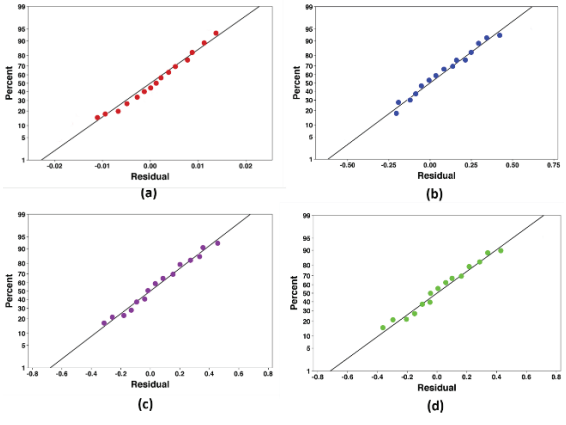

Figure 7. Normal probability plot of the residuals for the pumping power, (**a**): φ = 0%, (**b**): φ = 1%, (**c**): φ = 3%, and (**d**): φ = 5%.

The second-order equations with all the mentioned terms are provided due to the results of the numerical experiments to create a mathematical model to predict the value of the heat transfer coefficient and pumping power for each studied condition. The relevant correlations are tabulated in Table 9.

Table 9. Correlations of the heat transfer coefficient and pumping power.

Concentration	Heat Transfer Coefficient	Pumping Power
0%	h = 3805 − 147.48 W + 27.90 D + 1.4795 W^2 − 0.475 WD	P = 83.0 − 5.523 W + 6.225 D +0.07260 W^2 − 0.10915 WD
1%	h = 3672 − 141.83 W + 26.85 D + 1.4224 W^2 − 0.4603 WD	P = 90.6 − 5.944 W + 6.546 D +0.07772 W^2 − 0.11477 WD
3%	h = 3653 − 140.30 W + 24.61 D + 1.4014 W^2 − 0.4227 WD	P = 102.5 − 6.607 W + 7.053 D +0.08572 W^2 − 0.12357 WD
5%	h = 4747 − 186.98 W + 34.62 D + 1.8924 W^2 − 0.610 WD	P = 109.4 − 7.046 W + 7.492 D +0.09143 W^2 − 0.1314 WD

The Pareto charts are drawn to demonstrate the effect of each term on both responses. These charts for the HTC and pumping power in each condition are shown in Figures 8 and 9, respectively.

The Pareto charts show that the effect of the optimization is more intense in the higher concentration. The effect of the channel width and cylinder diameter increase around 20.8% and 18% by enhancing the concentration from 0% to 5%. In contrast, the pumping power response is not sensitive to the nanofluid concentration. Further, the channel width has the highest and lowest impact on the HTC and pumping power, respectively.

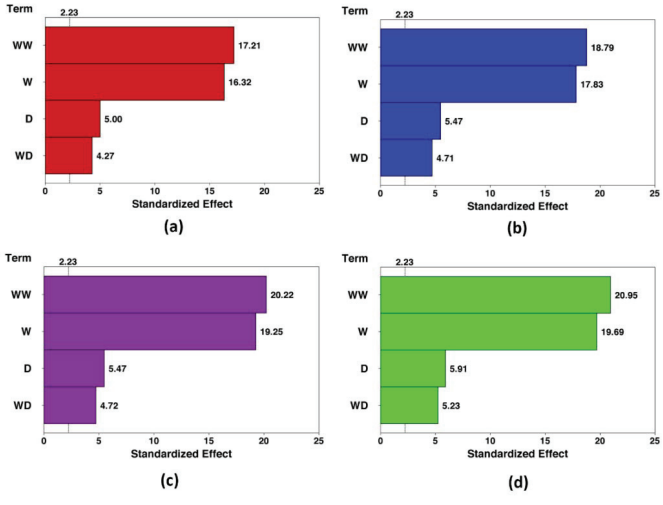

Figure 8. Pareto chart of the standardized effects (response is HTC, $\alpha = 0.05$). (**a**): $\varphi = 0\%$, (**b**): $\varphi = 1\%$, (**c**): $\varphi = 3\%$, and (**d**): $\varphi = 5\%$.

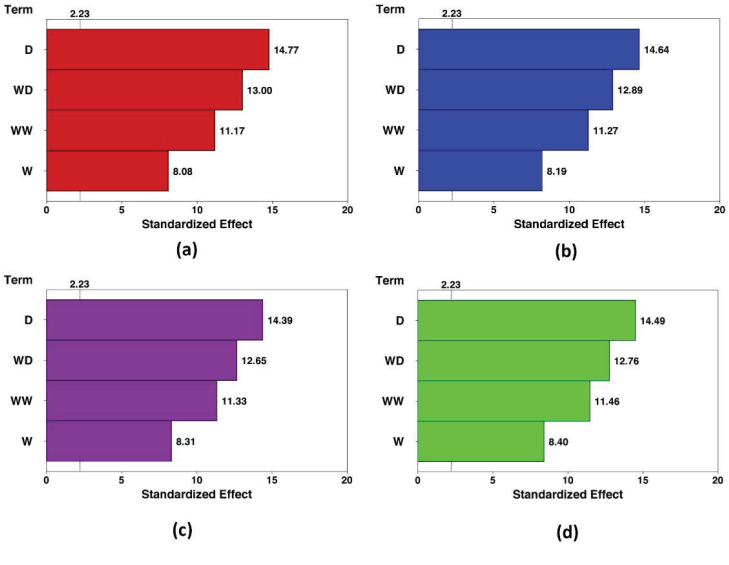

Figure 9. Pareto chart of the standardized effects (response is pumping power, $\alpha = 0.05$). (**a**): $\varphi = 0\%$, (**b**): $\varphi = 1\%$, (**c**): $\varphi = 3\%$, and (**d**): $\varphi = 5\%$.

The main effects of the plots are drawn to better identify the impact of the input variables on the responses, as shown in Figures 10 and 11. As can be seen, the fin radius has the least effect on the HTC and pumping power compared with the channel width and cylinder diameter. Moreover,

it should be noted that a wavy fin with a smaller radius will result in better thermal performance because the area of heat transfer is increased. The channel side is the most effective factor in all concentrations. Figure 10 illustrates the HTC in terms of the channel dimension change, where it denotes that at φ = 5%, by decreasing the W from 50 to 45 mm, the HTC improves by about 49%. Further, the cylinder diameter change indicates the enhancement of about 12% by increasing the D from 25 to 27.5 mm. Regarding Figure 11, decreasing the W from 50 to 45 mm intensifies the pumping power by about 94%. In comparison, it increases by about 37% with the increment of the D from 25 to 27 mm. All in all, for the enhancement of the same magnitude in the HTC, the W causes a smaller increase in the pumping power. Hence, in the Pareto chart, the W has the highest and lowest effect on the HTC and the pumping power, respectively. Figures 10 and 11 show the result that an increment of the D accompanied by the W decrement can have, which results in a hydraulic diameter reduction. The mass flow rate increases the Re, and higher HTCs are expected in higher Reynolds numbers.

As it is mentioned, the RSM can not only be utilized to illustrate the impact of some input variables on certain response variables but is also an easy way to predict the optimal values. In this study, the optimization is performed to achieve the optimum geometry by the NSGA-II method based on the controlled elitism concepts. The pros of the NSGA-II overweighting method are a regularly distributed Pareto-optimal front and suitable for detecting. The Pareto-optimal front is used for non-convex multi-objective problems to avoid time-consuming delays. Moreover, it is applied to represent the Pareto-optimal solutions in a single run. This method also supports multiple objectives and constraints and targets at reaching the global optimum (Figure 3). In this method, after generating 600 samples per iteration, three candidate points are predicted, while a maximum of 20 iterations is set up [51]. The objective functions in the current survey are selected to maximize the HTC and minimize the pumping power with the same importance level. Table 10 represents the candidate points generated by the RSM.

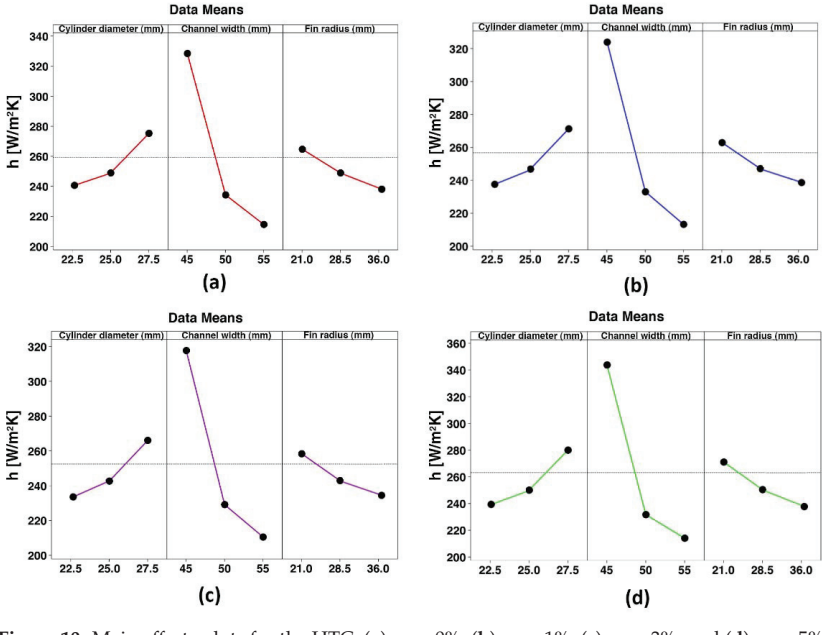

Figure 10. Main effects plots for the HTC. (**a**): φ = 0%, (**b**): φ = 1%, (**c**): φ = 3%, and (**d**): φ = 5%.

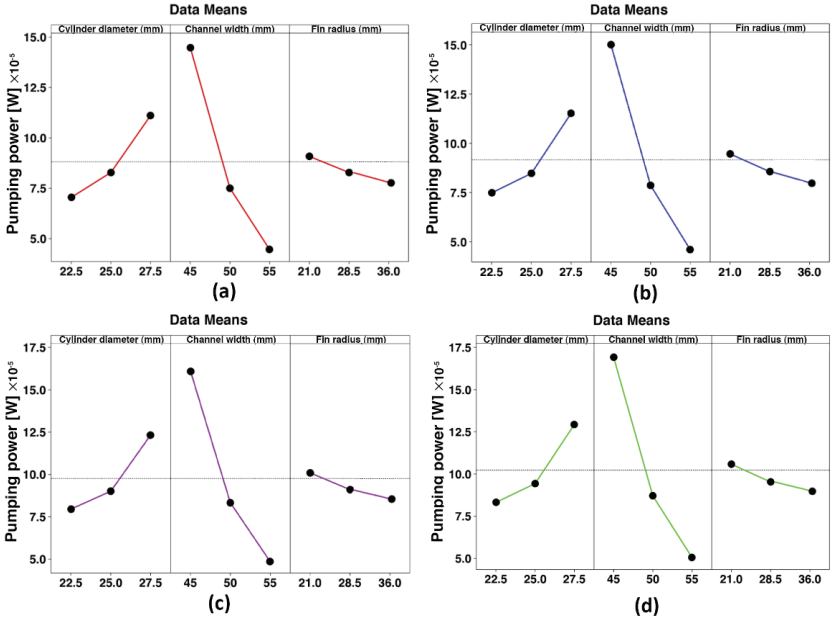

Figure 11. Main effects plots for the pumping power. (**a**): φ = 0%, (**b**): φ = 1%, (**c**): φ = 3%, (**d**): φ = 5%.

Table 10. Predicted candidate points provided by the response surface optimization.

	Candidate NO.	Cylinder Diameter (mm)	Channel Width (mm)	Fin Radius (mm)	h (W/m^{2}K)	Pumping Power × 10^{-5} (W)
0%	1	22.50	45.00	21.00	314.16	11.1
	2	24.23	45.01	21.35	326.62	12.9
	3	22.58	45.39	24.52	298.43	10.7
1%	1	22.53	45.01	21.08	308.00	11.5
	2	22.71	45.10	23.04	306.10	11.6
	3	24.16	45.04	28.62	316.16	13.4
3%	1	22.50	45.00	21.00	307.85	12.4
	2	22.51	45.02	23.58	306.53	12.3
	3	22.70	45.00	26.04	307.48	12.6
5%	1	22.50	45.00	21.00	327.17	13.0
	2	22.53	45.01	23.79	326.03	12.3
	3	22.78	45.01	30.78	327.04	13.3

According to Table 10, the optimum points to maximize HTC while minimizing the pumping power are determined. Adding the nanoparticles at a constant mass flow rate changes the Reynolds number. Thus, it would be better to assess the hydrothermal characteristics of the channel at constant Reynolds numbers instead of constant mass flow rates. Figure 12a demonstrates the convective HTC at the channel exit in terms of the Reynolds number at different concentrations for the channel with a W = 45 mm and D = 22.5 mm. It can be perceived that the convective HTC improves when the Reynolds number is enhanced.

Consequently, the convective HTC intensifies by almost 21.5% when the Reynolds number is increased from 250 to 1,000 at φ = 3%. Additionally, enhancing the concentration augments this parameter because adding the nanoparticles intensifies the thermal conductivity, which improves the rate of heat transfer. Therefore, when the concentration increases from 0% to 5% at Re = 1000, the convective HTC improves by about 46.2%.

Hydraulic characteristics, including the pumping power and pressure drop of the channel, also should be noted since they indicate the energy consumption rate needed for the operation of the channel. The pressure loss and heat transfer are enhanced by adding the nanoparticles; however, the pressure loss increment is undesirable.

Figure 12b shows the concentration effect on the pumping power in the different Reynolds numbers for the channel with a W = 45 mm and D = 22.5 mm. From the figure, it is expected to have a higher HTC while obtaining a smaller pumping power. It can be noted that the pumping power is intensified when either the Reynolds number or the concentration is increased. The velocity gradient increases when the Reynolds number enhances; therefore, the pressure loss augments. Moreover, increasing the Reynolds number enhances the velocity and leads to a higher rate of fluid flow. Consequently, the pumping power is signified by the Reynolds number (see Equation (19)). Therefore, the pumping power value at Re = 1000 is almost 17 times higher than that at Re = 250 for φ = 5%. Moreover, the viscosity, augmented by adding nanoparticles, increases the pressure loss, and as a result, the pumping power is raised. For instance, a 170% enhancement is seen in the pumping power when the concentration is increased from 0% to 5% at Re = 1000. Further, it should be noted that the impact of nanoparticle dispersion in the pumping power is more intense at higher Reynolds numbers.

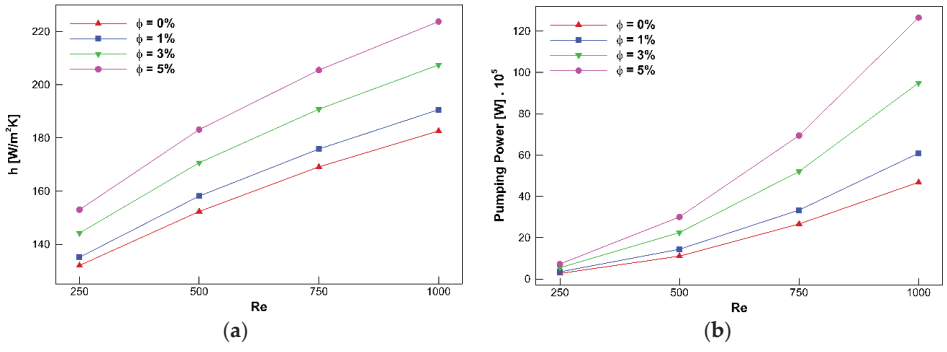

Figure 12. Convective HTC (**a**) and pumping power (**b**) versus Reynolds number for concentrations from 0% to 5% for the channel with a H = 45 mm and D = 22.5 mm.

Figure 13 displays the effect of the volume concentration on the Nusselt number of the nanofluid for four Reynolds numbers. Accordingly, the Nusselt number in the different Reynolds numbers is signified with any rise in the volume concentration. Enhancing the particle density increases the momentum and HTC. It should be noted that the nanofluid viscosity intensifies when the particle volume concentration augments. As a result, by the concentration increment, the nanofluid pressure loss increases compared with the base fluid. Figure 13 also illustrates the variations in the pressure loss for Al_2O_3/water in terms of the volume concentrations at four Reynolds number. Like the base fluid, increasing the Reynolds number at a constant concentration raises the nanofluid pressure loss. For instance, by changing the Reynolds number from 500 to 1000 at a 3% volume concentration, the pressure loss intensifies by almost 70%. The slope of pressure loss experiences growth with the volume concentration.

Figure 14 illustrates the convective HTC at the channel exit and the pumping power in terms of the Reynolds number for the channel with basic dimensions (Table 2) with a 3% concentration. The optimum values for the channel dimensions are obtained, and one of them is evaluated in Figure 14, such that the convective HTC enhances while the pumping power has a negligible increment. For instance, in Re = 500, when the geometry is optimized, the HTC enhances by almost 8.8%, while the pumping power rises by about 18%. In contrast, by increasing the concentration from 1% to 3%, only a 7.6% enhancement in HTC is achieved, while the pumping power rises by about 60%.

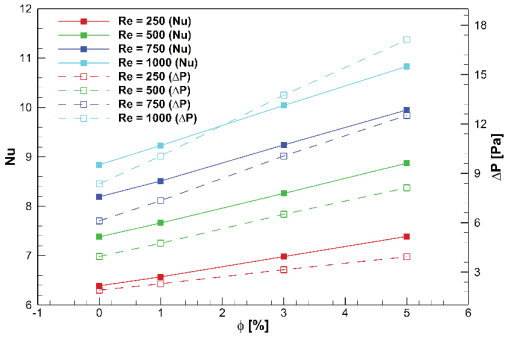

Figure 13. Variation of Nusselt number and pressure drop in terms of volume concentration at four Reynolds number obtained from the current optimized dimensions (H = 45 mm and D = 22.5 mm).

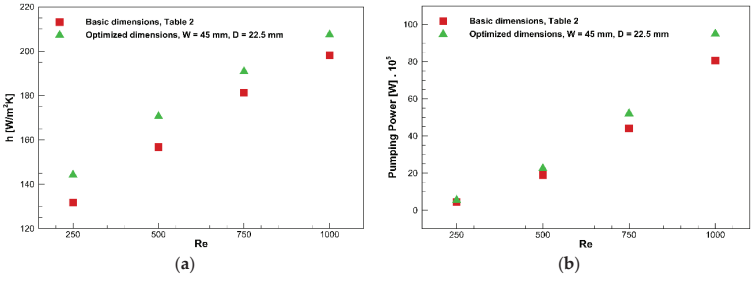

Figure 14. Comparison of the convection HTC (**a**) and pumping power (**b**) obtained from the current optimization and basic dimensions (Table 2) for the water/Al_2O_3 nanofluid at φ = 3%.

For a better evaluation of the heat transfer variation with the geometry changing, the temperature contour at the channel exit is illustrated in Figure 15 for two Reynolds numbers at φ = 3%. It can be seen that the nanofluid experiences a lower temperature at the wall, for both Reynolds at an optimized channel. It shows a higher rate of heat transfer in the channel with the optimized dimensions. Moreover, the dimensions of the two channels are displayed in Table 11.

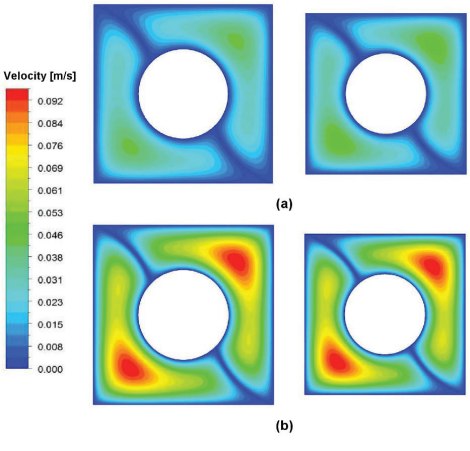

Figure 15. Velocity contour comparison between the channel with the base size (left Figure) and the optimum size (right Figure) at the channel exit at φ = 3% for: (**a**) Re = 500, and (**b**) Re = 1000.

Table 11. The dimension of channels compared in Figure 15.

	L (m)	W (mm)	D (mm)	R (mm)
Base size	3	50	50	25
Optimum size	3	45	22.5	21

4. Conclusions

In the present research, the impacts of geometry properties of a minichannel including the cylinder diameter, channel width, and fin radius on the convective heat transfer coefficient and pumping power in concentrations of 0%, 1%, 3%, and 5% of Al_2O_3/water nanofluid is assessed. The second-order models are demonstrated to recognize the correlation between the independent and response variables. The results are presented based on the constant mass flow rate and a constant Reynolds number. The main results achieved from the current study are as follows:

- The R^2_{adj} is found to be more than 99% for each response in the various concentrations by the ANOVA;
- Applying the NSGA-II indicates that the effect of the channel width and cylinder diameter improves by about 20.8% and 18% through increasing the concentration from 0% to 5%;
- The pumping power response is not sensitive to the nanofluid concentration;
- The smaller the fin radius, the higher the HTC and pumping power;
- Channel width has the highest and lowest effect on the HTC and pumping power, respectively;
- The optimization for the concentration of 3% demonstrates that in Re = 500 when the geometry is optimized, the HTC enhances about 8.8%, while the pumping power increases by almost 18%. In contrast, by increasing the concentration from 1% to 3%, merely a 7.6% enhancement in the HTC occurs, while the pumping power intensifies around 60%.

Author Contributions: Conceptualization, A.A.A. and M.A.; methodology, A.A.A. and M.A.; software, A.A.A. and M.A.; validation, A.A.A. and M.A.; formal analysis, A.A.A. and M.A.; investigation, A.A.A. and M.A.; resources, H.M.A., M.G., and M.R.S.; data curation, A.A.A. and M.A.; writing—original draft preparation, A.A.A. and M.A.; writing—review and editing, H.M.A., M.R.S., and M.G.; visualization, A.A.A. and M.A.; supervision, H.M.A., M.R.S. and M.G.; project administration, H.M.A., M.G. and M.R.S.; funding acquisition, H.M.A. All authors have read and agreed to the published version of the manuscript.

Funding: This research received no external funding.

Conflicts of Interest: The authors declare no conflict of interest.

Nomenclature

Cp	Specific heat, J/kg.K
D	Cylinder diameter, m
g	Gravity Acceleration, m/s^2
h	Convective heat transfer coefficient, W/m^2.K
k	Heat Conductivity, W/m.K
m	Mass, kg
Nu	Nusselt number
P	Pressure, Pa
Q	Heat flux, W/m^2
R	Fin radios, m
Re	Reynolds Number
t	Time, s
T	Temperature, K
V	Velocity, m/s
W	Channel height, m

x	Axial length, m
Greek symbols	
ρ	Density, kg/m^3
μ	Dynamic Viscosity, Pa.s
φ	Volume concentration
Subscripts	
bf	Base fluid
m	mean
nf	nanofluid
P	Particle
Abbreviations	
ANOVA	Analysis of variance
CCD	Central composite design
CD	Crowding distance
DOE	Design of experiments
FVM	Finite volume method
HTC	Heat transfer coefficient
NSGA	Non-Dominated Sorting Genetic Algorithm
RSM	Response surface methodology

References

1. Bahiraei, M.; Ahmadi, A.A. Thermohydraulic performance analysis of a spiral heat exchanger operated with water–alumina nanofluid: Effects of geometry and adding nanoparticles. *Energy Convers. Manag.* **2018**, *170*, 62–72. [CrossRef]
2. Sarafraz, M.M.; Tlili, I.; Tian, Z.; Khan, A.R.; Safaei, M.R. Thermal analysis and thermo-hydraulic characteristics of zirconia–water nanofluid under a convective boiling regime. *J. Therm. Anal. Calorim.* **2019**. [CrossRef]
3. Nazari, S.; Ellahi, R.; Sarafraz, M.M.; Safaei, M.R.; Asgari, A.; Akbari, O.A. Numerical study on mixed convection of a non-Newtonian nanofluid with porous media in a two lid-driven square cavity. *J. Therm. Anal. Calorim.* **2019**. [CrossRef]
4. Heydari, A.; Akbari, O.A.; Safaei, M.R.; Derakhshani, M.; Alrashed, A.A.; Mashayekhi, R.; Shabani, G.A.; Zarringhalam, M.; Nguyen, T.K. The effect of attack angle of triangular ribs on heat transfer of nanofluids in a microchannel. *J. Therm. Anal. Calorim.* **2018**, *131*, 2893–2912. [CrossRef]
5. Ahmadi, A.A.; Khodabandeh, E.; Moghadasi, H.; Malekian, N.; Akbari, O.A.; Bahiraei, M. Numerical study of flow and heat transfer of water-Al_2O_3 nanofluid inside a channel with an inner cylinder using Eulerian–Lagrangian approach. *J. Therm. Anal. Calorim.* **2018**, *132*, 651–665. [CrossRef]
6. Goodarzi, M.; Tlili, I.; Tian, Z.; Safaei, M.R. Efficiency assessment of using graphene nanoplatelets-silver/water nanofluids in microchannel heat sinks with different cross-sections for electronics cooling. *Int. J. Numer. Methods Heat Fluid Flow* **2019**, *30*, 347–372. [CrossRef]
7. Esfe, M.H.; Esfandeh, S.; Rejvani, M. Modeling of thermal conductivity of MWCNT-SiO_2 (30: 70%)/EG hybrid nanofluid, sensitivity analyzing and cost performance for industrial applications. *J. Therm. Anal. Calorim.* **2018**, *131*, 1437–1447. [CrossRef]
8. Safaei, M.R.; Hajizadeh, A.; Afrand, M.; Qi, C.; Yarmand, H.; Zulkifli, N.W.B.M. Evaluating the effect of temperature and concentration on the thermal conductivity of ZnO-TiO_2/EG hybrid nanofluid using artificial neural network and curve fitting on experimental data. *Phys. A Stat. Mech. Appl.* **2019**, *519*, 209–216. [CrossRef]
9. Li, Z.X.; Renault, F.L.; Gómez, A.O.; Sarafraz, M.M.; Khan, H.; Safaei, M.R.; Bandarra Filho, E.P. Nanofluids as secondary fluid in the refrigeration system: Experimental data, regression, ANFIS, and NN modeling. *Int. J. Heat Mass Transf.* **2019**, *144*, 118635. [CrossRef]
10. Esfe, M.H.; Hajmohammad, H.; Toghraie, D.; Rostamian, H.; Mahian, O.; Wongwises, S. Multi-objective optimization of nanofluid flow in double tube heat exchangers for applications in energy systems. *Energy* **2017**, *137*, 160–171. [CrossRef]

11. Shahsavar, A.; Moradi, M.; Bahiraei, M. Heat transfer and entropy generation optimization for flow of a non-Newtonian hybrid nanofluid containing coated CNT/Fe_3O_4 nanoparticles in a concentric annulus. *J. Taiwan Inst. Chem. Eng.* **2018**, *84*, 28–40. [CrossRef]
12. Maghsoudi, P.; Siavashi, M. Application of nanofluid and optimization of pore size arrangement of heterogeneous porous media to enhance mixed convection inside a two-sided lid-driven cavity. *J. Therm. Anal. Calorim.* **2019**, *135*, 947–961. [CrossRef]
13. Ghasemi, A.; Hajmohammad, M. Minimum-weight design of stiffened shell under hydrostatic pressure by genetic algorithm. *Steel Compos. Struct.* **2015**, *19*, 75–92. [CrossRef]
14. Box, G.E.; Wilson, K.B. On the experimental attainment of optimum conditions. *J. R. Stat. Soc. Ser. B Methodol.* **1951**, *13*, 1–38. [CrossRef]
15. Bahiraei, M.; Heshmatian, S. Application of a novel biological nanofluid in a liquid block heat sink for cooling of an electronic processor: Thermal performance and irreversibility considerations. *Energy Convers. Manag.* **2017**, *149*, 155–167. [CrossRef]
16. Bahiraei, M.; Gharagozloo, K.; Alighardashi, M.; Mazaheri, N. CFD simulation of irreversibilities for laminar flow of a power-law nanofluid within a minichannel with chaotic perturbations: An innovative energy-efficient approach. *Energy Convers. Manag.* **2017**, *144*, 374–387. [CrossRef]
17. Liu, F.; Cai, Y.; Wang, L.; Zhao, J. Effects of nanoparticle shapes on laminar forced convective heat transfer in curved ducts using two-phase model. *Int. J. Heat Mass Transf.* **2018**, *116*, 292–305. [CrossRef]
18. Bahiraei, M.; Godini, A.; Shahsavar, A. Thermal and hydraulic characteristics of a minichannel heat exchanger operated with a non-Newtonian hybrid nanofluid. *J. Taiwan Inst. Chem. Eng.* **2018**, *84*, 149–161. [CrossRef]
19. Ghasemi, S.E.; Ranjbar, A.; Hosseini, M. Thermal and hydrodynamic characteristics of water-based suspensions of Al_2O_3 nanoparticles in a novel minichannel heat sink. *J. Mol. Liq.* **2017**, *230*, 550–556. [CrossRef]
20. Bahiraei, M.; Majd, S.M. Prediction of entropy generation for nanofluid flow through a triangular minichannel using neural network. *Adv. Powder Technol.* **2016**, *27*, 673–683. [CrossRef]
21. Bergman, T. Analysis of heat transfer enhancement in minichannel heat sinks with turbulent flow using H_2O–Al_2O_3 nanofluids. *J. Electron. Packag.* **2009**, *131*, 021008. [CrossRef]
22. Danish, M.; Yahya, S.M.; Saha, B.B. Modelling and optimization of thermophysical properties of aqueous titania nanofluid using response surface methodology. *J. Therm. Anal. Calorim.* **2020**, *139*, 3051–3063. [CrossRef]
23. Esfe, M.H.; Tilebon, S.M.S. Statistical and artificial based optimization on thermo-physical properties of an oil based hybrid nanofluid using NSGA-II and RSM. *Phys. A Stat. Mech. Appl.* **2020**, *537*, 122126.
24. Esfe, M.H.; Motallebi, S.M. Four objective optimization of aluminum nanoparticles/oil, focusing on thermo-physical properties optimization. *Powder Technol.* **2019**, *356*, 832–846. [CrossRef]
25. Sarafraz, M.; Tlili, I.; Tian, Z.; Bakouri, M.; Safaei, M.R. Smart optimization of a thermosyphon heat pipe for an evacuated tube solar collector using response surface methodology (RSM). *Phys. A Stat. Mech. Appl.* **2019**, *534*, 122146. [CrossRef]
26. Jing, D.; Hu, S.; Hatami, M.; Xiao, Y.; Jia, J. Thermal analysis on a nanofluid-filled rectangular cavity with heated fins of different geometries under magnetic field effects. *J. Therm. Anal. Calorim.* **2020**, *139*, 3577–3588. [CrossRef]
27. Saxena, V.; Kumar, N.; Saxena, V.K. Multi-objective optimization of modified nanofluid fuel blends at different TiO_2 nanoparticle concentration in diesel engine: Experimental assessment and modeling. *Appl. Energy* **2019**, *248*, 330–353. [CrossRef]
28. Kumar, S.; Dinesha, P. Optimization of thermal parameters in a double pipe heat exchanger with a twisted tape using response surface methodology. *Soft Comput.* **2018**, *22*, 6261–6270. [CrossRef]
29. Rashidi, S.; Bovand, M.; Esfahani, J.A. Structural optimization of nanofluid flow around an equilateral triangular obstacle. *Energy* **2015**, *88*, 385–398. [CrossRef]
30. Han, H.; Yu, R.; Li, B.; Zhang, Y. Multi-objective optimization of corrugated tube inserted with multi-channel twisted tape using RSM and NSGA-II. *Appl. Therm. Eng.* **2019**, *159*, 113731. [CrossRef]
31. Han, H.; Yu, R.; Li, B.; Zhang, Y.; Wang, W.; Chen, X. Multi-objective optimization of corrugated tube with loose-fit twisted tape using RSM and NSGA-II. *Int. J. Heat Mass Transf.* **2019**, *131*, 781–794. [CrossRef]

32. Esfe, M.H.; Amiri, M.K.; Bahiraei, M. Optimizing thermophysical properties of nanofluids using response surface methodology and particle swarm optimization in a non-dominated sorting genetic algorithm. *J. Taiwan Inst. Chem. Eng.* **2019**, *103*, 7–19. [CrossRef]
33. Rashidi, M.M.; Nasiri, M.; Shadloo, M.S.; Yang, Z. Entropy generation in a circular tube heat exchanger using nanofluids: Effects of different modeling approaches. *Heat Transf. Eng.* **2017**, *38*, 853–866. [CrossRef]
34. Maleki, H.; Safaei, M.R.; Alrashed, A.A.; Kasaeian, A. Flow and heat transfer in non-Newtonian nanofluids over porous surfaces. *J. Therm. Anal. Calorim.* **2019**, *135*, 1655–1666. [CrossRef]
35. Azwadi, C.N.; Adamu, I.M. Turbulent force convective heat transfer of hybrid nano fluid in a circular channel with constant heat flux. *Adv. Res. Fluid Mech. Therm. Sci.* **2016**, *19*, 1–9.
36. Maleki, H.; Safaei, M.R.; Togun, H.; Dahari, M. Heat transfer and fluid flow of pseudo-plastic nanofluid over a moving permeable plate with viscous dissipation and heat absorption/generation. *J. Therm. Anal. Calorim.* **2019**, *135*, 1643–1654. [CrossRef]
37. Nasiri, H.; Jamalabadi, M.Y.; Sadeghi, R.; Safaei, M.R.; Nguyen, T.K.; Shadloo, M.S. A smoothed particle hydrodynamics approach for numerical simulation of nano-fluid flows. *J. Therm. Anal. Calorim.* **2019**, *135*, 1733–1741. [CrossRef]
38. Bahiraei, M.; Mazaheri, N.; Aliee, F.; Safaei, M.R. Thermo-hydraulic performance of a biological nanofluid containing graphene nanoplatelets within a tube enhanced with rotating twisted tape. *Powder Technol.* **2019**, *355*, 278–288. [CrossRef]
39. Safaei, M.; Togun, H.; Vafai, K.; Kazi, S.; Badarudin, A. Investigation of heat transfer enhancement in a forward-facing contracting channel using FMWCNT nanofluids. *Numer. Heat Transf. Part A Appl.* **2014**, *66*, 1321–1340. [CrossRef]
40. Sheikholeslami, M.; Ganji, D. Nanofluid convective heat transfer using semi analytical and numerical approaches: A review. *J. Taiwan Inst. Chem. Eng.* **2016**, *65*, 43–77. [CrossRef]
41. Kherbeet, A.S.; Mohammed, H.A.; Ahmed, H.E.; Salman, B.H.; Alawi, O.A.; Safaei, M.R.; Khazaal, M.T. Mixed convection nanofluid flow over microscale forward-facing step—Effect of inclination and step heights. *Int. Commun. Heat Mass Transf.* **2016**, *78*, 145–154. [CrossRef]
42. Cavazzuti, M. *Optimization Methods: From Theory to Design Scientific and Technological Aspects in Mechanics*, 1st ed.; Springer: Berlin/Heidelberg, Germany, 2013.
43. Anderson, M.J.; Whitcomb, P.J. *RSM Simplified: Optimizing Processes Using Response Surface Methods for Design of Experiments*; Productivity Press: New York, NY, USA, 2004.
44. Arani, A.A.A.; Akbari, O.A.; Safaei, M.R.; Marzban, A.; Alrashed, A.A.; Ahmadi, G.R.; Nguyen, T.K. Heat transfer improvement of water/single-wall carbon nanotubes (SWCNT) nanofluid in a novel design of a truncated double-layered microchannel heat sink. *Int. J. Heat Mass Transf.* **2017**, *113*, 780–795. [CrossRef]
45. Ebrahimnia-Bajestan, E.; Niazmand, H.; Duangthongsuk, W.; Wongwises, S. Numerical investigation of effective parameters in convective heat transfer of nanofluids flowing under a laminar flow regime. *Int. J. Heat Mass Transf.* **2011**, *54*, 4376–4388. [CrossRef]
46. Chandrasekar, M.; Suresh, S.; Bose, A.C. Experimental investigations and theoretical determination of thermal conductivity and viscosity of Al_2O_3/water nanofluid. *Exp. Therm. Fluid Sci.* **2010**, *34*, 210–216. [CrossRef]
47. Vajjha, R.S.; Das, D.K. Experimental determination of thermal conductivity of three nanofluids and development of new correlations. *Int. J. Heat Mass Transf.* **2009**, *52*, 4675–4682. [CrossRef]
48. Vajjha, R.S.; Das, D.K.; Kulkarni, D.P. Development of new correlations for convective heat transfer and friction factor in turbulent regime for nanofluids. *Int. J. Heat Mass Transf.* **2010**, *53*, 4607–4618. [CrossRef]
49. Sieder, E.N.; Tate, G.E. Heat transfer and pressure drop of liquids in tubes. *Ind. Eng. Chem.* **1936**, *28*, 1429–1435. [CrossRef]
50. Heris, S.Z.; Etemad, S.G.; Esfahany, M.N. Experimental investigation of oxide nanofluids laminar flow convective heat transfer. *Int. J. Heat Mass Transf.* **2006**, *33*, 529–535. [CrossRef]
51. Deb, K.; Pratap, A.; Agarwal, S.; Meyarivan, T. A fast and elitist multiobjective genetic algorithm: NSGA-II. *IEEE Trans. Evol. Comput.* **2002**, *6*, 182–197. [CrossRef]

nanomaterials

MDPI

Article

Investigation of Heat Transfer and Pressure Drop in Microchannel Heat Sink Using Al_2O_3 and ZrO_2 Nanofluids

Muhammad Zia Ullah Khan [1], Emad Uddin [1], Bilal Akbar [2], Naveed Akram [2,3,*], Ali Ammar Naqvi [1], Muhammad Sajid [1], Zaib Ali [1], Md. Yamin Younis [2] and Fausto Pedro García Márquez [4,*]

[1] Department of Mechanical Engineering, School of Mechanical and Manufacturing Engineering (SMME), National University of Science and Technology, Islamabad 44000, Pakistan; engr.ziaullah1992@gmail.com (M.Z.U.K.); emaduddin@smme.nust.edu.pk (E.U.); ali_ammar@smme.edu.pk (A.A.N.); m.sajid@smme.nust.edu.pk (M.S.); zaib.ali@smme.nust.edu.pk (Z.A.)

[2] Department of Mechanical Engineering, Mirpur University of Science and Technology (MUST), Mirpur-10250 (AJK), Pakistan; bilal.akbar@must.edu.pk (B.A.); myyounis.me@must.edu.pk (M.Y.Y.)

[3] Department of Mechanical Engineering, Faculty of Mechanical Engineering, University of Malaya, Kuala Lumpur 50603, Malaysia

[4] Ingenium Research Group, University of Castilla-La Mancha, 13071 Ciudad Real, Spain

* Correspondence: naveed.me@must.edu.pk (N.A.); faustopedro.garcia@uclm.es (F.P.G.M.); Tel.: +60-111-608-1148 (N.A.); +34-926-95300 (F.P.G.M.)

Received: 20 August 2020; Accepted: 7 September 2020; Published: 9 September 2020

Abstract: A new micro heat exchanger was analyzed using numerical formulation of conjugate heat transfer for single-phase fluid flow across copper microchannels. The flow across bent channels harnesses asymmetric laminar flow and dean vortices phenomena for heat transfer enhancement. The single-channel analysis was performed to select the bent channel aspect ratio by varying width and height between 35–300 μm for Reynolds number and base temperature magnitude range of 100–1000 and 320–370 K, respectively. The bent channel results demonstrate dean vortices phenomenon at the bend for Reynolds number of 500 and above. Thermal performance factor analysis shows an increase of 18% in comparison to straight channels of 200 μm width and height. Alumina nanoparticles at 1% and 3% concentration enhance the Nusselt number by an average of 10.4% and 23.7%, respectively, whereas zirconia enhances Nusselt number by 16% and 33.9% for same concentrations. On the other hand, thermal performance factor analysis shows a significant increase in pressure drop at high Reynolds number with 3% particle concentration. Using zirconia for nanofluid, Nusselt number of the bent multi-channel model is improved by an average of 18% for a 3% particle concentration as compared to bent channel with deionized water.

Keywords: laminar flow; conjugate heat transfer; dean vortices; Nusselt number; friction factor

1. Introduction

Intelligent systems being used in recent times come equipped with microprocessor chips which allow for increased functionality, occupy less space, and provide greater portability. While the development of microelectronic devices continues to provide convenience to humankind, however, the reduced durability of such devices due to their heat-sensitive nature remains a persistent problem.

In most practical applications, heat transfer between one or more fluids takes place through heat exchangers. For cooling of Micro-Electro-Mechanical Systems (MEMS), micro heat exchangers serve as a solution to the heating problem at small scales. With applications ranging from small phones to significant industrial heat generating units, the advantage of heat exchangers being used at micro-scale

lies with their compact size, low material cost, mobility, and better performance. Much like their conventional counterparts, the micro heat exchanger consists of confined ducts that constrain the flow of fluid or gas stream. The higher surface area to volume ratio provided by microchannels results in reduced thermal resistance and higher heat transfer rates. The heat transfer rates for microchannel heat exchangers are dependent upon the performance of fluids, with the thermal conductivity of fluid restricting the achievable heat transfer rates. However, the introduction of nanoparticles inside the base fluid can help overcome such barriers. Such mixtures, known as nanofluids consist of a base fluid and solid particles, are developed by mixing a suspension of nanoparticles in base fluids.

In 1981, Tuckerman and Pease [1] demonstrated that a confined flow of liquid could aid in increasing convective heat dissipation from the electronic chip through the application of high aspect ratio microchannels. The detailed study by Peterson et al. [2] concluded that heat sinks perform at their best when the heat exchanger is properly in contact with the electronic device junction. Tuckerman [3] further performed numerical analysis on the efficient cooling system for dissipating 1000 W/cm^2 heat while maintaining structure temperature inside the limit of the safe functionality of transistors. Moon and Jhong [4] numerically and experimentally investigated the cooling performance of micro heat exchanger on stacked multi-chip modules with single-phase laminar flow. Amirah et al. [5] performed numerical and experimental investigations for single and multi-channel micro heat exchanger configurations using a range of hydraulic diameters, concluding that transition from laminar to turbulent flow occurs at Reynolds number magnitude of 1600 and that the presence of significant conjugate effect results in the difference between numerical and experimental results. While working at a micro-scale, a question arises about whether or not the conventional flow and heat transfer theories can be safely applied to micro-scale flows. Some studies contradict conventional theories [6,7]. However, other studies were unable to find a significant difference between flow and heat transfer for conventional and micro-scale applications. The absence of difference concludes that discrepancies in literature can be a result of scaling effect and uncertainties which can arise due to viscous heating, surface roughness, properties dependent on temperature, and entrance and conjugate heat transfer [8–11]. While considering scaling effects, axial wall conduction is also a significant problem that contributes to the decrease in the thermal efficiency of the microchannel heat exchanger. Experimental and numerical studies demonstrate that, by increasing the thermal conductivity of the micro heat exchangers, axial wall conduction can also increase, resulting in lower overall thermal efficiency. Therefore, the conclusion is that low thermal conductivity materials are efficient for resisting axial wall conduction [12,13]. However, the use of low thermal conductivity material for heat transfer has limited applications.

Various studies utilize numerical simulations as a tool for predicting the behavior of microchannels, as they tend to provide flexibility in design aspects allowing for greater opportunity in exploring new channels and design variations. A numerical study on microchannel heat exchangers conducted by Liu and Garimella [14] showed that for laminar flow across channels both microscale and conventional channels have the same behavior for a range of hydraulic diameters. Xu et al. [15] numerically studied the flow characteristics for Reynolds number range of 20–4000, showing that flow characteristics in microchannels are similar to Navier–Strokes predicted behavior, suggesting that deviation in early studies could be due to error in dimensions. Hetsroni et al. [16] validated the available experimental data through numerical studies by considering hydrodynamic characteristics of laminar flow inside a micro heat exchanger with uniform flux while keeping necessary allowance for channel geometry, wall conduction, energy dissipation, and physical properties of the fluid. Allen et al. [17] experimentally and numerically investigated fluid flow and heat transfer in copper micro heat exchangers considering constant heat base temperature. Results from the experiments were found to be in good agreement with simulation results. Heat transfer enhancement in curved microchannel has been studied by many researchers concluding a significant increase in Nusselt number with little increase in pressure drop when the curved microchannel is compared to straight microchannel [18–21].

Sui et al. [22] performed experimental and numerical analysis on wavy microchannels, concluding that an increase in heat transfer was disproportionate to the increase in the corresponding increase in pressure drop for wavy microchannel due to the formation of dean vortices. Wang et al. [23] performed a numerical study on friction factor and Nusselt number in curved channels, concluding that the increase in mean Nusselt number and friction factor occurs as a result of vortex generation due to the effect of buoyancy.

Diverging-Converging plenum geometry of triangular-shaped was used due to its better flow distribution for the multi-channel model [4,24]. Sehgal et al. [25] studied convective heat transfer and pressure drop of the microchannel with top and side inlet plenum and found side inlet to be 13% more efficient. Balaji et al. [26] concluded inlet and outlet in-line with microchannel evenly distributes the pressure drop.

In recent times, the use of nano-scale technology has emerged widely and revolutionized several technological fields. Nanofluid technology is one specific area where a homogenous mixture of nanoparticles and a base fluid is used to develop nanofluids. Such fluids have vast applications in tribology [27,28], heat transfer enhancement [29–32], and biomedical filed [33–35].

Since these fluids form a colloidal solution of the solid-liquid particles, therefore, the computational domain for nanofluids can be evaluated using either Eulerian or Lagrangian approach, depending upon the application. For a simplifying model, to minimize the computational effort, in engineering applications, like heat exchanger, the Eulerian approach is preferred [29]. However, in biomedical application, the Lagrangian approach is considered more effective, as the primary focus is on the study of Brownian motions and interaction of individual particles [33,36].

Nanofluids are commonly used in heat transfer units for performance enhancement of cooling fluids. Convective heat transfer using nanofluids, like Al_2O_3 [37–39], ZrO_2 [39,40], CNT [41,42], CuO [38], Cu [38], and TiO_2 [43,44], have been investigated in numerical studies. Williams et al. [39] investigated the heat transfer and pressure drop in horizontal tubes under turbulent flow conditions by performing experimental analysis on setup using alumina-water (Al_2O_3)- and zirconia-water (ZrO_2)-based nanofluids. Rea et al. [40] experimentally investigated convective heat transfer and pressure drop in vertical heated tubes in laminar flow conditions using Al_2O_3 and ZrO_2 nanofluids with enhancement in heat transfer coefficient [45–49]. Thus, the design of geometry, selection of nanofluids types, and concentration contributes to obtaining high thermal effectiveness.

This study focused on the numerical analysis of bent microchannel for evaluating the behavior of the fluid flow and conjugate heat transfer. The microchannel design is the most critical parameter as it can be harnessed to achieve maximum heat transfer with a lesser corresponding increase in pressure drop. Geometry, flow, and temperature of the single microchannels are varied to achieve the desired performance. Variations in width, height, the hydraulic diameter of the channel for a range of Reynolds number, and base temperatures were studied. Analysis on a single channel with a 25-degree bend was performed by varying width and height to obtain the best geometric parameter for multi-channel. Alumina and zirconia nanoparticles were introduced in the optimum bended single channel to calculate Thermal Performance Factor (TPF). After the selection of a single channel, a multi-channel micro heat exchanger was analyzed with and without nanoparticles, providing a comprehensive design of micro heat exchanger with multiple design parameter considerations.

2. Materials and Methods

2.1. Geometric Configuration and Computational Domain

2.1.1. Single Channel

The numerical study of conjugate heat transfer problem accounts for convective heat transfer through fluid-solid interface and conductive heat transfer within both the solid and fluid domains. The geometry of single channel with fix length is shown in Figure 1. The effect of bend in the conventional straight channel was investigated to determine the changes in pressure drop and Nusselt

number. The geometrical parameters of the channel with its width and height were varied between 35–300 µm. Table 1 provides dimensional details of single channel for optimum bend angle selected through numerical study. The length of a single channel was kept such that it covers the entire 28 × 7-mm cross-section of the electronic chip when introduced in the multi-channel model.

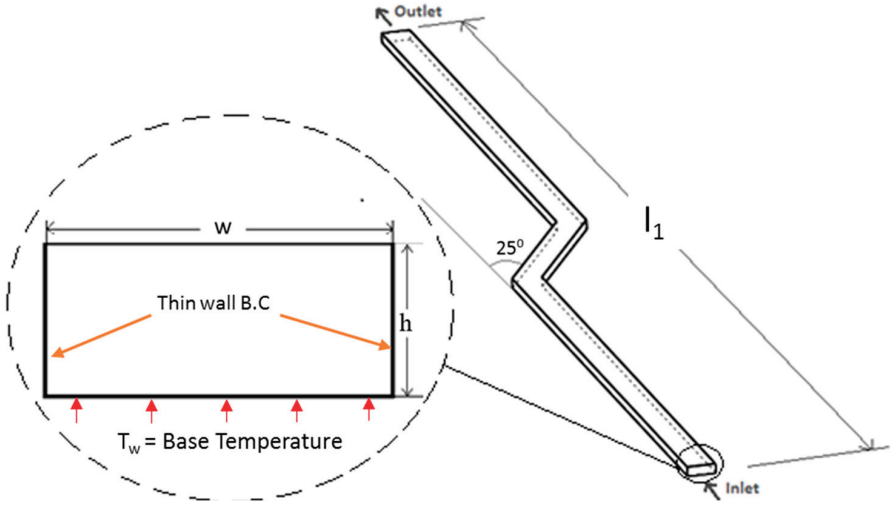

Figure 1. Single channel geometric parameters.

2.1.2. Multi-Channel

The multi-channel configuration given in Figure 2 was developed using a series of single channels after carefully analyzing performance parameters for each geometric variation across single channels, as discussed in the previous section. The performance of multi-channel was investigated by varying channel height and base temperature at Reynolds number range from 100–1000 while keeping the length and width of all channels the same. The dimensional constraint for the multi-channel model is also given in Table 1.

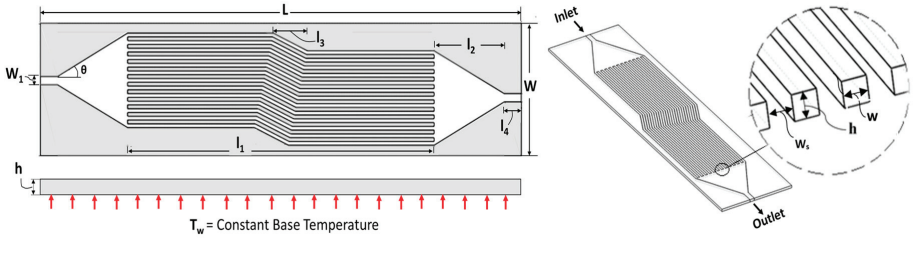

Figure 2. Multi-channel configuration (solid with grey color and fluid with white color).

Table 1. Multi-channel model corresponding parameters.

Symbol	Dimension (μm)
l_1	18,000
l_2	4120
l_3	2000
l_4	1000
w_1	440
w	200
w_s	200
L	28,300
W	7000

2.2. Mathematical Formulation

The working fluid for the present case was de-ionized water with temperature-dependent properties, while the solid material was copper with fixed properties, as given in Table 2. The conjugate heat transfer problem was simplified using the below-mentioned assumptions and idealizations:

1. 3D incompressible fluid with the steady-state formulation.
2. Constant density and variable specific heat, viscosity, and thermal conductivity with respect to temperature is used for fluid. Viscosity, specific heat, and thermal conductivity are a piece-wise linear function of temperature, as shown by Peiyi et al. and Okhotin et al. [50,51].
3. Constant wall temperature is assumed, considering uniform temperature distribution throughout the channel base.
4. Constant solid properties are used, with side walls having the adiabatic condition.
5. Radiation and viscous dissipation are neglected.

Table 2. Temperature dependent fluid and fix solid properties.

Properties	Deionized Water [50,51]	Copper [52]
μ_f (Pa.s)	$0.0194 - 1.065 \times 10^{-4}T + 1.489 \times 10^{-7}T^2$	–
k_{nf} (W/m.k)	$-0.829 + 0.0079T - 1.04 \times 10^{-5}T^2$	387.6
C_{pf} (J/kg.k)	$5348 - 7.42T + 1.17 \times 10^{-2}T^2$	381
ρ_f (kg/m^3)	998.2	8978

By considering the above assumptions, governing equations for the description of fluid flow and heat transfer can be given as:

Conservation of mass:

$$\nabla.(\rho \mathbf{V}) = \mathbf{0}; \tag{1}$$

Conservation of momentum:

$$\mathbf{V}.\nabla(\rho \mathbf{V}) = -\nabla p + \nabla.(\mu \nabla \mathbf{V}); \tag{2}$$

Conservation of energy (Fluid):

$$\mathbf{V}.\nabla\left(\rho C_p T_f\right) = \nabla.(k_f \nabla T_f); \tag{3}$$

Conservation of energy (Solid):

$$\nabla.(k_{so} \nabla T_{so}) = 0. \tag{4}$$

The uniform velocity boundary condition was applied at inlet and pressure outlet condition at the outlet, as the flow was assumed to be incompressible. The sidewall boundaries were assigned no-slip condition, whereas top and sidewall were assigned adiabatic condition, and constant temperature was applied on the bottom wall. The boundary conditions given in Figure 1 show a thin wall boundary condition applied to the channel sides. It was assigned in ANSYS Fluent (Canonsburg, PA, USA) to model conjugate heat transfer without modeling solid geometry, and a fixed value of wall thickness for thin-wall model was assigned as half of the channel width.

2.3. Numerical Procedures and Parameter Definition

The design, meshing, and analysis tools available within ANSYS 18.1 (Canonsburg, PA, USA) were used for the study of microchannels. The design modeler tool was used to develop the model, and the inbuilt meshing tool was used to generate a structured non-uniform mesh using hexahedron elements, as shown in Figure 3, for computational domain discretization. The mesh was accomplished in the meshing module with minimum mesh orthogonality of 0.96734, the maximum aspect ratio of 1.2, and a maximum skewness of 0.16. The viscous laminar model was used with a Semi-Implicit Method for Pressure Linked Equations (SIMPLE) scheme for solving pressure velocity coupling [5]. Second-order upwind scheme was used for solving momentum and energy equations. Converging criteria for governing equations were set to 10^{-5}. The average mesh elements for single-channel were 3.2 million, whereas, for the multi-channel model, the average mesh elements were 25 million. The analysis was performed using the Fluent module within ANSYS 18.1 software, and computation was performed on dual Xeon X5650 12 core processor with 72 gigabytes RAM. The average computation time for a single channel model was two hours, whereas the average computation time for the multi-channel model was 48 h.

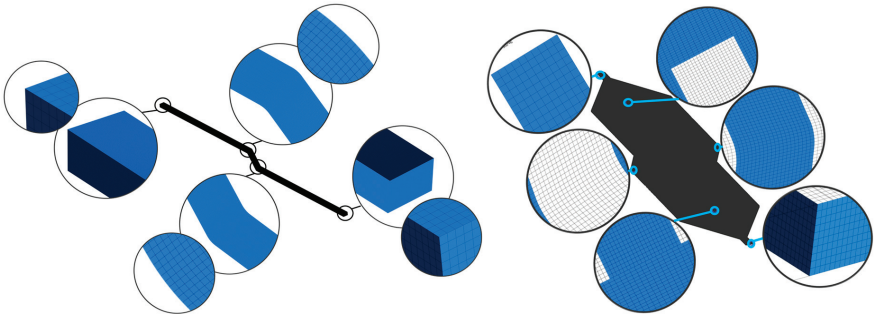

Figure 3. Single (Left) and Mmulti-channel (Right) mesh.

2.3.1. Friction Factor

The numerical results are evaluated in terms of certain performance parameters, namely friction factor and Nusselt number. The Reynolds number (Re) is a function of liquid density (ρ); dynamic viscosity (μ); and Inlet velocity v_{in} of fluid, and hydraulic diameter (D_H) of the channel is defined by Equation (5):

$$Re = \frac{\rho D_H v_{in}}{\mu}, \tag{5}$$

where

$$D_H = \frac{2wh}{(w+h)}. \tag{6}$$

The friction factor and pumping power is calculated by Equations (7) and (8):

$$f = \frac{D_H}{L_c} \frac{2\,\Delta P}{\rho\, v_{in}^2}, \tag{7}$$

$$P_{power} = \Delta P\, \dot{V}, \tag{8}$$

where: $\dot{V}$ is the volume flow rate of fluid, L_c is the length of the microchannel understudy, and ΔP is the pressure difference calculated by subtracting pressure of outlet going fluid from inlet coming.

Hansel [53] suggested a friction factor equation for the analytical formulation of pressure drop by substituting f in Equation (9).

$$f = \frac{64}{Re\left[\frac{2}{3} + \frac{11h}{24w}\left(2 - \frac{h}{w}\right)\right]}. \tag{9}$$

Upadhye et al. [54] used pressure drop and Poiseuille number equation to analytically find pressure drop in a microchannel.

$$\Delta P = \frac{2P_o \rho\, v_{in}^2}{Re} \frac{L}{D_H}. \tag{10}$$

Poiseuille number equation in friction factor form is expressed by Equation (11) [55]:

$$P_o = fRe. \tag{11}$$

In Equation (11), the value of P_o can be calculated from Shah and London [56] for the microchannel:

$$P_o = 24\left(1 - 1.13553\alpha_{ch} + 1.9467\alpha_{ch}^2 - 1.7012\alpha_{ch}^3 + 0.9564\alpha_{ch}^4 - 0.2537\alpha_c^5\right), \tag{12}$$

where α_{ch} is the aspect ratio of the microchannel.

2.3.2. Heat Transfer

Heat transfer co-efficient values h is necessary to determine microchannel thermal performance. Non-dimensional parameter Nusselt number is considered for heat transfer evaluation of micro heat exchanger. Nusselt number (Nu) is expressed by Equation (13):

$$Nu = \frac{hD_H}{k}. \tag{13}$$

h can also be represented in total heat rate form by Equation (14):

$$h = \frac{Q}{A_{ht}\, \Delta T}, \tag{14}$$

where ΔT is the difference in temperature between the solid surface and flowing fluid, and

$$Q = \dot{m} C_p (T_o - T_i). \tag{15}$$

The energy balance depicting fluid flow through a microchannel, with assumptions of constant base temperature (T_w), negligible accumulation of mass, and no change in property with time, is given by Equation (16):

$$C_p \dot{m} (T_o - T_i) = hA_{ht} \frac{T_o - T_i}{\ln\left(\frac{T_w - T_i}{T_w - T_o}\right)}. \tag{16}$$

Equation (15) can be substituted into Equation (16) for obtaining non-dimensional Nusselt number (Nu) [57] form given by Equation (17):

$$Nu = \left(\frac{D_H}{k}\right) \ln\left(\frac{(T_s - T_i)}{(T_s - T_o)}\right)\left(\frac{\dot{m} C_p}{A_{ht}}\right), \tag{17}$$

where k is the thermal conductivity of fluid at mean temperature; C_p is the specific heat of fluid at mean temperature; T_s is bottom wall temperature; T_i is fluid inlet temperature; $\dot{m}$ is the mass flow rate of fluid; T_o fluid outlet temperature; and A_{ht} is the area of base at which temperature is applied.

2.3.3. Nanofluids

The heat transfer by nanofluids depends on their thermos-physical properties that are a function of nanoparticle volume percentage (∅) in relation to the properties of water and nanoparticles [39,40]. The density and specific heat of nanoparticles is defined as follows:

$$\varnothing\ \rho_{np} + (1 - \varnothing)\ \varnothing\rho_f, \tag{18}$$

$$\frac{\varnothing\ \rho_{np}C_{np} + (1 - \varnothing)\ \rho_f C_f}{\rho_{nf}}, \tag{19}$$

where ρ_{np} and C_{np} represent density and specific heat of nanoparticles. The National Institute of Standards and Technology (NIST) database was used for alumina and zirconia properties (Table 3).

Table 3. Nanoparticles' properties.

Property	Alumina	Zirconia
$\mathbf{C_{np}}$ (J/kgk)	880	418
$\boldsymbol{\rho_{np}}$ (kg/m^3)	3920	5600

The temperature-dependent thermal conductivity (k_{nf}) and viscosity (μ_{nf}) of nanofluids in curve fitting form is expressed as follows:

Alumina-water:

$$k(\varnothing, T) = k_f(T)(1 + 4.5503\varnothing), \tag{20}$$

$$\mu(\varnothing, T) = \mu_f(T)\ \exp\left[\frac{4.91\varnothing}{(0.2092 - \varnothing)}\right]. \tag{21}$$

Zirconia-water:

$$k(\varnothing, T) = k_f(T)\left(1 + 2.4505\varnothing - 29.867\varnothing^2\right), \tag{22}$$

$$\mu(\varnothing, T) = \mu_f(T)\left(1 + 46.801\varnothing + 550.82\varnothing^2\right). \tag{23}$$

The constraint of the temperature range for these equations is between 20 °C and 80 °C for the volumetric concentration of 6% in the case of alumina and 3% for zirconia.

Equation (24) represents TPF, which is utilized as a parameter for the selection of microchannel by comparing the thermo-hydraulic performance of channels.

$$TPF = \frac{\frac{Nu}{Nu_o}}{\left(\frac{f}{f_o}\right)^{\frac{1}{3}}}. \tag{24}$$

3. Results and Discussion

3.1. Grid Independence

Since the finite volume method involves discretization of the domain into a finite number of volumes, grid independence is the first necessary step towards the numerical solution of problems. Grid independence studies are conducted on successively dense mesh sizes to predict a stage where the result stabilizes and the variation between numerical and analytically formulated results becomes almost negligible. The grid independence in terms of pressure drop magnitudes has been shown both in graphical and tabular form in Figure 4 and Table 4, respectively. A closer look at the pressure

drop curve shows that, for a coarse mesh, the simulation error is significant; however, as the mesh becomes relatively dense, the numerical solver can capture additional pressure losses across the bends and provides a much more accurate solution as we approach 1 million mesh elements. Upon further increasing the mesh density, we observe stabilization of results as the number of elements is increased from 2.8 to 4.3 million with no discernable increase in pressure drop magnitude. Therefore, a mesh of 4.3 million elements having an acceptable error of 5.5%, in comparison with the analytical solution given by Upadhye et al. [54]'s relation, is chosen as the optimum size.

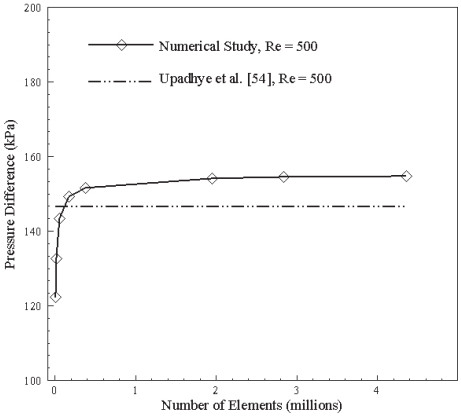

Figure 4. Grid independence and comparison with the analytical solution.

Table 4. Single channel mesh characteristics.

Number of Elements	Pressure Drop (kPa)	Analytical [54]	% Error
11,664	122.3	146.5	16.5
22,350	132.6	146.5	9.5
59,486	143.4	146.5	2.1
181,000	149.3	146.5	1.8
384,813	151.5	146.5	3.3
1,958,264	154.2	146.5	5.2
2,844,375	154.6	146.5	5.5
4,373,200	154.7	146.5	5.5

3.2. Data Validation and Reduction

The Poiseuille number approach used by Upadhye et al. [54] was used to validate the pressure drop in bended channels. The results were also counter-validated using the Hansel relation [53]. Both these relations provide analytical results for straight channel configuration, and the graph given in Figure 5 shows the numerical data validation for a single bend channel. It can be seen that, at a low Reynolds number, straight channel equations suit well with a 25-degree bend channel, but, at high Reynolds number values, the effect of bend becomes prominent, and error in pressure drop increases to a maximum of 8% for Upadhye's and 12% for Hansel's solution. At a low Reynolds number, the effect of dean vortices is not prominent, resulting in no increased pressure drop; therefore, the results are in good agreement with straight channel relations. However, an increase in Reynolds number enhances the formation of dean vortices. Hence, the effect of bend becomes prominent. Thus, numerical simulation defies Upadhye's and Hansel's approach at a high Reynolds number. The Nusselt number

was validated through the experimental study of Chen et al. [57], showing a maximum of 8% error when compared with numerical study for Reynolds number range of 500 to 1000.

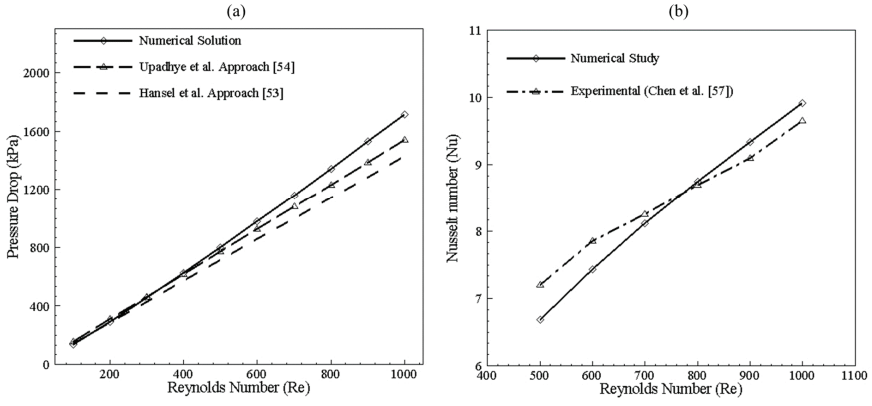

Figure 5. (**a**) Pressure drop validation for microchannel. (**b**) Nusselt number validation for microchannel.

Design of microchannel involves a trade-off between Nusselt number and friction factor since they represent the convective heat transfer rate and pressure drop, respectively. For single-channel models, a total of 360 cases are formulated for a Reynolds number range of 100–1000 at varying cross-sections and base temperatures. For data reduction, a total number of 360 single-channel case studies are reduced to 64 by using the design point approach. The design point approach involves the selection of optimum points by plotting the Nusselt number (Nu) and friction factor (f) at different Reynolds numbers. The intersection points of these curves are chosen as the design point for each specific model, as shown in Figure 6.

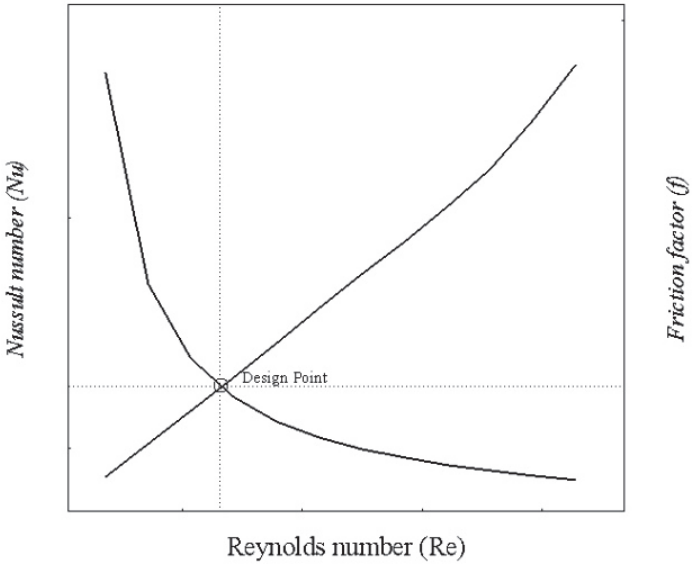

Figure 6. Design point selection depending upon performance parameters.

3.3. Bend Selection

The selection of bend is executed by considering geometric constraints as chip size and the number of channel adjustments in the multi-channel model. Furthermore, performance evaluation in the form of Nusselt number and pressure drop, as well as the formation of dean vortices, is also considered. By considering geometric constraints angle is limited to range 0° to 45°. Figure 7 depicts graphical information about Nusselt number and pressure drop for 200 × 200 µm channel at different Reynolds numbers. It can be observed from Figure 7a that, until 300 Reynolds number, no significant change in Nusselt number is visible by changing the bend angle. However, at 300 and above, improvement is significant, which can be correlated with velocity contours in Figure 8. Furthermore, with increment in the Reynolds number, a rise in pressure drop can be seen in Figure 7b.

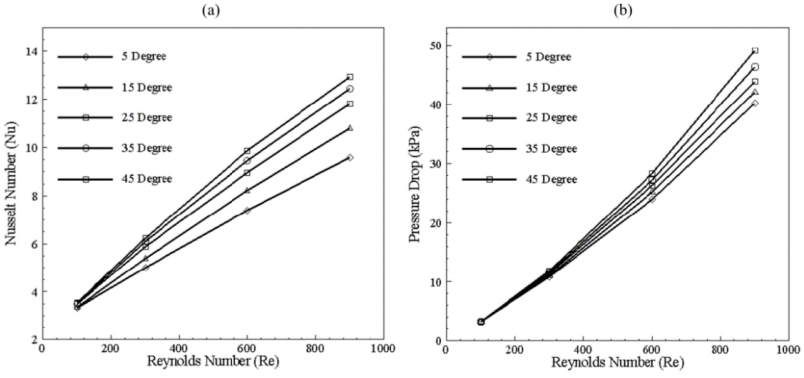

Figure 7. (**a**) Nusselt number variation with change in bend angle at different Reynolds numbers. (**b**) Pressure drop variation with change in bend angle at different Reynolds numbers.

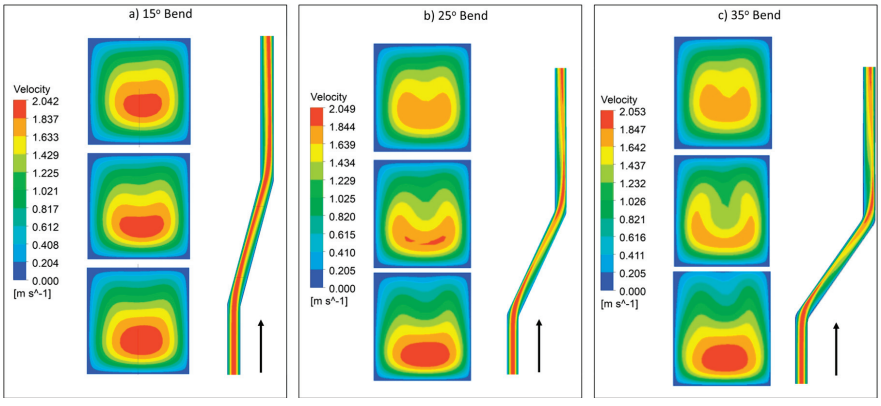

Figure 8. Velocity contours formation at different bend angles for Re = 300. (**a**) Contours at different cross-sections of 15° bend. (**b**) Contours at different cross-sections of 25° bend. (**c**) Contours at different cross-sections of 35° bend.

It can be observed that, after 15° change in angle, a sudden increase in Nusselt number with Reynolds number is visible compared to change in angle from 25° to onwards. A comparison of Figures 7a and 8 demonstrates that, due to the generation of dean vortices in the 25° bend channel, Nusselt number increased. It is identified that, with the 25° to onward bend, Nusselt number and pressure drop increases in equal proportion. Therefore, considering the increase in Nusselt number, generation of dean vortices, and consideration of geometric constraints, 25° angle was selected for

the multi-channel model. The longitudinal cross-section of the microchannel in Figure 8 depicts the mixing of fluid by variation in its contours at the bend region.

The study focuses on improving convective heat transfer by introducing a bend in the straight channel, which will increase convective heat transfer by asymmetric laminar flow, dean vortices generation, and increased flow length of the channel. Since this configuration provides the dean vortices and increased fluid contact with a heated surface, the pressure drops and heat transfer magnitudes for such bended channels are studied. From gathered design points, the 25° angle is selected, and a comparison with the straight channel of the same length is made, which shows a 5.3% increase in Nusselt number, while an increase in pressure drop is 3.3%, as shown in Figure 5. The angle is selected while considering the Nusselt number and pressure drop as performance parameters and space covered as a geometric parameter. The occupied space due to bend is of most concern as an increase in angle will widen the overall size of a single channel, creating difficulty in the multi-channel arrangement of bend channels.

The performance of 200 × 200 μm in the form of thermal effects can be seen in Figure 9a, depicting TPF greater than 1 for Reynolds number from 100–900. TPF value greater than 1 represents more heat transfer than pressure drop when bend channel is compared with the benchmark of the straight channel. Thus, bend will enhance thermal performance. Figure 9b illustrates that using the bend channel improves Nusselt number with increasing Reynolds number when compared with the straight channel of the same dimension of 200 × 200 μm; however, increment in pressure drop can also be observed. Thus, for the single channel case, a significant effect of Nusselt number can be achieved when the Reynolds number is higher. Figure 10 depicts the selection of the design point for 200 × 100 μm width and height channel at 320 K and 325 K temperature. With the increase of Reynolds number, lower values of friction factor can be observed, whereas the overall Nusselt number increases. It can be seen that, by varying base temperature, points of intersection of Nusselt number and friction factor changes, showing a trend that will be discussed for all single channel configurations. Data is reduced by plotting only design points in further study for all combinations of cross-sectional dimensions.

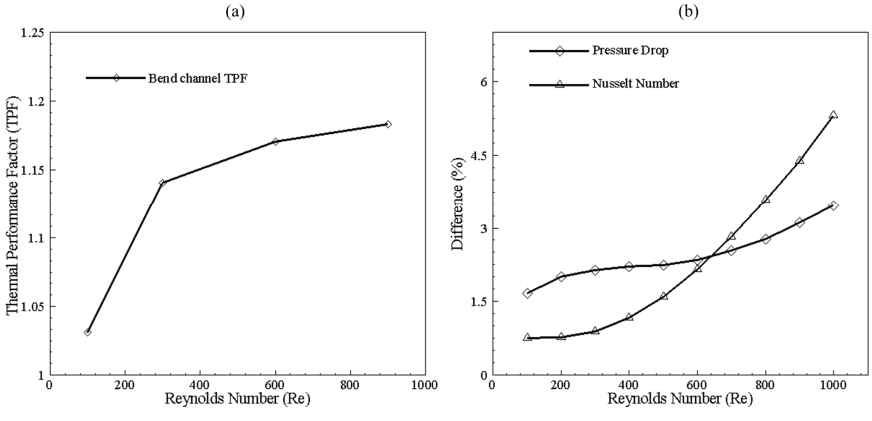

Figure 9. (**a**) Thermal Performance Factor (TPF) of bend channel (200 by 200 μm) with the straight channel (200 by 200 μm) as a benchmark. (**b**) The performance difference of bend channel (200 by 200 μm) with the straight channel (200 by 200 μm).

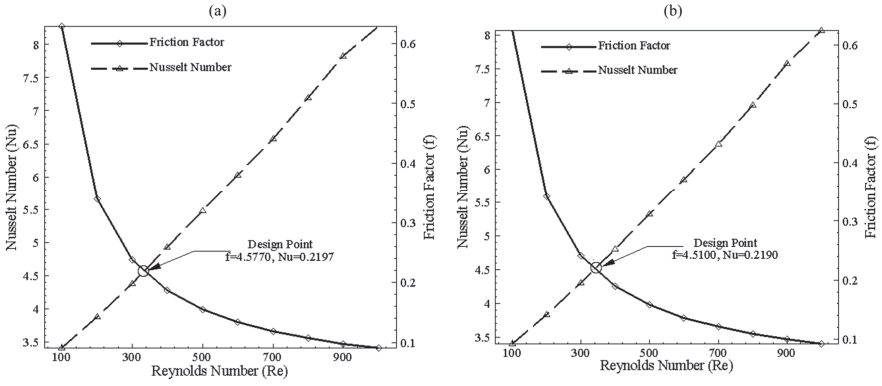

Figure 10. Nusselt number (Nu) and Friction factor (f) for 200 μm width and 100 μm height at (**a**) 320 K and (**b**) 325 K temperature.

3.4. Single Channel Configuration

The 25° bend angle is employed in the study of microchannel at different cross-sections to find the optimum aspect ratio for multi-channel consideration. Table 5 shows a range of width and height for optimum selection.

Table 5. Studied channels with corresponding parameters.

Group	Width Range μm	Height Range μm	Temperature K	Number of Cases
G1	35–300	35–300	320	120
G2	35–300	35–300	325	120
G3	35–300	35–300	365	120
G4	35–300	35–300	370	120

Following the same technique of design point selection optimum points of pressure drop and Nusselt number for G1, G2, G3, and G4 were gathered. The surface contour of the design point values of friction factor and Nusselt number is generated and discussed.

The friction factor and Nusselt number for G1 and G2 at 320 K and 325 K can be seen in Figure 11. It depicts that friction factor increases slightly when the width is varied by keeping height between 35 to 100 μm; however, high friction factor is obtained by varying height, while keeping width between 35 to 100 μm. By keeping a width between 35 to 100 μm and varying height minimum, the Nusselt number value is obtained due to less area in the bottom surface; thus, convective heat transfer is less. However, maximum Nusselt number is obtained above the width and height of 150 μm due to sufficient convective heat transfer; hence, a threshold limit for width and height is found.

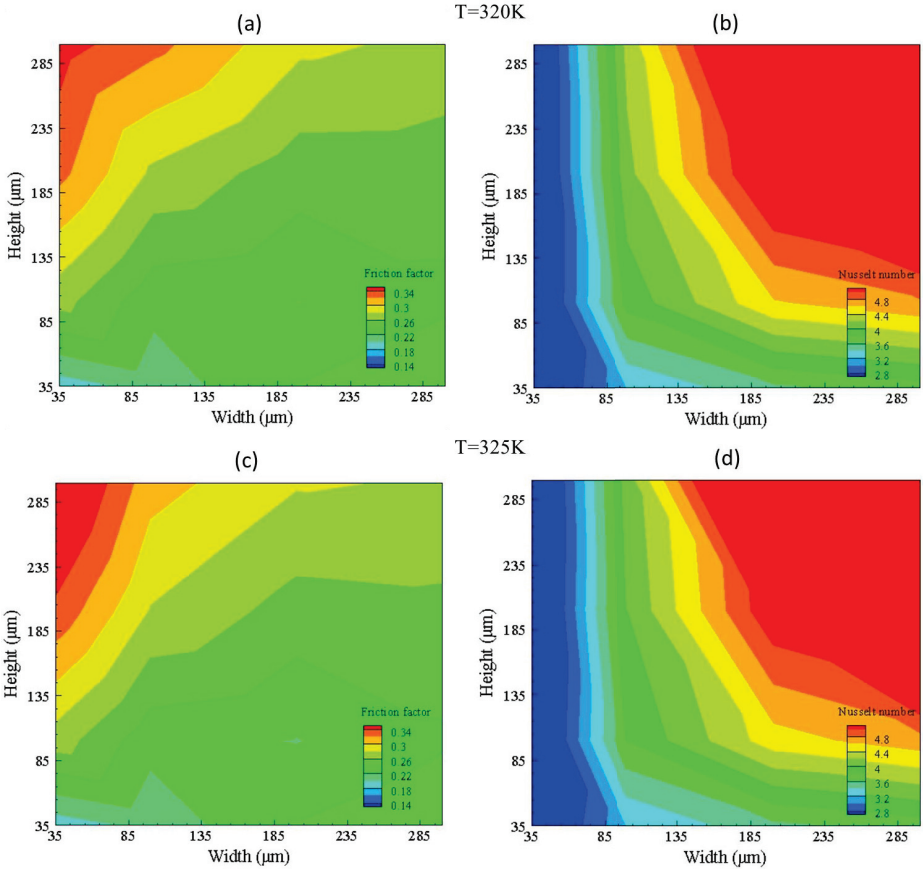

Figure 11. Friction factor (**a**,**c**) and Nusselt number (**b**,**d**) contours for group G1 (320 K) and G2 (325 K).

The high temperature analysis represented in Figure 12 shows the same behavior as that of friction factor and Nusselt number in the case of low temperatures; but, for high temperature, high maximum friction factor and low Nusselt number is seen due to the increase of friction at high temperature as the fluid excitation energy increases on heating and thus increases resistance. For the Nusselt number, at high temperature, convective heat transfer is reduced, resulting in increased conductive heath transfer hindering fluid capability of carrying heat. Nusselt number can be increased by increasing the flow rate, but this will compromise the friction factor, resulting in high pressure drop.

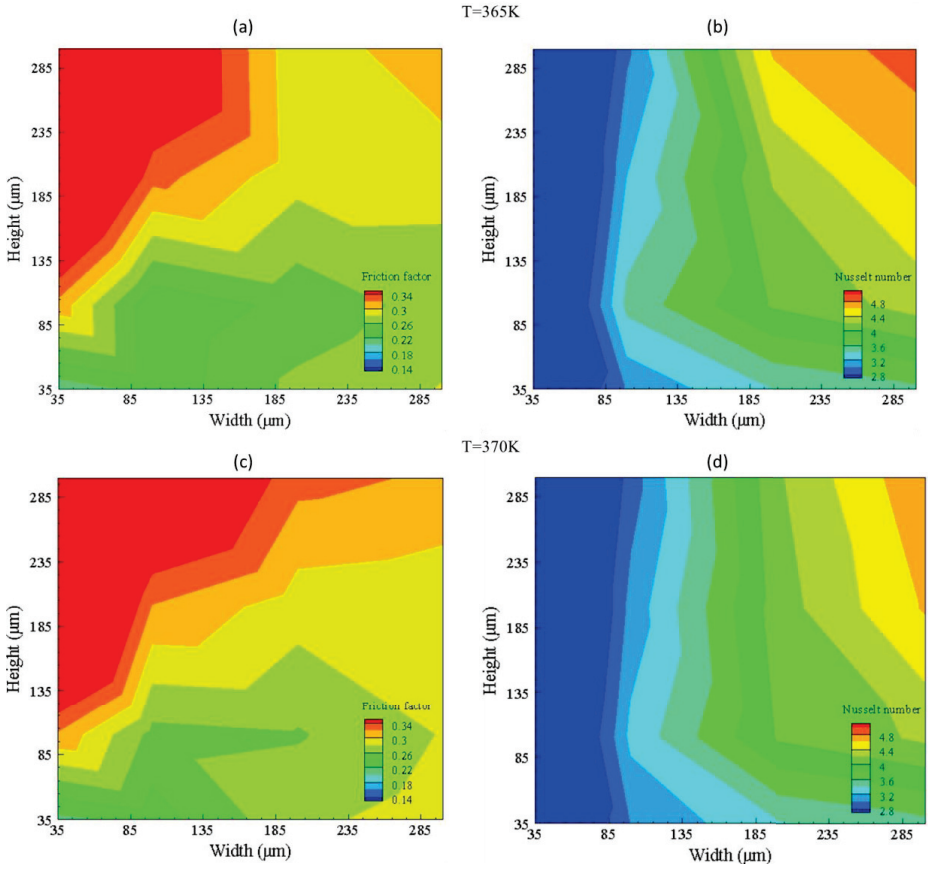

Figure 12. Friction factor (**a**,**c**) and Nusselt number (**b**,**d**) contours for group G3 (365 K) and G4 (370 K).

The pressure drops across the microchannel is an essential factor in designing the micro heat exchanger as it contributes to the selection of a pump. Figure 13 shows pressure drop contours of design points showing that, for low temperature, the width of 35 μm and variation of height results in high pressure drop, whereas, in its inverse case, pressure drop is less, which is due to increased contact area by increasing the width, reducing fluid viscosity, and resulting in less pressure drop. For high temperatures, the same effect can be seen. Visualizing pressure drop from low temperature (320 K) to high temperature (370 K) shows that pressure drop decreases due to a decrease in viscosity by an increase in temperature.

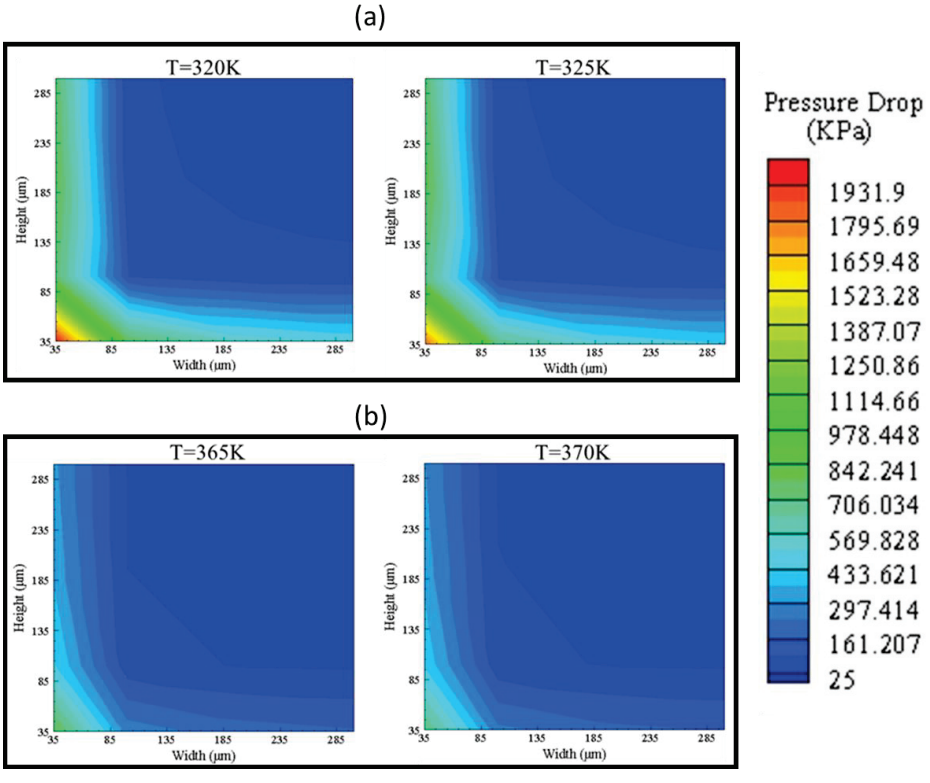

Figure 13. Pressure drop contours of (**a**) G1, G2 and (**b**) G3, G4.

Results of pressure drop and Nusselt number of all geometric ranges for both width and height from 35 to 300 µm is shown in Figure 14. For low temperature, maximum Nusselt number and minimum pressure drop can be achieved with a height of 200 µm and a width of 300 µm. Likewise, for high temperature, the same width and height show the best performance, but pressure drop and Nusselt number values of 365 K and 370 K is lower than 320 K and 325 K. The trend is shown in Figure 14 is different from typical behavior like in Figure 10 because it involves plotting of intersection design points at different width and height values. It can be observed that, as base temperature is increased, pressure drop decreases with little decrement in Nusselt number, as compared to the geometry of the same parameter. The reason for the decrement of pressure drop is due to a decrease in fluid viscosity and Nusselt number decrease due to an increase in thermal boundary layer thickness, which decreases temperature gradient.

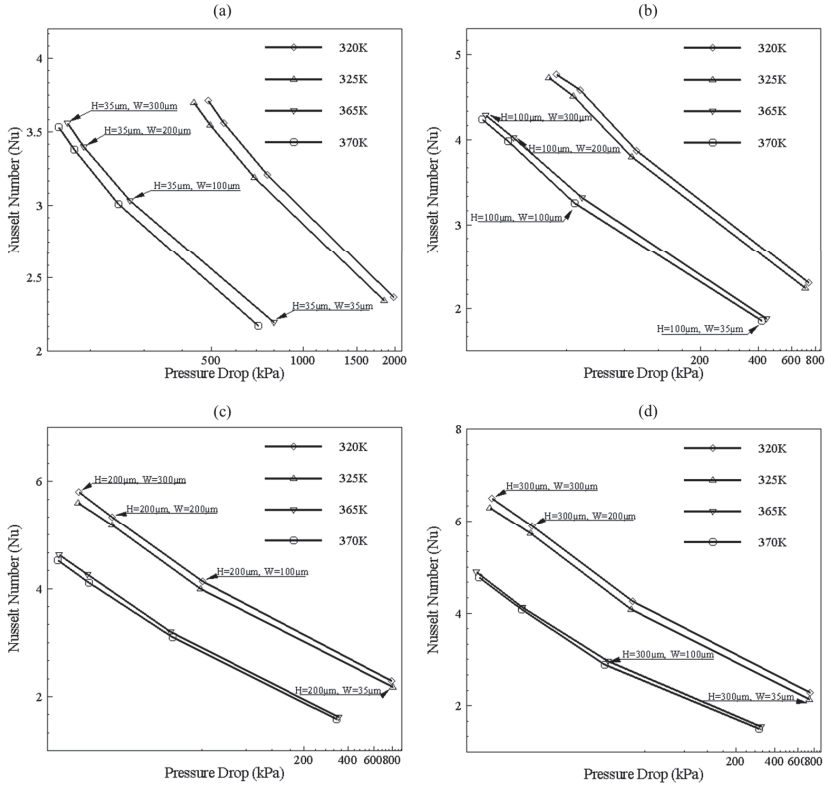

Figure 14. Channel selection based on pressure drop and Nusselt number (Nu). (**a**) Channel data with height 35 μm and width varying from 35–300 μm, from right to left in graph points, (**b**) Channel data with height 100 μm and width varying from 35–300 μm, from right to left in graph points, (**c**) Channel data with height 200 μm and width varying from 35–300 μm, from right to left in graph points, and (**d**) Channel data with height 300 μm and width varying from 35–300 μm, from right to left in graph points.

Figure 15 demonstrates cross-sectional planes of the microchannel selected by the design point method. Temperature contours of the channel with 325 K base temperature can be seen at the inlet (x = 0), before bend (x = 8 mm), after bend (x = 20 mm), and at the outlet (x = 18). It can be seen that, for Reynolds number 100 and 900, 200 × 300 μm width and height channel are unable to carry a sufficient amount of heat from inlet to outlet, whereas the other three channels are very useful. Furthermore, the purpose of a bend can be seen clearly for Reynolds number 900 wherein heat is diffusing more in the channel as fluid moves across channel bends.

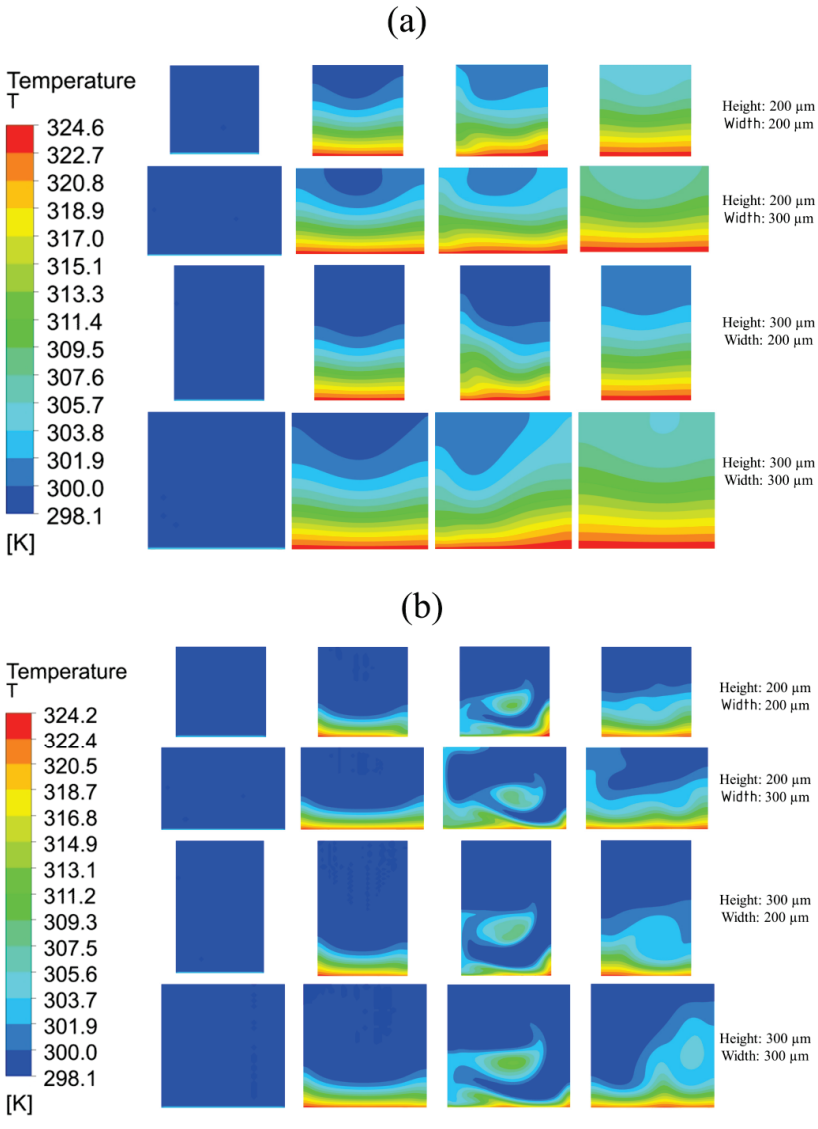

Figure 15. Temperature distribution in single microchannel at different cross-sections with 325 K base temperature: (**a**) Reynolds number = 100; (**b**) Reynolds number = 900.

Temperature contours in Figure 16 show that, for Reynolds number 100, channels with 300 × 200 μm width and height, respectively (rectangular), as well as 200 × 200 μm (square) channel, performed best in dissipating heat from inlet to outlet. However, for Reynolds number of 900, all channels other than of 200 × 300 μm width and height, respectively, showed good performance due to high base contact area.

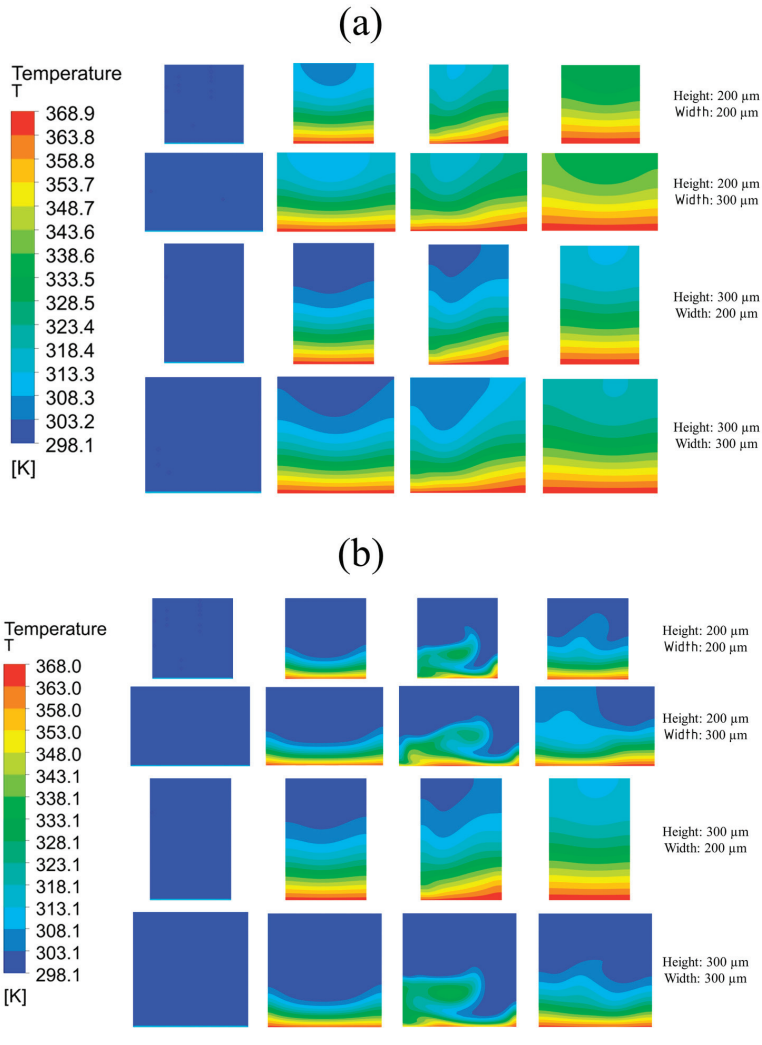

Figure 16. Temperature distribution in single microchannel at different cross-sections with 370 K base temperature: (**a**) Reynolds number = 100; (**b**) Reynolds number = 900.

Flow Behavior at the Bend

In this study, flow behavior at the bend involves the generation of secondary or dean vortices after Reynolds number value of 500. Velocity contours are shown in Figure 17 for 200 µm width, and height depicts that, at the initial edge of bend (x = 8 mm), no vortices are available, but the effect of the bend is starting to appear on outer edges, whereas at the middle of bend, counter-rotating vortices are visible because of velocity difference phenomena. Vortices help in the diffusion of heat and increase convective heat transfer at the expense of pressure drop in the channel. At the outer edge of the bend, the vortices effect becomes minimum. Non-symmetric behavior of the velocity contours is due to an increase in the kinetic energy of fluid molecule, which increases the average speed of molecules, and, as the channel is heated only from bottom side, behavior of velocity contours is developed accordingly. Figures 17–20 depict velocity behavior at a low base temperature of 325 K and at a high base temperature of 370 K, where velocity difference can be observed due to temperature dependent fluid parameters.

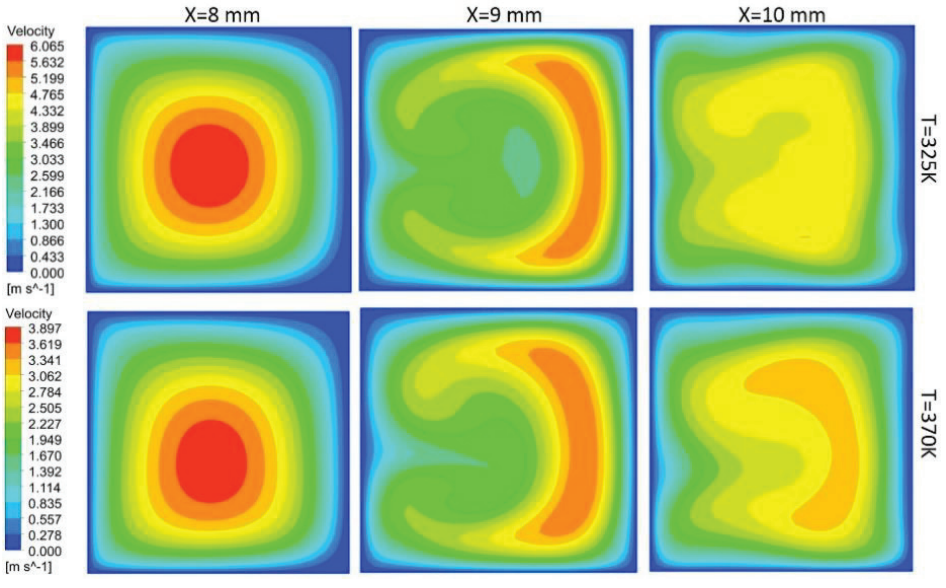

Figure 17. Dean vortices at 200 μm width and 200 μm height for Re = 600.

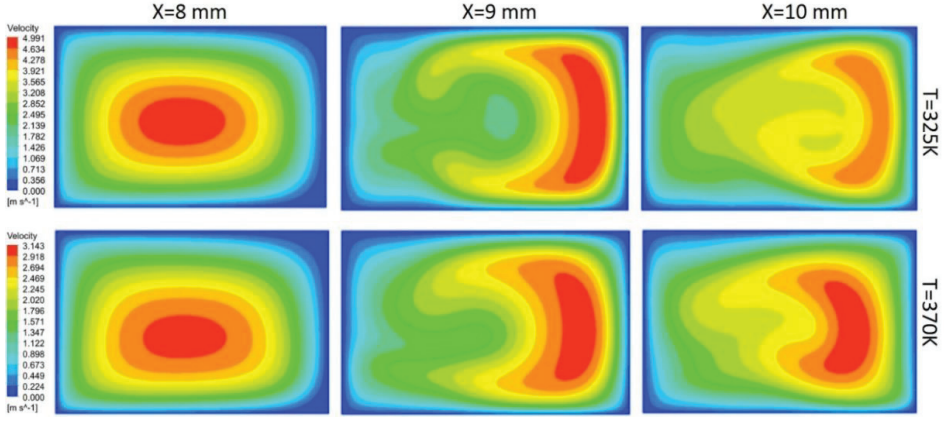

Figure 18. Dean vortices at 300 μm width and 200 μm height for Re = 600.

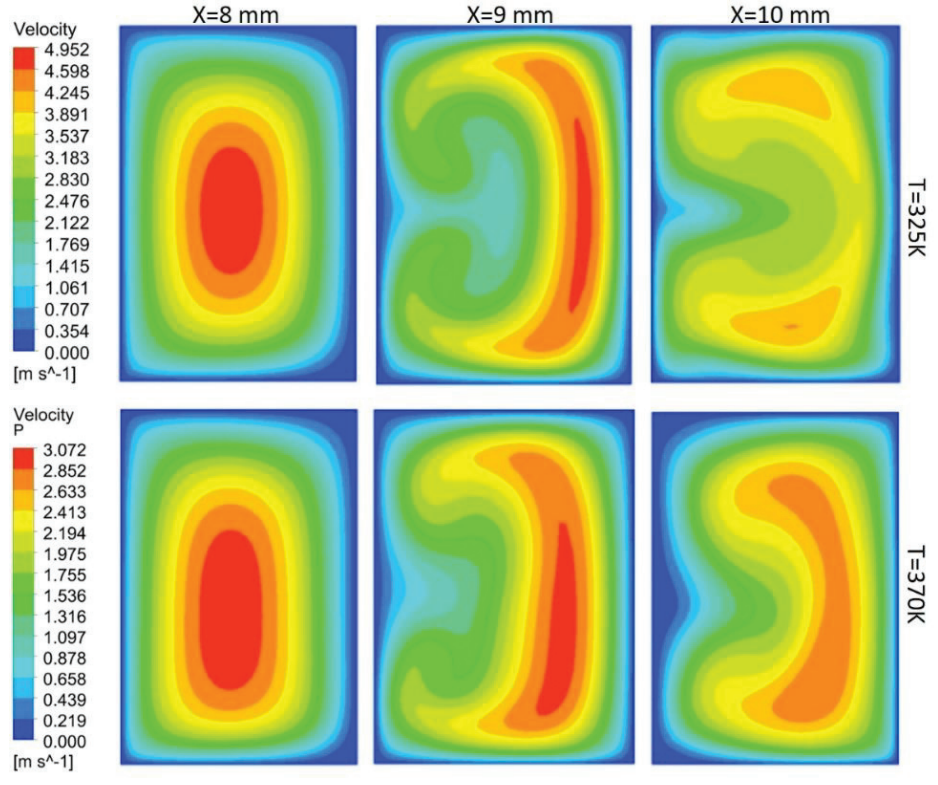

Figure 19. Dean vortices at 200 μm width and 300 μm height for Re = 600.

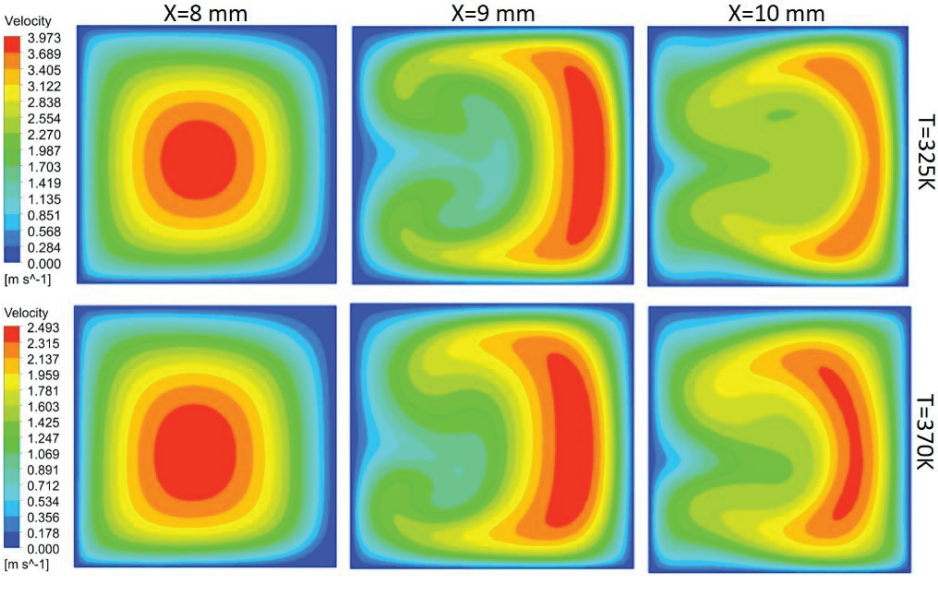

Figure 20. Dean vortices at 300 μm width and 300 μm height for Re = 600.

Figure 18 depicts the behavior of dean vortices in the channel of 300 μm width and 200 μm height. The velocity of a fluid on the outer wall is more whereas the effect of vortices at the inner wall is less due to more width of the channel than the height, making less convective heat transfer. Vortices in Figure 19 are more symmetric than others due to less contact of channel base with fluid; hence, less fluid particles kinetic energy can be observed through contours. Comparison of the channel with 300 μm width and 200 μm height (rectangular shape) with the channel of width and height 300 μm (square channel) vortices from Figures 18 and 20 shows that more heat diffusion is possible in the square channel due to more vortices' dispersion in the square channel.

Kang et al. [4] study showed that an increasing number of channels increases the performance of a micro heat exchanger. In addition, flow uniformity increases by using microchannel with a small width, long length and sizeable manifold area [26,58]. Hasan et al. [59] studied the effect of channel geometry on micro-heat exchanger performance and concluded that the square channel provided the best overall performance than a rectangular channel.

TPF was used to evaluate the overall thermos-hydraulic performance of the channel by comparing the performance of the required channel with the benchmark channel. Figure 21 depicts TPF found using Equation (24), where Nu and f represent Nusselt number and friction factor of required channel, and Nu_0 and f_0 represent that of benchmark channel. TPF of more than one represents a higher convective heat transfer than the benchmark channel. In Figure 21, B100 represents a benchmark width of 100 microns, and w200 represents a width of 200 microns for the channel in which performance is to be compared. It can be observed clearly that the transfer of channel width from 100 microns to 200 microns shows greater TPF value as compared to width change from 200 microns to 300 microns. The width of 200 microns is satisfied for a low base temperature of 320 K to a high base temperature of 370 K.

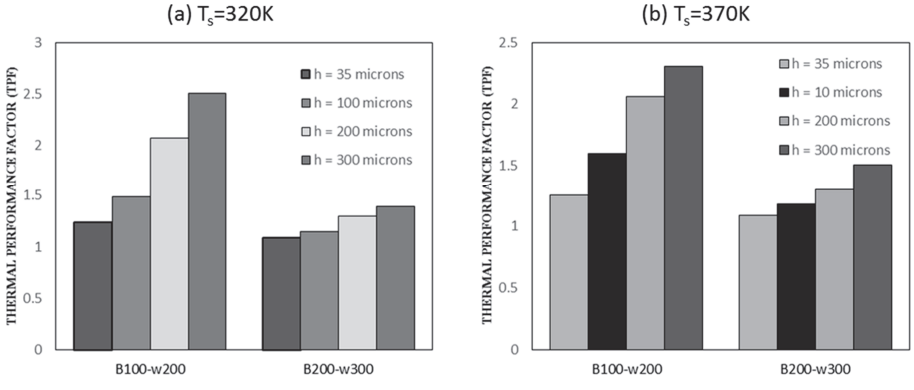

Figure 21. (**a**) TPF for single channel with 320 K base temperature. (**b**) TPF for single channel with 370 K base temperature.

Figure 22 portrays the validation of single microchannel considering different concentrations of alumina nanoparticles. The numerical methodology predicts the performance of channel with at maximum of 8% difference from reference study [30]. It can be observed that increase in concentration reduces the wall temperature, thus improving the cooling effect.

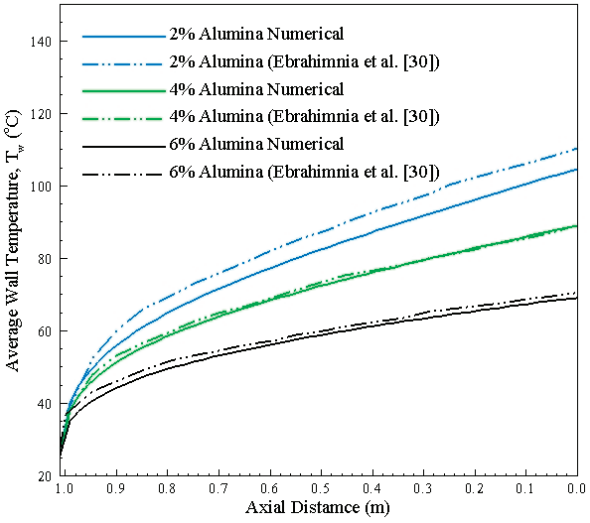

Figure 22. Average wall temperature (T_w) along the length of channel.

Figure 23 clearly depicts that, for Reynolds number value of 100, no significant difference in Nusselt number is available, whereas, for higher Reynolds number, a surge in Nusselt number in the case of the bend channel is prominent. It can be observed that the overall trend of Nusselt number remains same with increase in Reynolds number for alumina and zirconia, with and without concentration. Furthermore, zirconia showed a higher Nusselt number than alumina for 1% and 3% of nanoparticles concentration. Curve fitting correlation for Nusselt number variation with Reynolds number range from 100 to 1000 Reynolds number is represented in Table 6. The average R-squared value of these equations is 0.99.

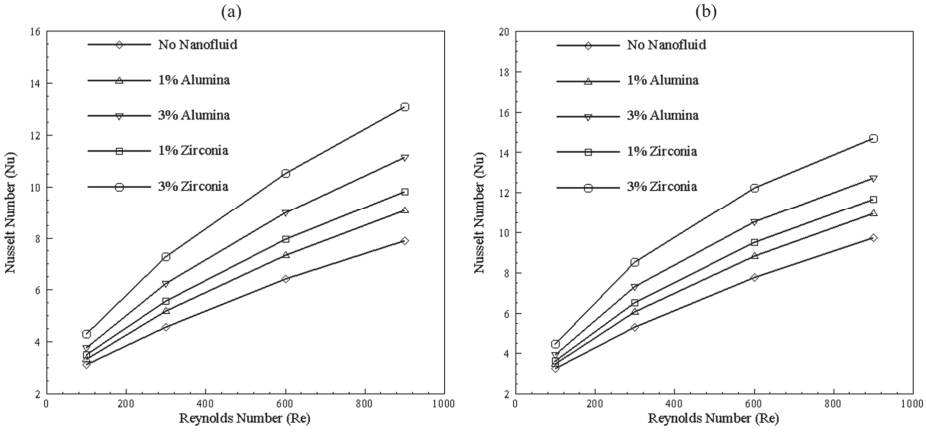

Figure 23. Effect of nanoparticles type and concentration on (**a**) straight and (**b**) bend channel.

Table 6. Correlations of Nusselt number based on curve fitting.

Channel	No Nanofluid	1% Alumina	3% Alumina	1% Zirconia	3% Zirconia
Straight	$0.4396Re^{0.42}$	$0.4058Re^{0.4533}$	$0.3891Re^{0.4911}$	$0.3973Re^{0.4686}$	$0.4186Re^{0.5042}$
Bend	$0.3177Re^{0.50}$	$0.3109Re^{0.5227}$	$0.3365Re^{0.5365}$	$0.3138Re^{0.532}$	$0.3715Re^{0.5442}$

TPF represents effectiveness of heat transfer enhancement technique. Figure 24 depicts effectiveness of bend channel by considering straight channel of same nanoparticles concentration as benchmark. It can be seen that using nanofluids enhances the heat transfer, as TPF in all cases is above 1. It can be observed that, for higher Reynolds number, friction factor dominates; thus, the slope of TPF starts decreasing at high Reynolds number. Furthermore, for 3% nanoparticles concentration, for both nanoparticles, the lowest performance is observed, depicting increasing in friction factor. However, when best performance is considered in comparison to without nanoparticles, 1% alumina concentration at Reynolds number of 300 standout. Likewise, for zirconia 1%, concentration with 600 Reynolds number proved best.

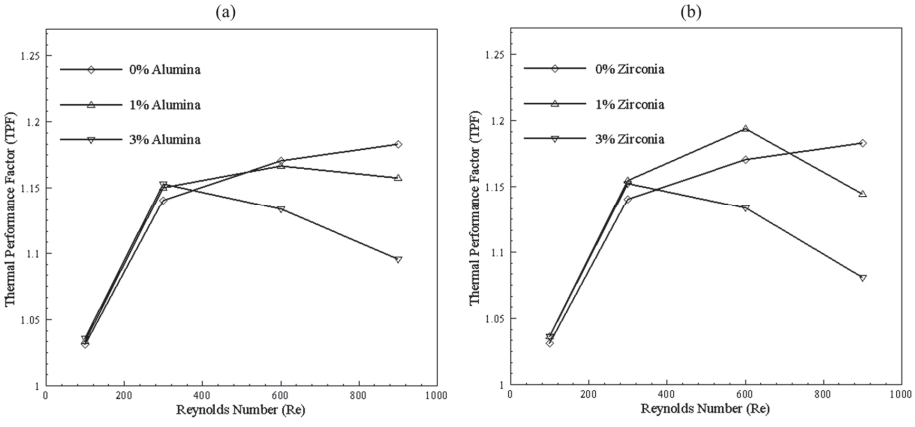

Figure 24. TPF of 200 µm width and height bend channel with (**a**) alumina concentration and (**b**) zirconia concentration with straight channel as benchmark.

3.5. Multi-Channel Configuration

3.5.1. Multi-Channel without Nanoparticles

Thus, the width of 200 microns is adjusted for multi-channel micro heat exchanger analysis. The number of channels is set to 13 for adjusting 200-micron channel in the complete multi-channel chip as depicted in Figure 2. Table 7 provides information about cases for multi-channel.

Table 7. Cases for simple and modified multi-channel design.

Group	Width (µm)	Height (µm)	Temperature (K)
1	200	100–200	320
2	200	100–200	325
3	200	100–200	365
4	200	100–200	370

Figure 25 shows the temperature distribution of two multi-channel models for Reynolds number 100 and 600. The outlet temperature of the channel with the width and height of 200 × 100 µm is higher than a channel with width and height of 200 × 200 µm for both high and low temperatures, but Nusselt number of the channel with 200 × 200 µm width and height is more significant due to more mass flow rate and bigger hydraulic diameter, as can be seen in Figure 26. Furthermore, fluid reaches near base temperature earlier in 200 × 100 µm channel. It can be seen that the temperature in

the middle of microchannel reaches the base temperature slower than side walls due to the higher velocity in the middle of the microchannel.

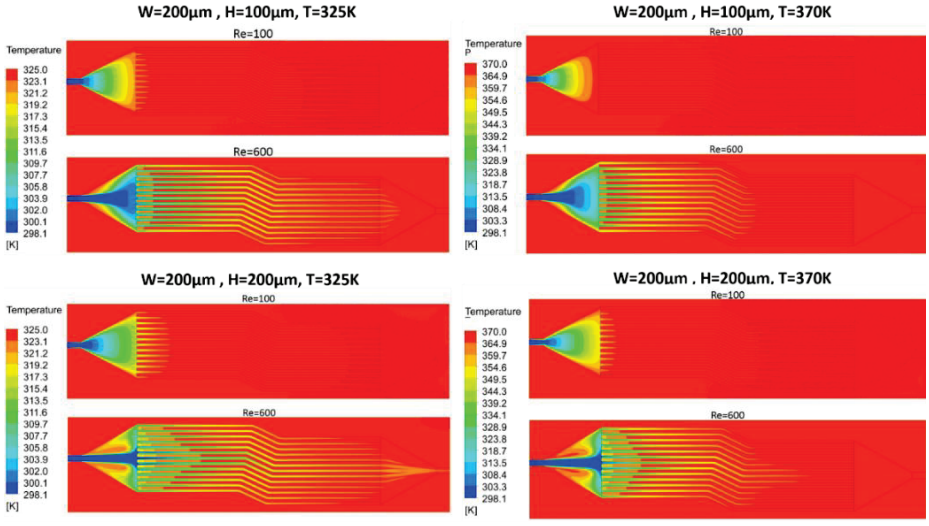

Figure 25. Temperature distribution in multi-channel for 325 K and 370 K temperature.

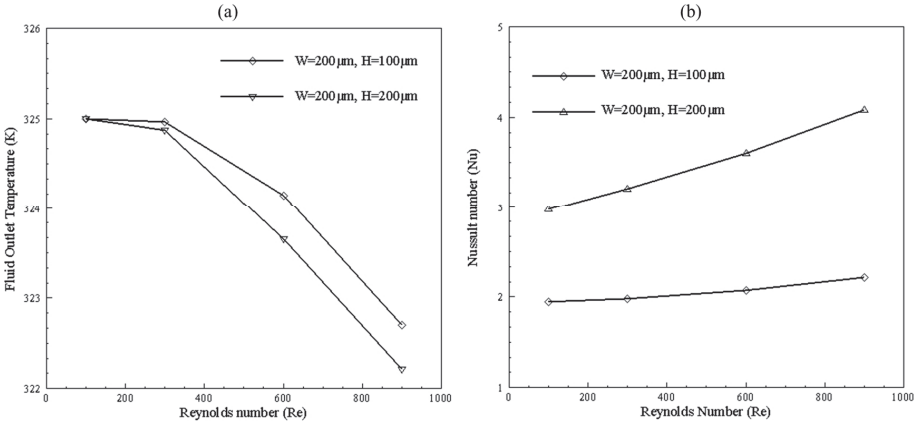

Figure 26. (**a**) Fluid outlet temperature and (**b**) Nusselt number at different Reynolds number.

Some high temperature zones can be seen after inlet for Reynolds number of 600. Low temperature area is due to the high velocity of fluid having less time to carry heat, whereas high temperature fluid contour is due to the low velocity of the fluid at expansion after entering plenum. By varying height from 100 to 200 µm, increase in Nusselt number is observed from 33% to 50%.

3.5.2. Multi-Channel with Nanoparticles

The effect of nanoparticles on Nusselt number (Nu) can be observed in Figure 27 in the form of percentage increase. The Nusselt number in case of zirconia is more than alumina showing a maximum of 20% increase in convective heat transfer at Reynolds number of 600. Furthermore, increase in concentration of particles enhanced the heat transfer. For concentration increase, a surge in performance can be observed for zirconia with concentration shift from 1% to 3%.

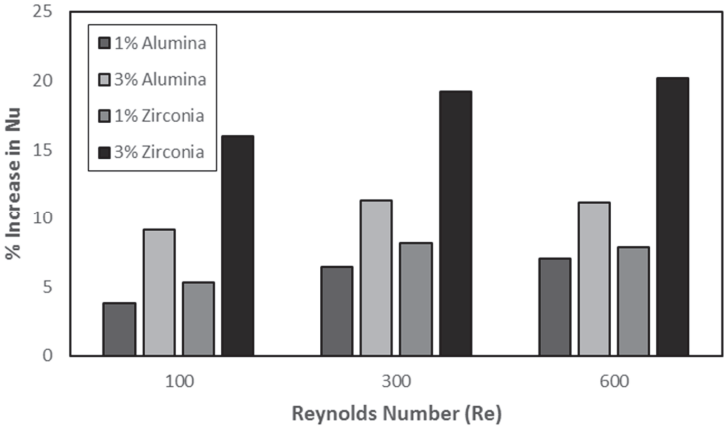

Figure 27. Percent increase in Nusselt number (Nu) by adding nanoparticles in multi-channel.

The effectiveness of multi-channel micro heat exchanger given in Figure 28 with respect to bended channel as base model depicts that zirconia with 3% particle concentration is suitable for heat transfer by exhibiting increased cooling in comparison to increased viscous losses due to nanoparticles. Moreover, with increase in Reynolds number, pressure drop in the channel with nanoparticles starts dominating, resulting in decrement of TPF slope.

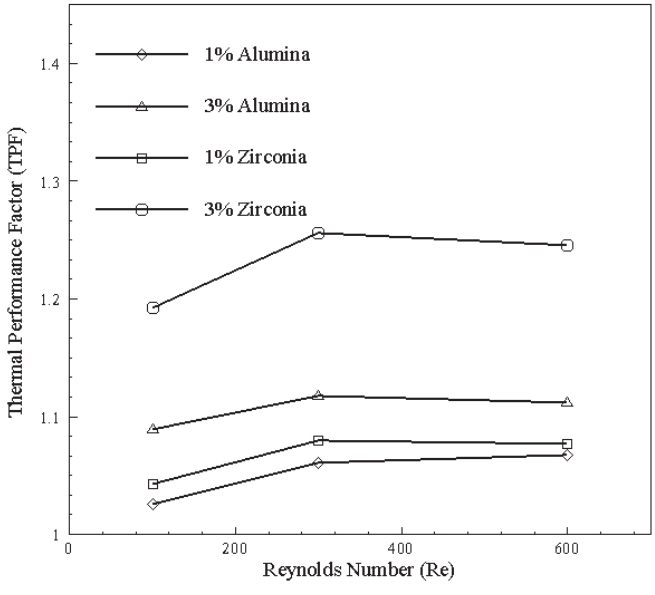

Figure 28. TPF of multi-channel micro heat exchanger with bend channel as benchmark.

Table 8 represents the Nusselt number correlations for 100 to 600 Reynolds number range with R-square value of 1.

Table 8. Correlations of Nusselt number based on curve fitting.

Nanoparticles	0%	1%	3%
Alumina	$3 \times 10^{-7}Re^2 + 0.001Re + 2.7808$	$-4 \times 10^{-7}Re^2 + 0.0018Re + 2.8255$	$-5 \times 10^{-7}Re^2 + 0.0019Re + 2.9944$
Zirconia	$3 \times 10^{-7}Re^2 + 0.001Re + 2.7808$	$-7 \times 10^{-7}Re^2 + 0.002Re + 2.8547$	$-7 \times 10^{-7}Re^2 + 0.0024Re + 3.2058$

4. Conclusions

Numerical study was performed on bended microchannels to investigate heat transfer and fluid flow physics. Single and multi-channel heat transfer performance was studied by using deionized water, as well as water-based nanofluids. The following results are concluded from our study:

1. For bended channels, the straight channel relations are reasonably valid at low Reynolds number with a 4% error in comparison to analytical results; however, at high Reynolds number, an increased error of up to a maximum to 17% can be seen due to an increase in pressure drop, non-uniformity of flow, and development of dean vortices.
2. Channels with less or equal height to that of width results in better convective heat transfer due to availability of more contact area with heated surface and increased space for asymmetric fluid to enter and leave bend. Moreover, secondary vortices phenomena are encountered due to the introduction of bend for channels of different hydraulic diameters, and it is found that the introduction of bend in channel significantly enhances the formation of dean vortices at Reynolds number greater than 500.
3. The increment in base temperature decreases the pressure drop due to a reduction in overall fluid viscosity and also decrease Nusselt number in comparison to low base temperature for the geometry of same parameter.
4. By utilizing performance parameters from the design point approach in Thermal Performance Factor (TPF) analysis, the performance of a single channel with 200 microns width is considered optimum and studied for height range from 35 to 300 microns for selection of multi-channel cross section.
5. For selected single channel, enhancement in thermal effectiveness is observed for both alumina and zirconia nanoparticles. At very low Reynolds number of around 100, nanofluids concentration showed no significant improvements. However, at very high Reynolds number, the TPF starts decreasing, representing dominance of pressure drop over convective heat transfer. Therefore, both alumina and zirconia with 1% and 3% concentration showed highest effectiveness at Re = 300. Maximum TPF value of 1.18 is achieved by zirconia with 1% concentration at Re = 600. It is seen that, by increasing nanoparticles concentration, pressure drop starts dominating at high Reynolds number.
6. For multi-channel with water as fluid, channel width is fixed at 200 μm and height is varied from 100 μm to 200 μm. Channel with 200 μm width and height showed a 33% to 50% increase in heat transfer for Reynolds number within a range of 100 to 900.
7. The introduction of nanofluids in 200 μm width and height multi-channel model showed enhancement in Nusselt number with an increase in Reynolds number from 100 to 600. The highest increment of 20% is observed in the case of zirconia, with 3% concentration at Re = 600. For 1% and 3% concentration of nanoparticles, zirconia outperformed alumina. Analysis of TPF showed that, after Re = 300, the slope of curve starts flattening in the case of 1% alumina and starts decreasing in the case of 1% and 3% zirconia and alumina 3% concentration, depicting increase in pressure loss with high concentration and Reynolds number due to increased viscosity.

Author Contributions: Conceptualization, E.U., Z.A., and M.S.; methodology, B.A., M.Y.Y., and Z.A.; software, B.A. and N.A.; validation, M.Y.Y., M.S., F.P.G.M., and B.A.; formal analysis, M.Z.U.K., A.A.N., and N.A.; investigation M.Z.U.K., A.A.N., and E.U.; writing—original draft preparation, M.Z.U.K., M.S., and Z.A.; writing—review and editing, B.A., M.Y.Y., F.P.G.M., and N.A.; supervision, E.U., Z.A., F.P.G.M., and M.S. All authors have read and agreed to the published version of the manuscript.

Funding: The work reported herewith has been financially by the Universidad de Castilla-La Mancha, Plan Propio de Investigación, cofinanciadas por el Fondo Europeo de Desarrollo Regional (FEDER) (Ref. 01110G0137).

Conflicts of Interest: The authors declare no conflict of interest.

Abbreviations

l_1	Microchannel length (mm)
l_2	Plenum Length (mm)
l_3	Bend length (mm)
l_4	Inlet/Outlet length (mm)
w_1	Inlet/Outlet width (mm)
w	Width of microchannel (mm)
w_s	Space between microchannels (mm)
L	Multi-Microchannel model length (mm)
L_c	Microchannel model length (mm)
W	Microchannel model width (mm)
α_{ch}	Aspect ratio of microchannel
θ	Angle of plenum (mm)
Re	Reynolds Number
Nu	Nusselt Number
Nu_o	Benchmark Nusselt Number
f	Friction Factor
f_o	Benchmark Friction Factor
D_H	Hydraulic Diameter (mm)
A_{ht}	Base area of microchannel (mm^2)
Q	Total heat rate (J/s)
$\dot{m}$	Mass flow rate (kg/s)
$\dot{V}$	Volume flow rate (m^3/s)
h	Height of microchannel (mm)
v_{in}	Inlet velocity (m/s)
P_{power}	Pump power (W)
C_p	Specific heat (J/kg.k)
ρ	Fluid density (kg/m^3)
μ	Fluid Viscosity (Pa.s)
k	Thermal Conductivity (W/m.k)
T	Temperature (K)
T_W	Wall Temperature (K)
ΔT	Temperature Difference (K)
ΔP	Pressure Difference (Pa)
TPF	Thermal Performance Factor
Subscript	
f	Fluid (Water)
nf	Nanofluid
np	Nanoparticle
i	Inlet
o	Outlet
m	Mean
s	Source
so	Solid

References

1. Tuckerman, D.B.; Pease, R.F.W. High-performance heat sinking for VLSI. *IEEE Electron Dev. Lett.* **1981**, *2*, 126–129. [CrossRef]
2. Peterson, G.; Ortega, A. *Thermal Control of Electronic Equipment and Devices, in Advances in Heat Transfer*; James, T.F.I.J., Hartnett, P., Eds.; Elsevier: Amsterdam, The Netherlands, 1990; pp. 181–314.
3. Tuckerman, D.B. *Heat-Transfer Microstructures for Integrated Circuits*; Lawrence Livermore National Lab: Livermore, CA, USA, 1984.
4. Kang, M.K.; Shin, J.H.; Lee, H.H. Analysis of laminar convective heat transfer in micro heat exchanger for stacked multi-chip module. *Microsyst. Technol.* **2005**, *11*, 1176–1186. [CrossRef]
5. Sahar, A.M.; Özdemir, M.R.; Fayyadh, E.M.; Wissink, J.; Mahmoud, M.M.; Karayiannis, T.G. Single phase flow pressure drop and heat transfer in rectangular metallic microchannels. *Appl. Therm. Eng.* **2016**, *93*, 1324–1336. [CrossRef]
6. Lee, P.-S.; Garimella, S.V.; Liu, D. Investigation of heat transfer in rectangular microchannels. *Int. J. Heat Mass Transf.* **2005**, *48*, 1688–1704. [CrossRef]
7. Liu, J.-T.; Peng, X.-F.; Yan, W.-M. Numerical study of fluid flow and heat transfer in microchannel cooling passages. *Int. J. Heat Mass Transf.* **2007**, *50*, 1855–1864. [CrossRef]
8. Rosa, P.; Karayiannis, T.; Collins, M. Single-phase heat transfer in microchannels: The importance of scaling effects. *Appl. Therm. Eng.* **2009**, *29*, 3447–3468. [CrossRef]
9. Hrnjak, P.; Tu, X. Single phase pressure drop in microchannels. *Int. J. Heat Fluid Flow* **2007**, *28*, 2–14. [CrossRef]
10. Harms, T.M.; Kazmierczak, M.J.; Gerner, F.M. Developing convective heat transfer in deep rectangular microchannels. *Int. J. Heat Fluid Flow* **1999**, *20*, 149–157. [CrossRef]
11. Gonzalo, A.P.; Marugán, A.P.; Márquez, F.P.G. A review of the application performances of concentrated solar power systems. *Appl. Energy* **2019**, *255*, 113893. [CrossRef]
12. Bier, W.; Keller, W.; Linder, G.; Seidel, D.; Schubert, K.; Martin, H. Gas to gas heat transfer in micro heat exchangers. *Chem. Eng. Proc. Process Intensif.* **1993**, *32*, 33–43. [CrossRef]
13. Stief, T.; Langer, O.U.; Schubert, K. Numerical investigations of optimal heat conductivity in micro heat exchangers. *Chem. Eng. Technol. Ind. Chem. Plant Equip. Process Eng. Biotechnol.* **1999**, *22*, 297–303. [CrossRef]
14. Liu, D.; Garimella, S.V. Investigation of liquid flow in microchannels. *J. Thermophys. Heat Transf.* **2004**, *18*, 65–72. [CrossRef]
15. Xu, J.; Song, Y.; Zhang, W.; Zhang, H.; Gan, Y. Numerical simulations of interrupted and conventional microchannel heat sinks. *Int. J. Heat Mass Transf.* **2008**, *51*, 5906–5917. [CrossRef]
16. Hetsroni, G.; Mosyak, A.; Pogrebnyak, E.; Yarin, L.P. Heat transfer in micro-channels: Comparison of experiments with theory and numerical results. *Int. J. Heat Mass Transf.* **2005**, *48*, 5580–5601. [CrossRef]
17. Phillips, W.A. Experimental and Numerical Investigation of Fluid Flow and Heat Transfer in Microchannels. Master's Thesis, Louisiana State University, Baton Rouge, LA, USA, 2008.
18. Mohammed, H.; Gunnasegaran, P.; Shuaib, N. Numerical simulation of heat transfer enhancement in wavy microchannel heat sink. *Int. Commun. Heat Mass Transf.* **2011**, *38*, 63–68. [CrossRef]
19. Lasbet, Y.; Auvity, B.; Castelain, C.; Peerhossaini, H. A chaotic heat-exchanger for PEMFC cooling applications. *J. Power Sour.* **2006**, *156*, 114–118. [CrossRef]
20. Rosaguti, N.R.; Fletcher, D.F.; Haynes, B.S. Low-Reynolds number heat transfer enhancement in sinusoidal channels. *Chem. Eng. Sci.* **2007**, *62*, 694–702. [CrossRef]
21. Soudagar, M.E.M.; Soudagar, M.E.M.; Kalam, M.A.; Sajid, M.U.; Afzal, A.; Banapurmath, N.R.; Akram, N.; Mane, S.D. Thermal analyses of minichannels and use of mathematical and numerical models. *Num. Heat Transf. Part A Appl.* **2020**, *77*, 497–537. [CrossRef]
22. Sui, Y.; Lee, P.; Teo, C. An experimental study of flow friction and heat transfer in wavy microchannels with rectangular cross section. *Int. J. Therm. Sci.* **2011**, *50*, 2473–2482. [CrossRef]
23. Wang, L. Buoyancy-force-driven transitions in flow structures and their effects on heat transfer in a rotating curved channel. *Int. J. Heat Mass Transf.* **1997**, *40*, 223–235. [CrossRef]
24. Lee, H.; Jeong, Y.; Shin, J.; Baek, J.; Kang, M.; Chun, K. Package embedded heat exchanger for stacked multi-chip module. *Sens. Actuator A Phys.* **2004**, *114*, 204–211. [CrossRef]

25. Sehgal, S.; Murugesan, K.; Mohapatra, S. Effect of channel and plenum aspect ratios on the performance of microchannel heat sink under different flow arrangements. *J. Mech. Sci. Technol.* **2012**, *26*, 2985–2994. [CrossRef]
26. Balaji, S.; Lakshminarayanan, S. Improved design of microchannel plate geometry for uniform flow distribution. *Can. J. Chem. Eng.* **2006**, *84*, 715–721. [CrossRef]
27. Gulzar, M. *Tribological Study of Nanoparticles Enriched Bio-based Lubricants for Piston Ring–Cylinder Interaction*; Springer: Berlin/Heidelberg, Germany, 2018.
28. Ahmed, W.; Chowdhury, Z.Z.; Kazi, S.N.; Johan, M.R.; Akram, N.; Oon, C.S. Effect of ZnO-water based nanofluids from sonochemical synthesis method on heat transfer in a circular flow passage. *Int. Commun. Heat Mass Transf.* **2020**, *114*, 104591. [CrossRef]
29. Rahman, M.; Billah, M.M.; Rahman, A.T.M.M.; Kalam, M.A.; Ahsan, A. Numerical investigation of heat transfer enhancement of nanofluids in an inclined lid-driven triangular enclosure. *Int. Commun. Heat Mass Transf.* **2011**, *38*, 1360–1367. [CrossRef]
30. Ebrahimnia Bajestan, E.; Niazmand, H.; Renksizbulut, M. Flow and heat transfer of nanofluids with temperature dependent properties. In Proceedings of the International Conference on Nanochannels, Microchannels, and Minichannels, Montreal, QC, Canada, 1–5 August 2010.
31. Ebrahimi, A.; Rikhtegar, F.; Sabaghan, A.; Roohi, E. Heat transfer and entropy generation in a microchannel with longitudinal vortex generators using nanofluids. *Energy* **2016**, *101*, 190–201. [CrossRef]
32. Akram, N.; Sadri, R.; Kazi, S.N.; Zubir, M.N.M.; Ridha, M.; Ahmed, W.; Soudagar, M.E.M.; Arzpeyma, M. A comprehensive review on nanofluid operated solar flat plate collectors. *J. Therm. Anal. Calorim.* **2019**, *139*, 1–35. [CrossRef]
33. Karvelas, E.; Karakasidis, T.; Sarris, I. Computational analysis of paramagnetic spherical Fe_3O_4 nanoparticles under permanent magnetic fields. *Comput. Mater. Sci.* **2018**, *154*, 464–471. [CrossRef]
34. Mathieu, J.-B.; Martel, S. Aggregation of magnetic microparticles in the context of targeted therapies actuated by a magnetic resonance imaging system. *J. Appl. Phys.* **2009**, *106*, 044904. [CrossRef]
35. Vartholomeos, P.; Mavroidis, C. In silico studies of magnetic microparticle aggregations in fluid environments for MRI-guided drug delivery. *IEEE Trans. Biomed. Eng.* **2012**, *59*, 3028–3038. [CrossRef]
36. Karvelas, E.; Lampropoulos, N.; Sarris, I.E. A numerical model for aggregations formation and magnetic driving of spherical particles based on OpenFOAM®. *Comput. Methods Prog. Biomed.* **2017**, *142*, 21–30. [CrossRef] [PubMed]
37. Akbarinia, A.; Laur, R. Investigating the diameter of solid particles effects on a laminar nanofluid flow in a curved tube using a two phase approach. *Int. J. Heat Fluid Flow* **2009**, *30*, 706–714. [CrossRef]
38. Fard, M.H.; Esfahany, M.N.; Talaie, M. Numerical study of convective heat transfer of nanofluids in a circular tube two-phase model versus single-phase model. *Int. Commun. Heat Mass Transf.* **2010**, *37*, 91–97. [CrossRef]
39. Williams, W.; Buongiorno, J.; Hu, L.-W. Experimental investigation of turbulent convective heat transfer and pressure loss of alumina/water and zirconia/water nanoparticle colloids (nanofluids) in horizontal tubes. *J. Heat Transf.* **2008**, *130*, 042412. [CrossRef]
40. Rea, U.; McKrell, T.; Hu, L.; Buongiorno, J. Laminar convective heat transfer and viscous pressure loss of alumina–water and zirconia–water nanofluids. *Int. J. Heat Mass Transf.* **2009**, *52*, 2042–2048. [CrossRef]
41. He, Y.; Men, Y.; Liu, X.; Lu, H.; Chen, H.; Ding, Y. Study on forced convective heat transfer of non-Newtonian nanofluids. *J. Therm. Sci.* **2009**, *18*, 20–26. [CrossRef]
42. Akram, N.; Sadri, R.; Kazi, S.N.; Ahmed, S.M.; Zubir, M.N.M.; Ridha, M.; Soudagar, M.; Ahmed, W.; Arzpeyma, W.; Tong, G.B. An experimental investigation on the performance of a flat-plate solar collector using eco-friendly treated graphene nanoplatelets–water nanofluids. *J. Therm. Anal. Calorim.* **2019**, *138*, 609–621. [CrossRef]
43. He, Y.; Men, Y.; Zhao, Y.; Lu, H.; Ding, Y. Numerical investigation into the convective heat transfer of TiO_2 nanofluids flowing through a straight tube under the laminar flow conditions. *Appl. Therm. Eng.* **2009**, *29*, 1965–1972. [CrossRef]
44. Ahmed, W.; Kazi, S.N.; Chowdhury, Z.Z.; Johan, M.R.B.; Akram, N.; Mujtaba, M.A.; Gul, M.; Oon, C.S. Experimental investigation of convective heat transfer growth on ZnO@ TiO_2/DW binary composites/hybrid nanofluids in a circular heat exchanger. *J. Therm. Anal. Calorim.* **2020**, *75*, 1–20.

45. Prasher, R.S.; Dirner, J.; Chang, J.-Y.; Myers, A.; Chau, D.; He, D.; Prstic, S. Nusselt number and friction factor of staggered arrays of low aspect ratio micropin-fins under cross flow for water as fluid. *J. Heat Transf.* **2007**, *129*, 141–153. [CrossRef]
46. Prasher, R.S.; Dirner, J.; Chang, J.-Y.; Myers, A.; Chau, D.; He, D.; Prstic, S. Nusselt number and friction factor of staggered arrays of low aspect ratio micropin-fins under cross flow for water as fluid. In Proceedings of the ASME International Mechanical Engineering Congress and Exposition, Chicago, IL, USA, 5–10 November 2006.
47. Mohammadian, S.K.; Reza Seyf, H.; Zhang, Y. Performance augmentation and optimization of aluminum oxide-water nanofluid flow in a two-fluid microchannel heat exchanger. *J. Heat Transf.* **2014**, *136*, 021701. [CrossRef]
48. Seyf, H.R.; Keshavarz Mohammadian, S. Thermal and hydraulic performance of counterflow microchannel heat exchangers with and without nanofluids. *J. Heat Transf.* **2011**, *133*, 081801. [CrossRef]
49. Chai, L.; Xia, G.; Wang, L.; Zhou, M.; Cui, Z. Heat transfer enhancement in microchannel heat sinks with periodic expansion–constriction cross-sections. *Int. J. Heat Mass Transf.* **2013**, *62*, 741–751. [CrossRef]
50. Okhotin, A.; Pushkarskii, A.; Gorbachev, V. *Thermophysical Properties of Semiconductors*; Atom Publ. House: Moscow, Russia, 1972.
51. Peiyi, W.; Little, W. Measurement of friction factors for the flow of gases in very fine channels used for microminiature Joule-Thomson refrigerators. *Cryogenics* **1983**, *23*, 273–277. [CrossRef]
52. Nath, P.; Chopra, K. Thermal conductivity of copper films. *Thin Solid Films* **1974**, *20*, 53–62. [CrossRef]
53. Hansel, C. *Mapping of Pressure Losses Through Microchannels With Sweeping-Bends of Various Angle and Radii*; University of Central Florida Orlando: Orlando, FL, USA, 2008.
54. Upadhye, H.R.; Kandlikar, S.G. Optimization of microchannel geometry for direct chip cooling using single phase heat transfer. In Proceedings of the International Conference on Nanochannels, Microchannels, and Minichannels, Rochester, NY, USA, 17–19 June 2004.
55. Kandlikar, S.; Garimella, S.; Li, D.; Colin, S.; King, M.R. *Heat Transfer and Fluid Flow in Minichannels and Microchannels*, 1st ed.; Elsevier: Oxford, UK, 2015; pp. 87–92.
56. Shah, R.K.; London, A.L. *Laminar Flow Forced Convection in Ducts: A Source Book for Compact Heat Exchanger Analytical Data*, 1st ed.; Differential Equations and Boundary Conditions; Academic Press: Cambridge, MA, USA, 2014; pp. 74–94.
57. Chen, C.; Teng, J.-T.; Cheng, C.-H.; Jin, S.; Huang, S.; Liu, C.; Lee, M.-T.; Pan, H.; Greif, R. A study on fluid flow and heat transfer in rectangular microchannels with various longitudinal vortex generators. *Int. J. Heat Mass Transf.* **2014**, *69*, 203–214. [CrossRef]
58. Pan, M.; Shao, X.; Liang, L. Analysis of velocity uniformity in a single microchannel plate with rectangular manifolds at different entrance velocities. *Chem. Eng. Technol.* **2013**, *36*, 1067–1074. [CrossRef]
59. Hasan, M.I.; Rageb, A.A.; Yaghoubi, M.; Homayoni, H. Influence of channel geometry on the performance of a counter flow microchannel heat exchanger. *Int. J. Therm. Sci.* **2009**, *48*, 1607–1618. [CrossRef]

nanomaterials

MDPI

Article

Role of Rotating Cylinder toward Mixed Convection inside a Wavy Heated Cavity via Two-Phase Nanofluid Concept

Ammar I. Alsabery [1,2], Mohammad Ghalambaz [3,4], Taher Armaghani [5], Ali Chamkha [6,7,*], Ishak Hashim [2] and Mohsen Saffari Pour [8,9]

1 Refrigeration & Air-conditioning Technical Engineering Department, College of Technical Engineering, The Islamic University, Najaf 54001, Iraq; alsabery_a@ukm.edu.my
2 Department of Mathematical Sciences, Faculty of Science & Technology, Universiti Kebangsaan Malaysia, UKM Bangi 43600, Selangor, Malaysia; ishak_h@ukm.edu.my
3 Metamaterials for Mechanical, Biomechanical and Multiphysical Applications Research Group, Ton Duc Thang University, Ho Chi Minh City 758307, Vietnam; mohammad.ghalambaz@tdtu.edu.vn
4 Faculty of Applied Sciences, Ton Duc Thang University, Ho Chi Minh City 758307, Vietnam
5 Department of Engineering, Mahdishahr Branch, Islamic Azad University, Mahdishahr 75915-35618, Iran; armaghani.taher@yahoo.com
6 Institute of Research and Development, Duy Tan University, Da Nang 550000, Vietnam
7 Institute of Theoretical and Applied Research (ITAR), Duy Tan University, Hanoi 100000, Vietnam
8 Department of Mechanical Engineering, Shahid Bahonar University of Kerman, Kerman 76169-14111, Iran; mohsensp@kth.se
9 Division of Processes, KTH Royal Institute of Technology, 11428 Stockholm, Sweden
* Correspondence: alichamkha@duytan.edu.vn

Received: 14 April 2020; Accepted: 31 May 2020; Published: 9 June 2020

Abstract: The mixed convection two-phase flow and heat transfer of nanofluids were addressed within a wavy wall enclosure containing a solid rotating cylinder. The annulus area between the cylinder and the enclosure was filled with water-alumina nanofluid. Buongiorno's model was applied to assess the local distribution of nanoparticles in the host fluid. The governing equations for the mass conservation of nanofluid, nanoparticles, and energy conservation in the nanofluid and the rotating cylinder were carried out and converted to a non-dimensional pattern. The finite element technique was utilized for solving the equations numerically. The influence of the undulations, Richardson number, the volume fraction of nanoparticles, rotation direction, and the size of the rotating cylinder were examined on the streamlines, heat transfer rate, and the distribution of nanoparticles. The Brownian motion and thermophoresis forces induced a notable distribution of nanoparticles in the enclosure. The best heat transfer rate was observed for 3% volume fraction of alumina nanoparticles. The optimum number of undulations for the best heat transfer rate depends on the rotation direction of the cylinder. In the case of counterclockwise rotation of the cylinder, a single undulation leads to the best heat transfer rate for nanoparticles volume fraction about 3%. The increase of undulations number traps more nanoparticles near the wavy surface.

Keywords: mixed convection; thermophoresis and Brownian motion; wavy cavity; two-phase nanofluid concept; wavy heater; rotating circular cylinder

1. Introduction

Natural convection and heat transfer mechanisms in the annulus spaces have been the topic of many pioneer investigations due to its essential engineering applications. Such tools into enclosed spaces give strong non-linear behavior due to the effective coupling between the flow and heat

equation. Shu et al. [1] modeled the free convection heat transfer within a square outer cylinder and a circular central cylinder. The authors assumed an isothermal hot temperature at the cylinder and cold isothermal temperature at the enclosure boundaries. Shu et al. [1] probed the influence of the location of a cylinder toward the measure of the heat transfer and fluid circulation. They found that the top portion within the enclosure boundaries and cylinder has a significant use in the formation of the natural convection plume. In another study, Shu and Zhu [2] investigated the outcome of the aspect ratio (the ratio of cavity size/cylinder diameter) at the natural convection heat transfer, and they reported that both Rayleigh number and aspect ratio are critical to the flow patterns and thermal fields. The natural convection heat transfer in the annulus space among a cylinder and a square was also investigated by Ding et al. [3], Angeli et al. [4], and Alsabery et al. [5].

The present study involves the conjugate heat transfer, rotating cylinder, wavy wall enclosures and nanofluids. Hence, the literature works related to these topics are explored here. The natural convection heat transfer in enclosures containing solid thermal conductive blocks has been studied in some recent studies. The presence of a solid block contributes to the heat transfer inside the enclosure while it affects the fluid circulation. This type of problems is classified as conjugate heat transfer as the liquid and solid are in thermal interaction. Kuznetsov and Sheremet [6] modeled the free convection within an air-filled enclosure containing a solid block. The block enclosed a heat source. Jami et al. [7] examined the heat transfer in a cavity filled including solid cylinder at various locations. These authors reported that the area of the cylinder is the critical parameter testing the flow circulation and heat transfer.

Sheremet [8] examined the mechanism of heat transfer into a cylindrical cavity holding a solid heated block toward the bottom portion. The results show that a cylindrical cavity can be of essential advantages for the cooling of electronic components. Butler et al. [9] experimentally inspected the conjugate natural convection mechanism and heat transfer over a cylinder enclosed inside an air-filled cubic enclosure. The left and right vertical sidewalls of the cavity were at temperature difference while the other walls were insulated. The observations indicate that the presence of the cylinder could interfere with the structure of natural convection flow circulation in the enclosure. Various aspect of conjugate heat transfer toward a cavity such as radiation [10], mixed convection [11], and turbulent effects [12] have been addressed during past years.

The presence of a moving or rotating object changes the natural convection flow to the mixed convection. The moving objects have found numerous applications in engineering designs. For instance, a shaft of turbine or pump enclosed in a shell, rotation of gears in a casing, vibration of a thermal fin in an enclosed space, and fluid bearings with a slow rotation, and the receiver of a solar collector are just a few examples. Costa and Raimundo [13] displayed the combined convection and heat transfer mechanisms within a square hollow holding a rotating solid cylinder. The vertical surfaces of the cavity occurred with cold and hot temperatures, and the top and bottom surfaces remained insulated. The cylinder was rotating at a certain angular velocity and contributed into the flow circulation and heat transfer. The results show that the cylinder's size induces a notable impact on the fluid circulation and transfer since it confines the liquid area for fluid flow inside the cavity. However, the angular velocity of the cylinder is another important parameter. The cylinder rotation could improve the rate of the heat transfer at the enclosure aspect ratio (the cylinder radius to the cavity size) is large. However, in the case of small aspect ratio (small cylinder), the rotation of the cylinder could deteriorate the overall heat transfer inside the cavity. Wang et al. [14] studied the mixed convection technique and entropy generation of a rotating hollow cylinder within a square hollow. They found that the increase in rotation velocity boosts the total entropy generation. Many aspects of mixed convection and heat transfer mechanisms within the geometry of a rotating cylinder in a square cavity have been addressed. For example, the appearance of a porous medium layer [15], the location of rotating cylinder [16], rotation speed [17,18], and two rotating cylinders [19] have been explored in the literature.

Enclosures with wavy (curved) walls have numerous practical applications in solar systems, heat exchangers, and reactors. Hence, the convective heat transfer in enclosures with wavy walls has been investigated in numerous recent studies. Adjlout et al. [20] questioned the natural convection flow, including heat transfer in a tilted wavy wall cavity. They explored the influence of the number of the undulations of the wall on the heat transfer. The undulation of hot wall reduced the heat transfer rate for an inclination angle greater than 75°. Bhardwaj et al. [21] analyzed the natural convection heat transfer toward a porous-filled triangular cavity including a curved cold wall. They found that undulations on the cold wall improve the heat transfer rate. Considering the wavy wall forms, the entropy generation [22,23], non-uniform heating [24], partially heated wall [25,26], and micropolar fluids [27] have been investigated in recent years.

Using nanotechnology in the improvement of heat transfer, by scattering nanosized solids with high conductivity such as metal, metal oxide, and carbon single- and multi-layer tube in such base fluids as water, oil, and other standard coolants has been investigated in the past decades [28]. Using nanofluids is considered as a proper choice in fluid-based cooling. Heat transfer of nanofluids has, therefore, a wide variety of applications such as cooling electronic devices and chips. Considering the considerable bulk of calculations and hence the generated heat, CPU and electronic chips need fluids to be cooled, so nanofluids are cutting edge technology in this regard [29,30]. Therefore, modeling the nanofluid heat transfer is a significant problem in this field. Accurate modeling of the motion of nanoparticles into the base liquid has complexities. One of the recommended models for simulating the heat transfer of nanofluids is Buongiorno's two-phase approach. In this model, two bold movements of nanoparticles, due to changes of temperature and volume fraction distribution, are analyzed as valid parameters, along with other aspects of the classic equations of survival [31]. In addition, in this model, the non-uniform distribution of nanoparticles is studied. On the other hand, the migration of particles has an important role in heat transfer of nanofluid. As shown by Buongiorno [31], two migration term called Brownian movement and thermophoresis effects have a significant role in heat transfer of nanofluids. Many researchers have used Buongiorno's two-phase model to simulate the flow and heat transfer of nanofluids [32–39].

The accordance of mixed convection heat transfer due to the rigid rotating body is one of the challenges of nanofluids heat transfer, about which few articles have been published. In this study, by using Buongiorno's model, mixed convection of a nanofluid in the cavity, along with warm corrugated wall and a rigid rotating body, was analyzed. To the authors' knowledge and according to the literature mentioned above, the current study is unique and initiative. Moreover, when a nanofluid is synthesized, it is placed into the application to see how the synthesized nanofluid could improve the heat transfer. Various aspects, such as dynamic viscosity and migration of nanoparticles, would participate in the heat transfer behavior of a nanofluid.

2. Mathematical Formulation

The mixed convective heat transfers into a wavy-walled cavity by length L and continues as a rotating solid cylinder inside the center with radius r, as outlined in Figure 1. The left vertical surface preserves a fixed cold temperature (T_c) while the right wavy surface remains at a higher isothermal temperature (T_h). The bottom and top surfaces are maintained adiabatic. All the edges of the examined domain are expected to be impermeable, the fluid inside the hollow is a water-based nanofluid having Al_2O_3 nanoparticles, and the Boussinesq approximation remains applicable. In the present laminar flow study, the surface effects on the concentration distribution of nanoparticles are

neglected. Examining the assumptions mentioned above, the continuity, momentum, and energy equations regarding the laminar and steady convection are as follows:

$$\nabla \cdot \mathbf{v} = 0, \tag{1}$$

$$\rho_{nf}\mathbf{v} \cdot \nabla \mathbf{v} = -\nabla p + \nabla \cdot (\mu_{nf}\nabla \mathbf{v}) + (\rho\beta)_{nf}(T - T_c)\vec{g}, \tag{2}$$

$$(\rho C_p)_{nf}\mathbf{v} \cdot \nabla T = \nabla \cdot (k_{nf}\nabla T) - C_{p,p}J_p \cdot \nabla T, \tag{3}$$

$$\mathbf{v} \cdot \nabla \varphi = -\frac{1}{\rho_p}\nabla \cdot J_p, \tag{4}$$

Since the inner cylinder denotes a moving mass block including an associated force, the energy equation up the solid cylinder is:

$$(\rho C_p)_s \mathbf{v}_s \cdot \nabla T = \nabla \cdot (k_s \nabla T), \tag{5}$$

where $\mathbf{v}$ is the velocity vector, $\mathbf{v}_s = r \times \omega$ is the vector velocity over the solid cylinder surface, $\vec{g}$ means the gravitational acceleration vector, φ denotes the local nanoparticles volume fraction, and J_p is the mass flux of nanoparticles. According to the two-phase nanofluid model, nanoparticles mass flux can be formulated as:

$$J_p = J_{p,B} + J_{p,T}, \tag{6}$$

$$J_{p,B} = -\rho_p D_B \nabla \varphi, \quad D_B = \frac{k_b T}{3\pi\mu_f d_p}, \tag{7}$$

$$J_{p,T} = -\rho_p D_T \frac{\nabla T}{T}, \quad D_T = 0.26\frac{k_f}{2k_f + k_p}\frac{\mu_f}{\rho_f T}\varphi. \tag{8}$$

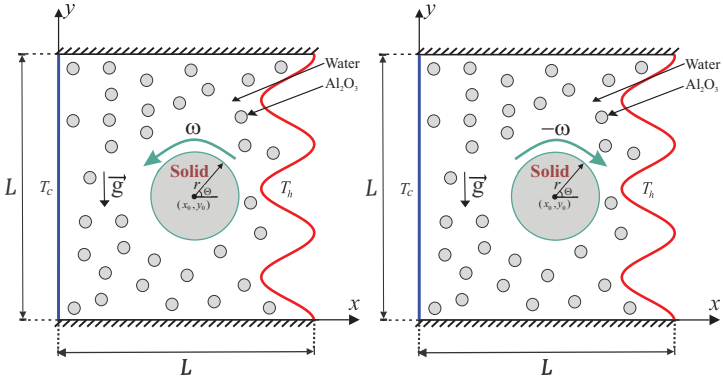

Figure 1. Schematic diagram of the physical model together with the coordinate system for: (**a**) Case 1, counterclockwise (CCW); and (**b**) Case 2, clockwise (CW).

The thermophysical properties of nanofluids including effective thermal diffusivity, heat capacitance, thermal expansion coefficient, and effective density are addressed as, respectively,

$$\alpha_{nf} = \frac{k_{nf}}{(\rho C_p)_{nf}}, \tag{9}$$

$$(\rho C_p)_{nf} = (1-\varphi)(\rho C_p)_f + \varphi(\rho C_p)_p, \tag{10}$$

$$(\rho\beta)_{nf} = (1-\varphi)(\rho\beta)_f + \varphi(\rho\beta)_p, \tag{11}$$

$$\rho_{nf} = (1-\varphi)\rho_f + \varphi\rho_p. \tag{12}$$

The thermal conductivity ratio of Al_2O_3-water nanofluids calculated by the Corcione model [40] is:

$$\frac{k_{nf}}{k_f} = 1 + 4.4\mathrm{Re}_B^{0.4}\mathrm{Pr}^{0.66}\left(\frac{T}{T_{fr}}\right)^{10}\left(\frac{k_p}{k_f}\right)^{0.03}\varphi^{0.66}, \tag{13}$$

where Re_B is shown as [40]:

$$\mathrm{Re}_B = \frac{\rho_f u_B d_p}{\mu_f}, \quad u_B = \frac{2k_b T}{\pi\mu_f d_p^2}. \tag{14}$$

Here, $k_b = 1.380648 \times 10^{-23}(J/K)$ is the Boltzmann constant, $l_f = 0.17$ nm is the mean path of fluid particles, and d_f is the molecular diameter of water given by Corcione [40] as:

$$d_f = \frac{6M}{N^*\pi\rho_f}, \tag{15}$$

where M denotes the molecular weight of the base liquid, N^* means the Avogadro number, and ρ_f is the density of the base liquid toward the regular temperature (310 K).

We propose the following non-dimensional variables:

$$\begin{gathered} X = \frac{x}{L},\ Y = \frac{y}{L},\ \mathbf{V} = \frac{\mathbf{v}L}{\nu_f},\ P = \frac{pL^2}{\rho_{nf}\nu_f^2},\ \varphi^* = \frac{\varphi}{\phi}, \\ D_B^* = \frac{D_B}{D_{B0}},\ D_T^* = \frac{D_T}{D_{T0}},\ \delta = \frac{T_h - T_c}{T_c}, \\ \theta = \frac{T - T_c}{T_h - T_c},\ \theta_s = \frac{T_s - T_c}{T_h - T_c},\ R = \frac{r}{L},\ \Omega = \frac{\omega L^2}{\alpha_f}. \end{gathered} \tag{16}$$

Applying the variables mentioned above, the following dimensionless governing equations are derived:

$$\nabla \cdot \mathbf{V} = 0, \tag{17}$$

$$\mathbf{V}\cdot\nabla\mathbf{V} = -\nabla P + \frac{\rho_f}{\rho_{nf}}\frac{\mu_{nf}}{\mu_f}\frac{1}{Re}\nabla^2\mathbf{V} + \frac{(\rho\beta)_{nf}}{\rho_{nf}\beta_f}Ri\cdot\theta, \tag{18}$$

$$\begin{aligned} \mathbf{V}\cdot\nabla\theta = {} & \frac{(\rho C_p)_f}{(\rho C_p)_{nf}}\frac{k_{nf}}{k_f}\frac{1}{Re\cdot\mathrm{Pr}}\nabla^2\theta + \frac{(\rho C_p)_f}{(\rho C_p)_{nf}}\frac{D_B^*}{Re\cdot\mathrm{Pr}\cdot Le}\nabla\varphi^*\cdot\nabla\theta \\ & + \frac{(\rho C_p)_f}{(\rho C_p)_{nf}}\frac{D_T^*}{Re\cdot\mathrm{Pr}\cdot Le\cdot N_{BT}}\frac{\nabla\theta\cdot\nabla\theta}{1+\delta\theta}, \end{aligned} \tag{19}$$

$$\mathbf{V}\cdot\nabla\varphi^* = \frac{D_B^*}{Re\cdot Sc}\nabla^2\varphi^* + \frac{D_T^*}{Re\cdot Sc\cdot N_{BT}}\cdot\frac{\nabla^2\theta}{1+\delta\theta}, \tag{20}$$

$$\mathbf{V}_s\cdot\nabla\theta = \frac{(\rho C_p)_{nf}}{(\rho C_p)_s}\frac{k_s}{k_{nf}}\nabla^2\theta, \tag{21}$$

where $\mathbf{V}$ shows the dimensionless vector of velocity (U_0, V_0), $D_{B0} = \frac{k_b T_c}{3\pi\mu_f d_p}$ is the reference coefficient of Brownian diffusion $\left(D_B^* = \frac{D_B}{D_{B0}}\right)$, $D_{T0} = 0.26\frac{k_f}{2k_f+k_p}\frac{\mu_f}{\rho_f T_c}\phi$ is the reference coefficient of thermophoretic diffusion $\left(D_T^* = \frac{D_T}{D_{T0}}\right)$, $Sc = \frac{\nu_f}{D_{B0}}$ is Schmidt number, $N_{BT} = \frac{\phi D_{B0} T_c}{D_{T0}(T_h - T_c)}$ is the parameter of diffusivity ratio (Brownian diffusivity/thermophoretic diffusivity), $Le = \frac{k_f}{(\rho C_p)_f \phi D_{B0}}$ is the Lewis number,

$Re = \frac{U_0 L}{\nu_f}$ is Reynolds number, $Ri = \frac{Gr}{Re^2}$ is Richardson number, and $\Pr = \nu_f/\alpha_f$ is the Prandtl number for the base fluid. The dimensionless boundary conditions of Equations (17)–(21) are:

On the adiabatic top horizontal wall:

$$U = V = 0,\ \frac{\partial \varphi^*}{\partial n} = 0,\ \frac{\partial \theta}{\partial n} = 0, \tag{22}$$

On the cold left vertical wall:

$$U = V = 0,\ \frac{\partial \varphi^*}{\partial n} = -\frac{D_T^*}{D_B^*} \cdot \frac{1}{N_{BT}} \cdot \frac{1}{1+\delta\theta} \frac{\partial \theta}{\partial n},\ \theta = 0, \tag{23}$$

On the heated right wavy wall: $A(1 - \cos(2N\pi X)),\ 0 \le Y \le 1$

$$U = V = 0,\ \frac{\partial \varphi^*}{\partial n} = -\frac{D_T^*}{D_B^*} \cdot \frac{1}{N_{BT}} \cdot \frac{1}{1+\delta\theta} \frac{\partial \theta}{\partial n},\ \theta = 1, \tag{24}$$

On the adiabatic bottom horizontal wall:

$$U = V = 0,\ \frac{\partial \varphi^*}{\partial n} = 0,\ \frac{\partial \theta}{\partial n} = 0, \tag{25}$$

$$\theta = \theta_s,\ \text{at the outer solid cylinder surface,} \tag{26}$$

$$U = -\Omega(Y - Y_0),\ V = \Omega(X - X_0),$$
$$\frac{\partial \varphi^*}{\partial n} = -\frac{D_T^*}{D_B^*} \cdot \frac{1}{N_{BT}} \cdot \frac{1}{1+\delta\theta} \frac{\partial \theta}{\partial n},\ \frac{\partial \theta}{\partial n} = K_r \frac{\partial \theta_s}{\partial n}, \tag{27}$$

where $K_r = k_s/k_{nf}$ is the thermal conductivity ratio upper the surface of the rotating conductive cylinder.

The boundary conditions for nanoparticles are dictated from the physics of nanofluid, in which the nanoparticles cannot penetrate the surface of the enclosure. The hydraulic boundary conditions are prescribed from the fact that the velocity of a fluid and the adjacent surface should be identical. The thermal boundary conditions simulate the heat transfer of a rotating shaft in a housing. The cavity is cooled by the side walls while the other side is subject to a process system of hot temperature.

Regarding the nanoparticles, we employed Buongiorno's mathematical model to investigate the concentration distribution of nanoparticles in the host fluid when the liquid is exposed to temperature gradients. The size of variation in the size of the nanoparticles can affect the concentration distribution of nanoparticles. As we used the average size of nanoparticles in a sample, the produced concentration distribution would also show the average of possible concentration distributions. Such outcomes could be adequate for most of the engineering designs.

The local Nusselt number (Nu_{nf}) evaluated at the hot wavy wall of the cavity is represented by:

$$Nu_{nf} = -\frac{k_{nf}}{k_f} \left(\frac{\partial \theta}{\partial W} \right)_W. \tag{28}$$

In addition, we can define the interface local Nusselt number (Nu_i) evaluated at the interface wall between the rotating conductive cylinder and the wavy-walled cavity as follows:

$$Nu_i = -\left(\frac{\partial \theta_s}{\partial S} \right)_S. \tag{29}$$

where W and S represent the total length of the wavy heater and the interface wall around the rotating solid cylinder, respectively. The average Nusselt number evaluated at the hot wavy wall is defined as follows:

$$\overline{Nu}_{nf} = \int_0^W Nu_{nf}\, \mathrm{d}W. \tag{30}$$

3. Numerical Method and Validation

The dimensionless form of the governing equations in Equations (17)–(21) controlled by dimensionless boundary conditions in Equations (22)–(27) were solved by the Galerkin weighted residual finite element method. First, we transferred the momentum equations in Equation (18) to the Cartesian X and Y coordinates as follows:

The momentum equation in the X-direction:

$$U\frac{\partial U}{\partial X}+V\frac{\partial U}{\partial Y}=-\frac{\partial P}{\partial X}+\frac{\rho_f}{\rho_{nf}}\frac{\mu_{nf}}{\mu_f}\frac{1}{Re}\left(\frac{\partial^2 U}{\partial X^2}+\frac{\partial^2 U}{\partial Y^2}\right). \tag{31}$$

The momentum equation in the Y-direction:

$$U\frac{\partial U}{\partial X}+V\frac{\partial U}{\partial Y}=-\frac{\partial P}{\partial Y}+\frac{\rho_f}{\rho_{nf}}\frac{\mu_{nf}}{\mu_f}\frac{1}{Re}\left(\frac{\partial^2 V}{\partial X^2}+\frac{\partial^2 V}{\partial Y^2}\right)+\frac{(\rho\beta)_{nf}}{\rho_{nf}\beta_f}Ri\,\theta \tag{32}$$

The Finite Element Method (FEM) was employed to solve the governing equations. Applying the FEM to the momentum in Equations (31) and (32) leads to the following process:

Primary, we applied the penalty FEM by excluding the pressure (P) including a penalty parameter (λ) as:

$$P=-\lambda\left(\frac{\partial U}{\partial X}+\frac{\partial V}{\partial Y}\right). \tag{33}$$

This led to the following momentum equations:

$$\begin{aligned}
U\frac{\partial U}{\partial X}+V\frac{\partial U}{\partial Y} &= \frac{\partial \lambda}{\partial X}\left(\frac{\partial U}{\partial X}+\frac{\partial V}{\partial Y}\right)+\frac{\rho_f}{\rho_{nf}}\frac{\mu_{nf}}{\mu_f}\frac{1}{Re}\left(\frac{\partial^2 U}{\partial X^2}+\frac{\partial^2 U}{\partial Y^2}\right),\\
U\frac{\partial V}{\partial X}+V\frac{\partial V}{\partial Y} &= \frac{\partial \lambda}{\partial Y}\left(\frac{\partial U}{\partial X}+\frac{\partial V}{\partial Y}\right)+\frac{\rho_f}{\rho_{nf}}\frac{\mu_{nf}}{\mu_f}\frac{1}{Re}\left(\frac{\partial^2 V}{\partial X^2}+\frac{\partial^2 V}{\partial Y^2}\right)+\frac{(\rho\beta)_{nf}}{\rho_{nf}\beta_f}Ri\,\theta.
\end{aligned} \tag{34}$$

The weak (or weighted-integral) formulation of the momentum equations was obtained by multiplying the equation with an internal domain (Φ) and integrating it over the computational domain. The following weak formulations were then obtained:

$$\begin{aligned}
&\int_\Omega\left(\Phi_i U^k\frac{\partial U^k}{\partial X}+\Phi_i V^k\frac{\partial U^k}{\partial Y}\right)\mathrm{dXdY}=\lambda\int_\Omega\frac{\partial\Phi_i}{\partial X}\left(\frac{\partial U^k}{\partial X}+\frac{\partial V^k}{\partial Y}\right)\mathrm{dXdY}\\
&\quad+\frac{\rho_f}{\rho_{nf}}\frac{\mu_{nf}}{\mu_f}\frac{1}{Re}\int_\Omega\Phi_i\left(\frac{\partial^2 U^k}{\partial X^2}+\frac{\partial^2 U^k}{\partial Y^2}\right)\mathrm{dXdY},
\end{aligned} \tag{35}$$

$$\begin{aligned}
&\int_\Omega\left(\Phi_i V^k\frac{\partial V^k}{\partial X}+\Phi_i V^k\frac{\partial V^k}{\partial Y}\right)\mathrm{dXdY}=\lambda\int_\Omega\frac{\partial\Phi_i}{\partial Y}\left(\frac{\partial U^k}{\partial X}+\frac{\partial V^k}{\partial Y}\right)\mathrm{dXdY}\\
&\quad+\frac{\rho_f}{\rho_{nf}}\frac{\mu_{nf}}{\mu_f}\frac{1}{Re}\int_\Omega\Phi_i\left(\frac{\partial^2 V^k}{\partial X^2}+\frac{\partial^2 V^k}{\partial Y^2}\right)\mathrm{dXdY}+\frac{(\rho\beta)_{nf}}{\rho_{nf}\beta_f}Ri\int_\Omega\Phi_i\theta^k\mathrm{dXdY},
\end{aligned} \tag{36}$$

where the superscript k is the relative index. The interpolation functions including any of the velocity distribution, temperature, and the nanoparticle distribution are approximated by employing a basis set $\{\Phi_j\}_{j=1}^N$ as,

$$\mathbf{V}\approx\sum_{j=1}^{N}\mathbf{V}_j\Phi_j(X,Y),\quad \theta\approx\sum_{j=1}^{N}\theta_j\Phi_j(X,Y),\quad \varphi^*\approx\sum_{j=1}^{N}\varphi_j^*\Phi_j(X,Y). \tag{37}$$

Then, the residual form of equations was computed by integrating the weak form of equations over a discrete domain:

$$\begin{aligned} R(1)_i &= \sum_{j=1}^{m} U_j \int_\Omega \left[\left(\sum_{j=1}^{m} U_j \Phi_j \right) \frac{\partial \Phi_j}{\partial X} + \left(\sum_{j=1}^{m} V_j \Phi_j \right) \frac{\partial \Phi_j}{\partial Y} \right] \Phi_i \mathrm{dXdY} \\ &\quad + \lambda \left[\sum_{j=1}^{m} U_j \int_\Omega \frac{\partial \Phi_i}{\partial X} \frac{\partial \Phi_j}{\partial X} \mathrm{dXdY} + \sum_{j=1}^{m} V_j \int_\Omega \frac{\partial \Phi_i}{\partial X} \frac{\partial \Phi_j}{\partial Y} \mathrm{dXdY} \right] \\ &\quad + \frac{\rho_f}{\rho_{nf}} \frac{\mu_{nf}}{\mu_f} \frac{1}{Re} \sum_{j=1}^{m} U_j \int_\Omega \left[\frac{\partial \Phi_i}{\partial X} \frac{\partial \Phi_j}{\partial X} + \frac{\partial \Phi_i}{\partial Y} \frac{\partial \Phi_j}{\partial Y} \right] \mathrm{dXdY}, \end{aligned} \tag{38}$$

$$\begin{aligned} R(2)_i &= \sum_{j=1}^{m} V_j \int_\Omega \left[\left(\sum_{j=1}^{m} U_j \Phi_j \right) \frac{\partial \Phi_j}{\partial X} + \left(\sum_{j=1}^{m} V_j \Phi_j \right) \frac{\partial \Phi_j}{\partial Y} \right] \Phi_i \mathrm{dXdY} \\ &\quad + \lambda \left[\sum_{j=1}^{m} U_j \int_\Omega \frac{\partial \Phi_i}{\partial Y} \frac{\partial \Phi_j}{\partial X} \mathrm{dXdY} + \sum_{j=1}^{m} V_j \int_\Omega \frac{\partial \Phi_i}{\partial Y} \frac{\partial \Phi_j}{\partial Y} \mathrm{dXdY} \right] \\ &\quad + \frac{\rho_f}{\rho_{nf}} \frac{\mu_{nf}}{\mu_f} \frac{1}{Re} \sum_{j=1}^{m} V_j \int_\Omega \left[\frac{\partial \Phi_i}{\partial X} \frac{\partial \Phi_j}{\partial X} + \frac{\partial \Phi_i}{\partial Y} \frac{\partial \Phi_j}{\partial Y} \right] \mathrm{dXdY} \\ &\quad + \frac{(\rho\beta)_{nf}}{\rho_{nf}\beta_f} Ri \int_\Omega \left(\sum_{j=1}^{m} \theta_j \Phi_j \right) \Phi_i \mathrm{dXdY}, \end{aligned} \tag{39}$$

where the relative index is denoted by the superscript k and subscripts of i and j represent the residual and node number, respectively. Here, m shows the iteration number. The integrals were performed by second-order Gaussian quadrature. The Newton–Raphson iteration algorithm was applied to iteratively solve the residual equations with the following stopping condition for every field variable:

$$\left| \frac{\Gamma^{m+1} - \Gamma^m}{\Gamma^{m+1}} \right| \leq \eta. \tag{40}$$

where m represents the iteration number and η is the convergence criterion.

To verify the current numerical data, the outcomes were compared with earlier published numerical outcomes achieved by Costa and Raimundo [13] concerning the problem of mixed convection heat transfer into a cavity filled with pure liquid and heated vertically into the presence of rotating cylinder, as depicted in Figure 2. The streamlines indicate the CW rotation for $\Omega = -500$, 0, and 500. At $\Omega = 500$, the streamlines are more powerful than $\Omega = 0$ and 500. In addition, the isotherms show horizontal lines for $\Omega = 0$ for both works. Besides, comparisons performed among the existing streamlines, isotherms, and nanoparticles volume fraction inside a free cavity and the numerical ones received by Corcione et al. [41] and Wang et al. [42] are demonstrated in Figure 3, where similar nanoparticle distribution is recorded. In addition, for natural convection flow in a cavity filled with nanofluid utilizing Buongiorno's two-phase model as exhibited in Figure 4a, the average heat transfer matched the experimental results of Ho et al. [43] and numerical outputs of Sheikhzadeh et al. [44] and Motlagh and Soltanipour [36] with various Rayleigh numbers toward $\phi = 0.03$. Figure 4b displays a comparison among the current outcomes and the experimental arrangements of Putra et al. [45] and the numerical result of Corcione et al. [41] using Buongiorno's model and for various Rayleigh numbers at $\phi = 0.01$, $N = 0$, and $R = 0$. Figure 5 gives alternative observations concerning the enhancement in the thermal conductivity and dynamic viscosity due to the addition of the Al_2O_3 nanoparticles with two different experimental outcomes and the numerical outcomes of Corcione et al. [41] as well. The maximum accuracy of the measurements of thermal conductivity in the study of Chon et al. [46] (experimental) was 3.90%. The accuracy of viscosity measurements in the study of Ho et al. [43] (experimental) was 1%. Based on those validations, the numerical results of the actual numerical code significance to a great level of reliability.

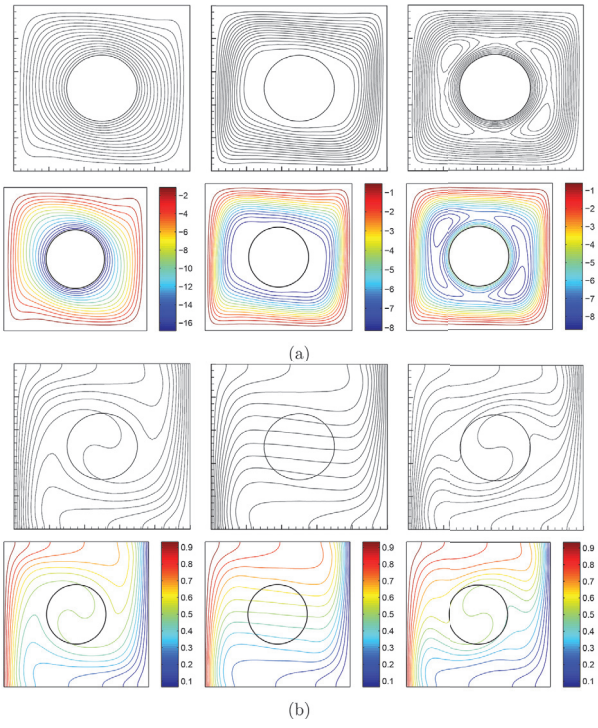

Figure 2. Comparisons between the results of (**top**) Costa and Raimundo [13] and (**bottom**) the present work for $\Omega = -500$ (**left**), $\Omega = 0$ (**middle**), and $\Omega = 500$ (**right**) of streamlines (**a**) and isotherms (**b**) at $Ra = 10^5$, $N = 0$, $K_r = 1$, $R = 0.2$, and $\mathrm{Pr} = 0.7$.

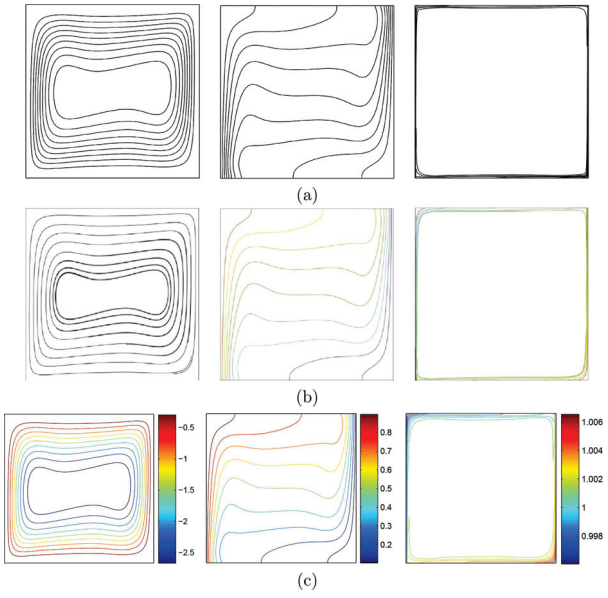

Figure 3. Validations of (**left**) streamlines, (**middle**) isotherms, and (**right**) nanoparticle distribution for (**a**) Corcione et al. [41], (**b**) Wang et al. [42], and (**c**) the present study at $Ra = 3.37 \times 10^5$, $\phi = 0.04$, $N = 0$, and $R = 0$.

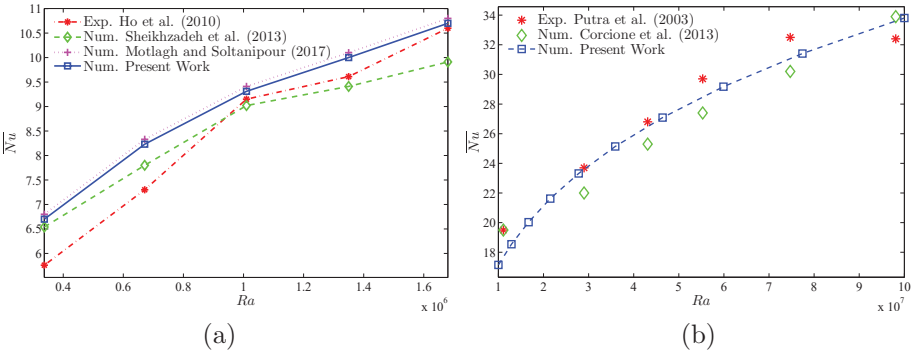

Figure 4. Comparisons of the average Nusselt number of the current numerical work with: (**a**) the experimental outcomes of Ho et al. [43], numerical outcomes of Sheikhzadeh et al. [44], and numerical outcomes of Motlagh and Soltanipour [36] with various Rayleigh numbers for $\phi = 0.03$; and (**b**) the experimental outcomes of Putra et al. [45] and the numerical outcomes of Corcione et al. [41] with various Rayleigh numbers at $\phi = 0.01$, $N = 0$, and $R = 0$.

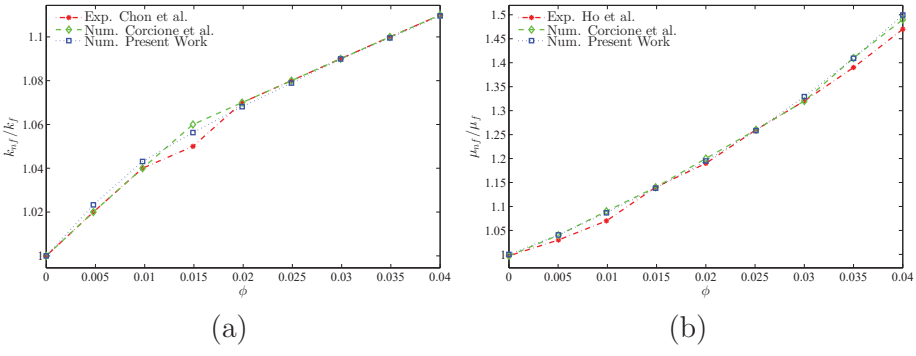

Figure 5. Comparisons of: (**a**) thermal conductivity ratio between the current numerical results, Chon et al. [46] (experimental), and Corcione et al. [41] (numerical); and (**b**) dynamic viscosity ratio of the current results with Ho et al. [43] (experimental) and Corcione et al. [41] (numerical) at $Ra = 3.37 \times 10^5$, $N = 0$, and $R = 0$.

4. Results and Discussion

Current segment displays numerical outcomes concerning the streamlines, isotherms, and nanoparticle distribution among two cases of the angular rotational velocity (Ω and $-\Omega$), Richardson number ($0.01 \leq Ri \leq 100$), nanoparticle volume fraction ($0 \leq \phi \leq 0.04$), number of undulations ($0 \leq N \leq 4$), and dimensionless radius of the rotating cylinder ($0.05 \leq R \leq 0.25$), where the values of other parameters are fixed at $Re = 100$, $k_s = 0.76$, $\mathrm{Pr} = 4.623$, $Le = 3.5 \times 10^5$, $Sc = 3.55 \times 10^4$, $\Theta = 360$, and $N_{BT} = 4.1$. The thermophysical properties of the base liquid and solid Al_2O_3 phases are tabulated in Table 1. Following the Buongiorno's model, the suspension of nanoparticles is assumed a dilute suspension, and, hence, the outcomes could be valid for low volume fractions of nanoparticles, i.e., $\phi < 0.05$.

Table 1. Thermophysical properties of base liquid with Al_2O_3 nanoparticles at $T = 310$ K [36,47].

Physical Properties	Base Liquid Phase (Water)	Al_2O_3
$k\,(\mathrm{Wm^{-1}K^{-1}})$	0.628	40
$\mu \times 10^6\,(\mathrm{kg/ms})$	695	–
$\rho\,(\mathrm{kg/m^3})$	993	3970
$C_p\,(\mathrm{J/kgK})$	4178	765
$\beta \times 10^5\,(1/\mathrm{K})$	36.2	0.85
$d_p\,(\mathrm{nm})$	0.385	33

Figures 6 and 7 show the changes of streamlines and isotherms among the changes of Richardson number (Ri) and also with clockwise and CCW rotations of the rigid body. In these figures, distribution of volume fraction and remarkable changes with the variations of Ri can be observed. In general, considering the momentum equation, the velocity of nanofluid increases with an increase of Ri, which is indicated in maximum amounts of streamlines. Another notable point observed in streamlines in both states is the occurrence of tiny whirlpools created by the increase of Ri. When Re is constant, an increase of Ri leads to increase of Gr, and with the addition of buoyancy, the pattern of flow increase and some whirlpools are observed at high values of Ri. In two states, as Ri increases, isothermal lines change with a certain trend, so that with the increase of Ri, isothermal lines of corrugated wall get closer to each other, as clearly observed at the lower corner of cavity. In the mentioned model, nanoparticles movement is affected by two factors: Brownian and thermophoresis. In the state of the low gradient for Ri, the temperature is very high. Thus, nanoparticles travel from the cool wall toward the warm one, as a result of the temperature gradient. Among the rise of Ri and drop of the gradient of temperature, the movement of nanoparticles will be confined to a couple of lines. However, due to Brownian motion, the movement of nanoparticles near the rotating rigid body is observable; therefore, as shown in Figure 6, the nanoparticles travel from the right wavy surface and middle of the cavity to the bottom and left walls, especially the corners of the left wall. This trend can also be seen for nanoparticle distribution in Figure 7. Furthermore, the thermophoresis force tends to move the nanoparticles in a direction opposite to the temperature gradient. At the hot side of a nanoparticle, the liquid molecules are with more energy, and the impact of collision of nanoparticles and the liquid molecules induces a net force. This net force, thermophoresis force, tends to move the nanoparticles from hot to cold. The Brownian motion tends to make the nanoparticles in the liquid uniform. Hence, the Brownian motion exerts a net force on the nanoparticles to move them from a high concentration area to a low concentration one. This way, the Brownian motion and thermophoresis forces adjust the distribution of nanoparticles in a liquid in the presence of notable temperature gradients.

Figure 8 reveals the variations of local Nu against the warm wall and rotating rigid body, with an addition of Ri. Since Ri raises, isothermal lines shown in Figure 6, near the corrugated wall, get closer and become more dense and therefore the temperature gradient increases. Local Nu is also expected to increase. The density of isothermal lines at the concave points of the corrugated wall is much higher than at the convex points, and hence the local Nu gets its maximum value at the concave points. By moving along the circumference of the rotating rigid wall, temperature gradient decreases and gets a negative value. This negative gradient firstly increases and then drops. Afterwards, isothermal lines will have a positive slope, and after passing the maximum point, the negative gradient decreases. This trend accounts for the occurrence of a minimum and a maximum location at the local Nu of the rotating rigid body. The same pattern is noticed for local Nu results in Figure 9.

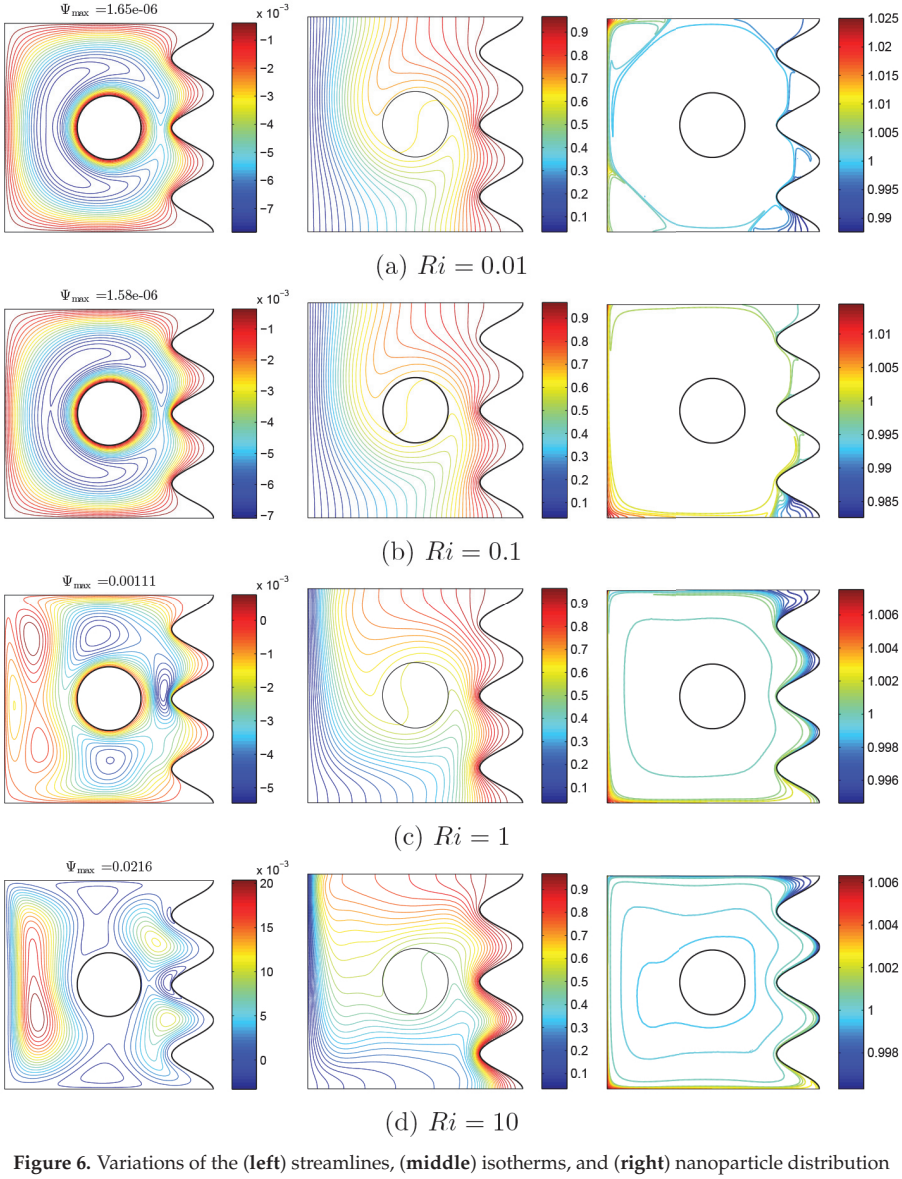

Figure 6. Variations of the (**left**) streamlines, (**middle**) isotherms, and (**right**) nanoparticle distribution evolution by Richardson number (*Ri*) for Case 1 (Ω), $\phi = 0.02$, $N = 3$, and $R = 0.15$.

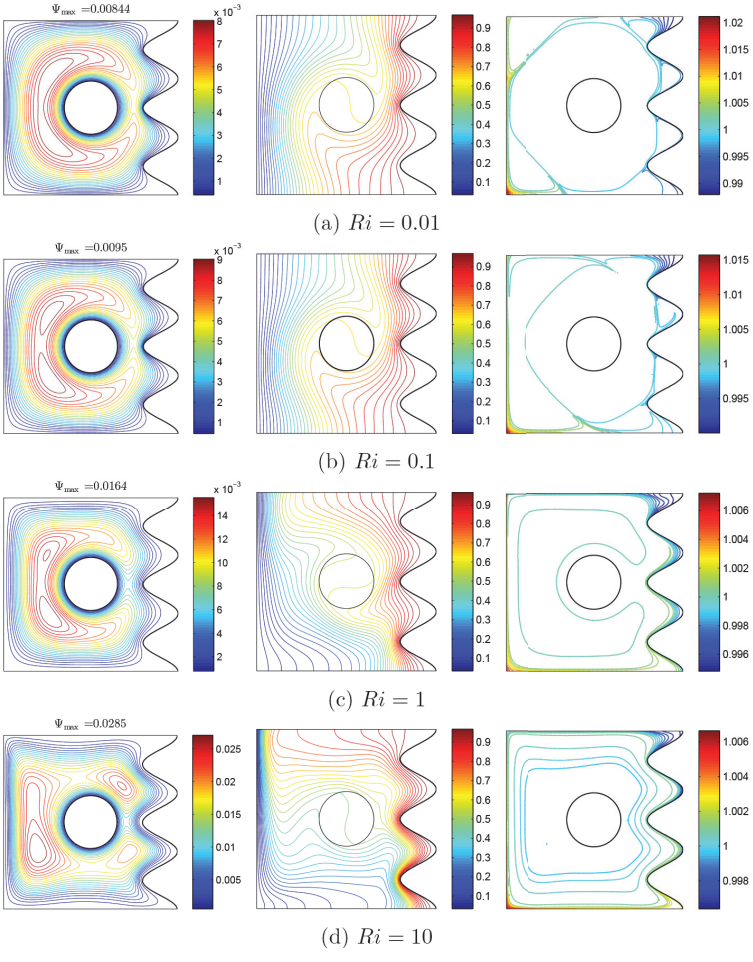

Figure 7. Variations of the (**left**) streamlines, (**middle**) isotherms, and (**right**) nanoparticle distribution evolution by Richardson number (*Ri*) for Case 2 ($-\Omega$), $\phi = 0.02$, $N = 3$, and $R = 0.15$.

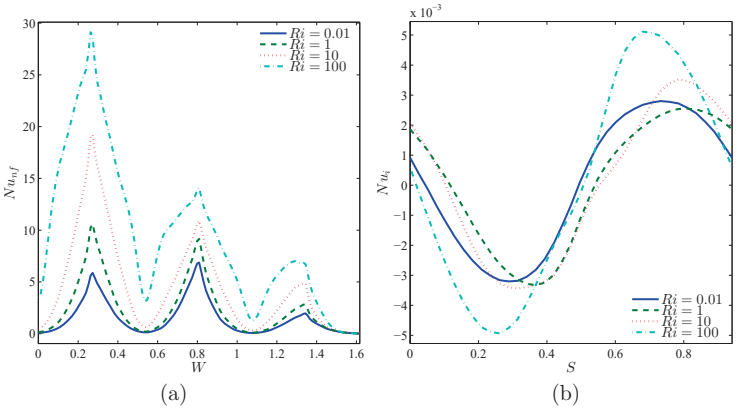

Figure 8. Variations of local Nusselt number interfaces with (**a**) *W* and (**b**) *S* for different *Ri* at Case 1 (Ω), $\phi = 0.02$, $N = 3$, and $R = 0.15$.

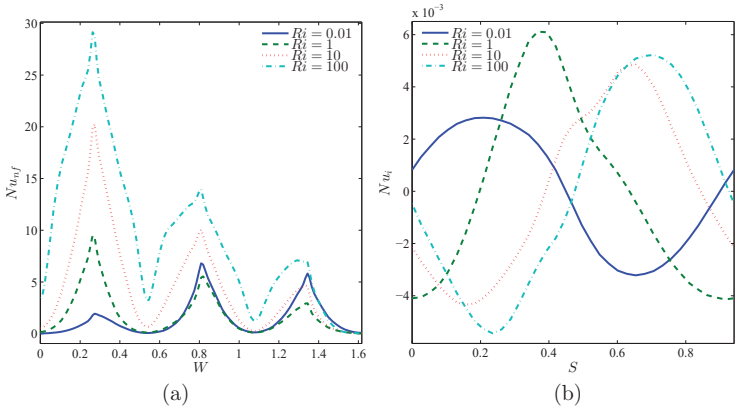

Figure 9. Variations of local Nusselt number interfaces with (**a**) W and (**b**) S for different Ri at Case 2 $(-\Omega)$, $\phi = 0.02$, $N = 3$, and $R = 0.15$.

Figure 10 shows the distribution of nanoparticles at the middle plane of the cavity ($Y = 0.5$) along the X-direction. Figure 10a,b depicts the results for the rotating Cases 1 and 2, respectively. As seen, both cases show similar behavior except the concentrations near the rotating cylinder. In both figures, a sharp variation of particles concentration next to the hot and cold surfaces can be observed. A high level of nanoparticles could be located at the cold surface. That is due to the thermophoresis effect, which tends to move the nanoparticles of hot to cold zones. Close to the heated surface, the concentration of nanoparticles is low. This is again due to the thermophoresis effect, which sweeps the particles away from the hot surface. The intensity of the concentration boundary layer remains minimum compared to the temperature and hydrodynamic boundary layers. This thin boundary layer is the results of the vast Lewis and Schmidt numbers for nanofluids.

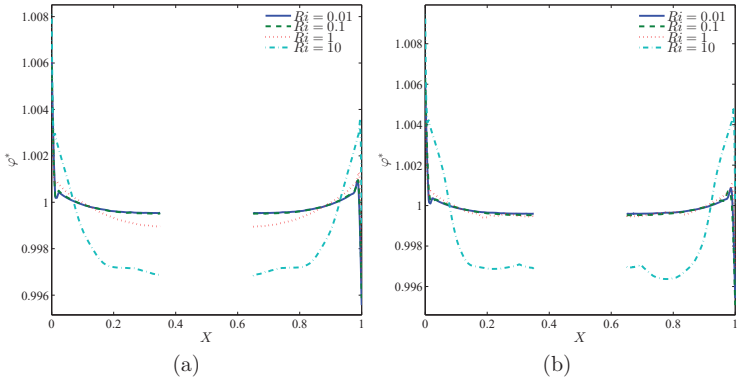

Figure 10. Variations of local normalized solid volume fraction interfaces with the horizontal center line ($Y = 0.5$) for different Ri at (**a**) Case 1 (Ω) and (**b**) Case 2 $(-\Omega)$ for $\phi = 0.02$, $N = 0$, and $R = 0.15$.

Far from the walls, where the temperature gradients are smooth, a uniform concentration of nanoparticles could be found. The consistent level of nanoparticles at such regions is due to the Brownian motion effects, which tend to move the nanoparticles of an enormous concentration area toward a low concentration one. At the center of the cavity, where the rotating disc is located, there are no nanoparticles, and, hence, there is no concentration gradient. In the case of low Richardson number, the influence of the cylinder's rotation on the concentration distribution is minimal since the rotation of the solid cylinder remains slow compared via the natural convection flow. In the case of high Ri,

the concentration profiles are greatly affected by the rotation and shifted downward. This downward shift is due to the change of the cold flow toward the down bottom of the cylinder.

Figure 11 represents the continuous increase of the average Nu, i.e., the heat transfer rate, with an increase of Ri, for both cases. However, the maximum increase of heat transfer is observed at the volume fraction of 3%. To investigate this trend with more analysis at constant amounts of Ri, the effects of variations of volume fraction toward the average Nu was analyzed (Figure 12). For all values of Ri, except for the case of $Ri = 0.01$, an optimum point is observed for the average Nu number. This means that, given a constant Re, Gr increases with the increase of Ri. Thus, forced convection is overshadowed by the free type. In the free convection of nanofluids, an addition of volume fraction along with the rise in viscosity points to the decrease of heat transfer and, hence, for the geometry studied, an increase of volume fraction after passing the maximum score heads to the reduction of Nu. $\phi = 0.03$ may be considered as the optimum point for volume fraction.

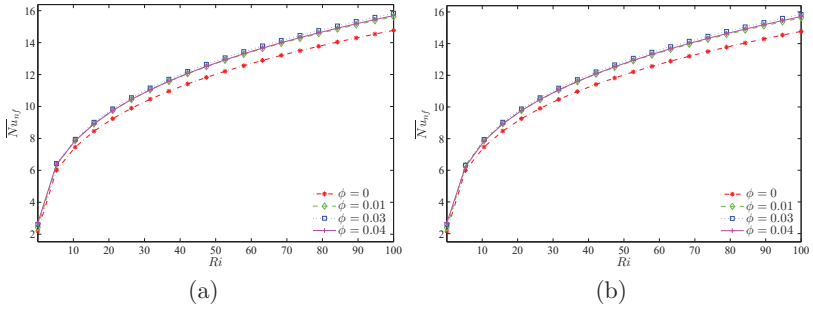

Figure 11. Variations of the average Nusselt number with Ri for different ϕ for (**a**) Case 1 (Ω) and (**b**) Case 2 ($-\Omega$) at $N = 3$ and $R = 0.15$.

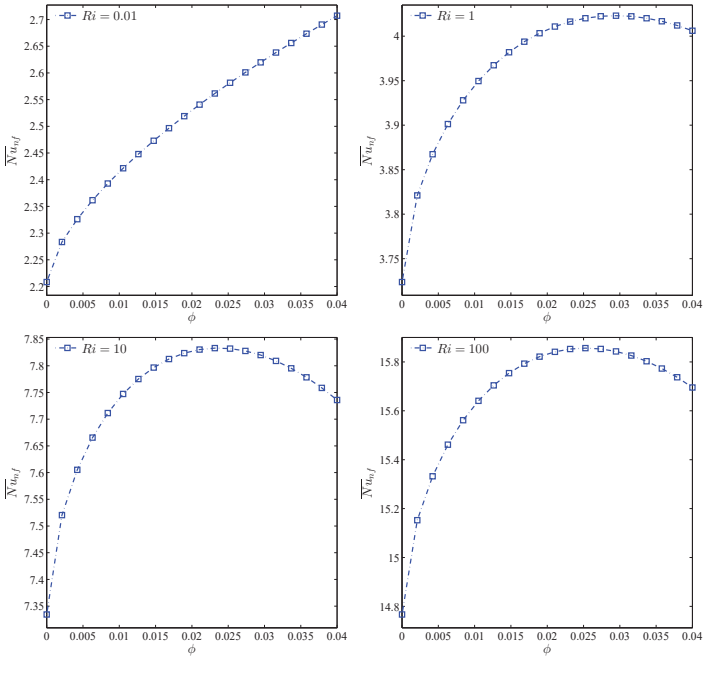

Figure 12. Variations of the average Nusselt number with ϕ for different Ri at Case 1 (Ω), $N = 3$ and $R = 0.15$.

Figure 13 reveals the impact of increasing the number of grooves toward the flow patterns, temperature, and heat transfer. At the two sides regarding the rigid body, streamlines have CCW rotations, so that they are pulled toward the corrugations as the right warm wall gets corrugated. The maximum value of streamline is seen at $N = 2$. Isothermal lines have a remarkable density above the cool wall and below the warm wall, so that the density will be highly noticeable at the concave points as the warm wall becomes corrugated. Primarily, the movement of nanoparticles has a meaningful symmetry around the rigid body, so that with corrugating the warm wall and accordingly the change of flow pattern and temperature, they are pulled into the concave regions of the warm wall (Figure 13). Generally, via increasing N, the nanoparticles migration decreases. The concentration of nanoparticles near the rotating cylinder at $N = 4$ is higher than other parts of the cavity. In different values of N, the level of nanoparticles at the corner of the left and bottom walls is very notable. Considering the isothermal lines, the maximum value of local Nu of the warm wall is seen at $N = 4$. However, at $X = L$ and $Y = 0$, the maximum value of Nu happens at $N = 0$. As noted above, local Nu has some peaks at the concave points. For local Nu, the rotating rigid body has its minimum and maximum values as a result of its high temperature gradient (Figure 14).

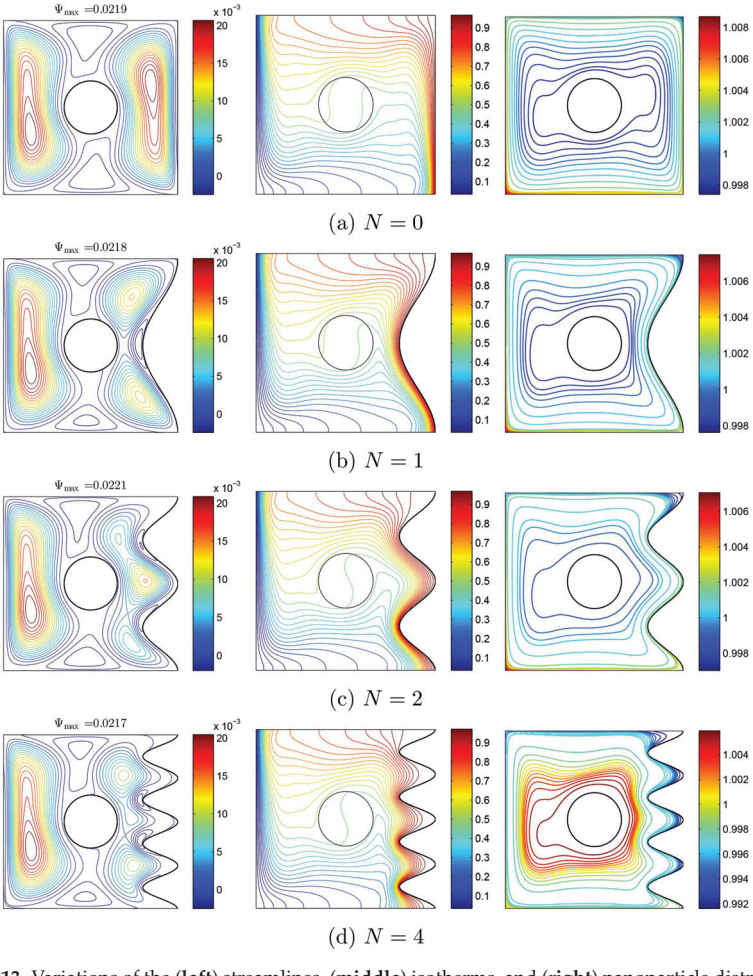

Figure 13. Variations of the (**left**) streamlines, (**middle**) isotherms, and (**right**) nanoparticle distribution evolution by number of undulations (N) for Case 1 (Ω), $Ri = 10$, $\phi = 0.02$, and $R = 0.15$.

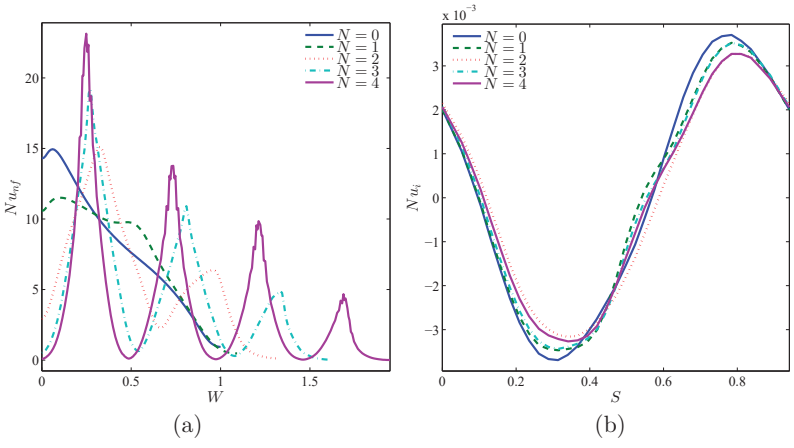

Figure 14. Variations of local Nusselt number interfaces with (**a**) W and (**b**) S for different N at Case 1 (Ω), $Ri = 10$, $\phi = 0.02$, and $R = 0.15$.

As displayed in Figure 15, the rate of heat transfer increases by the growth of Ri. At a relatively low number of undulations $N = 1$, the highest volume of heat transfer rate and also the maximum increase of it is observed by the rise of volume fraction of nanoparticles. The maximum amount of heat transfer rate is seen at $0.02 < \phi < 0.03$.

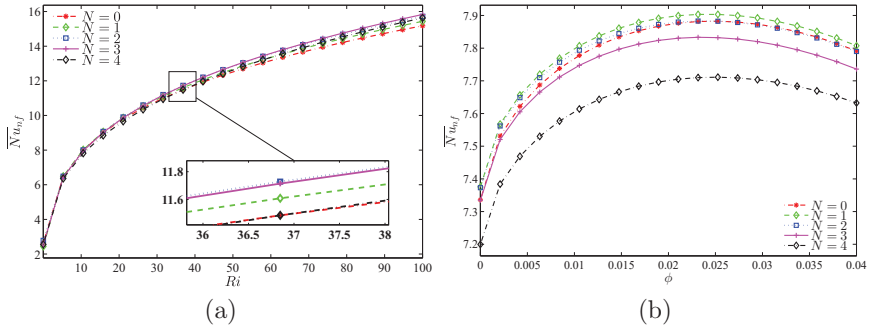

Figure 15. Variations of the average Nusselt number with (**a**) Ri and (**b**) ϕ for different N at Case 1 (Ω), $R = 0.15$.

Figures 16–18 show the effects of size of rotating rigid body toward the patterns of flow and heat transfer. Since the volume grows, vortexes get nearer to the body, and the rotations get more prominent because the route of nanofluid has more barriers as the area of rigid body has more cases and thus more massive vortexes are generated. At low values of R, the flow pattern makes the isothermal lines become horizontal at a large area of the middle region of cavity. However, with the increase of R, isothermal lines get a circle shape at the middle region and are still dense at the concave points of warm wall. For all values of R, nanoparticles move from the left corner of the lower surface toward the warm wall, especially the highest point of it. In addition, because of the movement of rigid body and the corroboration of the Brownian motion of nanoparticles, the accumulation of nanoparticles is also noticeable near the moving wall. This accumulation is maximum at $R = 0.05$.

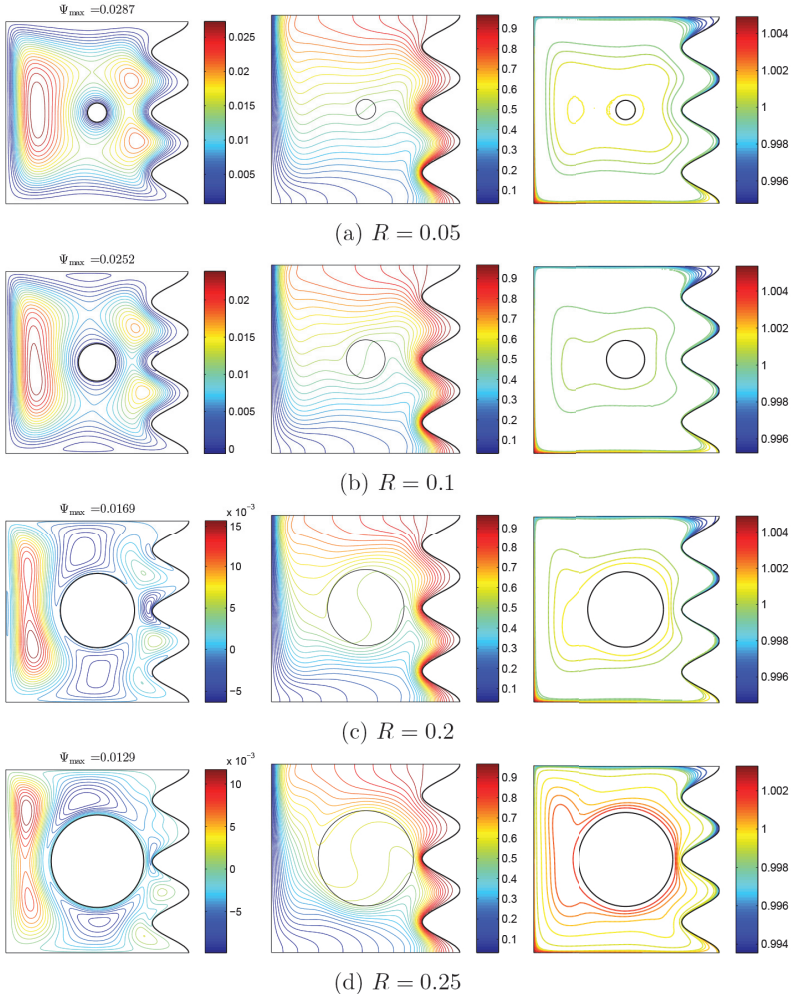

Figure 16. Variations of the (**left**) streamlines, (**middle**) isotherms, and (**right**) nanoparticle distribution evolution by the radius of the rotating cylinder (R) for Case 1 (Ω), $Ri = 10$, $\phi = 0.02$ and $N = 3$.

Considering the density of isothermal lines, the maximum amount of local Nu is seen at the first concave region of all amounts of R. At the second concave region, considering the proximity of rotating rigid body, the value of local Nu is maximum for large values of R, especially for $R = 0.25$. At the last concave region, density of isothermal lines becomes very low and Nu is expected to be lower at the third peak, compared to the other two peaks. This is clearly observed in Figure 17a. At $R = 0.25$, as a result of density at the first two peaks and remarkable reduction of temperature gradient at the last concave region, the behavior of local Nu is highly noticeable. Considering the isothermal lines, Nu of rotating body may be described this way: nearly at the beginning of motion on the wall, temperature gradient is negative, while at the symmetrically opposite region is positive. Thus, a Sin behavior in the Nu of rotating wall, including a negative minimum and a positive maximum, is observed. Considering the aggregation of temperature gradient at $R = 0.25$ and the presence of vortexes, local Nu has a remarkable growth at its positive maximum, in comparison with other values of R (Figure 17b).

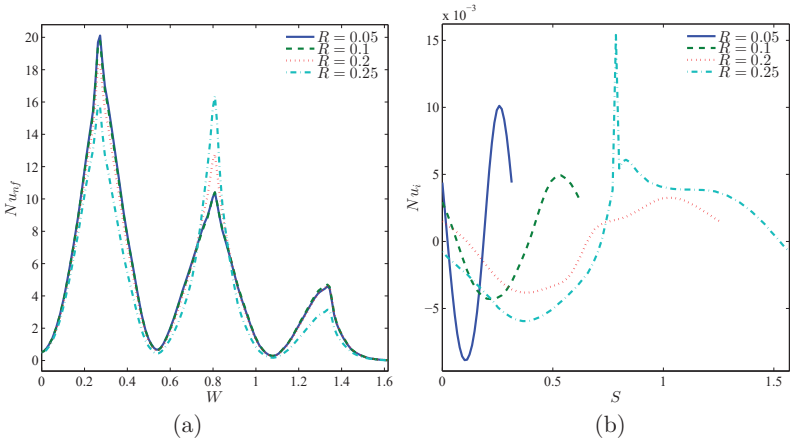

Figure 17. Variations of local Nusselt number interfaces with (**a**) W and (**b**) S for different R at Case 1 (Ω), $Ri = 10$, $\phi = 0.02$, and $N = 3$.

Considering Figure 18, the maximum value of the average Nu is seen at $R = 0.05$, while for low amounts of Ri, the maximum amount of average Nu occurs at $R = 0.25$. From $Ri \geq 10$ and at all values of R, the most significant heat transfer is detected at $R = 0.05$. With the increase of ϕ, a different behavior for heat transfer is seen with various values of R. For all values of R, an optimum value of ϕ is seen and, for various states of R, the following values for volume fraction can be offered, which result in the highest amount of heat transfer: $0.05 < R < 0.2$ and $\phi = 0.025$ as well as $R = 0.25$ and $\phi = 0.01$.

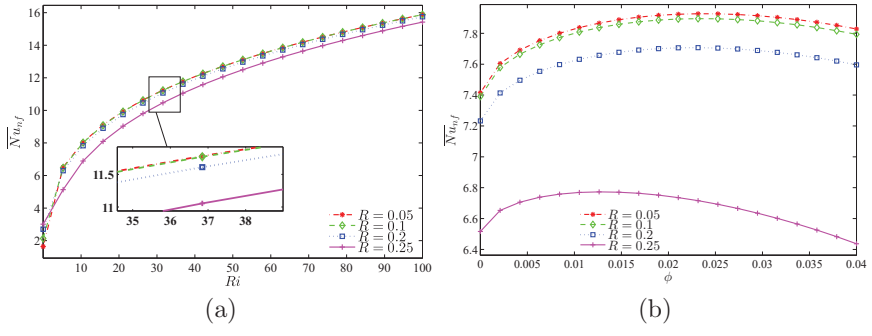

Figure 18. Variations of the average Nusselt number with (**a**) Ri and (**b**) ϕ for different R at Case 1 (Ω), $N = 3$.

5. Conclusions

Combined convection flow and heat transfer mechanisms toward an enclosed cavity including heated wavy surface and rotating circular cylinder were examined numerically using Buongiorno's two-phase approach. The current outcomes have directed the following concluding statements:

1. An addition of the average Nu with the rise of Ri, for both CW and CCW rotating, is experienced. In addition, the maximum increase of heat transfer is perceived toward the nanoparticles volume fraction of 3%.
2. The most significant amount of streamline is noticed at a relatively high number of undulations $N = 2$.

3. In the situation of rotating the solid cylinder in counterclockwise (Case 1), the maximum mean Nusselt number is observed at singular undulation $N = 1$ and the nanoparticles volume fraction in the range $0.02 < \phi < 0.03$.
4. For the case of ruled natural convection ($Ri \geq 10$) and all amounts of R, the maximum significance of heat transfer is recognized at $R = 0.05$.
5. For all amounts of R, an optimum value of ϕ is seen and, for various states of R, the following values for volume fraction can be offered, which result in the highest amount of the heat transfer rate: $0.05 < R < 0.2$, $\phi = 0.025$, and $R = 0.25$, $\phi = 0.01$.

Author Contributions: Conceptualization, A.I.A. and M.G.; methodology, A.I.A.; software, A.I.A., M.G. and T.A.; validation, A.I.A.; formal analysis, T.A., A.I.A. and M.S.P.; investigation, A.I.A., M.G., M.S.P. and T.A.; resources, I.H. and A.C.; write draft preparation, A.I.A., I.H., T.A., M.G., A.C. and M.S.P.; write and editing, A.I.A., I.H., T.A., M.G., A.C. and M.S.P.; visualization, A.I.A. and M.G.; supervision, I.H. and A.C. All authors have read and agreed to the published version of the manuscript.

Funding: We are grateful for the financial support received from the Malaysian Ministry of Education under the research grant FRGS/1/2019/STG06/UKM/01/2.

Acknowledgments: We thank the respected reviewers for their constructive comments, which clearly enhanced the quality of the manuscript.

Conflicts of Interest: The authors declare no conflict of interest.

References

1. Shu, C.; Xue, H.; Zhu, Y.D. Numerical study of natural convection in an eccentric annulus between a square outer cylinder and a circular inner cylinder using DQ method. *Int. J. Heat Mass Transf.* **2001**, *44*, 3321–3333. [CrossRef]
2. Shu, C.; Zhu, Y.D. Efficient computation of natural convection in a concentric annulus between an outer square cylinder and an inner circular cylinder. *Int. J. Numer. Methods Fluids* **2002**, *38*, 429–445. [CrossRef]
3. Ding, H.; Shu, C.; Yeo, K.S.; Lu, Z.L. Simulation of natural convection in eccentric annuli between a square outer cylinder and a circular inner cylinder using local MQ-DQ method. *Numer. Heat Transf. Part Appl.* **2005**, *47*, 291–313. [CrossRef]
4. Angeli, D.; Levoni, P.; Barozzi, G.S. Numerical predictions for stable buoyant regimes within a square cavity containing a heated horizontal cylinder. *Int. J. Heat Mass Transf.* **2008**, *51*, 553–565. [CrossRef]
5. Alsabery, A.I.; Gedik, E.; Chamkha, A.J.; Hashim, I. Effects of two-phase nanofluid model and localized heat source/sink on natural convection in a square cavity with a solid circular cylinder. *Comput. Methods Appl. Mech. Eng.* **2019**, *346*, 952–981. [CrossRef]
6. Kuznetsov, G.V.; Sheremet, M.A. Conjugate natural convection in an enclosure with a heat source of constant heat transfer rate. *Int. J. Heat Mass Transf.* **2011**, *54*, 260–268. [CrossRef]
7. Jami, M.; Mezrhab, A.; Naji, H. Numerical study of natural convection in a square cavity containing a cylinder using the lattice Boltzmann method. *Eng. Comput.* **2008**, *25*, 480–489. [CrossRef]
8. Sheremet, M.A. Unsteady conjugate thermogravitational convection in a cylindrical region with local energy source. *Thermophys. Aeromech.* **2011**, *18*, 447–458. [CrossRef]
9. Butler, C.; Newport, D.; Geron, M. Natural convection experiments on a heated horizontal cylinder in a differentially heated square cavity. *Exp. Therm. Fluid Sci.* **2013**, *44*, 199–208. [CrossRef]
10. Miroshnichenko, I.V.; Sheremet, M.A. Effect of Surface Emissivity on Conjugate Turbulent Natural Convection in an Air-Filled Cavity with a Heat Source. *Key Eng. Mater.* **2016**, *685*, 315–319. [CrossRef]
11. Nosonov, I.I.; Sheremet, M.A. Conjugate mixed convection in a rectangular cavity with a local heater. *Int. J. Mech. Sci.* **2018**, *136*, 243–251. [CrossRef]
12. Miroshnichenko, I.V.; Sheremet, M.A. Radiation effect on conjugate turbulent natural convection in a cavity with a discrete heater. *Appl. Math. Comput.* **2018**, *321*, 358–371. [CrossRef]
13. Costa, V.A.F.; Raimundo, A.M. Steady mixed convection in a differentially heated square enclosure with an active rotating circular cylinder. *Int. J. Heat Mass Transf.* **2010**, *53*, 1208–1219. [CrossRef]

14. Wang, T.; Huang, Z.; Xi, G. Entropy generation for mixed convection in a square cavity containing a rotating circular cylinder using a local radial basis function method. *Int. J. Heat Mass Transf.* **2017**, *106*, 1063–1073. [CrossRef]
15. Misirlioglu, A. The effect of rotating cylinder on the heat transfer in a square cavity filled with porous medium. *Int. J. Eng. Sci.* **2006**, *44*, 1173–1187. [CrossRef]
16. Hussain, S.H.; Hussein, A.K. Mixed convection heat transfer in a differentially heated square enclosure with a conductive rotating circular cylinder at different vertical locations. *Int. Commun. Heat Mass Transf.* **2011**, *38*, 263–274. [CrossRef]
17. Liao, C.C.; Lin, C.A. Mixed convection of a heated rotating cylinder in a square enclosure. *Int. J. Heat Mass Transf.* **2014**, *72*, 9–22. [CrossRef]
18. Alsabery, A.I.; Tayebi, T.; Chamkha, A.J.; Hashim, I. Effect of rotating solid cylinder on entropy generation and convective heat transfer in a wavy porous cavity heated from below. *Int. Commun. Heat Mass Transf.* **2018**, *95*, 197–209. [CrossRef]
19. Selimefendigil, F.; Öztop, H.F. Mixed convection of nanofluids in a three dimensional cavity with two adiabatic inner rotating cylinders. *Int. J. Heat Mass Transf.* **2018**, *117*, 331–343. [CrossRef]
20. Adjlout, L.; Imine, O.; Azzi, A.; Belkadi, M. Laminar natural convection in an inclined cavity with a wavy wall. *Int. J. Heat Mass Transf.* **2002**, *45*, 2141–2152. [CrossRef]
21. Bhardwaj, S.; Dalal, A.; Pati, S. Influence of wavy wall and non-uniform heating on natural convection heat transfer and entropy generation inside porous complex enclosure. *Energy* **2015**, *79*, 467–481. [CrossRef]
22. Dutta, S.; Biswas, A.K.; Pati, S. Natural convection heat transfer and entropy generation inside porous quadrantal enclosure with nonisothermal heating at the bottom wall. *Numer. Heat Transf. Part A Appl.* **2018**, *73*, 222–240. [CrossRef]
23. Alsabery, A.I.; Ismael, M.A.; Chamkha, A.J.; Hashim, I. Numerical investigation of mixed convection and entropy generation in a wavy-walled cavity filled with nanofluid and involving a rotating cylinder. *Entropy* **2018**, *20*, 664. [CrossRef]
24. Sheremet, M.; Pop, I.; Öztop, H.F.; Abu-Hamdeh, N. Natural convection of nanofluid inside a wavy cavity with a non-uniform heating. *Int. J. Numer. Methods Heat Fluid Flow* **2017**, *27*, 958–980. [CrossRef]
25. Pop, I.; Sheremet, M.; Cimpean, D.S. Natural convection in a partially heated wavy cavity filled with a nanofluid using Buongiorno's nanofluid model. *Int. J. Numer. Methods Heat Fluid Flow* **2017**, *27*, 924–940. [CrossRef]
26. Hashim, I.; Alsabery, A.; Sheremet, M.A.; Chamkha, A. Numerical investigation of natural convection of Al_2O_3–water nanofluid in a wavy cavity with conductive inner block using Buongiorno's two-phase model. *Adv. Powder Technol.* **2019**, *30*, 399–414. [CrossRef]
27. Miroshnichenko, I.V.; Sheremet, M.A.; Pop, I.; Ishak, A. Convective heat transfer of micropolar fluid in a horizontal wavy channel under the local heating. *Int. J. Mech. Sci.* **2017**, *128*, 541–549. [CrossRef]
28. Izadi, S.; Armaghani, T.; Ghasemiasl, R.; Chamkha, A.J.; Molana, M. A comprehensive review on mixed convection of nanofluids in various shapes of enclosures. *Powder Technol.* **2019**, *343*, 880–907. [CrossRef]
29. Nazari, M.; Karami, M.; Ashouri, M. Comparing the thermal performance of water, Ethylene Glycol, Alumina and CNT nanofluids in CPU cooling: Experimental study. *Exp. Therm. Fluid Sci.* **2014**, *57*, 371–377. [CrossRef]
30. Izadi, A.; Siavashi, M.; Rasam, H.; Xiong, Q. MHD enhanced nanofluid mediated heat transfer in porous metal for CPU cooling. *Appl. Therm. Eng.* **2020**, *168*, 114843. [CrossRef]
31. Buongiorno, J. Convective transport in nanofluids. *J. Heat Transf.* **2006**, *128*, 240–250. [CrossRef]
32. Maghrebi, M.J.; Nazari, M.; Armaghani, T. Forced convection heat transfer of nanofluids in a porous channel. *Transp. Porous Media* **2012**, *93*, 401–413. [CrossRef]
33. Saryazdi, A.B.; Talebi, F.; Armaghani, T.; Pop, I. Numerical study of forced convection flow and heat transfer of a nanofluid flowing inside a straight circular pipe filled with a saturated porous medium. *Eur. Phys. J. Plus* **2016**, *131*, 78. [CrossRef]
34. Zargartalebi, H.; Ghalambaz, M.; Noghrehabadi, A.; Chamkha, A.J. Natural convection of a nanofluid in an enclosure with an inclined local thermal non-equilibrium porous fin considering Buongiorno's model. *Numer. Heat Transf. Part A Appl.* **2016**, *70*, 432–445. [CrossRef]

35. Sheremet, M.A.; Pop, I. Natural convection in a square porous cavity with sinusoidal temperature distributions on both side walls filled with a nanofluid: Buongiorno's mathematical model. *Transp. Porous Media* **2014**, *105*, 411–429. [CrossRef]
36. Motlagh, S.Y.; Soltanipour, H. Natural convection of Al_2O_3-water nanofluid in an inclined cavity using Buongiorno's two-phase model. *Int. J. Therm. Sci.* **2017**, *111*, 310–320. [CrossRef]
37. Garoosi, F.; Jahanshaloo, L.; Garoosi, S. Numerical simulation of mixed convection of the nanofluid in heat exchangers using a Buongiorno model. *Powder Technol.* **2015**, *269*, 296–311. [CrossRef]
38. Kefayati, G. Mixed convection of non-Newtonian nanofluid in an enclosure using Buongiorno's mathematical model. *Int. J. Heat Mass Transf.* **2017**, *108*, 1481–1500. [CrossRef]
39. Alsabery, A.I.; Armaghani, T.; Chamkha, A.J.; Hashim, I. Conjugate heat transfer of Al_2O_3–water nanofluid in a square cavity heated by a triangular thick wall using Buongiorno's two-phase model. *J. Therm. Anal. Calorim.* **2019**, *135*, 161–176. [CrossRef]
40. Corcione, M. Empirical correlating equations for predicting the effective thermal conductivity and dynamic viscosity of nanofluids. *Energy Convers. Manag.* **2011**, *52*, 789–793. [CrossRef]
41. Corcione, M.; Cianfrini, M.; Quintino, A. Two-phase mixture modeling of natural convection of nanofluids with temperature-dependent properties. *Int. J. Therm. Sci.* **2013**, *71*, 182–195. [CrossRef]
42. Wang, L.; Yang, X.; Huang, C.; Chai, Z.; Shi, B. Hybrid lattice Boltzmann-TVD simulation of natural convection of nanofluids in a partially heated square cavity using Buongiorno's model. *Appl. Therm. Eng.* **2019**, *146*, 318–327. [CrossRef]
43. Ho, C.; Liu, W.; Chang, Y.; Lin, C. Natural convection heat transfer of alumina-water nanofluid in vertical square enclosures: An experimental study. *Int. J. Therm. Sci.* **2010**, *49*, 1345–1353. [CrossRef]
44. Sheikhzadeh, G.A.; Dastmalchi, M.; Khorasanizadeh, H. Effects of nanoparticles transport mechanisms on Al_2O_3-water nanofluid natural convection in a square enclosure. *Int. J. Therm. Sci.* **2013**, *66*, 51–62. [CrossRef]
45. Putra, N.; Roetzel, W.; Das, S.K. Natural convection of nano-fluids. *Heat Mass Transf.* **2003**, *39*, 775–784. [CrossRef]
46. Chon, C.H.; Kihm, K.D.; Lee, S.P.; Choi, S.U. Empirical correlation finding the role of temperature and particle size for nanofluid (Al2O3) thermal conductivity enhancement. *Appl. Phys. Lett.* **2005**, *87*, 3107. [CrossRef]
47. Bergman, T.L.; Incropera, F.P. *Introduction to Heat Transfer*, 6th ed.; Wiley: New York, NY, USA, 2011.

nanomaterials

MDPI

Article

Investigation of Overlapped Twisted Tapes Inserted in a Double-Pipe Heat Exchanger Using Two-Phase Nanofluid

Mehdi Ghalambaz [1,2], Hossein Arasteh [3], Ramin Mashayekhi [4], Amir Keshmiri [5], Pouyan Talebizadehsardari [6,7,*] and Wahiba Yaïci [8,*]

1 Institute of Research and Development, Duy Tan University, Da Nang 550000, Vietnam; mehdi.ghalambaz@duytan.edu.vn
2 Faculty of Electrical–Electronic Engineering, Duy Tan University, Da Nang 550000, Vietnam
3 Department of Mechanical Engineering, Isfahan University of Technology, Isfahan 8415683111, Iran; h.arasteh.iut@gmail.com
4 Research & Development Team, Couette Limited, Altrincham WA14 2PX, UK; info@couette.co.uk
5 Department of Mechanical, Aerospace and Civil Engineering (MACE), The University of Manchester, Manchester M13 9PL, UK; A.Keshmiri@manchester.ac.uk
6 Metamaterials for Mechanical, Biomechanical and Multiphysical Applications Research Group, Ton Duc Thang University, Ho Chi Minh City 758307, Vietnam
7 Faculty of Applied Sciences, Ton Duc Thang University, Ho Chi Minh City 758307, Vietnam
8 CanmetENERGY Research Centre, Natural Resources Canada, 1 Haanel Drive, Ottawa, ON K1A 1M1, Canada
* Correspondence: ptsardari@tdtu.edu.vn (P.T.); wahiba.yaici@canada.ca (W.Y.); Tel.: +44-115-8376859 (P.T.); +1-613-996-3734 (W.Y.)

Received: 30 July 2020; Accepted: 21 August 2020; Published: 24 August 2020

Abstract: This study investigated the laminar convective heat transfer and fluid flow of Al_2O_3 nanofluid in a counter flow double-pipe heat exchanger equipped with overlapped twisted tape inserts in both inner and outer tubes. Two models of the same (co-swirling twisted tapes) and opposite (counter-swirling twisted tapes) angular directions for the stationary twisted tapes were considered. The computational fluid dynamic simulations were conducted through varying the design parameters, including the angular direction of twisted tape inserts, nanofluid volume concentration, and Reynolds number. It was found that inserting the overlapped twisted tapes in the heat exchanger significantly increases the thermal performance as well as the friction factor compared with the plain heat exchanger. The results indicate that models of co-swirling twisted tapes and counter-swirling twisted tapes increase the average Nusselt number by almost 35.2–66.2% and 42.1–68.7% over the Reynolds number ranging 250–1000, respectively. To assess the interplay between heat transfer enhancement and pressure loss penalty, the dimensionless number of performance evaluation criterion was calculated for all the captured configurations. Ultimately, the highest value of performance evaluation criterion is equal to 1.40 and 1.26 at inner and outer tubes at the Reynolds number of 1000 and the volume fraction of 3% in the case of counter-swirling twisted tapes model.

Keywords: overlapped twisted tape; two-phase; heat transfer; nanofluid; double-pipe

1. Introduction

In thermal engineering systems, convective heat transfer involves wide applications, including fuel cells [1], refrigeration [2], electronic device cooling [3], solar air collectors [4], and aerospace engineering [5]. The rise of energy demand at the turn of the new century has provoked the attention of researchers in this field of study to promote the efficiency of thermal energy systems. To increase

the thermohydraulic performance of engineering systems, different techniques have been proposed, among which using twisted tape inserts has been widely used [6,7]. Twisted tape generates a swirl flow that disturbs boundary layers of velocity and temperature inside the tube, which directly improves the heat transfer coefficient in a tube [8–11]. Applying additive nanoparticles to the base fluid to enhance the thermophysical properties of the working fluid has also been considered as an effective technique to modify heat transfer [12,13]. The hybrid nanofluids such as Ag–MgO–water [14,15], Ag–TiO_2 [16], Cu–Al_2O_3 [16,17], and MgO–MWCNTs/EG [18] as well as using of nonencapsulated phase change material suspension [19] are also promising for enhancement of heat transfer. On the other hand, combining different techniques to promote the thermohydraulic performance of thermal engineering systems as much as possible has been paid a lot of attention in recent years [20,21].

One of the recent compound methods in heat transfer enhancement is the hybrid employment of nanofluids and inserted twisted tapes [22]. In what follows, the recent achievements of such problem are discussed. Some researchers have focused on the effects of pitch and width ratios of twisted tapes. Jaramillo et al. [23] used the twisted tape inserts in a parabolic collector. Their results indicate the higher thermal performance of the collector in low twisted ratios operating at low values of Reynolds number. This type of collector equipped with wall-detached twisted tape inserts was also investigated numerically by Mwesigye et al. [24]. They showed that, as twist ratio increases and width ratio reduces, the optimal Reynolds number enhances. A numerical study of a tri-lobbed tube equipped with twisted tapes was performed by Esfe et al. [25]. They showed that pitch ratio enhancement causes an increase in Nusselt number, friction factor, and overall thermal performance.

Using twisted tapes in double-pipe heat exchangers has also been examined by many researchers. The use of twisted tape elements in the inner tube of a double-pipe heat exchanger with clockwise and counterclockwise swirling directions was performed experimentally by Man et al. [26]. The results indicate a higher heat exchanger efficiency by using twisted tape inserts so that the highest PEC number was equal to 1.42 and was reported under the empirical conditions. The use of twisted tapes in a double-tubes at various pitch ratios was examined by Lim et al. [27]. They predicted heat transfer characteristics for different Reynolds number values. Ravi Kumar et al. [28] evaluated the thermal performance of a double-tube U-bend system inserting twisted tapes using the ε-NTU method and found higher effectiveness and number of heat transfer units.

Another enhancement technique of twisted tape inserts is to enhance the flow mixing and secondary flow effects by changing the geometry of twisted tapes. Saylroy and Eiamsa-ard [29] analyzed square-cut twisted-tape inserts in a circular tube and showed the highest PEC number of 1.37 with thermal performance improvement of about 1.32 times higher than the classically twisted tape inserts. In another study [30], they investigated the multi-channel twisted tapes with constant wall temperature. They showed an enhancement of laminar convection heat transfer by applying such twisted tapes. He et al. [31] applied to cross hollow twisted tape inserts in a tube to study the thermal characteristics empirically. They showed that the PEC number ranges from 0.87 to 0.98 for Reynolds numbers varying from 5600 to 18,000. Samruaisin et al. [32] embedded quadruple twisted tapes in a tube to analyze experimentally and numerically the efficacies of twisted tape arrangement and free space ratio in a turbulent regime. They reported the maximum value of 1.27 for PEC numbers in the range of studied operational conditions. Ruengpayungsak et al. [33] investigated centrally perforated twisted tape inserts numerically in both laminar and turbulent regimes. They reported the maximum value for PEC number equal to almost 8.92 and 1.33 for laminar and turbulent regimes, respectively. Hasanpour et al. [34] investigated a corrugated tube inserting twisted tapes using the optimization method on experimental tests. The maximum heat transfer rate is gained at V-cut twisted tape model, and the minimum pressure drop is achieved at perforated twisted tape model.

The application of using nanofluid combined with twisted tape is also studied. Sunder et al. [26] examined a solar water heater experimentally using passive techniques of nanofluid and twisted tape. They concluded that, for Reynolds number equal to 13,000 with 3% nanoparticles, 49.75% enhancement in heat transfer was achieved for the case in the presence of twisted tape with a pitch to diameter ratio

of 5, while it is equal to only 21% for the plain tube. Qi et al. [35] accomplished an experimental study of convective nanofluid employing rotating and static built-in twisted tapes. They showed that using rotating twisted tape along with the nanofluid results in a 101.6% enhancement in heat transfer.

Another form of twisted tape inserts technique to enhance the thermal performance over the pumping power penalty, namely overlapped twisted tapes. Hong et al. [36] conducted an empirical study of a spiral grooved tube equipped with twin overlapped twisted tapes with Reynolds numbers of 8000 to 22,000, showing an enhancement in both heat transfer and friction coefficient as the overlapped twisted ratio augments. In another study [36], they employed overlapped multiple twisted tapes in a similar experiment. They showed higher entropy generation due to friction resistance and lower entropy generation due to heat transfer for a higher number of tapes and lower overlapped twisted ratios. Eiamsa-Ard and Samravysin [37] conducted an empirical study on overlapped-quadruple twisted tape inserts comparing to typical quadruple twisted tape elements for various Reynolds number under a turbulent regime. They reported the maximum value of 1.58 for PEC number at Reynolds number of 5000. Eiamsa-Ard et al. [37] in a numerical and experimental study employed overlapped dual twisted tapes along with nanofluid using TiO_2 nanoparticles. They showed an 89% enhancement in heat transfer and 113% in thermal performance compared with the plain tube. Overlapped dual twisted tapes along with Al_2O_3 nanofluid were studied by Rudrabhiramu et al. [38]. They reported that using 1% nanofluid volume concentration and twisted tape twist pitch ratio of 2 causes the best result compared to all other captured cases.

According to the aforementioned literature review, the simultaneous implementation of various enhancement techniques leads to hybrid effects that offer higher thermal performance relative to the corresponding values achieved from each method. Applying both nanofluid and twisted tape inserts has been introduced as a promising way. However, reviewing the preceding papers reveals that the effects of overlapped twisted tape inserts in inner and outer tubes of double-pipe heat exchangers are rarely discussed in the literature. Motivated by this research gap, the main objective of this study was to investigate the heat transfer enhancement and fluid flow characteristics of Al_2O_3 nanofluid in a double-pipe counter flow heat exchanger equipped with overlapped twisted tape inserts in inner and outer tubes with the same and opposite angular directions. Different effective parameters, including Reynolds number and the volume fraction of nanoparticles, were also analyzed by various contour plots and diagrams.

2. Problem Statement

Figure 1 schematically shows the counter flow double-pipe system equipped with overlapped twisted tapes in inner and outer tubes. The inner and outer tubes diameters are 10 and 29 mm, the thickness of the twisted tape is 0.4 mm with equivalent pitches of 100 mm. Two models for embedding the overlapped twisted tapes are considered: in the first model, the inner and outer twisted tapes swirl in the same angular direction (Co-STT as an abbreviation of co-swirling twisted tapes), and, in the second model, the inner and outer twisted tapes swirl in an opposite angular direction (Counter-STT as an abbreviation of counter-swirling twisted tapes). The plain heat exchanger (PHE) is also studied compared with the twisted tape cases. Al_2O_3–water nanofluid enters the inner and outer tubes at a temperature of 300 K, considering four different Reynolds numbers.

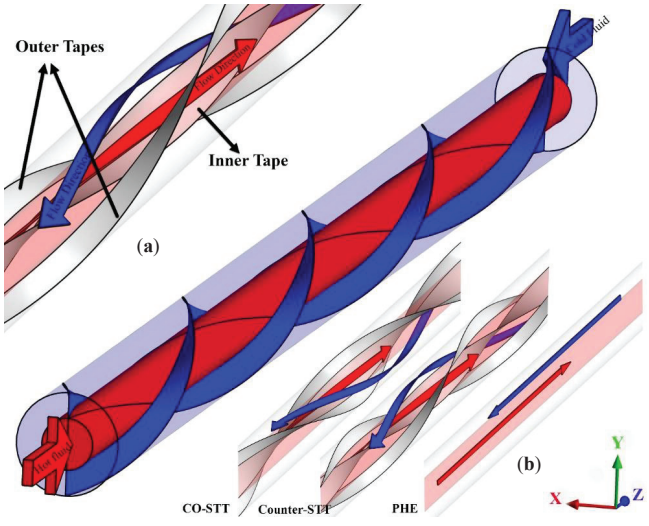

Figure 1. (**a**) Current study Schematic diagram with overlapped twisted tapes; and (**b**) comparison of the different proposed cases.

2.1. Governing Equations

A steady-state laminar incompressible Al_2O_3–water nanofluid flow neglecting the effects of radiation and viscosity losses is studied. The two-phase mixture model is used to simulate Al_2O_3 nanoparticles dispersed in water as follows:

- Continuity equation:

$$\vec{\nabla}.\left(\rho_m \vec{V}_m\right) = 0 \tag{1}$$

- Momentum equation:

$$\vec{\nabla}.\left(\rho_m \vec{V}_m \vec{V}_m\right) = -\vec{\nabla}p + \nabla.\left[\mu_m\left(\vec{\nabla}\vec{V}_m + \vec{\nabla}\vec{V}_m{}^T\right)\right] + \rho_m g + \vec{F} - \vec{\nabla}.\left(\sum_{k=1}^{n} \phi_k \rho_k \vec{V}_{dr,k}\vec{V}_{dr,k}\right) \tag{2}$$

where the drift velocity of the secondary phase drift is computed from:

$$\vec{V}_{dr,k} = \vec{V}_k - \vec{V}_m \tag{3}$$

- Energy equation:

$$\vec{\nabla}.\left[\sum_{k=1}^{n}\left(\rho_k c_{pk}\right)\phi_k \vec{V}_k T\right] = \vec{\nabla}.k_m \vec{\nabla}T \tag{4}$$

V_m and ρ_m are the average mass velocity and mixture density, respectively, which are determined as:

$$\vec{V}_m = 1/\rho_m\left(\sum_{k=1}^{n} \phi_k \rho_k \vec{V}_k\right) \tag{5}$$

$$\rho_m = \sum_{k=1}^{n} \phi_k \rho_k \tag{6}$$

In Equation (5), ϕ_k represents the volume fraction of the mixture kth phase.
The relative velocity for the two phases and the mixture viscosity are calculated as:

$$\vec{V}_{pf} = \vec{V}_p - \vec{V}_f \tag{7}$$

$$\mu_m = \sum_{k=1}^{n} \phi_k \mu_k \tag{8}$$

The relative velocity proposed by Manin [39] and Shiller Newman drag function [40] are used as follows:

$$\vec{V}_{pf} = \frac{\rho_p d_p^2 \left(\rho_p - \rho_m\right)}{18 \mu_f f_{drag} \rho_p} \left[g - \left(\vec{\nabla} . \vec{V}_m \right) \vec{V}_m \right] \tag{9}$$

$$f_{drag} = \begin{cases} 1 + 0.15 Re_p^{0.687} & ; \; Re_p \leq 1000 \\ 0.0183 Re_p & ; \; Re_p > 1000 \end{cases} \tag{10}$$

Hence, the drift velocity is given as:

$$\vec{V}_{dr,p} = \vec{V}_{pf} - \sum_{k=1}^{n} \left(\frac{\phi_k \rho_k}{\rho_m} \vec{V}_{fk} \right) \tag{11}$$

2.2. Nanofluid Thermo-Physical Properties

The thermophysical properties of water–Al_2O_3 nanofluid are presented in Equations (12)–(15). The density of water–Al_2O_3 nanofluid is calculated using Khanafer and Vafai [41] model as follows:

$$\rho_{nf} = (1 - \phi)\rho_f + \phi \rho_s \tag{12}$$

The specific heat capacity of water–Al_2O_3 nanofluid is defined using Bianco et al. [42] model as Equation (13):

$$\left(\rho c_p\right)_{nf} = (1 - \phi)\left(\rho c_p\right)_f + \phi \left(\rho c_p\right)_s \tag{13}$$

The effective dynamic viscosity of water–Al_2O_3 nanofluid is determined using Maiga et al. [43] model as below:

$$\mu_{nf} = \frac{\mu_f}{(1 - \phi)^{2/5}} \tag{14}$$

The effective conductivity of water–Al_2O_3 nanofluid is calculated using Qi et al. [35] model as the following equation:

$$k_{nf} = 1 + 2.72\phi + 4.97\phi^2 \tag{15}$$

The water–Al_2O_3 nanofluid with three values of volume fractions are listed in Table 1.

Table 1. Water–Al_2O_3 nanofluid thermo-physical properties.

Nanoparticle Properties				
	$\rho\left(\frac{kg}{m^3}\right)$	$c_p\left(\frac{J}{kgK}\right)$	$k\left(\frac{W}{mK}\right)$	$\mu(Pa\ s)$
	3880	733	36	-
Nanofluid Properties				
	$\rho\left(\frac{kg}{m^3}\right)$	$c_p\left(\frac{J}{kgK}\right)$	$k\left(\frac{W}{mK}\right)$	$\mu(Pa\ s)$
$\phi = 0$	998.2	4182	0.6	1.00×10^{-03}
$\phi = 0.01$	1027.018	4147.51	0.616618	0.001089
$\phi = 0.02$	1055.836	4113.02	0.633833	0.001199
$\phi = 0.03$	1084.654	4078.53	0.651644	0.001334

2.3. Boundary Conditions and Data Deduction

At the heat exchanger, inner and outer tubes inlet, uniform velocity and temperature profiles are applied to the boundary conditions. At the outlets, zero relative gauge pressure is considered. The outer wall of the outer tube is thermally isolated, and the coupled-wall boundary is used in the interface wall.

The hydrothermal parameters employed in this study are defined as follows:

$$D_h = \frac{4A}{P} \tag{16}$$

$$f = \frac{2\Delta P D_h}{\rho_{nf} U_m^2 L} \tag{17}$$

$$h = \frac{q}{T_w - T_b} \tag{18}$$

$$Nu_x = \frac{h_x D_h}{k} \tag{19}$$

$$Nu_{avg} = \frac{1}{L}\int_0^L Nu_x dx \tag{20}$$

$$PEC = \frac{Nu/Nu_0}{(f/f_0)^{1/3}} \tag{21}$$

3. Numerical Procedure

The commercial ANSYS-FLUENT code was employed in this study using the Coupled algorithm for velocity–pressure coupling using the second-order upwind scheme. The convergence criteria for energy and Navier–Stokes equations were considered 10^{-6}.

3.1. Grid Study

Figure 2 depicts the meshing of the computational domain, which is fully structured to enhance the quality of the results along with reducing the computational time. Finer mesh near the walls due to the presence of severe velocity and temperature gradients is also considered.

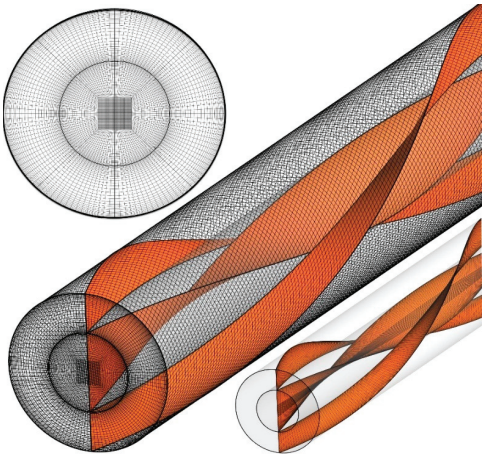

Figure 2. The meshing of the computational domain.

Grids with different numbers of mesh elements are examined considering the average Nusselt number as the criteria to examine the grid independency. Table 2 presents the cases considered for mesh independence analysis. The percentage of the difference between two consecutive grids are also presented. Case 5 is chosen for all the simulations, since using finer meshing leads to relative errors less than two percent.

Table 2. Grid independency analysis.

Case	Number of Elements	Nusselt Number	Error (%)
3	2,000,000	15.53	-
4	2,750,000	14.36	7.53
5	3,500,000	13.87	3.41
6	4,250,000	13.65	1.59
7	5,000,000	13.55	0.73

3.2. Validation

To verify the code, the experimental results of Qi et al. [35] for the average Nusselt number for laminar nanofluid flow in a circular tube made of stainless steel using stationary and rotating twisted tapes were used. They used a motor to drive the rotation of the twisted tape which was set to 5 RPM. They experimentally examined different concentrations of TiO_2/water nanofluid (0.1%, 0.3%, and 0.5%) at different Reynolds numbers (600–7000) in a circular tube, with inner diameter, thickness and length of 22, 2, and 1400 mm (only the middle section (1000 mm) was used as the test section), respectively, equipped with twisted tape inserts with the length, pitch size, width, and thickness of 1600, 100, 16, and 2 mm, respectively. They chose relatively low mass concentrations of nanoparticles to reach a better stability for the nanofluid. They discussed the results based on the line relationship between the shear stress and shear rate that TiO_2 nanofluids can be approximately regarded as a kind of Newtonian fluid, and the non-Newtonian effects can be ignored.

Figure 3 displays the average Nusselt number for the stationary twisted tape with nanofluid volume concentration of 0.5% at different Reynolds numbers ranging from 600 to 2200. As shown, the results are in excellent agreement with the experimental data of Qi et al. [35] where the maximum difference is less than 3.5%, as displayed in Table 3.

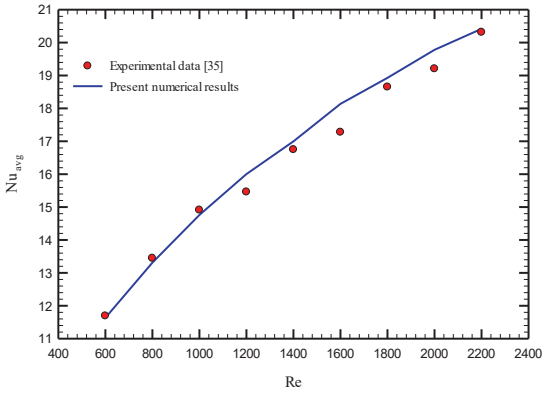

Figure 3. Validation results with the study of Qi et al. [35]. Reproduced with permission from [35]. Copyright Elsevier, 2020.

Table 3. Deviation of current numerical results from experimental data [35]. Reproduced with permission from [35]. Copyright Elsevier, 2020.

Experimental Data [35]	Present Numerical Results	Error (%)
11.6901	11.6316	0.5004
13.4444	13.31	0.9997
14.9064	14.7573	1.0002
15.462	16.0032	3.5002
16.7485	16.9997	1.4999
17.2749	18.1386	4.9998
18.6491	18.9288	1.4998
19.2047	19.7808	2.9998
20.3158	20.4174	0.5001

4. Results

Two models for embedding the overlapped twisted tapes were considered: in the first model, the inner and outer twisted tapes swirl in the same angular direction (Co-STT), and, in the second, model, the inner and outer twisted tapes swirl in an opposite angular direction (Counter-STT). The proposed models were analyzed for four Reynolds numbers (250, 500, 750, and 1000) employing Al_2O_3 nanofluid at four concentrations (0, 1, 2, and 3%). It should be noted that, in the following, first, the different cases shown in Figure 1 are examined using pure water as the HTF to find the best configuration. Then, for the best system, the effects of nanoparticle concentration are assessed.

4.1. Effect of Double-Pipe Configurations

The distribution of bulk temperature in the heat exchanger inner and outer tubes throughout the channel length for water as the working fluid at various Reynolds numbers is displayed in Figure 4. The fluid temperature from the inlet to outlet is different for inner and outer tubes so that the fluid flowing through the outer tube experiences fewer changes than that for the inner tube. The reason is because of the difference in mass flow rate values of inner and outer tubes since the higher mass flow rate at the outer tube causes fewer changes in the fluid temperature along the heat exchanger length. It is also visible that the fluid temperature undergoes more changes in lower Reynolds numbers due to the lower fluid velocity resulting in more time for fluids flowing through the inner and outer tubes from the heat exchanger's inlet to outlet to exchange heat. Another point that is visible in this figure is that, at a given Reynolds number, the fluid outlet temperature in PHE is different compared with Co-STT and Counter-STT cases so that the twisted tape cases show a higher temperature difference between the heat exchanger inlet and outlet in comparison with the PHE. In fact, at a given Reynolds number, higher variation in fluid temperature from inlet to outlet implies higher heat transferring between the fluid flowing through inner and outer tubes resulting in higher heat exchanger efficiency. As a result, applying twisted tapes in both tubes of the heat exchanger causes a thermal enhancement. The reason is that in the twisted tape cases, secondary flow is created as a result of flow swirling, which consequently improves the flow mixing, disturbs the thermal boundary layer and enhances the heat transfer rate. In other words, the twisted tape redirects the colder core fluid with a better cooling capability to the heat exchanger interface wall causing higher thermal performance of the system.

For a better comparison between the bulk temperature distributions of the proposed cases along the heat exchanger length at a given Reynolds number, Figure 5 illustrates the local bulk temperature at the Re = 250. It is visible that the temperature difference of the heat exchanger's inlet and outlet is higher in Co-STT and Counter-STT cases in comparison with the PHE. Comparing the two cases of Co-STT and Counter-STT, a slightly higher fluid temperature difference of the heat exchanger's inlet and outlet is visible in the Counter-STT case due to the opposite angular direction of the twisted tapes in the inner and outer tubes.

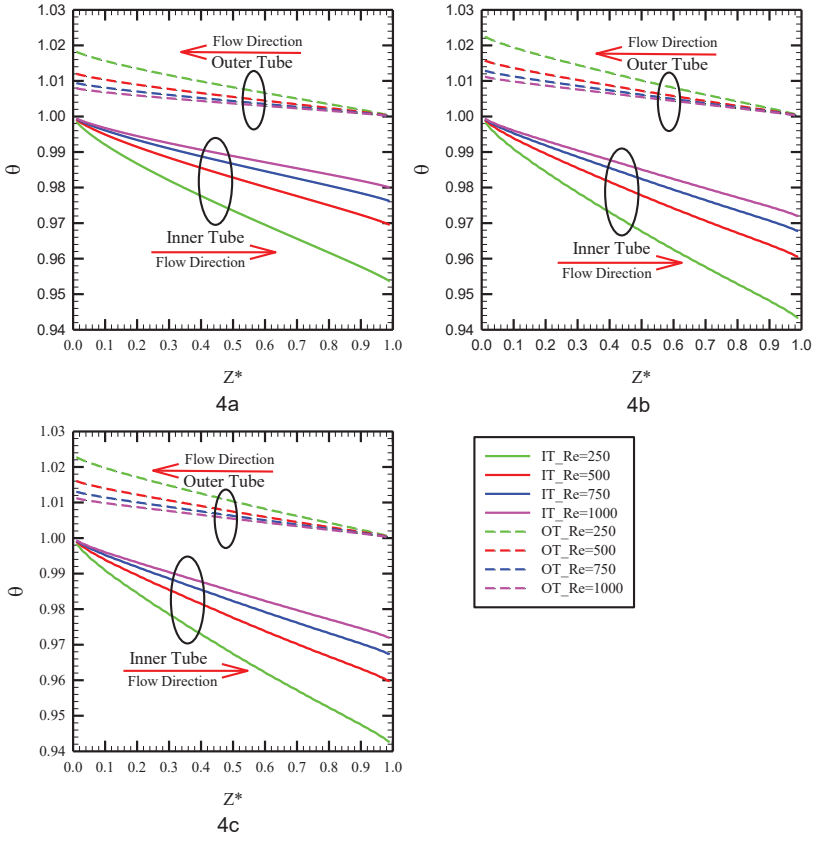

Figure 4. Local bulk temperature distribution along the length of the tube at Reynolds number of 250 for: (**a**) PHE; (**b**) Co-STT; and (**c**) Counter-STT.

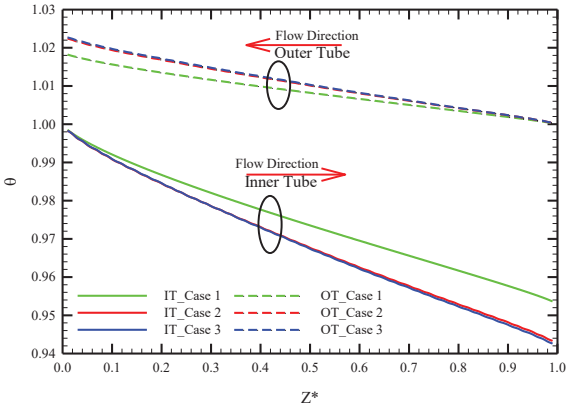

Figure 5. Local bulk temperature distribution along the length of the tube for PHE, Co-STT and Counter-STT at Reynolds number of 250.

Figure 6 displays the heat flux between the inner and outer tubes for different proposed cases. As shown, the transferred heats for the double-pipe inserts (Cases 2 and 3) are much higher than that for Case 1. Besides, Case 3 has a slight advantage compared with Case 2 according to the transferred heat flux between the pipes. For example, for the Reynolds number of 250 and $\phi = 0$, the heat flux for Case 3 is 6.67 W, which is 29.62 and 4.82% higher than Cases 1 and 2, respectively.

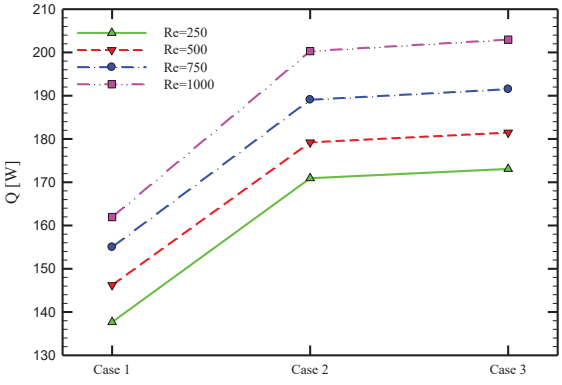

Figure 6. Local bulk temperature distribution along the length of the tube for PHE, Co-STT and Counter-STT at Reynolds number of 250.

To better quantify the heat transfer rate, the average variations of the Nusselt number of the heat exchanger's inner and outer tubes for various cases of PHE, Co-STT, and Counter-STT are shown in Figure 7 at four different Reynolds number. Using Co-STT and Counter-STT cases increases the average Nusselt number by about 35.24 and 42.09% at Reynolds number of 250; 43.18 and 52.46% at Reynolds number of 500; 54.15 and 61.05% at Reynolds number of 750; and 66.20 and 68.69% at Reynolds number of 1000 with respect to the PHE, respectively. Analyzing the enhanced Nusselt number percentage for different cases of the inserted twisted tape implies that the Counter-STT case leads to higher thermal performance compared with the Co-STT case, and both are significantly better in heat transfer enhancement than PHE. In addition, higher Nusselt number values for higher Reynolds numbers due to the enhancement of the advection phenomenon and more fluid momentum is visible at this figure.

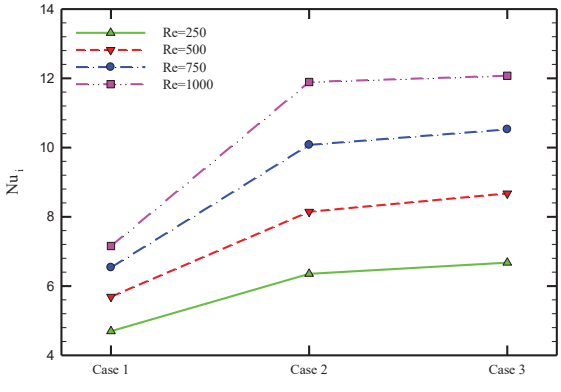

Figure 7. Average Nusselt number for PHE, Co-STT, and Counter-STT at various Reynolds numbers.

Figure 8 demonstrates the friction coefficient variations for the cases of PHE, Co-STT, and Counter-STT at different Reynolds numbers. Applying twisted tape increases the friction coefficient due to the added surface area and flow blockage created by the twisted tape inserted in the tube. Furthermore, there is no difference between the friction coefficient values of the Co-STT and Counter-STT cases as the secondary flow intensity, added surface area, and flow blockage effects are the same in both cases. Moreover, the friction coefficient decreases at higher Reynolds numbers. This can be explained using Equation (17) in which there exists velocity to the power of two in the denominator of friction coefficient correlation.

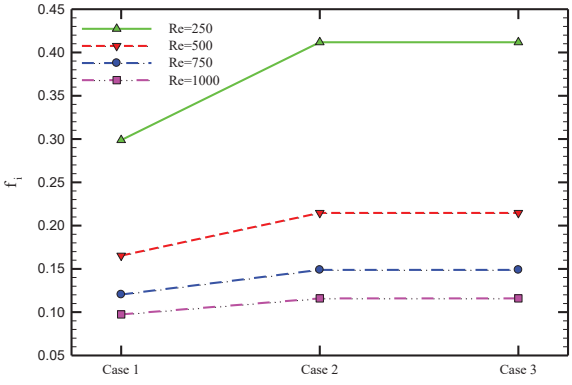

Figure 8. Variations of friction coefficient for different cases of PHE, Co-STT, and Counter-STT at various Reynolds numbers.

Figure 9 shows the cross-sectional velocity contours for PHE, Co-STT, and Counter-STT at Re = 250. It is visible that applying the twisted tapes at both inner and outer tubes redirects the core fluid with higher velocity and heat transfer capacity to the vicinity of the interface wall causing higher thermal performance. There is no difference between the velocity contours of Co-STT and Counter-STT cases since the direction of the twisted tape does not affect the velocity distribution. In addition, comparing the red colors of different cases, showing higher velocity at the fluid core, it can be implied that the twisted tapes create a secondary flow and better mixing causing higher velocity and advection phenomenon near the interface wall, and, as a result, a higher heat transfer rate is obtained.

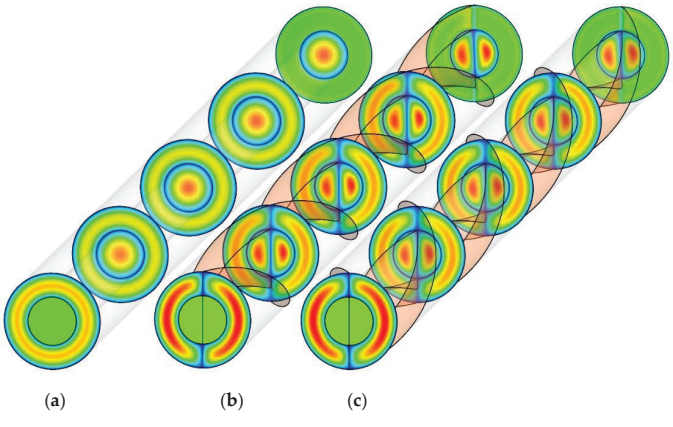

Figure 9. Cross-sectional velocity contours at the Reynolds number of 250 for: (**a**) PHE; (**b**) Co-STT; and (**c**) Counter-STT.

Figure 10 displays the cross-sectional temperature contours for PHE, Co-STT, and Counter-STT at the Reynolds number of 250. The PHE temperature contours show the normal development of thermal boundary layer in both inner and outer tubes as the fluid flows through the unit; however, the temperature contours at the cases of Co-STT and Counter-STT are different so that the thermal boundary layer disturbance occurs and secondary flow and better flow mixing affect the boundary layer causing higher heat exchanger efficiency. Moreover, looking at the temperature distributions at the tubes' outlet implies the fact that using twisted tape causes a higher amount of fluid to participate in the heat transfer process between the tubes due to the presence of secondary flow and better flow mixing by substituting the fluid near the interface wall with the core fluid and vice versa. Comparing the temperature distribution for the two cases of Co-STT and Counter-STT shows that, in the Counter-STT case, the secondary flow at both tubes causes the regions with thinnest thermal boundary layer in both tubes to be in direct contact with each other and are placed in the same angular direction, resulting in higher thermal performance in comparison with Co-STT case. Thus, the regions in the outer tube with the thinnest thermal boundary layer are in direct contact with the regions in the inner tube with the thickest thermal boundary layer.

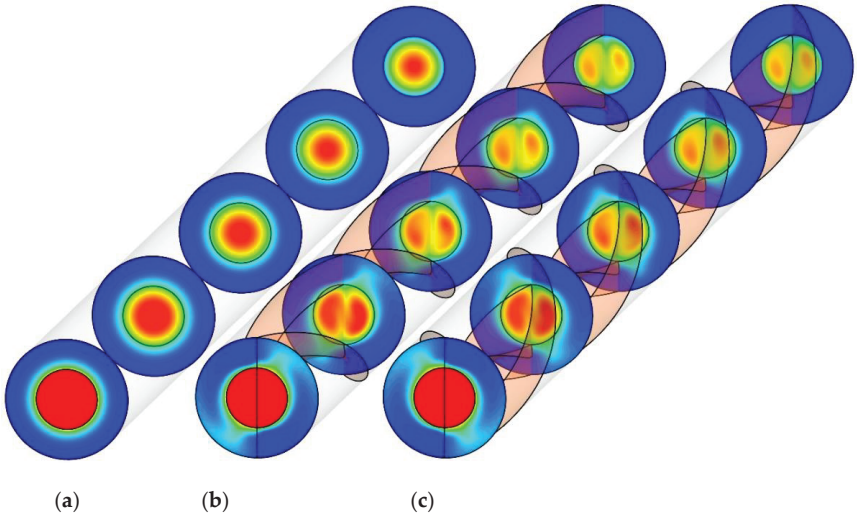

Figure 10. Cross-sectional temperature contours at Reynolds number of 250 for: (**a**) PHE; (**b**) Co-STT; and (**c**) Counter-STT.

Figure 11 illustrates the temperature contour at the interface wall of the heat exchanger for PHE, Co-STT, and Counter-STT at the Reynolds number of 250. The temperature distribution on the interface wall implies the intensity of the secondary flow affecting the interface wall. In the PHE, the temperature enhances uniformly as the fluid flows along the heat exchanger length showing the thermal boundary layer development. In contrast, in the presence of twisted tapes in the inner and outer tubes, the disturbance in the thermal boundary layer increases, which is enhanced in Counter-STT compared with Co-STT, implying higher thermal performance.

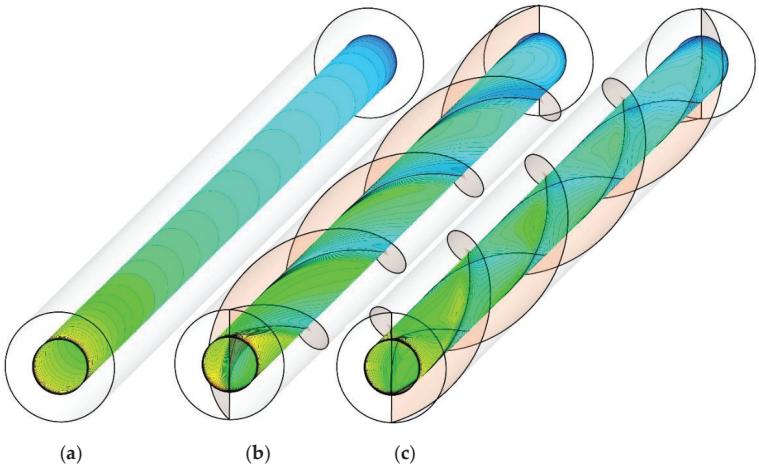

Figure 11. Temperature contours on the interface wall of the heat exchanger at Reynolds number of 250 for: (**a**) PHE; (**b**) Co-STT; and (**c**) Counter-STT.

4.2. Effect of Nanoparticle Concentration on the Performance of Counter-STT Compared with Co-STT

To investigate the effects of Al_2O_3 nanofluid in the case of Counter-STT, Figure 12 depicts the variations of Nusselt number at the inner and outer tubes in terms of Reynolds number at various volume concentrations of the nanofluid. For all Reynolds numbers, adding nanoparticles to the base-fluid augments the Nusselt number at both inner and outer tubes of the heat exchanger results in the higher thermal efficiency of the heat exchanger. Dispersing nanoparticles modifies the fluid thermal properties, including thermal conductivity, resulting in a higher heat transfer rate.

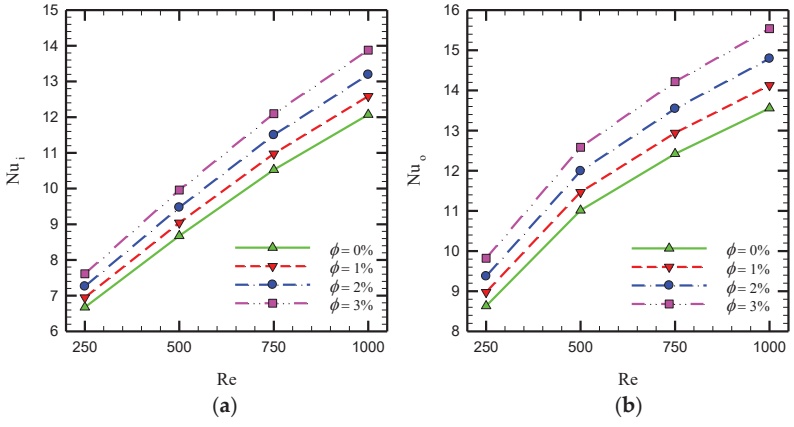

Figure 12. Average Nusselt number for different volume fractions of nanoparticles in terms of Reynolds number for Counter-STT case at (**a**) inner and (**b**) outer tubes of the heat exchanger.

Figure 13 depicts the variations of friction factor at the inner and outer tubes in terms of Reynolds number at various volume concentrations of the nanofluid in the case of Counter-STT. Using nanoparticles enhances the viscosity of the fluid, causing higher friction coefficient magnitudes. Moreover, using nanofluids in such geometries, including twisted tape inserts causing intense flow mixing and secondary flow, seems to be beneficial as it prevents undesirable phenomena, including the possible agglomeration and sedimentation of nanoparticles.

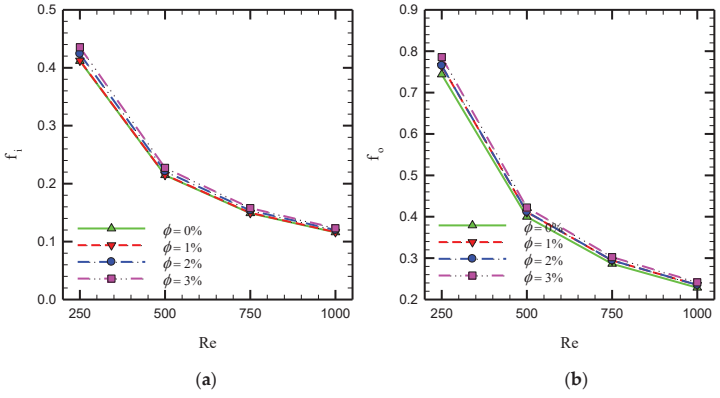

Figure 13. Variations of friction coefficient in terms of Reynolds number for different volume fractions of nanoparticles for Counter-STT case (**a**) inner and (**b**) outer tubes of the heat exchanger.

As discussed above, the twisted tape inserts augment both the heat transfer rate as a desirable objective and friction coefficient as an undesirable parameter. Therefore, there is a trade-off between the benefits of using twisted tape in thermal performance enhancement and the side effects in forcing more pumping power to the system. To analyze this issue, the dimensionless PEC introduced in Equation (21) is discussed here. In fact, this number is employed to evaluate the practical use of any enhancement techniques in the viewpoint of energy-saving potential. Generally, higher values of PEC imply superior energy saving. Figure 14 illustrates the PEC parameter for PHE, Co-SST, and Counter-SST at the inner and outer tubes. Using nanofluid and increasing its volume concentration results in higher PEC values showing more enhanced heat transfer than enhanced friction coefficient in such configurations. In addition, it can be observed that, for a higher Reynolds number, the PEC number enhances as well, implying better energy saving in higher velocities of the inlet fluid flowing through both inner and outer tubes. Moreover, the figure shows that the Counter-STT model yields higher PEC values compared with that for the Co-STT model in all Reynolds numbers and nanofluid volume concentrations. Ultimately, the highest value of PEC number is equal to 1.40 and 1.26 in the inner and outer tubes, which are found at Re = 1000, the volume fraction of 3%, and Counter-STT model.

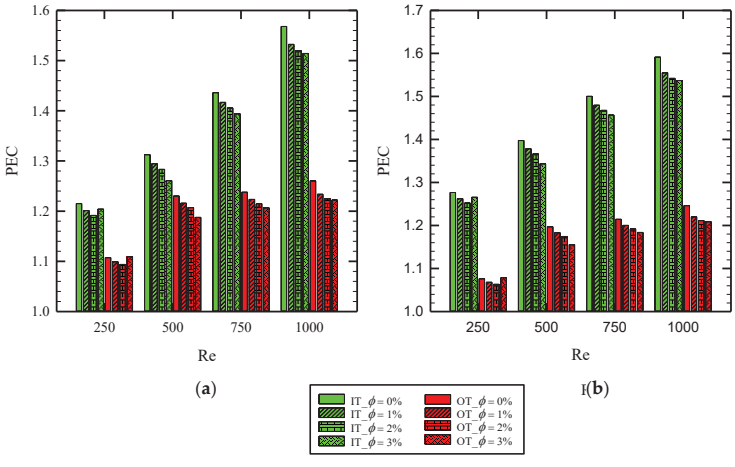

Figure 14. PEC parameter at different Reynolds numbers and nanoparticles volume fractions for different cases of: (**a**) Co-STT; and (**b**) Counter-STT.

5. Conclusions

Benefiting from the compound heat transfer enhancement techniques of overlapped twisted tape and nanofluid, this study numerically investigated the flow of Al_2O_3 nanofluid through a counter flow double pipe in which both inner and outer tubes are equipped with overlapped twisted tape inserts in two models of the same (Co-STT) and opposite (Counter-STT) angular directions. A parametric study was conducted to evaluate the effect of key design variables, including the angular direction, Reynolds number, and nanofluid volume fraction on the thermo-hydraulic characteristics of such a configuration. Dimensionless number of PEC was employed to assess the trade-off between enhancement in heat transfer and pressure drop. The following outcomes are obtained from this study:

- Using Co-STT and Counter-STT, respectively, increase the average Nusselt number by about 35.2–66.2% and 42.1–68.7% over the Reynolds number ranging 250–1000 due to the creation of secondary flow and more intense flow mixing in the presence of overlapped twisted tape inserts. Ultimately, it was shown that the highest values of PEC number are equal to 1.40 and 1.26 for the inner and outer tubes, respectively, which are found at the Reynolds number of 1000, the volume fraction of 3% and Counter-STT model. The finding of this research provides a framework for researchers working on novel combined techniques for heat transfer enhancement.

Author Contributions: R.M. and P.T. performed and designed the numerical simulations; H.A., R.M. and A.K. analyzed the data and performed the discussion; M.G., H.A., A.K. and W.Y. wrote the paper. All authors have read and agreed to the published version of the manuscript.

Funding: The APC was funded by Wahiba Yaïci from CanmetENERGY Research Centre, Natural Resources Canada.

Conflicts of Interest: The authors declare no conflict of interest.

Nomenclature

A	area (m^2)	**Greek symbols**	
c_p	specific heat transfer (J/kg.K)	ϑ	kinematic viscosity (m^2/s)
f	friction coefficient	μ	dynamic viscosity (kg/ms)
f_0	friction coefficient of plain channel	ρ	density (kg/m^3)
F	body force (N)	ϕ	nanofluid concentration
g	gravitational acceleration (m/s^2)	θ	dimensionless temperature
h	heat transfer coefficient (W/m^2K)	**Subscripts**	
k	thermal conductivity (W/mK)	ave	average
n	number of phases	b	bulk
p	pressure (Pa)	m	mixture
q″	heat flux (w/m^2)	f	fluid
Re	Reynolds number	i	inner tube
T	temperature (K)	o	outer tube
V	velocity vector (m/s)	nf	nanofluid
V_{dr}	drift velocity	**Abbreviations**	
V_f	fluid velocity	Co-STT	co-swirling twisted tapes
V_p	particle velocity	Counter-STT	counter-swirling twisted tapes
		PHE	plain heat exchanger
		IT	inner tube
		OT	outer tube

References

1. Hosseini, M.; Afrouzi, H.H.; Arasteh, H.; Toghraie, D. Energy analysis of a proton exchange membrane fuel cell (PEMFC) with an open-ended anode using agglomerate model: A CFD study. *Energy* **2019**, *188*, 116090. [CrossRef]
2. Keshtkar, M.M.; Talebizadeh, P. Multi-Objective Optimization of a R744/R134a Cascade Refrigeration System: Exergetic, Economic, Environmental, and Sensitive Analysis (3ES). *J. Therm. Eng.* **2019**, *5*, 237–250. [CrossRef]

3. Arshad, A.; Jabbal, M.; Sardari, P.T.; Bashir, M.A.; Faraji, H.; Yan, Y. Transient simulation of finned heat sinks embedded with PCM for electronics cooling. *Therm. Sci. Eng. Prog.* **2020**, *18*, 100520. [CrossRef]
4. Boulemtafes-Boukadoum, A.; Boualbani, R.; Benzaoui, A.; El Mokretar, S. 3D numerical investigation of convective heat transfer and friction in solar air collector's channel roughened by triangular ribs. In Proceedings of the AIP Conference Proceedings, Poznan, Poland, 11 December 2019; p. 020037. [CrossRef]
5. Zhang, T.; Geng, S.; Mu, X.; Chen, J.; Wang, J.; Wu, Z. Thermal Characteristics of a Stratospheric Airship with Natural Convection and External Forced Convection. *Int. J. Aerosp. Eng.* **2019**, *2019*. [CrossRef]
6. Bellos, E.; Tzivanidis, C. Enhancing the Performance of Evacuated and Non-Evacuated Parabolic Trough Collectors Using Twisted Tape Inserts, Perforated Plate Inserts and Internally Finned Absorber. *Energies* **2018**, *11*, 1129. [CrossRef]
7. Chaedir, B.A.; Kurnia, J.C.; Chen, L.; Jiang, L.; Sasmito, A.P. Numerical Investigation of Ventilation Air Methane Catalytic Combustion in Circular Straight and Helical Coil Channels with Twisted Tape Insert in Catalytic-Monolith Reactors. *Catalysts* **2020**, *10*, 797. [CrossRef]
8. Chougule, S.S.; Nirgude, V.V.; Sahu, S.K. Experimental study on laminar forced convection of Al2O3/water and multiwall carbon nanotubes/water nanofluid of varied particle concentration with helical twisted tape inserts in pipe flow. *Heat Transf. Eng.* **2018**, *39*, 806–818. [CrossRef]
9. Gunes, S.; Karakaya, E. Thermal characteristics in a tube with loose-fit perforated twisted tapes. *Heat Transf. Eng.* **2015**, *36*, 1504–1517. [CrossRef]
10. Patil, S.V.; Babu, P.V. Heat transfer and pressure drop studies through a square duct fitted with increasing and decreasing order of twisted tape. *Heat Transf. Eng.* **2014**, *35*, 1380–1387. [CrossRef]
11. Wijayanta, A.T.; Mirmanto; Aziz, M. Heat transfer augmentation of internal flow using twisted tape insert in turbulent flow. *Heat Transf. Eng.* **2020**, *41*, 1288–1300. [CrossRef]
12. Arasteh, H.; Mashayekhi, R.; Ghaneifar, M.; Toghraie, D.; Afrand, M. Heat transfer enhancement in a counter-flow sinusoidal parallel-plate heat exchanger partially filled with porous media using metal foam in the channels' divergent sections. *J. Therm. Anal. Calorim.* **2019**, 1–17. [CrossRef]
13. Eisapour, M.; Eisapour, A.H.; Hosseini, M.; Talebizadehsardari, P. Exergy and energy analysis of wavy tubes photovoltaic-thermal systems using microencapsulated PCM nano-slurry coolant fluid. *Appl. Energy* **2020**, *266*, 114849. [CrossRef]
14. Mehryan, S.; Ghalambaz, M.; Chamkha, A.J.; Izadi, M. Numerical study on natural convection of Ag–MgO hybrid/water nanofluid inside a porous enclosure: A local thermal non-equilibrium model. *Powder Technol.* **2020**. [CrossRef]
15. Ghalambaz, M.; Doostani, A.; Izadpanahi, E.; Chamkha, A.J. Conjugate natural convection flow of Ag–MgO/water hybrid nanofluid in a square cavity. *J. Therm. Anal. Calorim.* **2020**, *139*, 2321–2336. [CrossRef]
16. Benkhedda, M.; Boufendi, T.; Tayebi, T.; Chamkha, A.J. Convective heat transfer performance of hybrid nanofluid in a horizontal pipe considering nanoparticles shapes effect. *J. Therm. Anal. Calorim.* **2020**, *140*, 411–425. [CrossRef]
17. Mehryan, S.; Izadpanahi, E.; Ghalambaz, M.; Chamkha, A. Mixed convection flow caused by an oscillating cylinder in a square cavity filled with Cu–Al 2 O 3/water hybrid nanofluid. *J. Therm. Anal. Calorim.* **2019**, *137*, 965–982. [CrossRef]
18. Ghalambaz, M.; Sabour, M.; Pop, I.; Wen, D. Free convection heat transfer of MgO-MWCNTs/EG hybrid nanofluid in a porous complex shaped cavity with MHD and thermal radiation effects. *Int. J. Numer. Methods Heat Fluid Flow* **2019**, *29*, 4349–4376. [CrossRef]
19. Hajjar, A.; Mehryan, S.; Ghalambaz, M. Time periodic natural convection heat transfer in a nano-encapsulated phase-change suspension. *Int. J. Mech. Sci.* **2020**, *166*, 105243. [CrossRef]
20. Buschmann, M.H. Nanofluid heat transfer in laminar pipe flow with twisted tape. *Heat Transf. Eng.* **2017**, *38*, 162–176. [CrossRef]
21. Bahiraei, M.; Mazaheri, N.; Aliee, F. Second law analysis of a hybrid nanofluid in tubes equipped with double twisted tape inserts. *Powder Technol.* **2019**, *345*, 692–703. [CrossRef]
22. Eiamsa-ard, S.; Wongcharee, K.; Kunnarak, K.; Kumar, M.; Chuwattabakul, V. Heat transfer enhancement of TiO 2-water nanofluid flow in dimpled tube with twisted tape insert. *Heat Mass Transf.* **2019**, *55*, 2987–3001. [CrossRef]

23. Jaramillo, O.; Borunda, M.; Velazquez-Lucho, K.; Robles, M. Parabolic trough solar collector for low enthalpy processes: An analysis of the efficiency enhancement by using twisted tape inserts. *Renew. Energy* **2016**, *93*, 125–141. [CrossRef]
24. Mwesigye, A.; Bello-Ochende, T.; Meyer, J.P. Heat transfer and entropy generation in a parabolic trough receiver with wall-detached twisted tape inserts. *Int. J. Therm. Sci.* **2016**, *99*, 238–257. [CrossRef]
25. Esfe, M.H.; Mazaheri, H.; Mirzaei, S.S.; Kashi, E.; Kazemi, M.; Afrand, M. Effects of twisted tapes on thermal performance of tri-lobed tube: An applicable numerical study. *Appl. Therm. Eng.* **2018**, *144*, 512–521. [CrossRef]
26. Sundar, L.S.; Singh, M.K.; Punnaiah, V.; Sousa, A.C. Experimental investigation of Al2O3/water nanofluids on the effectiveness of solar flat-plate collectors with and without twisted tape inserts. *Renew. Energy* **2018**, *119*, 820–833. [CrossRef]
27. Lim, K.Y.; Hung, Y.M.; Tan, B.T. Performance evaluation of twisted-tape insert induced swirl flow in a laminar thermally developing heat exchanger. *Appl. Therm. Eng.* **2017**, *121*, 652–661. [CrossRef]
28. Kumar, N.R.; Bhramara, P.; Kirubeil, A.; Sundar, L.S.; Singh, M.K.; Sousa, A.C. Effect of twisted tape inserts on heat transfer, friction factor of Fe3O4 nanofluids flow in a double pipe U-bend heat exchanger. *Int. Commun. Heat Mass Transf.* **2018**, *95*, 53–62. [CrossRef]
29. Saysroy, A.; Eiamsa-ard, S. Periodically fully-developed heat and fluid flow behaviors in a turbulent tube flow with square-cut twisted tape inserts. *Appl. Therm. Eng.* **2017**, *112*, 895–910. [CrossRef]
30. Saysroy, A.; Eiamsa-Ard, S. Enhancing convective heat transfer in laminar and turbulent flow regions using multi-channel twisted tape inserts. *Int. J. Therm. Sci.* **2017**, *121*, 55–74. [CrossRef]
31. He, Y.; Liu, L.; Li, P.; Ma, L. Experimental study on heat transfer enhancement characteristics of tube with cross hollow twisted tape inserts. *Appl. Therm. Eng.* **2018**, *131*, 743–749. [CrossRef]
32. Samruaisin, P.; Changcharoen, W.; Thianpong, C.; Chuwattanakul, V.; Pimsarn, M.; Eiamsa-ard, S. Influence of regularly spaced quadruple twisted tape elements on thermal enhancement characteristics. *Chem. Eng. Process. Process. Intensif.* **2018**, *128*, 114–123. [CrossRef]
33. Ruengpayungsak, K.; Saysroy, A.; Wongcharee, K.; Eiamsa-Ard, S. Thermohydraulic performance evaluation of heat exchangers equipped with centrally perforated twisted tape: Laminar and turbulent flows. *J. Therm. Sci. Technol.* **2019**, *14*, JTST0002. [CrossRef]
34. Hasanpour, A.; Farhadi, M.; Sedighi, K. Intensification of heat exchangers performance by modified and optimized twisted tapes. *Chem. Eng. Process. Process. Intensif.* **2017**, *120*, 276–285. [CrossRef]
35. Qi, C.; Wang, G.; Yan, Y.; Mei, S.; Luo, T. Effect of rotating twisted tape on thermo-hydraulic performances of nanofluids in heat-exchanger systems. *Energy Convers. Manag.* **2018**, *166*, 744–757. [CrossRef]
36. Hong, Y.; Du, J.; Wang, S. Experimental heat transfer and flow characteristics in a spiral grooved tube with overlapped large/small twin twisted tapes. *Int. J. Heat Mass Transf.* **2017**, *106*, 1178–1190. [CrossRef]
37. Eiamsa-Ard, S.; Samravysin, P. Characterization of Heat Transfer by Overlapped-Quadruple Counter Tapes. *J. Heat Transf.* **2018**, *140*. [CrossRef]
38. Rudrabhiramu, R.; Kumar, K.H.; Kumar, K.K.; Rao, K.M. Heat Transfer Enhancement Using Overlapped Dual Twisted Tape Inserts with Nanofluids. In *Advances in Applied Mechanical Engineering*; Springer: New York, NY, USA, 2020; pp. 123–130. [CrossRef]
39. Manninen, M.; Taivassalo, V.; Kallio, S. *On the Mixture Model for Multiphase Flow*; Technical Research Centre of Finland: Espoo, Finland, 1996.
40. Goossens, W.R.A. Review of the empirical correlations for the drag coefficient of rigid spheres. *Powder Technol.* **2019**, *352*, 350–359. [CrossRef]
41. Khanafer, K.; Vafai, K. A critical synthesis of thermophysical characteristics of nanofluids. *Int. J. Heat Mass Transf.* **2011**, *54*, 4410–4428. [CrossRef]
42. Bianco, V.; Manca, O.; Nardini, S.; Vafai, K. *Heat Transfer Enhancement with Nanofluids*; CRC Press: Boca Raton, FL, USA, 2015.
43. Maiga, S.E.B.; Palm, S.J.; Nguyen, C.T.; Roy, G.; Galanis, N. Heat transfer enhancement by using nanofluids in forced convection flows. *Int. J. Heat Fluid Flow* **2005**, *26*, 530–546. [CrossRef]

MDPI
St. Alban-Anlage 66
4052 Basel
Switzerland
Tel. +41 61 683 77 34
Fax +41 61 302 89 18
www.mdpi.com

Nanomaterials Editorial Office
E-mail: nanomaterials@mdpi.com
www.mdpi.com/journal/nanomaterials

MDPI
St. Alban-Anlage 66
4052 Basel
Switzerland

Tel: +41 61 683 77 34
Fax: +41 61 302 89 18

www.mdpi.com

ISBN 978-3-0365-2170-1